3D printing of gyroid structures for superior structural behaviour

Catarina Maia Moreira da Silva

Dissertação de Mestrado

Orientador: Prof. Jorge Lino
Co-orientador: Prof. Jorge Belinha

Mestrado Integrado em Engenharia Mecânica

Julho 2019

"Uma busca começa sempre com a sorte de principiante. E termina sempre com a prova de conquistador."

Paulo Coelho

Esta página foi intencionalmente deixada em branco.

Abstract

Additive manufacturing (AM) has been taking place in the industries over the last years. This new emerging technology was firstly seen only as a prototyping technique however now it is considered as a manufacturing process. It presents many possibilities not only to replace in many situations traditional manufacturing processes but also to complement and improve them. Nevertheless, there is still a huge knowledge gap that needs to be filled by research. This is the lack of predictability regarding to the mechanical properties of the specimens and the use of superior structures, that are only possible to manufacture by AM.

The present dissertation was proposed under the scope of a simulation project of Polylactic Acid (PLA) parts made from a low cost additive manufacturing process, fused filament fabrication (FFF). The main goal of this dissertation is to have experimental output in order to verify the software output, but also to understand the possibility of replacing the traditional infill by superior structures, more specific the gyroid one. First of all a 3D printer was assembled, afterwards the influence of the deposition orientation in the mechanical properties was studied. Finally, the gyroid infill influence in the specimens mechanical properties and the gyroid's properties was investigated.

Finally, the results were analysed and it was possible to conclude that for the most uniaxial load situations the best orientation deposition is the 0°, since the filament orientation is the same as the load one. On the other hand, the gyroid structure presents extraordinary properties in impact or compression situations in the construction direction (z). However while conducting standard tests the gyroid behaviour was not as good since the direction of the test was perpendicular to the gyroid's construction one.

Keywords: Additive manufacturing, Fused Filament Fabrication, low cost 3D printer, gyroid structure

Esta página foi intencionalmente deixada em branco.

Resumo

O fabrico aditivo (FA) tem vindo a ocupar um lugar de destaque nos últimos anos. Esta nova tecnologia emergente foi vista inicialmente como um método de prototipagem rápida, contudo atualmente é considerada outro processo de produção. Esta apresenta diversas possibilidades, não só para substituir em várias situações os processos atuais mas também para os completar e melhorar. Não obstante, ainda existe um grande lacuna na industria que necessita ser preenchida com conhecimento obtido através da investigação científca. Esta lacuna reside na falta de predictabilidade no que toca às propriedades mecânicas dos provetes e o uso de estruturas superiores, que são apenas possíveis obter através de FA.

Esta dissertação foi proposta no âmbito de um projeto de simulação de peças fabricadas em PLA em máquinas de baixo custo (FFF). O principal objetivo desta dissertação é obter dados experimentais para verificar os dados obtidos pelo software de simulação, e adicionalmente estudar a possibilidade de substituir o preenchimento tradicionalmente usado por estruturas superiores, mais especificamente o *gyroid*. Inicialmente foi construída uma impressora 3D, de seguida foi estudada a influência de orientação de deposição nas propriedades mecânicas dos provetes. Finalmente, foi investigada a influência do preenchimento *gyroid* nas propriedades mecânicas dos provetes e ainda as propriedades do mesmo.

No final, os resultados foram analisados e foi possível concluir que para a maioria das situações de carga uniaxial a melhor orientação de deposição é 0°, uma vez que o filamento é orientado na mesma direção que a carga. Por outro lado, a estrutura *gyroid* apresenta propriedades muito favoráveis quando sujeita a situações de impacto e compressão na direção de construção (z). Contudo, quando foram realizados os ensaios normalizados, o comportamento do *gyroid* não foi tão vantajoso como esperado uma vez que a direção de teste foi perpendicular à direção de construção do *gyroid*.

Palavras-chave: Fabrico aditivo, Fabricação por extrusão de filamento fundido, impressoras 3D de baixo custo, estrutura *gyroid*

Esta página foi intencionalmente deixada em branco.

Acknowledgements

This work would not be possible without the contributions of some, who directly or indirectly had their role to play in this endeavour. I dedicate this work to all of those mentioned below and I sincerely hope that I can meet the expectations of everyone that contributed to this project.

First, I would like to express my gratitude to my tutor, Prof. Jorge Lino, who gave me the opportunity to work in a forthcoming area as additive manufacturing and always gave me all the necessary support and material to do the best work possible. I also thank Prof. Jorge Belinha for his expertise and availability to help clear all my doubts.

I would also like to thank to the entire team from *laboratório de desenvolvimento de produto e serviços* from DEMec for all their support with my technical and theoretical questions.

I must extend my appreciation to Engineer Eduardo Marques, researcher from DEMec, for the realisation of the impact tests.

I would also like to acknowledge Andreia Durães, technical assistant from INEGI, for the realisation of the Charpy impact tests and to Emilia Soares, technical assistant from DEMec, for helping me with the utilisation of the stereo binocular microscope.

Furthermore, I must show my appreciation to my friends who I had the pleasure to meet in these last five years who made my journey in FEUP unforgettable and a lot easier. Thanks specially to those that in a more direct or indirect way always find the patience to help me with my thesis.

Finally, I want to express my gratitude to my family, my parents and brother, without them any of my achievements with be possible. Thank you for the unconditional support and for always helping me fulfill my objectives, and specially for making me the person I am today.

The author truly acknowledges the work conditions provided by the Applied Mechanics Division (SMAp) of the department of mechanical engineering (DEMec) of Faculty of Engineering of the University of Porto (FEUP), and by the MIT-Portugal project "MIT-EXPL/ISF/0084/2017", funded by Massachusetts Institute of Technology (USA) and "Ministério da Ciência, Tecnologia e Ensino Superior - Fundação para a Ciência e a Tecnologia" (Portugal).

Additionally, the authors gratefully acknowledge the funding of Project NORTE-01-0145-FEDER-000022 - SciTech - Science and Technology for Competitive and Sustainable Industries, cofinanced by Programa Operacional Regional do Norte (NORTE2020), through Fundo Europeu de Desenvolvimento Regional (FEDER).

Finally, the author acknowledges the synergetic collaboration with the collaborators of "Computational Mechanics Research Laboratory CMech-Lab" (ISEP/FEUP/INEGI), and its director, Prof.Dr. Jorge Belinha, and its senior advisors, Prof.Dr. Renato Natal Jorge and Prof.Dr. Lúcia Dinis.

Esta página foi intencionalmente deixada em branco.

Contents

Esta página foi intencionalmente deixada em branco.

Acronyms

Acronyms

AM	Additive Manufacturing
ASTM	American Society for Testing and Materials
BJ	Binder Jetting
CAD	Computer Aided Design
DEMec	Departamento de Engenharia Mecânica
DG	Double Gyroid
FDM	Fused Deposition Modelling
FE	Finit Element
FEUP	Faculdade de Engenharia da Universidade do Porto
FFF	Fused Filament Fabrication
INEGI	Instituto de Ciência e Inovação em Engenharia Mecânica e Engenharia Industrial
LDPS	Laboratório de Desenvolvimentos de Produtos e Serviços
MIT	Massachussets Institute of Technology
MJ	Meterial Jetting
PJP	Plastic Jet Printing
PLA	Polylactic Acid
Polyjet	Photopolymer jetting
RepRap	Replicating Rapid Prototyper
SD	Standard Deviation
SG	Surface Gyroid
SLS	Selective Laser Sintering
STL	Stereolithography

Symbols

σ	Stress	ΔL_0	increase
ε	Strain	μ_n	Poisson's ratio
E	Modulus	F	Load
k	Coefficient	d	distance
A	Area	l	length
L	Length	b	width
L_0	Initial length	h	thickness
s	deflection		

Esta página foi intencionalmente deixada em branco.

List of Figures

List of Tables

Chapter 1

Introduction

The work composes the master thesis for the conclusion of the Master's degree in Mechanical Engineering at FEUP (2018/2019), specialisation of Production, Conception and Manufacturing. This thesis was made under the scope of the Mechanical Engineer Department and the project Simul3F: *"Development of new numerical tools and constitutive models to simulate the fused filament fabrication – a low-cost additive manufacturing process"*. This report was done in order to describe the work produced during the second semester of the final 5^{th} year.

1.1 Contextualisation and motivation

In 1987 the first commercial use of Additive Manufacturing (AM) appeared with the coming of a stereolitography (SL) printer designed by a company named 3D Systems. Rapidly other companies started developing and commercialising different versions of this process. In 1991 three new AM technologies were commercialised, including Fused Deposition Modeling (FDM) by Stratasys. As late as 1996 the first low cost 3D printers were introduced to the market. At this time Stratasys announced the Genisys machine, which used an extrusion process similar to Fused Deposition Modeling (FDM).

By 2011 several industries were adopting AM as their main method of manufacturing. It was only at this year that a crucial thing happened, a key FDM patent expired, inexpensive equipment in the form of kits and fully assembled machines based on the RepRap open-source project became available. Since their introduction, these low-cost personal systems have experienced very strong growth [1].

Nowadays, AM has an essential role in the era of Industry 4.0. The utilisation of modern manufacturing technologies within the context of high pace prototyping plays an important part in economic competitiveness, due to the necessity for mass customisation [2].

The biggest challenges for FDM machines being widely used in the industry is its difficulty to predict quantitatively the influence of the printing parameters on the printed parts and the influence of the different structures in order to achieve superior structural behaviour. During the

preliminary research done, a gap of knowledge about structural behaviour in 3D prints was found in the literature.

Finally, this project was in agreement with a personal preference for processing technologies which meant the proposed challenged was of great individual interest.

1.2 Objectives of the dissertation

The main objectives of this dissertation were:

- After conducting a market research, the advantages and disadvantages of the existing products were found and this knowledge was used to assemble a 3D printer;
- Establish a base-line about the importance of the printing parameters, especially the deposition orientation on the part's mechanical properties;
- Study the foam structures and understand the main characteristics of the gyroid structure;
- Observe the influence of the gyroid infill density in the part's mechanical properties;
- Compare the gyroid infill with the conventional infill process.

1.3 Proposed project

The project where the present dissertation is included, consists of the development of a simulation software in order to create a constitutive model of the fused filament fabrication process using a low cost 3D printer. Its main goal is to fill a gap of knowledge in this area and allow its users to predict the mechanical properties of the 3D printed parts. The development of this thesis was done in order to produce the 3D printed parts and test them mechanically to corroborate the simulations results.

The methodology followed during the accomplishment of this project consisted of a set of tasks that can be summarised as follow:

1. Literature review;
2. Designing and assembly of a low cost 3D printer;
3. Planning and design of test specimens as function of the printing parameters;
4. Dimensional control and weighing of test specimens;
5. Mechanical test and data analysis.

This project was divided in four different stages, in order to fulfil the objectives proposed before. This stages are:

1. **Stage 1:** Market research was done about existing 3D printers and the respective advantages and disadvantages. Afterwards, it was possible to assemble a 3D printer from scratch based on the market possibilities.

2. **Stage 2:** Determine the influence of the filament deposition orientation in the mechanical properties of the printed specimens. Therefore, it was tested in four different orientations, 0°, 90°, ± 45° and 45 °. Tensile, compression and flexural tests were conducted according to the specific standards for these specimens.

3. **Stage 3:** Understand the influence on the gyroid infill and its density in the specimens' mechanical properties. Hence, three different densities were tested: 20%, 50% and 80% and the tests were conducted the same way as in the previous stage plus two impact tests, a Charpy one and another that is basically a compression at high velocity.

4. **Stage 4:** In this last stage the gyroid's behaviour in compression with and without an outside perimeter was studied, this test wasn't according to any standard, and also the gyroid's structure anisotropy was studied, therefore a gyroid unitary structure was compressed in the three directions.

1.4 Structure of the Document

A specific report structure was determined in the beginning of this project, shown in the figure 1.1. Starting off with the context of this project, an initial bibliographic review was done. This was divided in three parts: additive manufacturing, focusing on the filament fused deposition method, low cost printers, in order to decide which printer to build and to understand the influence of the printing parameters, and foam structures, focusing on the gyroid one. After that, there is the methodology chapter, where the project stages and the experimental procedure of the mechanical tests are described. Afterwards, the following chapter sums up the results and respective discussions and explanations for each mechanical test of each stage. Finally, the global conclusions that outcome from this project, and also some possible future works are presented.

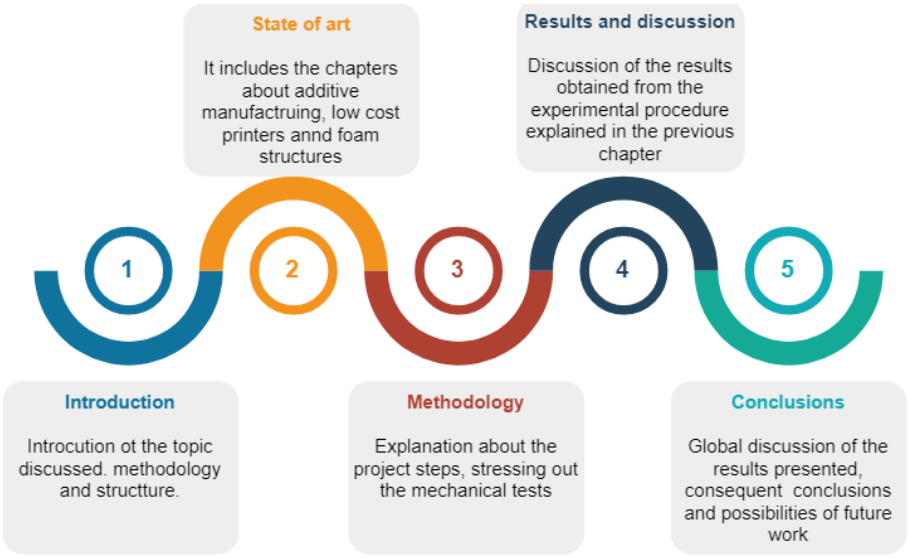

Figure 1.1 Report structure scheme.

Chapter 2

Additive Manufacturing

In this chapter a revision will be done on the literature about the topics most relevant for this dissertation.

2.1 Brief Introduction

Additive Manufacturing, commonly known as 3D printing, is defined by the ISO/ASTM standard 52900 as the process of joining materials to make parts from 3D model data, usually layer upon layer, as opposed to subtractive and formative manufacturing methodologies. On the other hand, the same ISO standard defines 3D printing as the fabrication of objects through the deposition of a material using a print head, nozzle, or another printer technology [3, 4].

This technology has been growing rapidly these last years because of the many advantages it has to the users, therefore to both personal (hobby) and industrial users. As shown in figure 2.1 additive manufacturing technologies can be used in several different industries, ranging from Industrial/business to architectural (the "other" category refers to a wide range of industries where it can be included oil, gas, etc.) [3].

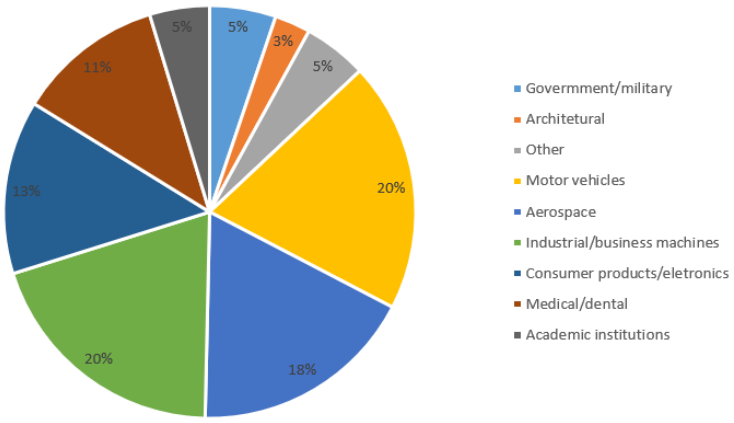

Figure 2.1 Main uses of additive manufacturing technologies in industries. Adapted from [3]

Consequently AM technologies are used for several different endings such as functional parts to presentation models (figure 2.2)

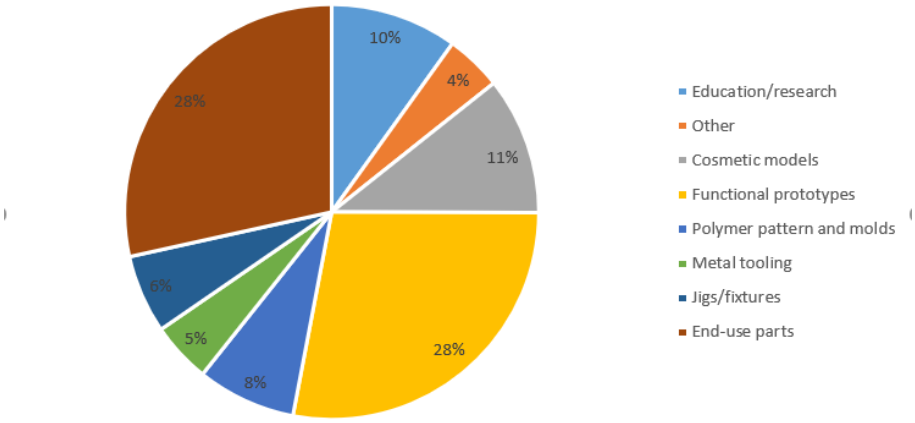

Figure 2.2 Additive manufacturing technologies applications. Adapted from[3]

As it has been said before the additive manufacturing industry has been growing over the last eight years, since the average annual growth of both products and services over the past four years (2015-2018) was around 24.4%.

It is considered an additive manufacturing industrial system when a system is sold for 5000 euros or more , the ones that are less than that are called desktop or low cost 3D printers.

Since 2009 there was an accentuated growth of industrial systems. With an increase from 2017 of 17.8%, the estimated growth in 2017 was 25.1% and 4.2% in 2016, the following chart shows these growth (2.3) [3].

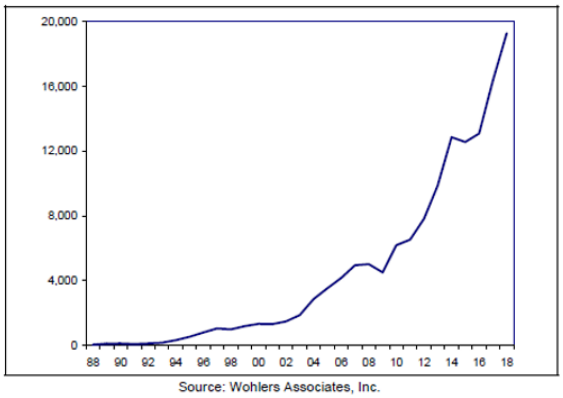

Figure 2.3 Growth of industrial technologies, units vs.years [3].

In parallel to the sales of desktop printers, such as products from RepRap, Formlabs, Makerbot, Ultimaker, etc., have shown and astounding growth. From 2017 to 2018 there was an increase of 10.56% on sales, as it is shown in figure 2.4.

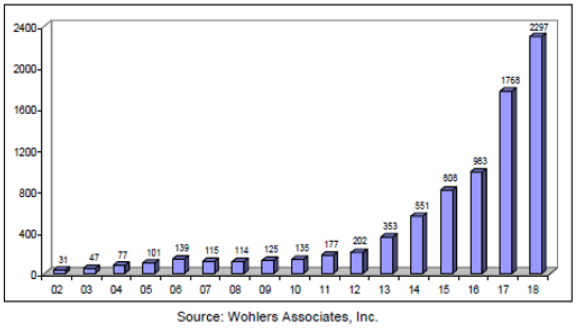

Figure 2.4 Growth of sales of desktop printers, units vs.years [3].

In 2018 the average selling price of a desktop 3D printer was 1020 euros compared to 967 euros in 2016. On the other hand, in 2017 the average selling price for an industrial system was 83324 euros which was a reduction of 8814 euros compared to the previous year [3].

The additive manufacturing of a part has three different aspects (figure 2.5) [5]:

- **Design in a CAD software;**
- **Obtainment of the G-Code;**
- **Printing.**

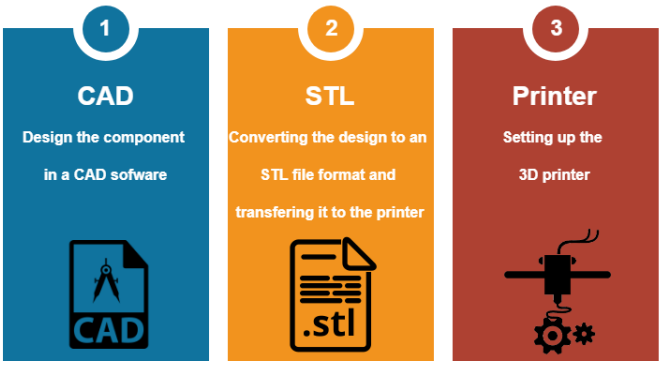

Figure 2.5 3D printing process. Adapted from [5]

The ISO/ASTM 52900 standard categorises the AM technologies in seven distinct processes, such as [3]:

- **Material Extrusion:** additive process in which material is selectively dispensed through a nozzle or orifice;
- **Material Jetting:** process in which droplets of build material are selectively deposited;
- **Binder Jetting:** process in which a liquid bonding agent is selectively deposited to join powder materials;

- **Sheet lamination:** an additive manufacturing process in which sheets of material are bonded to form a part;
- **VATphotopolymerization:** an additive manufacturing process in which liquid photopolymer in a VAT is selectively cured by light- activated polymerization;
- **Powder Bed Fusion:** an additive manufacturing process in which thermal energy selectively fuses regions of a powder bed;
- **Directed Energy Deposition:** an additive manufacturing process in which focused thermal energy is used to fuse materials by melting as they are deposited.

2.2 Material Extrusion Processes

Material Extrusion consists of the deposition of material that is selectively dispensed through a nozzle or orifice. Consequently, the extruded materials are not limited to melted thermoplastics, viscous liquids and slurries can be loaded into syringes or hoppers and dispensed without any phase change of the material. So, ceramics, composites, metal-filled clays, concrete, food and living cells suspended in hydrogel or another substance can be extruded by this method, shown in figure 2.6.

The oversimplification of this process is that the machine forces a semi-liquid material through the nozzle as either the extrusion head or the build platform moves in *xy* plane. After one layer is completed, the build platform moves down (or the extrusion head moves up), and the next layer is extruded bonding to the previous one. Therefore, theoretically, any material that can be put in a *pasty* state and then harden by either physical or chemical action can be processed with this principle. Consequently, depending on the material, the nozzle can go from the room temperature to the specific melting temperature, which happens in the thermoplastics extrusion. So, the most important aspect is that the material filament while being dispensed solidifies and bonds to the build platform or the filament already deposited there. The solidification can be either physical, cooling, or chemical, ex. photopolimerization.

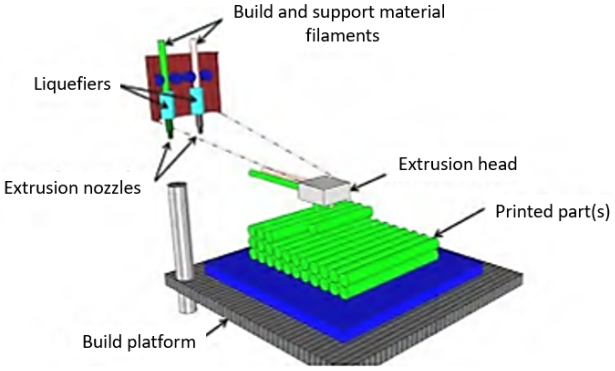

Figure 2.6 Material extrusion scheme. Adapted from [3]

The feeding "head" is also controlled to initiate and interrupt the extrusion according to the need of material deposition in the specific zones of the part that is being build. On demand of the system is that the extrusion must be done at constant pressure during the deposition, so that, combined with a controlled speed, the filament section is constant [3, 6].

Finally, compared to other AM processes, the material extrusion is often less expensive and relatively easy to design, manufacture and operate. However, this process is usually slower then others since the material is dispensed through a small nozzle (0,2-0,4mm usually) and the time it takes to fill a big area is long.

There are several variations of this process either developed or being developed related with the material feeding. The most common technique is to feed the extrusion with a continuous material filament of a bigger diameter that is driven by rollers and pushed to the interior of the head (figure 2.7 a). The filament behaves like a piston in the entry of the system extrusion, before it melts applying a pressure on the forward melting material. Since the feed is continuous the pressure ejects the material through the nozzle. The main limitation of this system is the materials that can be used, the filament must have mechanical properties that ensure no buckling before the entry in the extrusion head. Additionally the material must have a continuous flow. The most common problems seen in this system are the filament creeping, due to possible diameter variations along the filament length, the filaments' temperature increase before entering in the nozzle head, compromising its function as piston, and even the extrusion temperature variations, that can increase the necessary pressure to dispense the material. As an alternative to avoid the failures mentioned previously the material used should be in the shape of fine serrated rods, with the profile of racks on the sides (figure 2.7 b). Another option is to use a material powder or granulate to be processed by an extruder screw, or the material could be melted and forced to go through the nozzle (figure 2.7 c). Finally, the feed can be done with the material already in the semi-liquid form, using a piston or just pressure, to extrude the material, the system can be heated or not depending on the material properties (figure 2.7 d, e) [6].

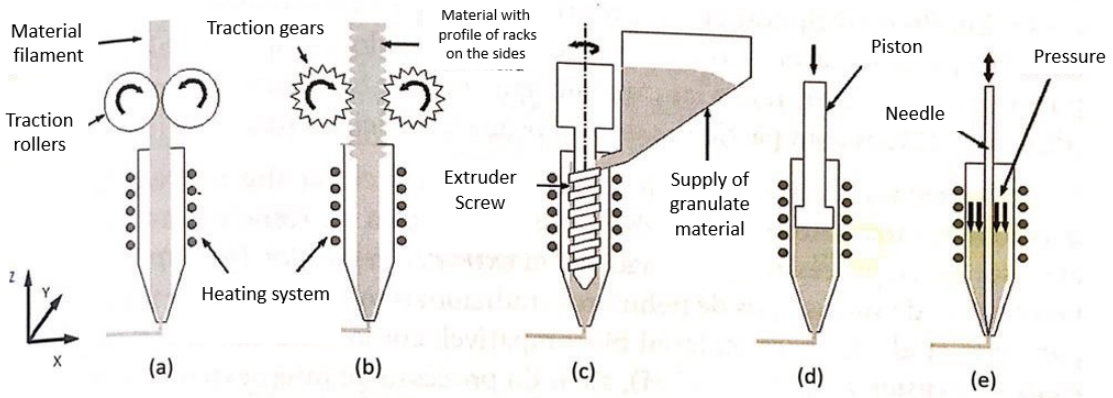

Figure 2.7 Material feeding principals: (a) continuous material filament, (b)fine serrated rods, with the profile of a racks on the sides, (c) material powder or granulate to be processed by an extruder screw, (d) piston, (e) pressure. Adapted from [6]

2.2.1 Filament Fused Deposition

The Additive Manufacturing technology adopted in this project is a Material Extrusion process, more specifically Fused Filament Fabrication (FFF). The main difference between FFF and Fused Deposition Modelling concerns more in the legal aspects then in the technological one. FDM is the designation for a technology and commercial brand patented by Stratasys. The designation FFF was adopted later on, boosted by the open source concept, RepRap, as a more generic way to present the additive material extrusion manufacturing throw the material deposition passing by a nozzle. There have been other designations as Plastic Jet Printing (PJP) [6, 7, 8].

In this process, first of all a geometric model of conceptual design is created on a CAD software, that uses .STL ou IGES formatted files. Afterwards it is imported to a software that automatically generates support structures and slices the CAD file into horizontal layers. The slice thickness can be set manually between 0.178 and 0.356 mm according to the parts' needs. Then, the tool paths are generated and uploaded to the machine as a g-code. As it has already been outlined in the previous section a semi-liquid material is extruded through the head and than deposited in ultra thin layers, since the air surrounding the head is at a temperature below the material's melting point, the material solidifies quickly. The head follows the path obtained previously, generating the desired layer (shown in figure 2.8). The machine can have two extruders, which is very helpful in order to print the supports in a different soluble material [4, 7].

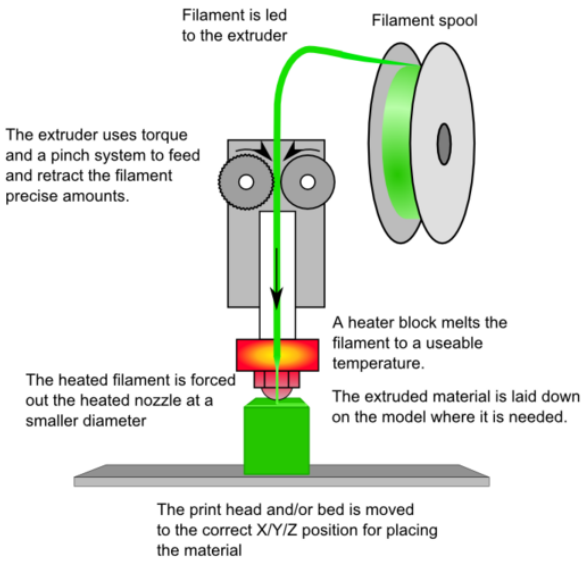

Figure 2.8 Fused Filament Deposition scheme [8].

Parameters such as material column strength, material flexural modulus, material viscosity, positioning accuracy, layer widths, deposition speed, volumetric flow rate, tip diameter, envelope temperature and part geometry affect the performance and functionality of the system [6].

2.2.1.1 3D printers Models

First of all there are two categories of printer important to distinguish [7]:

- **Professional ones:** have an outside solid structure to protect the mechanical and electrical part, work with a close source software and patented operative systems. The user doesn't have much freedom to set up the printer settings (shown in figure 2.9);
- **Non professional ones:** low cost printer, with open source software and hardware, better explained further in section 2.2.1.3 (shown in figure 2.10).

Figure 2.9 Professional printer, Rize One from Rize3D [9].

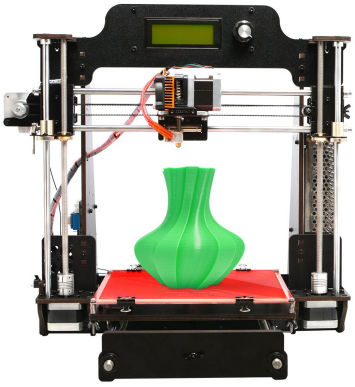

Figure 2.10 Non professional printer from Geetech [10].

This project will be focused on non professional, also known as low cost printers.
FFF printers are divided according to its movement [7, 11]:

- **Cartesian:** based on the Cartesian coordinate system in mathematics, this technology uses three-axis: X, Y, and Z to determine the correct positions and direction of the print head (shown in figure 2.11). There are two types according to the extruder movement:
  - *Gantry:* the extruder moves in X and Z axis (cartesian XZ Head setup);

  - *Build platform with a descending motion:* the build platform is on the upper zone of the printer, and descends while the extruder prints in the XY plane (cartesian XY Head setup)

- **Delta:** these machines operate with Cartesian coordinates. This involves a round printing plate that is combined with an extruder that is fixed at three triangular points. Each of the three points then moves up and down, thereby determining the position and direction of the print head, shown in figure 2.11;

- **Polar:** its' positioning is not determined by the X, Y, and Z coordinates, but by an angle and length. This means that the plate rotates and moves at the same time, with the extruder moving up and down;

- **Robotic arms:** 3D printing has begun to incorporate robotic arms into their production process, most notably seen in the 3D printing of homes and buildings, this technology still remains in the development stage.

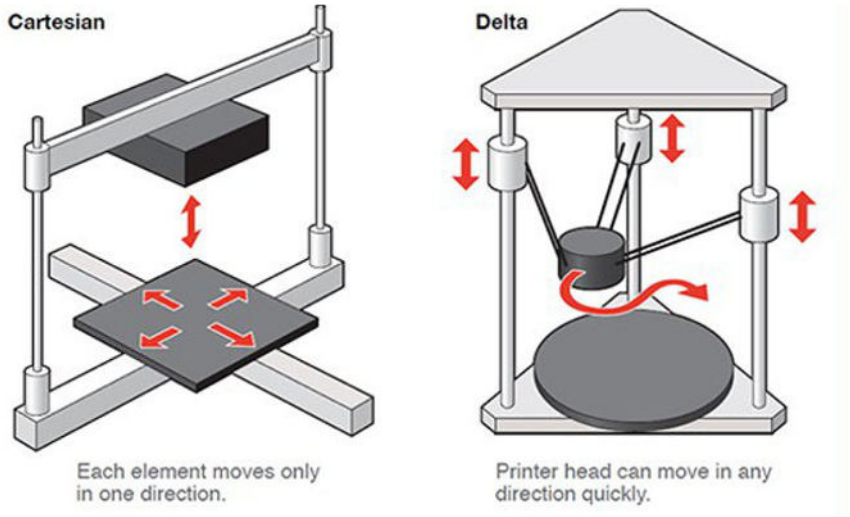

Figure 2.11 Cartesian printer movement (left), delta printer movement (right) [11].

In conclusion, the 3D printer type chosen for this project is a cartesian XZ head setup due to adversities and time reasons, it will be further explained in chapter 4.

A cartesian 3D printer has the following components (shown in figure 2.12), all these component will be explained and chosen in chapter 4 [12]:

- Controller board;
- Filament;
- Frame;
- Stepper motors;

- Belts;
- Threaded rods;
- End stops;
- Power Supply;
- Print Bed;
- Print Head;
- Feeder System;
- User interface and connectivity.

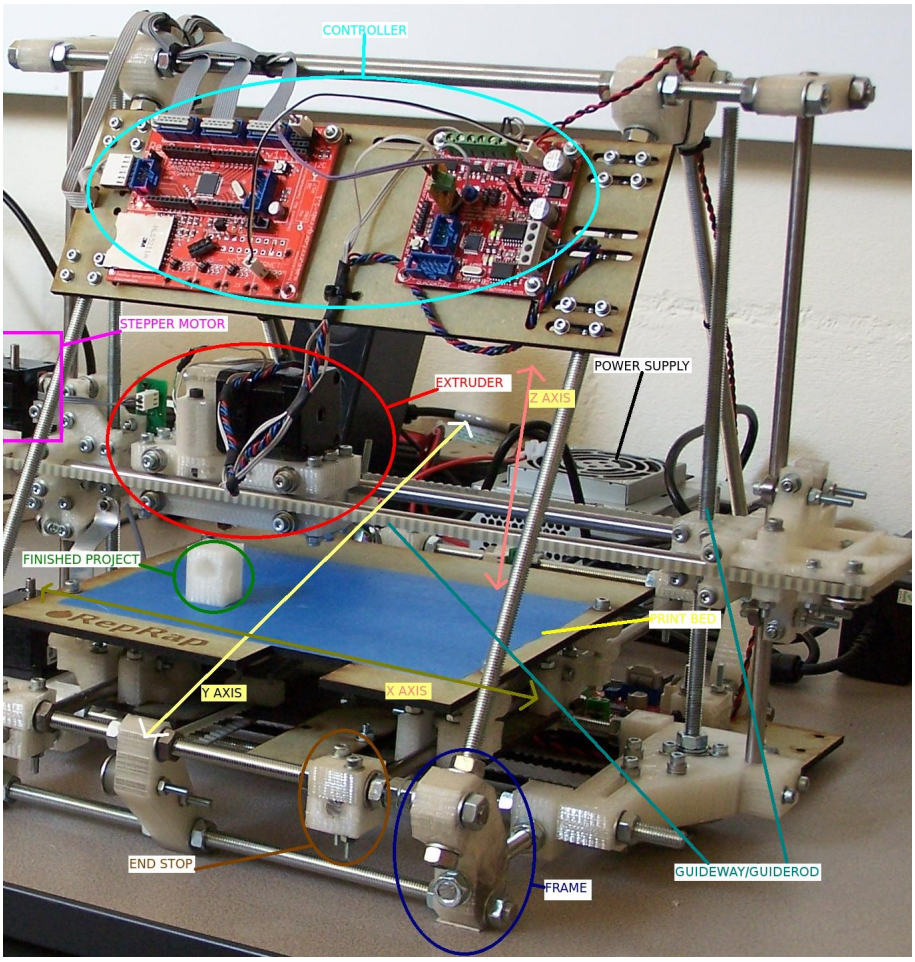

Figure 2.12 3D printer components [13].

Finally it is important to distinguish the two extrusion methods used in cartesian printer: **Direct and bowden**, both shown in figure 2.13. Both set-ups use an extruder to push filament through a heated nozzle, either directly or through a bowden tube [14].

Table 2.1 Direct extrusion vs Bowden [14].

Type of extrusion	Characteristics	Pros	Cons
Direct	The extruder pushes the filament directly into the nozzle;	Better Extrusion Faster Retraction Less Power Motor Wider Range of materials	Burdened movements
Bowden	It is mounted on the printer's frame; Pushes and pulls filament through a long PTFE bowden tube into the hot end;	Cleaner movements Larger Build Volume Compact Size	More powerful motor Slower Response time Smaller range of materials

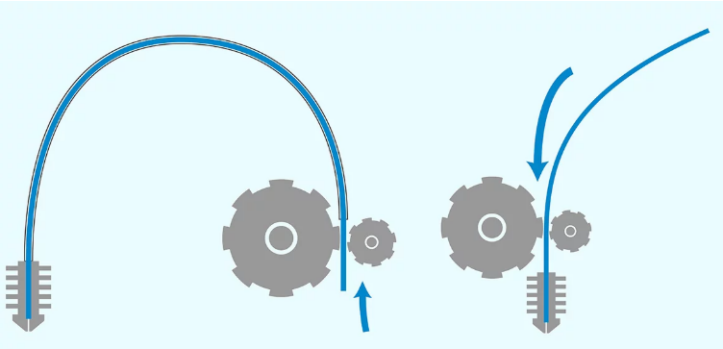

Figure 2.13 Bowden vs. Direct extrusion [14].

2.2.1.2 Materials

The common filament diameter used in FFF printers is 1.75mm or 2.85mm. FFF mostly uses thermoplastics due to its mechanical properties which makes them easier to use achieving good results. The most common thermoplastics used are: PLA, ABS, PC, Nylon, PP, Ultem and a mixture for any 2 types of these materials. Every material has its main advantages and disadvantages, it is up to the user which one to use according to the printer and final goal [6, 5, 15]:

- ***Polylactic Acid* (PLA):** it is a biodegradable polyester which does not occur naturally, derives primarily from annually renewable resources (maize/corn). Its melting temperature is within the range 180-230°C. The PLA filament isn't expensive, the average price for 1kg is 26,5€. It is available in natural (translucent white) or in many bright colours, solid or half transparent, and the printed objects have a beautiful smooth surface. There is a special variant of PLA that is soft or flexible, it should be extruded at lower temperature and very low speed, it can be used to print flexible joints, belts, tires, etc. It can also be used for medical application, for example orthopedic devices, replacing temporary titanium screws and sutures fro absorbed ones [16].

- ***Acrylonitrile Butadine Styrene* (ABS):** has a good ratio between properties and price, bridges a gap between higher performance engineering thermoplastics such as PC and commodity materials such as PS. Its melting temperature is within the range 210-260°C. ABS filament cost more or less the same as PLA, and it is also a common printing material. An

ABS part should be printed on a heated bed, around 100°C covered with *Kapton* tape in order to improve bonding to the build platform. The main advantage of ABS over PLA is that the resulting parts are more robust, less brittle, and more resistant to higher temperatures.

- ***Polycarbonate* (PC):** due to its useful engineering properties over a wide temperature range, became established in applications requiring a combination of properties, particularly impact resistance and transparancy. Its melting temperature is around 270-300°C, the filament price is still quite expensive around 80€/kg.
- **Nylon**: known for its strength, light weight and durability. It should be extruded at a higher temperature compared to PLA, around 245°C. It is mainly used to print parts that need high resistance and low surface friction. However, it is way more expensive when compared to those two since the filament cost is the double.
- ***Polyvinyl Alcohol* (PVA)**: it is a water soluble plastic polymer that can be used to print support structures for PLA and ABS parts, since it dissolves easily in warm water while the print's surface is left intact. Its printing temperature is around 170°C.
- ***Polypropylene* (PP)**: low cost plastic with good mechanical performance and a huge variety of applications. Its melting temperature is around 160°C.
- **Ultem**: amorphous thermoplastic, similar characteristics to PEEK. It is cheaper but also has lower impact strength and usable temperature. Its melting temperature is around 217°C.

Additionally, many thermoplastics are being used such as [17]:

- **Thermoplastic polyurethane (TPU)**: is appropriated for production of durable elastomer parts with additive manufacturing. The 3D printing material enables prototyping of high functioning, durable and complex parts with the expected material properties found in an elastomeric material. The parts present good tear resistance, fatigue, memory, and recovery associated with elastomeric materials;
- **Thermoplastic elastomer (TPE)**: is a soft thermoplastic elastomer specially formulated to simulate rubber-like flexibility and functionality. This material maintains high flexibility and has excellent shape retention. It has an inherent surface texture and modest feature definition, and can be finished in a few basic color options;
- **Thermoplastic copolyester (TPC)**: it can be used for the same application as TPU and TPE, but for more extreme environments, like outdoors. Usually the work at a extrusion temperature around 225-235°C but don't require a heated bed.

2.2.1.3 Open Source Software and Hardware

Open Source has gained popularity with the rise of the Internet, which provided access to diverse productions models, communication paths, and interactive communities. Even though initially it

was just related to software, it is now being applied to many other areas. Therefore in this section it will be briefly presented both software and hardware open sources.

By definition an open source software is a software which the human-readable source code is made available under a copyright license. Therefore, it allows the user to change and improve the software and then distribute it in modified or unmodified form. In conclusion, open source software is the most prominent example of open source development and often compared to user generated content. A good example of an open source software applied in 3D printing is the ReplicatorG. It is a printing program being used by MakerBot Replicator, Thing-O-Matic, Cup-Cake CNC, RepRap machine, or generic CNC machine. It presents many advantages such as ability to process a GCode or STL file, has a cross platform, easy to install and finally is based on the familiar Arduino/Processing environments.

An open source hardware is a computer and electronic hardware designed in the same fashion as Open Source software. It was primarily used in reflection of the free information's release about hardware design, such as schematics, bill of materials, PCB layout data. When referring to open source hardware it is impossible to not refer its biggest example the Arduino board (figure 2.14). Arduino's hardware is completely open source (under CC), with design files and specifications available, control software (under GPL) and documentation (also under CC). The only thing non-free about it is the trademarked name. Therefore, this micro-controller board can be found in the heart of a many Open Source hardware devices, specially 3D printers.

Figure 2.14 Arduino board used in a low cost 3D printer [18].

Finally it is not possible to talk about open source hardware without referring to firmware. It is pre-compiled and flashed on to the printer board. It is configured with human editable files located on an SD-card plugged into the printer electronics. As such, there is no need for ordinary users to compile the software nor install any development tools. The software can receive G-Code from the USB port, the serial port, the SD card, the Ethernet or WiFi interface via http [19].

In conclusion, an open source 3D printer is a printer whose hardware and software is available to the public, typically under a license. The information can be used by anyone to build, or improve the 3D printer [18, 8].

2.3 Material Jetting: PolyJet technology

Since in the last stage of the project it will be study the anisotropy of the gyroid structure it was also decided to print it using a material jetting process. Since, it presents less anisotropy because the polyjet machine available is a professional one and the FDM ones are non professional, therefore it will be possible to compare both results.

The Material Jetting (MJ) process uses inkjet printing heads to deposit droplets of build material. They are dispensed selectively as the printing head(s) move along the building plataform. The materials used in this techonolgy are mostly photopolymers or wax-like materials [3]. One of the most used MJ techonolgies is the Polyjet from Stratasys.

Polyjet produces smooth, accurate parts, prototypes and tooling, with a layer resolution and accuracy down to 0.1 mm. In the phase of pre-processing, after uploading a 3D CAD file into the software, it automatically calculates the placement of photopolymers and support material. The production itself can be explained succinctly as a carriage of four or more print heads and ultraviolet (UV) lamps move along the work space depositing, in the defined places, droplets of photopolymers, that solidify when exposed to UV light, shown in Figure 2.15. This process happens layer by layer. In the spots where there are overhangs or complex shapes it is required a support, a removable material is jetted. The support material can be removed with water, by hand or with a solution bath [20].

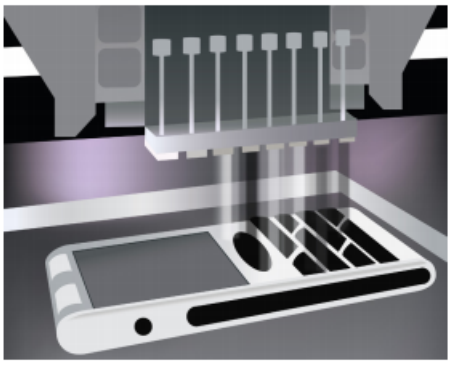

Figure 2.15 Polyjet technology process [20].

The printer used is a **Object Eden260V** from Stratasys (figure 2.16), with a building volume of 255x252x200 mm and the material is VeroGray from Stratasys. In table 2.2 it is represented some of the printer's specifications [21].

Table 2.2 Object Eden260V specifications [21].

Support Material	SUP705 (waterjet removable)
Resolution	X-axis: 600 dpi Y-axis: 600 dpi Z-axis: 1600 dpi
Printing Modes	High speed: 30 microns resolution High quality: 16 microns resolution
Minimum layer thickness	Horizontal build features: 16 microns

Figure 2.16 Object Eden260V from Stratasys [21].

Comparing the FDM technology on a professional printer, not a low cost one like the ones used in this dissertation, with the polyjet regarding to (figure 2.17) [20]:

- **Process time:** it is highly dependent on the resolution chosen, if the surfaces are smooth and the required mechanical properties. On average, both technologies have similar total elapsed times;
- **Pre-process:** both technologies offer very simple file processing, that can make ready-to-print files in less than five minutes. However, FDM unlike polyjet allows the user to adjust the building process to math the applications' demands;
- **Post-process:** related with support removal and part cleaning, there are similarities between both technologies. FDM has either a fully automated soak in a tank to remove soluble supports or a manual step that removes rigid, breakaway supports with simple hand tools. On

the other hand, polyjet demands a manual step to remove the material support by spraying with a WaterJet;

- **Office Environment:** both FDM and Polyjet require very little special requirements, only a minimal plumbing and electrical work;
- **Ease of use:** both technologies are relatively user-friendly beginning with the simplicity of file setup;
- **Surface finish:** depending on the final use it is possible to decide between one of the technologies. If the goal is a near-paint-ready surface or flexibility polyjet is the best option. On the hand, FDM allows to have stronger, long lasting and dimensionally stable parts;
- **Accuracy:** for dimensional accuracy FDM and Polyjet platforms have similar results for just built parts. However, over the time and under a load FDM materials are more dimensionally stable;
- **Size:** Both Polyjet and FDM machines offer a similar building range of build volume. Nonetheless, the FDM entry-level of build volume is smaller.

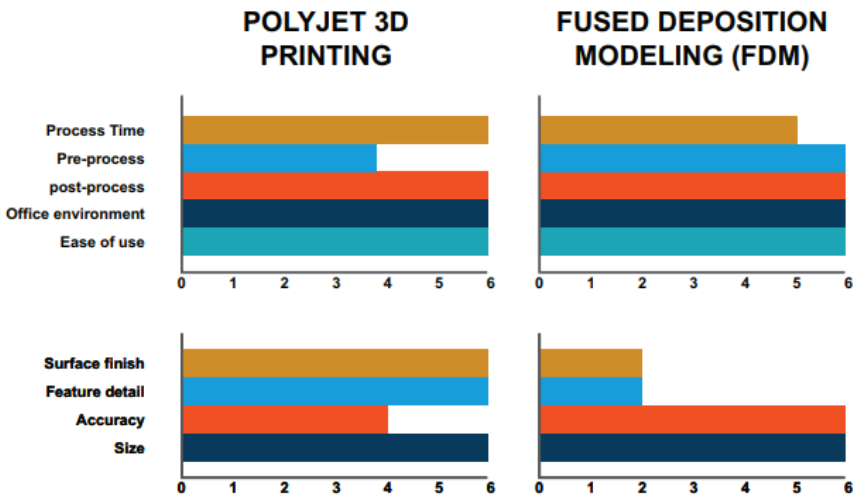

Figure 2.17 Comparison of polyjet and FDM technologies from 0 (very poor quality) to 5 (excellent quality) [20].

Esta página foi intencionalmente deixada em branco.

Chapter 3

Low cost 3D printers

This chapter is divided into four parts:

- Market research on existing low cost 3D printers and choosing which one to have when building a new one from scratch;
- Study about the printing parameters;
- Depth study about the infill influence;
- Investigation about the foam structures, specially the gyroid one.

3.1 Existing Products

In this section a comparison will be done between existing low cost 3D printers regarding to: price, building volume, Z-axis positioning accuracy, XY-axis positioning accuracy, frame material and finally users' opinion.

Low cost printers aim to replicate the professional ones at a smaller scale and price tag. The key features of desktop printers are [22]:

- **Price:** Their prices have been decreasing over the last six years, however higher-end printer such as MakerBot Replicator still cost over 1800€. Filament spools cost between 20 and 50€;
- **Materials:** Since thermoplastics melt when heated and solidify at room temperature, it makes them perfect for any user, the most used ones are ABS and PLA, which were already described in the section 2.2.1.2;
- **Standardisation:** The filament size is now standardised at 1.75 mm diameter and the layer height is 0.1mm;
- **Aesthetics:** since most low cost printer are designed for home use, aesthetics and design tend to be important factor for these type of users;

- **Software:** once again since the target market of these printers is also home users, the software must be easy to use and accessible from multiple devices;

- **Community:** consumer 3D printing has developed a strong community of enthusiastic users who like to share their designs with open source communities;

The biggest limitations and challenges faced by low cost printers are [22]:

- **Build Volume:** The build volume of a desktop printer rarely exceeds 250x250x250 mm, therefore this is the usual size limitation of the print;

- **Resolution:** they usually print only at 100 microns;

- **Materials:** most low cost printers can only print some type of thermoplastics;

- **Speed:** slow speed and random (sometimes frequent) printing errors are the major problems of the widespread adaptation of 3D printing;

- **Accuracy:** even though with every printer that is launched the accuracy is improving, it is still challenging to get complex and very detailed prints.

AII3DP, the world's leading 3D printing magazine, did a ranking of the low cost printers in accordance with the amount of money the users want to spend on them. Therefore the Creality Ender 3, Anycubic i3 Mega, Creality CR-10S and Original Prusa i3 MK3S will be analysed [23].

Creality Ender 3 (Table 3.1, Figure 3.1)

Table 3.1 Ender 3 main properties and advantages and disadvantages [24].

Price (around)	180€
Building Volume	220x220x250 mm
Maximum layer resolution	0.1 mm
Print Precision	+/- 0.1 mm
Frame Material	Aluminium
Pros	Open source Compact Design High quality prints are achievable Easy to assemble
Cons	Manual Calibration Adhesion sometimes needed to get prints to stick to bed Flimsy bed needs to be re-levelled from time to time

Figure 3.1 Creality Ender3 [24].

Anycubic i3 Mega (Table 3.2, Figure 3.2)

Table 3.2 Anycubic i3 Mega main properties and advantages and disadvantages [25].

Price (around)	268€
Building Volume	210x210x205 mm
Maximum layer resolution	0.1-0.4 mm
Resolution	50 μm
Frame Material	Aluminium
Pros	Fast and responsive user interface Very good part quality for low price Sturdy frame
Cons	Not very upgrade friendly Quite noisy Semi-automatic bed calibration advertised as automatic bed calibration

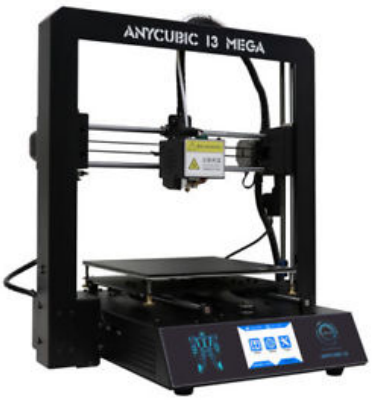

Figure 3.2 Anycubic i3 Mega [25].

Creality Cr-10S (Table 3.3, Figure 3.3)

Table 3.3 Cr-10s main properties and advantages and disadvantages [26].

Price (around)	446€
Building Volume	300x300x400 mm
Maximum layer resolution	0.1-0.4 mm
Resolution	100 microns
Frame Material	Aluminium
Pros	Heated bed with borosilicate glass plate (resulting in good adhesion) Power loss resume feature Massive build volume Outstanding print quality Offers a second rod for the z-axis (resulting in less wobble)
Cons	Print bed is slow to heat up No enclosure

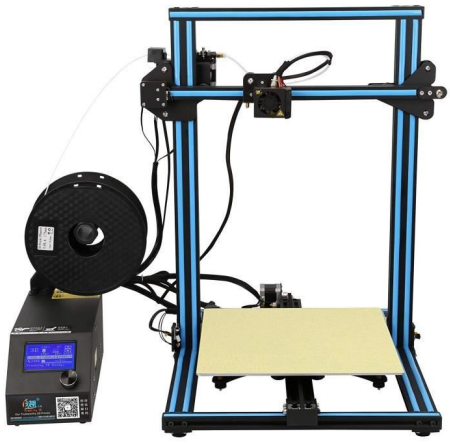

Figure 3.3 Creality CR-10S [26].

Prusa i3 MK3

Table 3.4 Prusa i3 MK3 main properties and advantages and disadvantages [27].

Price (around)	892€
Building Volume	250 x 210 x 200 mm
Maximum layer resolution	0.05 μm
Frame Material	Aluminium
Pros	Excellent Documentation Removable Magnetic Print bed Crash Detection
Cons	Bed adhesion problems 3D printed components don't have the best quality

Figure 3.4 Prusa i3 Mk3 [27].

3.1.1 User needs

After analysing the main features from existing low cost 3D printers and the features needed for the machine for this project it is possible to outline the main needs and respectively importance (5 - essential to 1 - not necessary) are (strategy based in the book of Ulrich *et. al* [28]):

Table 3.5 User Needs.

Number	Need	Importance
1	Good quality parts	5
2	Noise level	3
3	Robust printer	4
4	Good bed adhesion	5
5	Automatic calibration	2
6	Attractive Design	1
7	Second rod for z axis	2
8	Open Source	5

Therefore, it was decided to build two different printers based on the **Creality Ender 3** and the **Creality CR10s**, since they have an identical way to work. In order to improve the existing Creality Ender3 the one will have, in similarity to the existing CR10s, a heated bed with borosilicate glass plate, since this improves the bed adhesion and consequently the parts' quality [29].

3.2 Printing parameters

As it has been mentioned before the slicing software used is Slic3r, therefore, the printing settings mentioned will be the ones regarding to this software, however, it is important to outline that all these parameters are present and need to defined regardless the software used. In Slic3r the setting are divided in three categories: print, filament, printer.

Consequently it will be deeply described the print settings:

- **Layer Height:** it allows to define the step height (Z axis). In order to get parts with a good finish it is necessary to choose a small layer height (<0.1mm), that way the surfaces are softer however it takes longer time to print. The ideal is to find a balance between the print timing and the surface quality needed;
- **First layer height:** this is usually defined as a percentage from the normal layer height, it is also possible to define in mm. It is recommended to define the first layer height higher in order to improve the bed adhesion and avoid that the print starts warping;
- **Perimeters:** establishes the minimum number of external vertical walls to print. In very thin parts it is possible to choose only one perimeter, however it is important to take into account that it decreases the part rigidity considerably;
- **Solid layers:** in the first and last layers (top and bottom) it is possible to have solid layer in order to improve the rigidity by increasing the density;
- **Randomise Starting points:** defines the beginning of a layer deposition in random points, when this option is chosen the filament excess in the beginning point decreases;
- **Infill:** defines the infill density and type, being 0% hollow and 100% solid. For prototypes it is usual to use an infill percentage between 30 and 40% and for parts that require full rigidity it should be around 70-80% at least;
- **Fill angle:** angle of the infill's deposition;
- **Skirt and Brim:** a skirt is a perimeter line showing the outside border of the printing area. On the other hand, a brim enlarges the footprint of the printing area to get better adhesion;
- **Support Material:** when the part has a hanging feature between 0°and 45°it is necessary to add a support material in order to make sure it does not fall;
- **Speed:** the total speed is defined from all the printing and non printing speeds;

Besides the print settings it is also important to adjust the ones related with the filament, being those:

- **Diameter:** its the diameter of the filament used;
- **Extrusion multiplier:** defines the relations between the stepper motor's gears;

- **Extruder (Temperature):** establishes the extruder temperature, it is possible to define a different one for the first layers and the rest;
- **Bed (Temperature):** temperature of the building platform, as in the extruder temperature, it is also possible to choose a different one for the first layer and the rest;
- **Cooling:** defines when the cooler is activated and the cooling speed.

Finally, the printer setting are related with its dimensions, nozzle diameters and any offset used [7].

In conclusion, according to Kohad *et. al* [30] the main FFF process parameters are (shown in figure 3.5):

- **Build orientation:** the way the part is orientated in the build platform (X, Y or Z);
- **Layer thickness:** thickness of the layer that is deposited by the nozzle;
- **Air gap:** gap between adjacent raster tool paths on the same layer;
- **Raster angle:** angle of the raster pattern with respect to the X axis on the bottom part layer (0°to 90°);
- **Raster width:** width of the material bead used for raster, it varies based on nozzle tip size;
- **Contour:** width of the contour tool path that surrounds the pat curves;
- **Number of contours**
- **Contour to contour air gap:** gap between contours when the part fill style is set to multiple contours;
- **Perimeter to raster air gap:** gap between the inner most contour and the edge of the raster fill inside the contour.

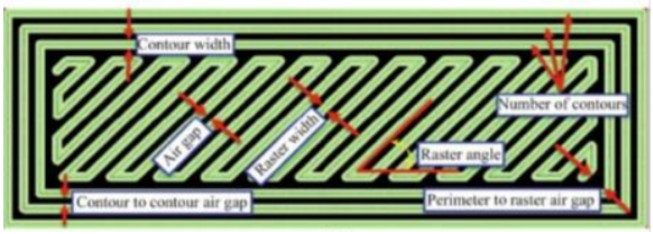

Figure 3.5 FDM tool path parameters[30].

Additionally, the performance parameters, those that are most significant to optimise, are:

- Build time;
- Flexural Strength;

- Surface Roughness;
- Feed Stock Material consumption;
- Dimensional Accuracy.

In conclusion, in this study the authors concluded that [30]:

- The **Build time** is mainly affected by the **layer thickness and air gap**;
- The **Flexural Strength** is also mainly affected by layer thickness and air gap;
- Finally, the **Surface roughness** was mostly influenced by the **layer thickness and path width**.

3.3 Influence of the Infill

In this section it will be studied the influence of the infill in the specimen's mechanical properties. As it was stressed out previously it is possible to choose in the slicing software the type of infill used, its percentage and orientation.

After analysing the study of Lanzotti *et. al* [31], where the importance of the infill orientation (alternating between 0°, 18°, 45°, 72° and 90°) (as shown in Figure 3.6), layer thickness and number of shell perimeters were tested. The parameters flow rate, speed, density, bed temperature, printing temperature and outline overlap were set as constant. Before, concluding the importance of these parameters the authors suggested to modify the geometry of the specimen in order to overcome failures occurred in the fillet during the preliminary testes, since the specimens failed at the minimum cross section. Therefore, it consists of a modification of the fillet geometry using a parabolic profile tangent to the middle part of the specimen. In the end it was possible to conclude that:

- Increasing the number of perimeters, which are orientated along the longitudinal direction, the number of fibers, which withstand the tension load increase until the infill orientation is 0°, so the number of perimeters is ineffective, as all fibers are lying along the longitudinal direction;
- The strength increases as the layer thickness and the number of perimeters increase;
- The maximum value of Elastic Modulus is reached when all the fibers are orientated along the loading line, so the highest Elastic Modulus is obtained with an infill orientation of 0°.
- It is possible to observe a decrease in strength as the infill orientation approaches 90°and an increase as the number of perimeters walls increase.

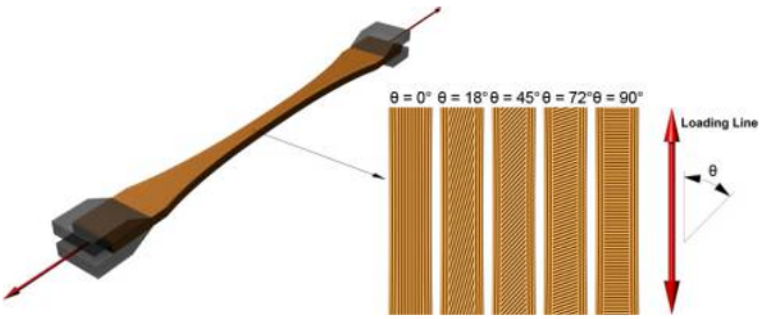

Figure 3.6 Boundary conditions and relative angle between infill and loading line [31].

In contrast to what was stated by Lanzotti *et. al*, T. Letcher *et. al* when testing the influence of the raster orientation (0°, 90° and 45°) on the tensile and flexural resistance of PLA 3D printed specimens built in a low cost 3D printer, concluded that [32]:

- The greater tensile results were obtained for the 45° raster orientation (average ultimate stress is 64.03 MPa and average modulus of elasticity is 3.60 GPa). The difference between the average ultimate stress obtained for this raster orientation and for the 0° is around 8.7% and difference between elasticity modulus is around 7.5%;

- The greater flexural results were obtained for the 0° raster orientation (ultimate stress is 102.20 MPa and flexural modulus of elasticity is 3.2 GPa).

Consequently, it is possible to conclude that regarding to the orientation that provides the best tensile properties it is common to notice slight discrepancies in the literature.

According to C. Dudesco *et. al* [33], that conducted a research about the infill rate, infill pattern and raster orientation of 3D printed parts using a FDM printer and ABS, all this parameters influence the specimens mechanical properties. The specimens were done according to the following parameters:

- **Infill rate:** 20%, 40%, 60%, 80% and 100%;

- **Infill pattern:** triangular, grid, rectilinear, full honeycomb, fast honeycomb, wiggle (figure 3.7);

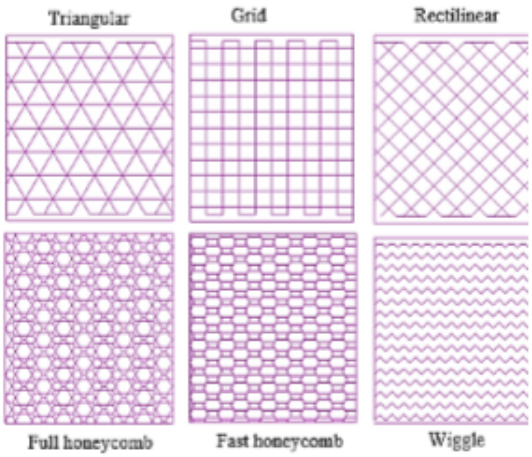

Figure 3.7 Infill patterns: triangular (top left), grid (top middle), rectilinear (top right), full honeycomb (bottom left), fast honeycomb (bottom middle), wiggle (bottom right) [33].

As it was expected the specimen strength increases with infill rate (figure 3.8 a). Interestingly the elongation at maximum stress for 100% infill, 2,7%, was the value of ABS filament elongation (figure 3.8 b). For the specimens that don't have 100% infill density the E-modulus can be calculated considering apparent cross section, therefore, ignoring the void inside the part, the calculation can also be adjusted by multiplying the cross section area by the infill rate (adjusted cross section). The apparent E modulus also increased with the increase of infill percentage (Figure 3.8 c) and the adjusted E modulus can be obtained by multiplying the apparent modulus with the *(1-Infill rate)*.

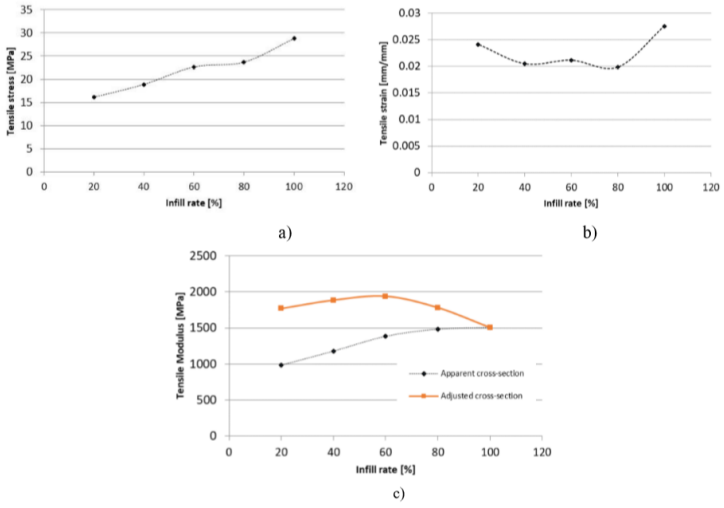

Figure 3.8 Variation with the infill rate: (a) tensile stress, (b) tensile strain at maximum stress and (c) Young's modulus [33].

Regarding to the infill pattern triangular, hexagonal, grid 0°-90° and 45°-45° are all comparable in terms of strength and E-modulus. Elongation at break is between 2% and 2.8% with the smallest value for the fast honeycomb pattern (Figure 3.9).

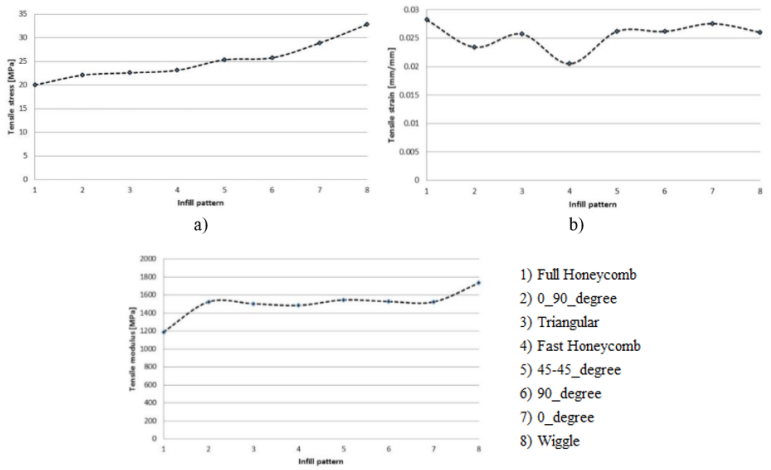

Figure 3.9 Variation of (a) tensile stress, (b) tensile strain at maximum stress and (c) Young's modulus with the infill pattern [33].

When studying the influence of the infill percentage on the compressive strength of PLA samples obtained by FDM, using a rectilinear infill. It was possible to conclude that the strength of samples with 20% to 65% density presented a sharp rise of the compressive strength, being the highest obtained with 100% as expected (Figure 3.10) [34].

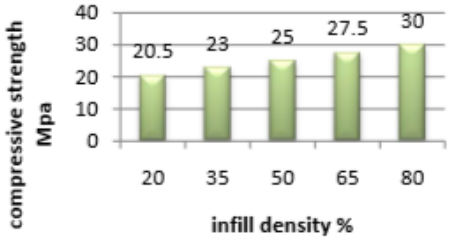

Figure 3.10 Influence of the infill percentage on the compressive strength [34].

Finally, in order to study the effects of infill patterns on the mechanical performance of lightweight 3D-printed cellular parts, made from PLA by FDM, five different infill patterns were chosen: hexagonal (H), square (S), triangular (T), square diagonal (SD) and reinforced square diagonal (RSD) (figure 3.11) [35].

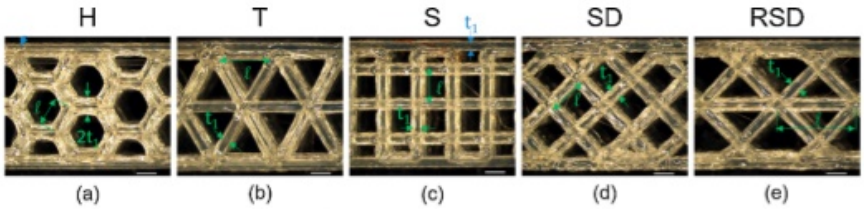

Figure 3.11 Optical image of the five different infill patterns: hexagonal (a), square (c), triangular (b), square diagonal (d) and reinforced square diagonal (RSD). Adapted from [35].

After executing the mechanical and flexural tests it was possible to conclude that [35]:

- The hexagonal structure has the best balance in mechanical performance while the square diagonal presents the least;
- Under uniaxial tensile loading the square structure shows the best performance.

After analysing the last research articles it was possible to understand the infill importance and the use of different types of infill, such as the honeycombs, to achieve lighter 3D parts with better mechanical performance. It was decided to study foam structures, to achieve parts with superior mechanical behaviour, deepening in the gyroid structure, for equal resistance to compression regardless the solicitations' direction. Cellular solids, which include foams, honeycombs and regularly repeating lattice structures, have been investigated because of their many useful properties, highlighting their ability to absorb compressive energy effectively, act as heat exchangers, and provide acoustic and vibrational damping [36].

3.4 Foam Structures

Materials with a cellular structure made with an interconnected network of struts or plates appear in the nature as wood, cancellous bone and cork. Of course, based on those there are also many man-made cellular materials in the form of honeycomb-like materials and foams. Even thought initially these structures could only be done by a limited range of materials, now they can be made from many different polymers, metals, ceramics and glasses (shown in figure 3.12). Consequently they are extensively used in lightweight sandwich panels, separating two strong stiff faces from a lightweight core to create a structure resistance to bending and buckling [37].

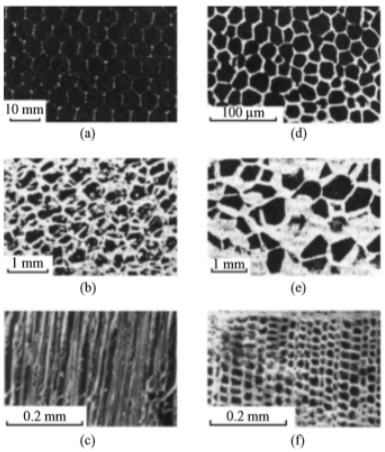

Figure 3.12 Micrographs of cellular materials: (a) aluminium honeycomb, (b) cork, (c) polyurethane foam, (d) polyethylene foam, (e) and (f) orthogonal views of cedar [37].

Polymeric materials are widely used as foamed structures, the wide range of cellular morphological and functional characteristics allows them to be used in numerous applications where their lightweight, among many other attributes, makes them very interesting and appealing [38]. One of their many interests is that they are energy-absorbing structures, characterised by high

deformability and plasticity. These modified materials can be used in very demanding industries such as military, transportation, aircraft and automotive [39]. The characteristics inherent to foams are insulation, energy conservation, sound attenuation and absorption, shock absorption and light weighting [38].

A potential classification for these foams, according to their potential end-use, is:

- **Structural foams:** used in building and construction, transportation, marine, tanks, food and drink containers, etc.
- **Flexible foams:** bedding and furniture, absorbents, footwear, textiles, etc.
- **Speciality foams:** bio-medical or space applications.

The majority of polymeric foam products are made from polyurethane (PU), polyethylene (PO), polystyrene (PS) and polyvinyl chloride (PVC) [38].

According to the association *Global Industry Analysts*, from 2010 to 2016 there was an increase of 0.9 US Trillion dollars of construction spending benefits for polymeric foams in building and construction end-use industry. It is expected that in 2020 this number will go up to 10.4 and in 2025 to 13.5 US trillion dollars [40].

Finally, it is important to outline that polymeric foams can be divided in two different types: thermoplastics (can usually be broken down and recycled) or thermosets (harder to recycle because tend to be cross-linked) [38].

On the other hand, the foams can be divided by:

- **Open Celled Foams:** all the polymers reside in the struts, and there are no window membrane materials (shown in figure 3.13).

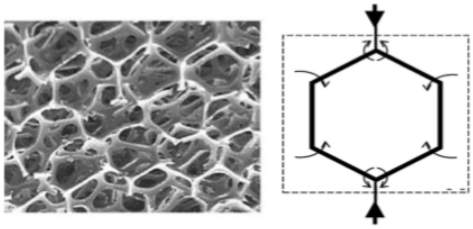

Figure 3.13 Open cell foam and deformation [38].

- **Closed Cell Foams:** the polymer is distributed between the struts and cell window membranes (shown in figure 3.14).

A good example of use structural foams is in the energy absorption management in the automotive industry, where lightweight structural rigid foams are added in order to improve the vehicle strength and increase the passengers safety. It is used through filling the thin walled, hollow metal structures in vehicles with rigid polymer foams. While the use of structural rigid foam to fill the

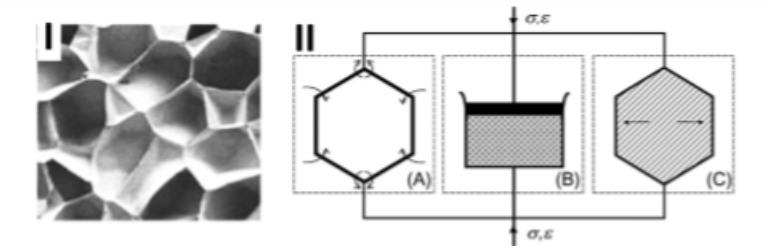

Figure 3.14 Close cell foam and deformation [38].

steel beams results in improved strength and it can also help to reduce the vehicle weight, this can reduce the weight up to 16.2 kg [38].

The properties of cellular materials are determined by a large number of geometric and structural properties. The most important one of them is the relatively density, determined by the ratio between the density of the material and the density of the solid material from which it is made.

A typical stress-strain curve for a cellular material is shown in figure 3.15. It is evident the three different regimes of behaviour [37]:

- At **relatively low loads** the material is linear elastic;
- At **some critical level of load** the cells begin to collapse by elastic buckling, plastic yielding or brittle fracture, depending on the nature of the cell wall properties;
- Cell collapse then progresses at a **roughly constant load** producing a horizontal yield plateau corresponding to the cells' collapse;
- The stress then rises steeply as the material densifies.

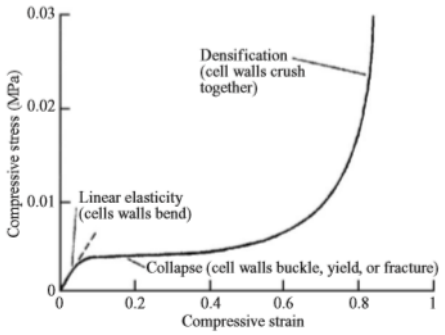

Figure 3.15 Typical stress-strain curve for a cellular material in uniaxial compression [37].

The plastic behaviour of cellular material subjected to in-plane compressive load has been studied using a combination of experimental and computational approaches by several researchers. Foams made from materials which have a plastic yield point collapse plastically when loaded beyond the linear elastic regime. Plastic collapse, due to elastic bucking effects, material yielding or micro fractures, gives a long plateau to the stress-strain curve, through the strain is not recoverable.

Before reaching the collapse point, and consequently failure, these materials undergo significant nonlinear plastic deformation [41].

According to the Ulm *et. al* each of these regimes of behaviour is related to the mechanism by which the cells deform within that regime [37].

By observing the honeycomb model and the foams in a scanning electron microscope it is revealed that the initial linear elasticity is produced by bending in the cell walls. The cell collapse is a result of elastic buckling in elastomeric honeycombs and foams and by plastic yielding of the micro struts, and finally by brittle crushing which leads to fracture.

When in tension, the foams behaviour is characterised by a linear elastic period that is determined by the same modulus of the material in compression. At slightly larger strains buckling as in compression is not possible, instead the cell edges rotate toward the tensile axis. After a strain of approximately 0.3, increasing strain requires the stretching of the cell walls (these stages are shown in figure 3.16. Therefore, failure in tension is by the propagation of a single crack [37].

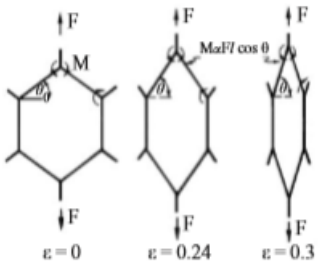

Figure 3.16 Alignment of the cell edges during tensile loading [37].

3.5 Gyroid Structures

The gyroid is a triply periodic minimal surface (shown in figure 3.17 a), like the Weair-Phelan structure, the kelvin foam, Schwarz P and D surfaces, with zero mean curvature.The porous solid structure is obtained by filling the space on one side of the surface (shown in figure 3.17 b). It was firstly identified by Alan Schonen in 1970. It presents the topology of an open celled foam [42]. Because of the gyroid's complex structure it is only possible to be produced by additive manufacturing [43].

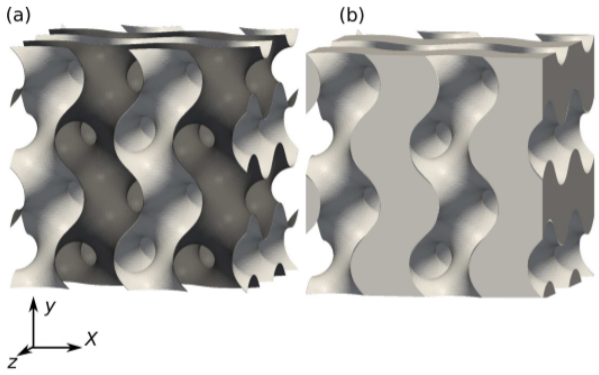

Figure 3.17 (a) gyroid minimal surface, (b) gyroid lattice obtained by in-filling on side of the surface [42].

The gyroid surface can be obtained by the expression:

$$\sin(\frac{2\pi}{a}x)\cos(\frac{2\pi}{a}y)+\sin(\frac{2\pi}{a}y)\cos(\frac{2\pi}{a}z)+\sin(\frac{2\pi}{a}z)\cos(\frac{2\pi}{a}x)=t. \tag{3.1}$$

Where a is the unit cell size and t controls the volume surrounded by the Gyroid surface. The gyroid surface segments the space in two interconnected regions, forming connected gyroid cellular structures (or networks) for each region. The gyroid foam, also known as double gyroid (DG), is the substantialization of gyroid surface when being given a thickness and comprised of a wall of solid material bounded by two unconnected void regions (shown in the figure 3.18) [44].

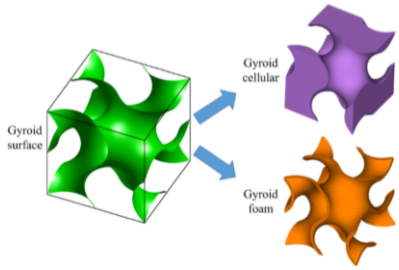

Figure 3.18 Schematics of Gyroid Surface, Cellular and Foam [44].

The gyroid morphology has been seen in many different physical systems, such as during the phase separation of diblock copolymers, in the scales of butterfly wings, since their beautiful iridescent colours are caused gyroid made of chitin and air [42, 43].

As it has been mentioned previously one of the most interesting properties of the gyroid structure is its behaviour in compression. Therefore, it is important to do an in depth study of its behaviour when subjected to an uniaxial uniform load. As it is shown in figure 3.19, when the cellular structure is subjected to this kind of force, the inclined struts will bend under action of the force component $F\cos\Theta$. Since the centre of the struts has the smallest cross-section, there would be large deformations and stresses at this position, which contributes to the highest level of equivalent stress and deformation. At the same time, the upper and bottom surfaces of the inclined strut

are subjected to tensile and compressive stresses respectively, which are caused by the bending deformation of the inclined struts, and may accelerate the fracture initiation [45].

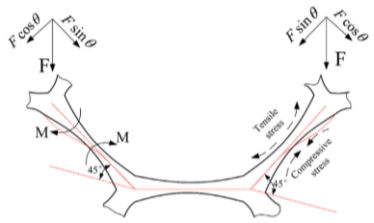

Figure 3.19 Schematic of the free body diagram of the struts under uniaxial compression testing [45].

I. Makery *et. al* [46] has conducted a study in order to understand, among other properties, the compressive behaviour of a double gyroid (DG) lattice done by metal additive manufacturing, SLM. As it is possible to observe in figure 3.20 , it was tested four different cell sizes of 9, 6, 4.5 and 3 mm.

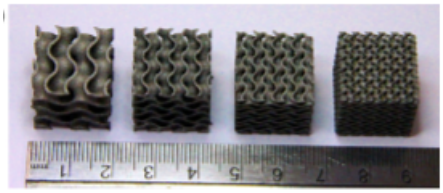

Figure 3.20 SLM manufactured specimens with cell size of 9, 6, 4.5 and 3 mm [46].

After doing compression tests it was possible to observe that compressive failure mode of the gyroid is related to the size of its constituents cells, generally specimens with 9 mm cells exhibited a very different crushing behaviour than those with 3 mm cell, that have 6 cells in each direction (shown in figures 3.21, 3.22, 3.23, 3.24). For the 9 mm cells the failure was due to brittle fracturing of the cell walls, and was characterised by the propagation of a crack(s), often with the main component of the direction of crack propagation parallel to the applied load. On the other hand, for the cells with 3 mm the failure was due to diagonal shear. Finally, the structures with cell size of 4.5 mm present successive collapse of cells in planes perpendicular to the manufacturing and loading direction (z). This type of structural failure resulted in stress-strain curves, as shown in the figure 3.24 (b), where the strength was repeatedly lost and recovered as each layer collapsed and was compressed into the one below, the structure grew stronger after the densification of each layer, recovering up to 90% of the initial strength [46].

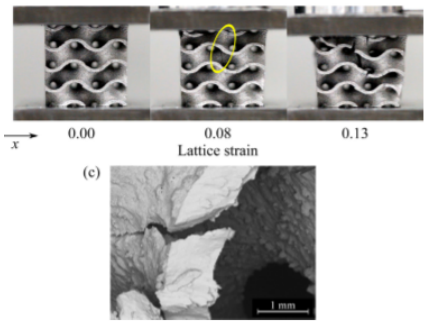

Figure 3.21 Low strain crack initiation and propagation in DG lattices with 9 mm cells (up) Fracture surface occurred in a lattice with 9 mm cells (down) [46].

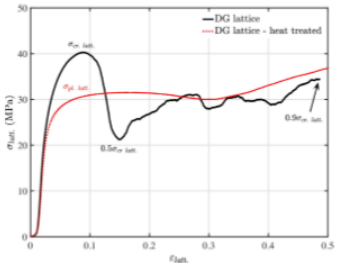

Figure 3.22 Stress-Strain of DG lattices with 3 mm cells [46].

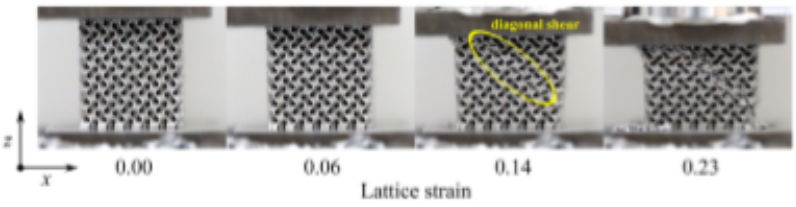

Figure 3.23 Diagonal shear failure in double gyroid lattices with 3 mm cells [46].

That is also observed in the work conducted by *Lei Yang*, that has done an analysis of the volume fraction influence of the compression behaviour of gyroid specimens done by SLS. In this work nearly all the fractures occurred at the centre of inclined struts, this was consistent with the FE analysis results obtained in that project (Figure 3.25). Since the specimens where done by Ti-6Al-4V alloy at ambient temperature, brittle fracture is the main failure mode of the cellular structures. In conclusion, the large strain with the tensile stress of the upper surface produced by the bending deformation result in fracture of the inclined struts of DG cellular structure under a low level of overall deformation in testing.

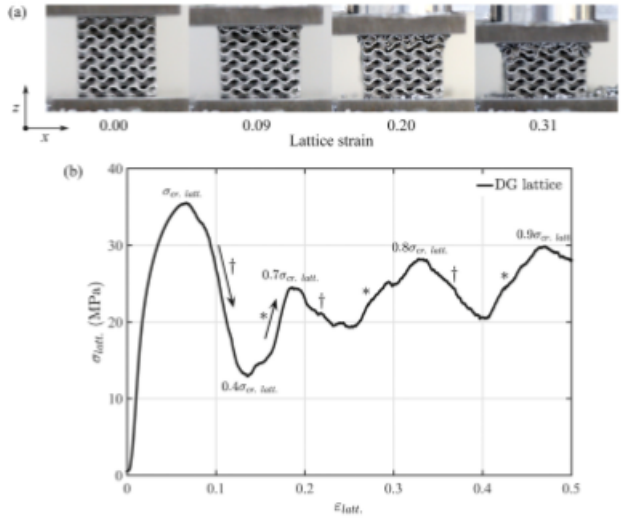

Figure 3.24 Successive layer collapse and densification of DG lattice with 4.5 mm cells (a) video frames during compression, (b) resulting stress-strain curve [46].

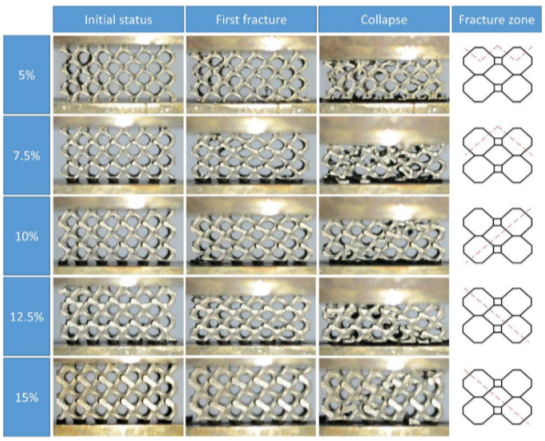

Figure 3.25 Fractures and collapses of the SG cellular structures with different volume fractions of 5%, 7.5%, 10%, 12.5% ad 15% [45].

As it is shown in figure 3.26 , the FE (finit elements) numerical and the experimental strain-stress curves of the SG cellular materials are quite similar. It is important to outline that the main difference between them is that the compression testing has an initial non linear strain stage that can be attributed to the rough upper surface of the cellular that is quite normal for SLM-built components, unevenness under-surface when they are cut off from the base-plate and contact clearance of the joints of the equipment [45].

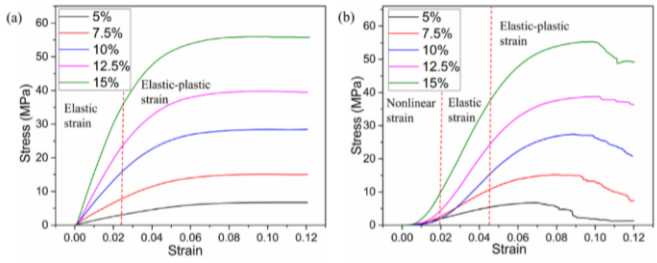

Figure 3.26 Stress-strain curves of the SG cellular structures with unit cell size of 4.5mm and different volume fractions from (a) FE analysis and (b) uni-axial compression testing [45].

The gyroid structure also presents very interesting behaviour in an impact situation. In the study of the impact resistance of different types of lattice structures manufactured by SLM made from aluminium powder, $AlSi_{10}Mg$, it was tested 5 different structures, among them the gyroid one. The structure is shown in figure 3.27 and the penetration body (indentor) had a spherical shape [47].

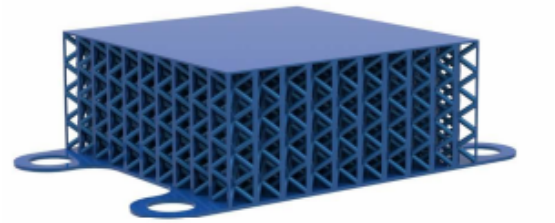

Figure 3.27 Representative impact resistance sample (not the gyroid one) [47].

The energy absorbed by the gyroid structure was around 23,56 J, the specimen after impact is shown in figure 3.28. In conclusion, the gyroid structure showed similar result under impact loading as the other two best structures. Its advantage is that its stiffness is the same for all loading directions [47].

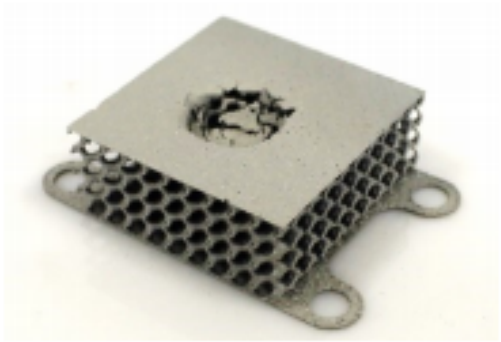

Figure 3.28 Gyroid sample after impact. Adapted from [47].

The gyroid tensile specimen, shown in figure 3.29, presents different behaviour if it is built in the horizontal or vertical direction as it is possible to observe in the stress-strain curve of the tensile

test with 15% volume fraction and 3mm cell size (figure 3.30). It is observed approximately a 66% increase in the tensile properties when the specimen is built vertically, because the tension load direction that was applied in parallel to vertical building direction. Which means that the vertical struts in the vertical building direction samples when subjected to tensile tension are stronger than horizontal struts that were built perpendicular to the building direction. For samples built in horizontal direction, the horizontal struts were subjected to tension load. Additionally, it was possible to conclude that the increase of unit cell size leads to increase of struts and they become weaker due to the deformation of material without support material [48].

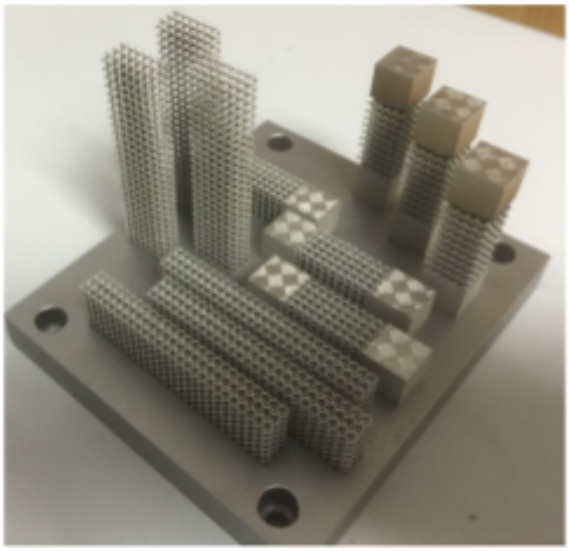

Figure 3.29 316L stainless steel samples at different building direction in the platform [48].

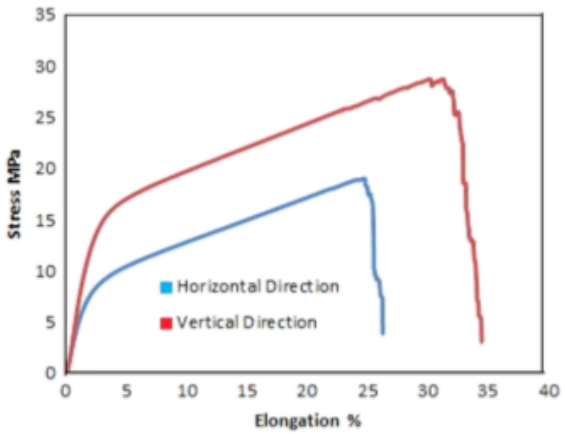

Figure 3.30 Stress-strain curves of the tensile tests on the structures with 15% volume fraction and 3mm cell size, built in the vertical and horizontal directions [48].

Finally, it is also essential to study the isotropy of the gyroid structures when subjected to compression, this is its equal behaviour in compression regardless the solicitation's direction. As

it is possible to observe in figure 3.31, there is no noticeable difference between horizontal and vertical orientations, even when compared with the FE results. For higher relative densities the difference between the horizontal and vertical orientation is slightly bigger but not enough to be noticeable (this data is from a Polyamide specimens produced by SLS) [49].

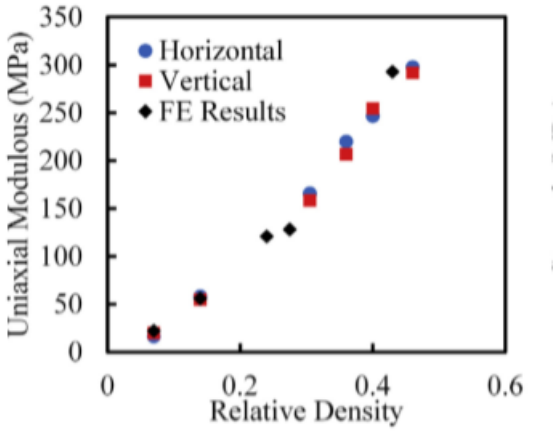

Figure 3.31 Experimental and computational results of compressive uniaxial modulus at a strain rate of $0.01s^{-1}$ [49].

In conclusion this structure presents very interesting properties, giving to the geometry a more important role than the material itself [50]. Therefore, its ability to work as an infill, will be further studied, in order to achieve lighter parts with enhanced behaviour in compression.

Chapter 4

Experimental work

In this chapter it will be approached the experimental work, therefore, the materials and methods present in this dissertation.

4.1 Materials

The following materials are utilised in this dissertation: PLA, used for all the specimens, and VeroGray, used in order to build specimens to test the gyroid's isotropy.

4.1.1 PLA

The PLA was provided by *Formfutura*, its commercial name is Premium PLA. When compared with general PLA it is slightly harder, with an excellent stability and has a slightly faster crystallisation process of the 3D printed layers [51]. In table 4.1 the properties of this PLA, as well as the respective test methods to achieve them, are shown.

Table 4.1 Properties of the Premium PLA from Formfutura [51].

Properties	**Typical Value**	**Test Method**
Density	1.25 g/cc	ASTM D1505
Melt flow rate	6.0 g/10min	-
Impact Strength	3,4 kJ/m^2	(ISO 179)
Tensile strength	105 MPa	ASTM D882
Tensile modulus	3145 MPa	ASTM D882
Elongation at break	175%	ASTM D882
Flexural strength	$\pm$ 54.4 MPa	-
Print temperature	$\pm$ 190-225°	-
Melting temperature	$\pm$ 210 $\pm$ 10°	
Visc. at softening temp.	$\pm$ 62°	ISO 306
Diameter	**Tolerance**	**Roundness**
1.75mm	$\pm$ 0.05 mm	$\geq$ 95%
2.85mm	$\pm$ 0.10 mm	$\geq$ 95%

4.1.2 Polyjet Materials

The material used in the polyjet machine is VeroGray and the support material is SUP705. It is part of the Vero ^{TM} family and it is the one that provides best detail visualisation, without glare or darkness [52].

Table 4.2 Properties of the VeroGray from Stratasys [53].

Properties	Typical Value	Test Method
Tensile Strength	58 MPa	ASTM D638
Elongation at break	10%-25%	ASTM D638
Modulus of Elasticity	2500 MPa	ASTM D638
Flexural Strength	93 MPa	ASTM D790
Flexural Modulus	2700 MPa	ASTM D790
Izod Notched Impact	25 J/m	ASTm D256
Shore D Hardness	85 D	
Heat Deflection Temperature	48°	ASTM D648 @264psi
Z resolution	30 μm	

The support material, SUP 705, is removable with water.

4.2 Methods

In this section the experimentation and modelling work will be explained and further developed. It is important to outline that the stages of the project were (shown in figure 4.1):

- **Stage 1:** Assembly of a 3D printer;
- **Stage 2:** Print and mechanical testing (tensile, compression, bending) of the specimens with 100% infill, alternating the printing orientation;
- **Stage 3:** Print and mechanical testing (tensile, compression, bending, charpy and impact) of the specimens with gyroid infill, alternating the infill's density;
- **Stage 4:** Print and compression testing of unitary gyroid models, in order to test it's isotropy, and that of cubes from gyroid infill with and without outside perimeter;

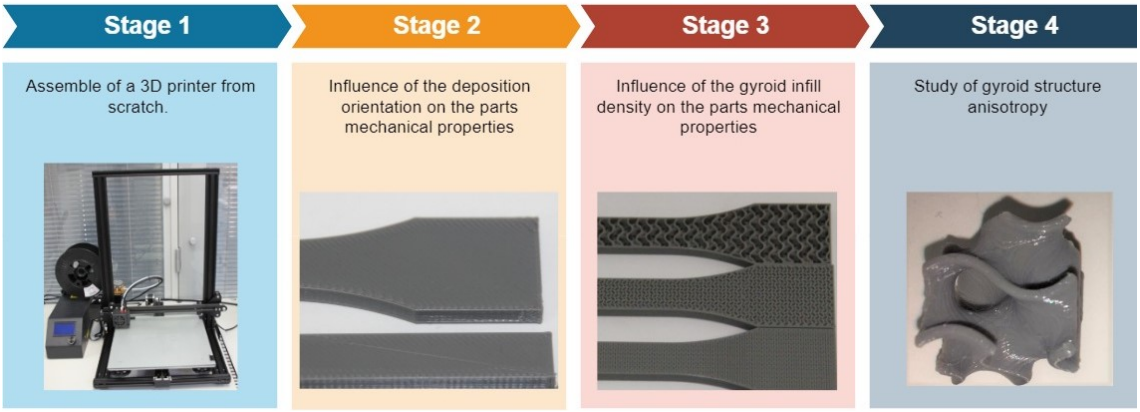

Figure 4.1 Project's work flow.

4.2.1 Assemble of a 3D printer

In this section the process of building a 3D printer will be described. As it has been mentioned before in section 3.1 it was decided to assemble two different printers based on an Ender 3 and a CR10-s, in order to produce the specimens of the first and remaining stages.

For this reason the first step was to understand what kind of products the competitors of these particular printers have on the market. After doing that research it was possible to understand the main steps that need to be taken into account when building a 3D printer from scratch, such as [54]:

1. **Choosing the motion structure and frame:** firstly it is necessary to decide between a cartesian XZ Head setup, a cartesian XY Head setup delta 3D printer, after the market research done in the previous chapter 3, it was decided to go for a **cartesian XZ Head setup**, basically for reasons of time and complexity.

2. **Choosing the parts:**

   - **Controller Board:** tells the motion components how to move and processes input from the sensors, among other functions. There are numerous controller boards on the market, such as SmoothieBoard, RAMBo, and RAMPS being the most popular, all of which offer excellent long-term value and can accommodate a dual extruder setup. The RepRap Arduino Mega Pololu Shield (**RAMPS**) is designed to fit the entire eletronics needed for a RepRap in one small package for low cost [54]. RAMPS interfaces an Arduino Mega, presenting plenty of space for expansion [55]. The RepRap Arduino-compatible Mother Board (**RAMBo**) is an all in one RAMPS class motherboard targeting convenience, reliability, and performance. It is compatible with most of RepRap firmwares [56]. The **Smoothieboard** is a controller board for RepRap 3D printers, the board is named smoothieboard so as the firmware that runs on it [57];

- **Power Supply Unit:** There are many market opportunities, the main thing to take in consideration is the materials that will be used, since, for example, ABS, Nylon and TPU require a print bed with high temperatures [54]. There are two main options in the market: **LED strip PSUs or ATX PSUs**. The first ones are switch-mode PSUs designed to supply a fixed DC 12V or 24V rail with relatively high current capabilities (from 15A to 30A or more). In the last couple of years, due to the development in LED lighting, they have become relatively inexpensive. Because of that they are used in many RepRap kits. LED PSUs are more than adequate for use in 3D printers. On the other hand, ATX PSUs have evolved over time adapting to the ever-changing PC market, so there is a lot of information about this one, collected by many hobbists [58]. In conclusion, a LED Strip PSU will be chosen, namely the: *MeanWell*, LRS 350-24V. This PSU has already been well tested and has good feedback. [59];

- **Print Bed:** if the print bed isn't heated it will only allow to print PLA, and even tough the present project is only with PLA, it is considered that they will have better properties when printed on a heated bed. It was decided in the section 3.1.1 that a glass print bed will be chosen because of the improved adhesion and part's quality [54]. It was important to go for a print bed that worked with 24V, therefore, after some market research, it was decided, for price-quality reasons, to go for a MK3 aluminium heatbed. The size was according to the size wanted for the two printers [60];

- **Filament feedding system:** it is necessary to choose between a bowden setup or a direct drive one. In the first one, the coldend and the hotend are physically separated from each other by a tube. The coldend is located somewhere in the frame and the hotend is connected to the motion components. Therefore, with this setup it is possible to achieve faster print speeds since the weight of the coldend (and its so called extruder motor) is not variable. On the other hand, in a direct drive setup the coldend and the hotend are directly connected to each other, which results in more weight for the gantry to carry. This one is often recommended for flexible filaments since it has a more straightforward structure. In conclusion, a **bowden setup** is chosen, since the prints made will be mainly with PLA and time is an important factor [54];

- **Print Head:** which is also called the extruder. It is composed by two different sections: coldend and hotend. The first one pulls and clamps the filament and pushes it towards the hotend. The second one melts the filament and deposits it on to the print bed via the nozzle. Of course, both of them affect what materials are possible to print and its quality. Two good combinations are an E3D titan extruder with an E3D V6 hotend and the bondtech QR Universal extruder and the Distech automation prometheus V2, both of them are quite expensive options [54]. After doing a market research on less expensive extruders it was found that the **MK8 Hotend** is also a good choice, being used in many printers, such as prusa, makerbot, anet, creality, it has good feedback [61];

- **Fans:** a 3D printer has a pair of fans, one as a heat sink fan (makes sure the filament from the coldend doesn't melt prematurely before reaching the nozzle) and one as a nozzle cooling fan (cools the filament as soon as it is deposited on the print bed). Sometimes it is also necessary to buy a fan for the motherboard [54, 62];
- **Stepper Motors:** compared to a regular DC motor, a stepper motor moves in increments or steps, making it ideal for precise movements. Stepper motors are connected to the three axes, driving the belts and the threaded rods or leadscrews. The extruder also needs a stepper motor, that drives the filament movement in the coldend, one that is widely used for this application is the NEMA 17 size [54, 63];
- **Belts:** are responsible for the motion transmission on the X and Y axes, they also affect the noise level and accuracy of the 3D printer. The most common belts used on 3D printers are GT2 [54];
- **End Stops:** prevent the 3D printer from moving past its range and act as a position references for the controller board. The most common are the mechanical ones, since they are cheaper and have a more straightforward setup;
- **Spool Holder:** it is up to the user where and how to assemble it, it is even common to print one after the printer is done.

3. **User Interface/Connectivity:** The ideal situation would be that a 3D printer can be connected via USB and has an on-board interface with SD card connectivity. For that reason the most logic option is to go for a standard LCD interface operated by either a dial, a knob or a set of buttons [54].

Consequently, after choosing the needed parts it was possible to assemble the 3D printer. First of all it was important to test all the components before proceeding to assembling of the 3D printer, so the extruder, the hotend, the motors, control boards and sensors were all tested in advance [64]. The following steps regarding to the 3D printers assembly were done to what was advised in literature, they will be very succinctly explained here [64, 65, 66, 67].

1. **Design 2D and 3D of the frame:** before proceeding with the next steps it is important to model the aluminium frame in order to know what are the necessary dimensions and space available, it will be based on the Ender 3 and CR 10 (shown in figure 4.2);

2. **Purchase the parts:** buy the parts mentioned above, either in a local store or online, on platforms such as eBay, depending on the money and time available for the project. For this project most of the parts were bought in an online Portuguese store;

3. **Assemble the printer:**

   (a) Assembly of the frame using bolts and washers;

   (b) Assembly of the heating bed, on top the borosilicate glass and on the bottom a thermistor to control the temperature;

(c) Assembly of the timing belt, in order to make it possible for the bed to move along the Y axis;

(d) Assembly of the step motors;

4. **Wiring the printer:** this part was done following the figure 4.3;

5. **Install the software:** install SLic3r on the computer;

6. **Install the firmware;**

7. **Test the printer.**

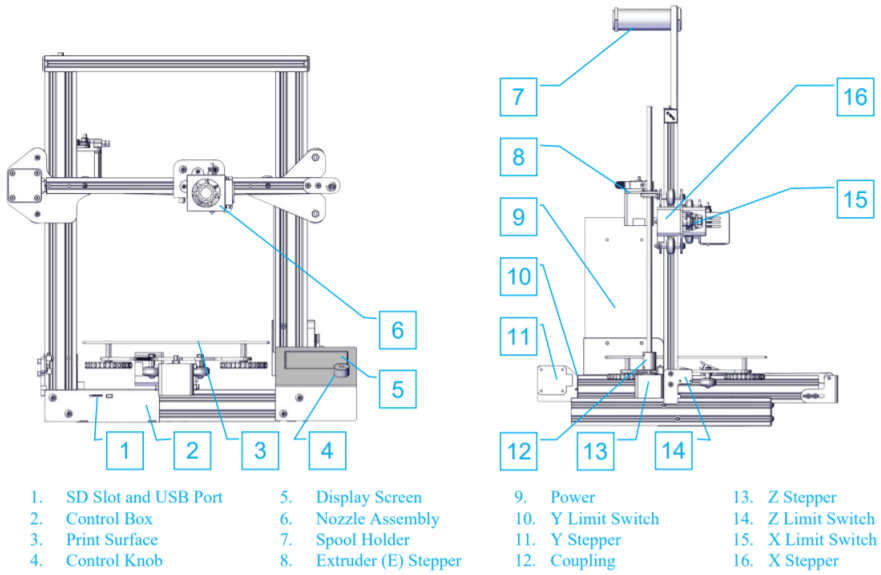

Figure 4.2 Structure in which the 3D printer was based [68].

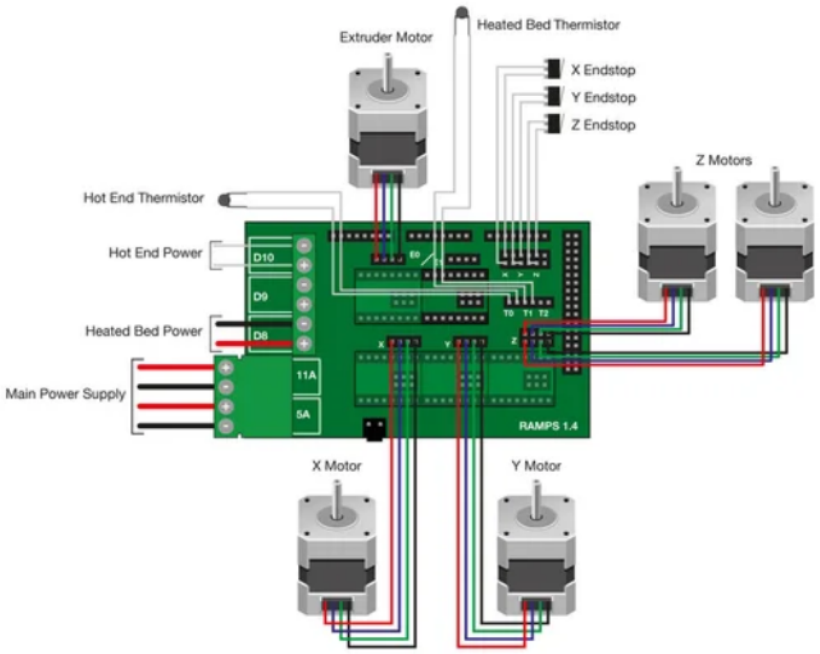

Figure 4.3 3D printer wiring [65].

The following troubleshooting steps 4.4 were followed during the construction and use of the 3D printers.

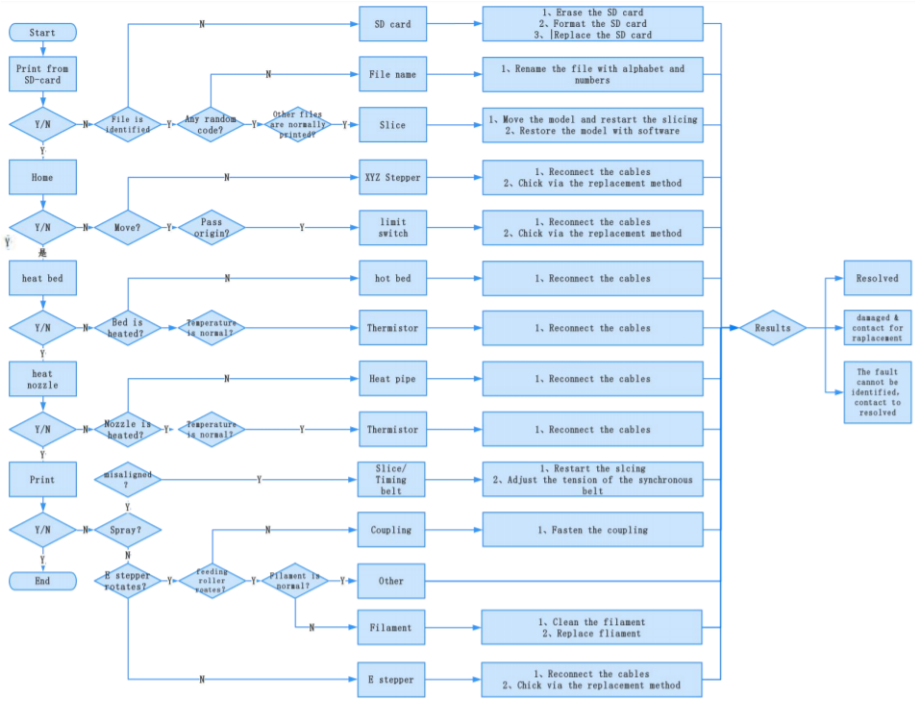

Figure 4.4 Troubleshooting scheme [68].

Afterwards, the calibration of the 3D printer was done following the steps in the following sources [69, 70].

In figure 4.5 the printer based on the CR10 is shown. In figure 4.6 the upgrade done to the extruder is shown, a modification of the plastic one to a brass one.

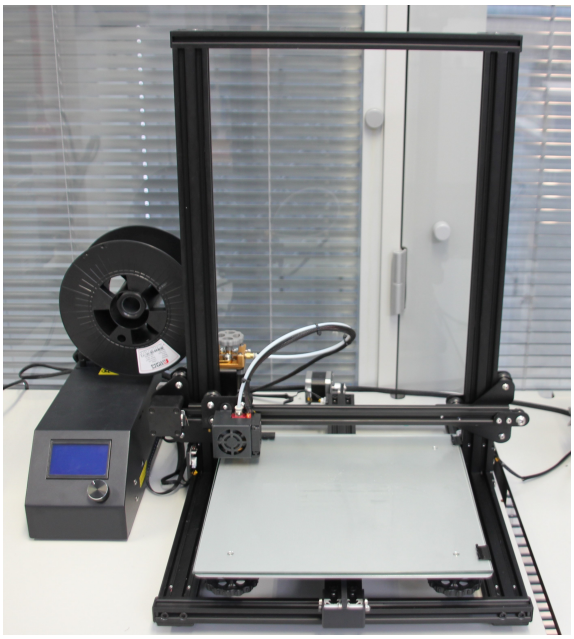

Figure 4.5 Printer based on a CR10.

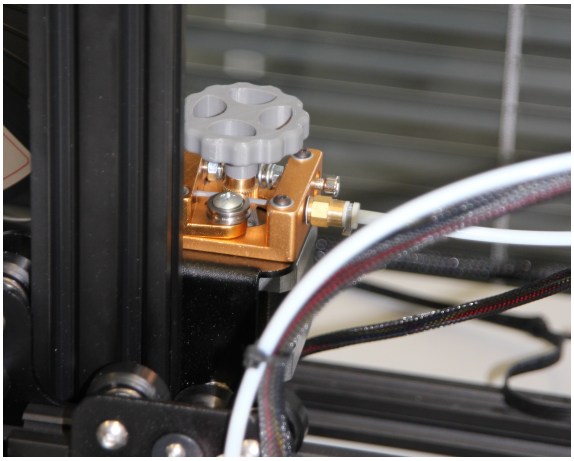

Figure 4.6 Upgrade: Brass extruder.

4.2.2 Instruments

In this section the instruments used during the realisation of the present thesis will be briefly described. They were:

- **Calipers:** to measure all the specimens (shown in Figure 4.7). This equipment belongs to *Laboratório de Desenvolvimento de Produto e Serviços* (LPDS), from FEUP;

The calipers which are used are digital calipers, *Mitutoyo* CD-6" ASX and their specifications are shown in table 4.3 [71].

Table 4.3 Mitutoyo Calipers specifications [71].

Range	**Accuracy**	**Mass**	**Resolution**	**Repeatability**
0-150 mm	$\pm$ 0.02 mm	168 g	0.01 mm	0.01 mm

Figure 4.7 *Mitutoyo* calipers used to specify dimensions.

- **Scale:** to weight all the specimens (shown in Figure 4.8). This equipment belongs to *Laboratório de Desenvolvimento de Produto e Serviços* (LPDS), from FEUP;

Table 4.4 HLD 300 scale specifications [72].

Plate Dimensions	**Capacity**	**Standard division**	**HR division**	**Linearity**	**Internal sensitivity**
ϕ120mm	300 g	0.05	0.005	$\pm$0.01 g	0.0005

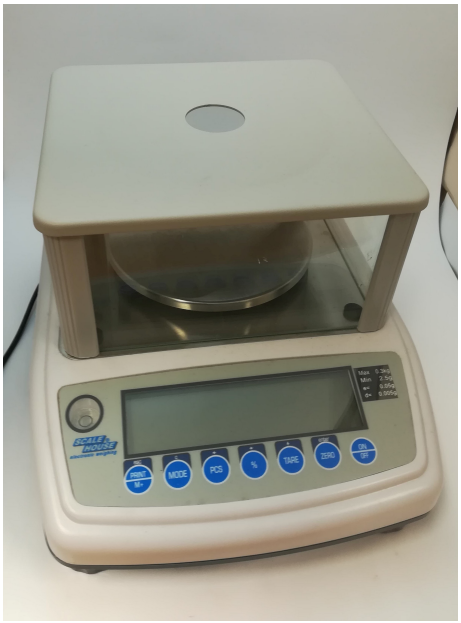

Figure 4.8 Scale used to measure the specimens' weight.

- **Stereo binocular microscope**: to observe the failure mode and important details of some specimens (shown in Figure 4.9). This equipment is from the *Laboratório de Metalografia* from FEUP.

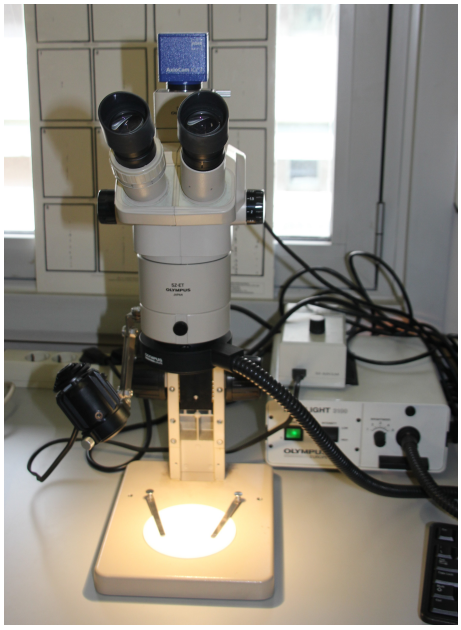

Figure 4.9 Stereo binocular microscope Olympus SZ-ET used to observe failure modes and important details.

4.2.3 Standard tests

In this section the mechanical tests that are conducted and the respective specimens according to the ISO standards are described. It is important to outline that in this project the stress and strain obtained are the engineering values.

4.2.3.1 Tensile

The principle of this test is that the specimen is extended along its major longitudinal axis at constant speed until the specimen fractures or until the stress (load) or the strain (elongation) reaches some predetermined value.

The tensile tests were done according to the ISO standard 527: *Plastics - Determination of Tensile Properties, Part 1: General principles(ISO 527-1) and Part 2: Test conditions for moulding and extrusion plastics (ISO 527-2)* [73, 74].

A typical stress/strain curve obtained after conducting this test is shown in the Figure 4.10, after analysing it is possible to determine the [73]:

- **Tensile stress at yield or yield stress (σ_y):** first stress at which an increase in strain occurs without an increase in stress, it is expressed in MPa;
- **Tensile stress at break (σ_B):** stress at which the specimen breaks, it is expressed in MPa;
- **Tensile strength (σ_M):** maximum tensile stress sustained by the test specimen during a tensile test, expressed in MPa;

- **Tensile strain at yield (ε_y):** tensile strain at the yield stress, expressed as a dimensionless ratio or in percentage (%);

- **Tensile strain at break (ε_B):** tensile strain at the tensile stress at break, it is expressed as a dimensionless ratio or in percentage (%);

- **Tensile strain at tensile strength (ε_M):** tensile strain at the point corresponding to tensile strength, is expressed as a dimensional ration or in percentage (%);

- **Modulus of elasticity or Young Modulus (E_t):** ratio between the difference and the σ_2 minus σ_1 to the corresponding values ε_2=0.0025 and ε_1=0.0005, it is expressed in MPa;

- **Poisson's ratio (μ_n):** negative ratio of the tensile strain, ε_n, in one of the two axes normal to the direction of pull, to the corresponding strain in the direction of pull within the initial linear portion of the longitudinal versus normal strain curve, expressed in dimensionless ratio.

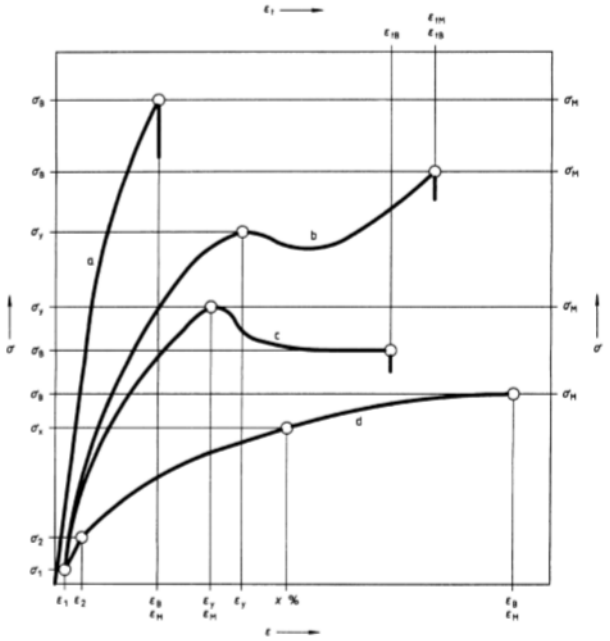

Curve a — Brittle materials
Curves b and c — Tough materials with yield point
Curve d — Tough materials without yield point

The points for the calculation of Young's modulus E_t according to **10.3** are indicated by (σ_1, ε_1) and (σ_2, ε_2), shown only for curve d (ε_1 = 0,000 5; ε_2 = 0,002 5).

Figure 4.10 Typical stress-strain curve [73].

The specimen type is 1B, its geometrical representation is shown in figure 4.11 and in table 4.5 the respective dimensions [74].

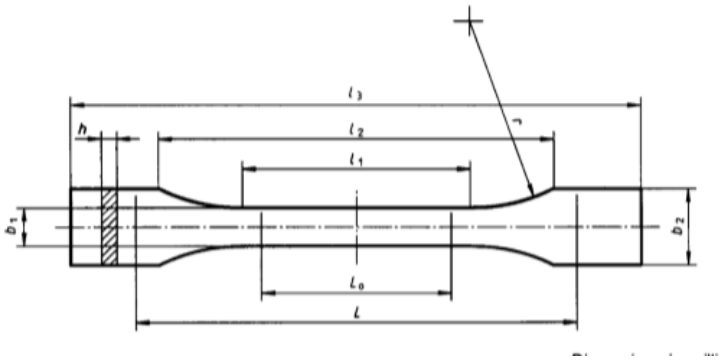

Figure 4.11 Tensile specimen's dimensions [74].

Table 4.5 Recommended dimensions for the tensile specimens [74].

Specimen type 1B	**Dimensions (mm)**
l_3 Overall length	150
l_1 Length of narrow parallel-side portion	60.0 ± 0.5
r Radius	$>= 60$
l_2 Distance between broad parallel-sided portions	106 to 120
b_2 Width at ends	20.0 ± 0.2
b_1 Width at narrow portion	10.0 ± 0.2
h Preferred thickness	4.0 ± 0.2
L_0 Gauge length	50.0 ± 0.5
L Initial distance between grips	$l_2^{+5}_{0}$

Therefore, the specimens were firstly designed in *Solidworks* according to the ISO and than converted to a *STL file*. Afterwards, all of them were carefully measured with calipers.

4.2.3.2 Flexural

This test is used to investigate the flexural behaviour of the test specimens and for determining the flexural strength, flexural modulus and other aspects of the flexural stress/strain relationship under the conditions defined. It applies to a freely beam, loaded at mid span (three point loading test).

The bending tests were done according to the ISO standard 178: *Plastics - Determination of Flexural Properties* [75].

A typical flexural stress/flexural strain curve is shown in Figure 4.12, after analysing it is possible to determine the [75]:

- **Flexural strength (σ_{fM}):** maximum flexural stress sustained by the test specimen during a bending test, it is expressed in [MPa];
- **Flexural strain at flexural strength (ε_{fM}):** flexural strain at maximum flexural stress, it is expressed in (%);

- **Flexural stress (σ_f):** nominal stress of the outer surface of the test at mid span, it is expressed in MPa where F is the applied force [N], L is the span [mm], b is the width [mm] and h is the thickness [mm]

$$\sigma_f = \frac{3FL}{2bh^2} \tag{4.1}$$

- **Flexural strain (ε_f):** nominal fractional change in length of an element of the outer surface of the test specimen at midspan, it is expressed in (%) where s is the deflection [mm], h is the thickness [mm] and L is the span [mm];

$$\varepsilon_f = \frac{6sh}{L^2} \tag{4.2}$$

$$\varepsilon_f = \frac{600sh}{L^2}(\%) \tag{4.3}$$

- **Flexural modulus($\mathbf{E}_f$)**: ratio between the stress difference to the corresponding strain difference, expressed in MPa. To determine the flexural modulus, calculate the deflections s_1 and s_2 corresponding to the given values of the flexural strain ε_{f1}=0.0005 and ε_{f2}=0.0025. Where s_i is on of the deflections [mm], ε_{fi} is the corresponding flexural strain, L is the span [mm], h is the thickness [mm]. And finally σ_{f2} is the flexural stress [MPa] measured at deflection s_1 and σ_{f2} is the flexural stress [MPa] measures at deflection s_2.

$$s_i = \frac{\varepsilon_{fi}L^2}{6h} \tag{4.4}$$

$$E_f = \frac{\sigma_{f2} - \sigma_{f1}}{\varepsilon_{f2} - \varepsilon_{f1}} \tag{4.5}$$

In the Figure 4.13 there is the geometrical representation of the specimens and in the table 4.6 its dimensions.

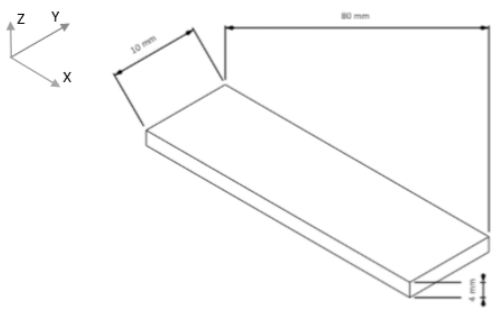

Figure 4.13 Bending specimen's dimensions [75].

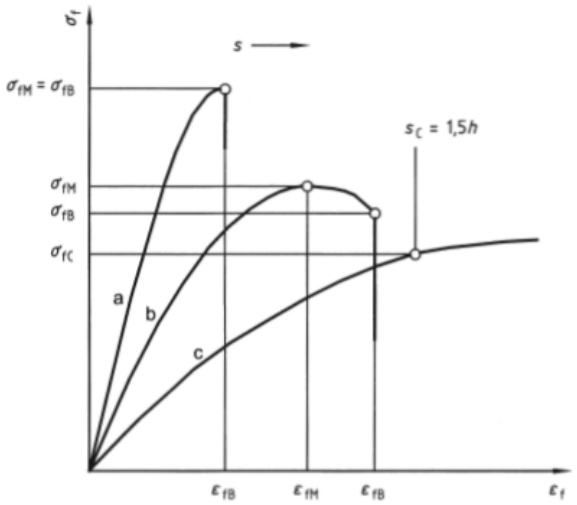

Curve a Specimen that breaks before yielding.
Curve b Specimen that gives a maximum and then breaks before the conventional deflection s_C.
Curve c Specimen that neither gives a maximum nor breaks before the conventional deflection s_C.

Figure 4.12 Typical curves of flexural stress versus flexural strain and deflection [75].

Table 4.6 Recommended dimensions for the bending specimens [75]

Specimen	**Dimensions (mm)**
l lenght	80 ± 2
b width	10.0 ± 0.2
h thickness	4.0 ± 0.2

Therefore, the specimens were firstly designed in *Solidworks* according to the ISO 178 and than converted to a *STL file*. Afterwards, all of them were carefully measured with calipers.

4.2.3.3 Compression

The principle of this test is that the specimen is compressed along its major axis at constant speed until the specimen fractures or until the load or the decrease in length reached a predetermined value. It is used to investigate the compressive behaviour of the test specimens and for determining the compressive strength, compressive modulus and other aspects of the compressive stress/strain relationship under the conditions defined. The compressive tests were done according to the ISO standard 604: *plastics - Determination of compressive properties* [76].

A typical stress-strain curve obtained after conducting the test is shown in the Figure 4.14, after analysing it, it is possible to determine the [76]:

- **Compressive stress at yield (σ_y):** first stress at which an increase in strain occurs without an increase in stress, it is expressed in MPa;
- **Nominal compressive yield strain (ε_{cy}):** strain corresponding to the compressive stress at yield σ_y, expressed as a dimensionless ratio or percentage (%);

- **Compressive stress at break (σ_B):** compressive stress at break of the test specimen, is expressed in MPa;
- **Nominal compressive strain (ε_C):):** decrease in length per unit original length L of the test specimen, it is expressed as a dimensionless ratio or percentage (%);
- **Compressive strength (ε_{cM}):** strain corresponding to the compressive strength (σ_M):, is expressed as a dimensionless ratio or percentage (%);
- **Nominal compressive strain at break ((ε_{cM}):):** strain at break of the test specimen, it is expressed as a dimensionless ratio or percentage (%).
- **Compressive modulus ($\mathbf{E}_c$):** ratio between the stress difference (σ_2-σ_1) and the corresponding strain difference (ε_2=0.0025 minus ε_1=0.0005), it is expressed in MPa.

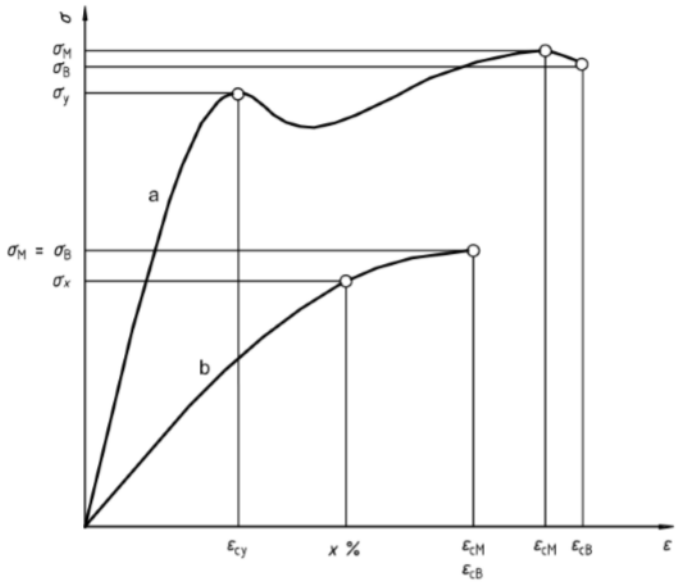

Figure 4.14 Typical compression stress/strain curve [76].

Figure 4.15 is the geometrical representation of the two specimens types used and in the table 4.7 the respective dimensions.

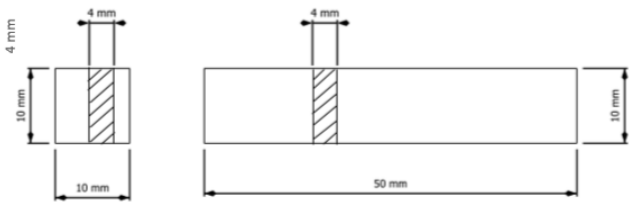

Figure 4.15 Compression specimen's dimensions [76].

Table 4.7 Recommended dimensions for the compressive specimens [76].

Type	***Measurement***	*Length, l*	*Width, b*	*Thickness, h*
A	Modulus	50 ± 2	10 ± 0.2	4 ± 0.2
B	Strength	10 ± 0.2		

Therefore, the specimens were firstly designed in *Solidworks* according to the ISO 604 and than converted to a *STL file*. Afterwards, all of them were carefully measured with calipers.

4.2.3.4 Experimental procedure

All the tensile, compression and flexural tests were done at *Laboratório de caracterização mecânica, da Secção de Tecnologia Mecânica e Gestão Industrial do Departamento de Eng. Mecânica no Instituto Superior Técnico*, and the treated results were sent in a pdf format. The testing system used was Instron 5960 Dual Column Testing System, the machine used was an Instron 5966 and the extensometers were axial clip-on extensometer 2630-111 and transverse clip-on extensometer W-E404-E (Figure 4.16). The machine details are shown in table 4.8.

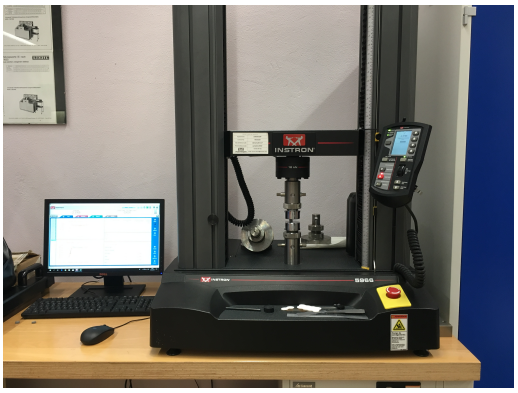

Figure 4.16 Testing machine Instron 5966.

Table 4.8 Instron 966 specification [77].

Capacity	10 kN
Vertical test space	1256 mm
Vertical test space (Extra-height model)	1712 mm

In table 4.9 it is stated the velocity for each of these tests.

Table 4.9 Mechanical test's parameters.

Test	**Stage**	**Velocity** (mm/min)
Tensile	2	1
Compression Type A (long)	2	1
Compression Type B (short)	2	5
Flexural	2	2
Tensile	3	1
Compression Type A (long)	3	1
Compression Type B (short)	3	5
Flexural	3	1

4.2.4 Impact tests

Impact strength is the measure of energy absorbed by a material when it is broken by a sudden blow, translates into its ability to develop an internal force multiplied by the deformation of the part without failure [78]. In the following sections it is described the impact tests.

4.2.4.1 Charpy impact test - ISO 179

This test is used to determine the Charpy impact strength of plastics under defined conditions. The charpy test will be done according to the standard ISO 179 (Part 1): *Plastics - Determination of Charpy impact strength of rigid materials*. [79]

After conducting the test it is possible to obtain the **Charpy impact strength** (α_{cN}), expressed in kJ/mm^2, it is given by the following equation:[79]

$$\alpha_{cN} = \frac{E_c}{hb_N} \times 10^3 \tag{4.6}$$

Where E_C is the corrected energy absorbed by breaking the test specimen [J], h is the thickness of the test specimen [mm] and b_N is the remaining width of the test specimen [mm].

Figure 4.17 is the geometrical representation of the specimens and in table 4.10 the respective dimensions.

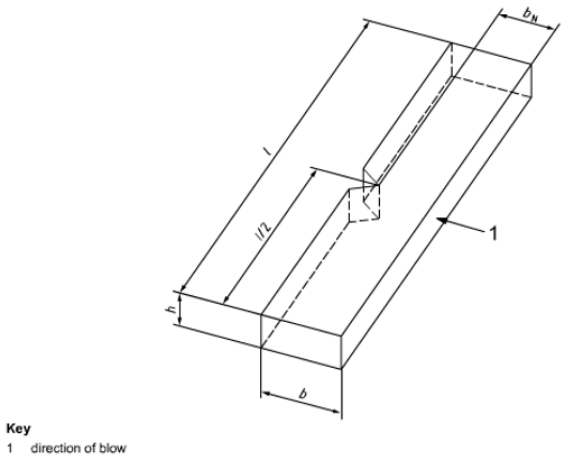

Figure 4.17 Charpy specimen's dimensions [79].

Table 4.10 Recommended dimensions for the Charpy specimens [79].

Specimen	**Dimensions (mm)**
l Length	50 ± 1
b Width	6.0 ± 0.2
h Thickness	4.0 ± 0.2
b_N Remaining width at notch tip	3.2 ± 0.2
r_N Notch tip radius	0.25 ± 0.05

Finally it is important to outline that for each condition it was produced 10 specimens.

Therefore, the specimens were firstly designed in Solidworks according to the ISO standard and than converted to a STL file. Afterwards, all of them were carefully measured with a caliper.

4.2.4.2 Experimental procedure

The Charpy impact strength was determined in a pendulum machine (*Tensometer Ltd*, Croydon, Reino Unido), shown in Figure 4.18. From all the weights available the one chosen was the **1/32 lb**.

Figure 4.18 Available weights for the Charpy test (left). Equipment used to do the Charpy tests (right).

4.2.4.3 High velocity test

Another test was performed as well in order to determine the impact strength. This test was very similar to a compression test but with very high speed, v=150 mm/s. It was only done in the third stage of the project, its main goal was to determine the absorbed energy by the gyroid structure.

Since the direction of blow in the Charpy test, referred to before, was perpendicular to the build deposition of the specimen. With this new test it was possible to determine the energy absorbed when the direction of blow was the same as the build deposition one, since the gyroid presents a better behaviour when the direction of blow is the same as the direction of deposition when being printed.

During this type of tests there are many peaks on F-t data record, because the falling head bounces off the sample and falls down again, so to determine the impact resistance only the first peak was used. The energy *E(s)* was obtained by the numerical integration of the F-s data records [80].

For this test it was decided to build cubic specimens, 20x20x20 mm, with an outside perimeter, as shown in the Figure 4.19. For each condition 3 specimens were build. The specimens were firstly designed in *Solidworks* according to the given dimensions and then converted to a *STL file*. Afterwards, all of them were carefully measured with calipers.

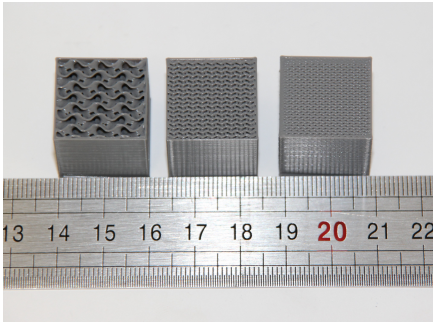

Figure 4.19 Impact test specimens 20%, 50%, 80% density (left to right respectively).

4.2.4.4 Experimental procedure

The machine used was a *Instron 8801*, as shown in the Figure 4.20. The test parameters were:

- **Velocity:** 150mm/s;
- **Height imposed:** 10mm (in order to assure that the machine plates wouldn't hit each other it was necessary to impose a certain height to the machine).

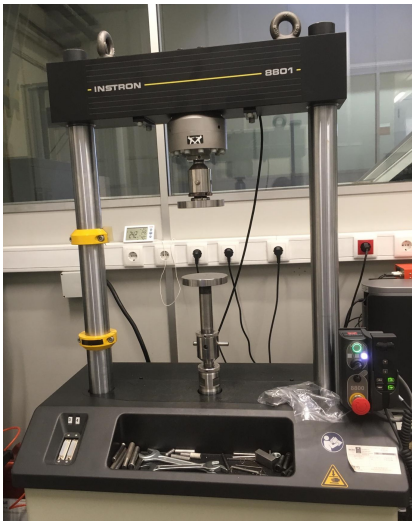

Figure 4.20 Equipment used to do the Impact tests.

4.3 Specimens to study the deposition orientation

The main goal in stage 2 was to determine the best deposition orientation, in order to do that it was tested with 100% linear infill density and four different orientations: 0°, 90°, 45°, ±45°. Afterwards, the tensile, compression and bending tests were done according to their respective ISO standards.

For this stage it was decided to print 10 specimens for each condition and for each test, being a total of 160 specimens. The printer used in this stage was the one based on an Ender 3 and the slicing software was *Simplify3D*, since this one allows to only have one angle infill. The printing parameters are shown in the following table 4.11.

Table 4.11 Stage 2: Printing Parameters.

Printing parameters		
Temperature (°C)	Printing Bed	60
	Extruder	210
Dimensions (mm)	ϕ extruder	0.4
	Layer height	0.2
	1st Layer Height	0.2
	1st Width	120
Velocity (mm/s)	Print	55
	Perimeters	27.5
	Infill	44
	XX_YY_axis	100
	1st Layer	16.5
	ZZ_axis	16.7
Number of perimeters		1

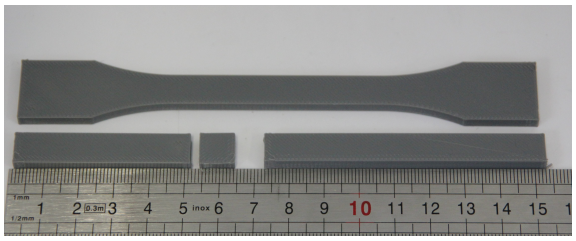

Figure 4.21 Stage 2 specimens : tensile, compression (2), flexural.

4.4 Specimens to study the gyroid infill

The main goal in stage 3 was to determine the influence of the gyroid infill in the specimens' mechanical properties, therefore it was tested with three different infill densities: 20%, 50% and

finally 80%. The infill was chosen in the slicing software, *Slic3r*. Afterwards the tensile, compression, bending and charpy tests were done according to their respective ISO standards. Also the impact test was conducted, as mentioned before. In figures 4.23 to 4.26 the 3 densities for each test are shown.

As it was mentioned before, for this stage the following specimens were produced according to the tests done:

- **Tensile:** 5 specimens;
- **Bending:** 5 specimens;
- **Compression:** 5 specimens;
- **Charpy:** 10 specimens;
- **Impact:** 3 specimens.

Therefore, it was printed a total of 84 specimens.

In this stage the printer Creality CR10 was used and the slicing software was *SLic3r* since this is the only open source free software that has the gyroid infill. As one of the points is to compare the tensile, bending and compression specimens of this stage with the ones from the previous one, the printing parameters chosen where the ones that showed the best likeliness between what was ideal for this machine and most similar to the one from the Stage 2, this is shown in table 4.12.

Table 4.12 Stage 3: Printing Parameters.

Printing parameters		
Temperature (°C)	Printing Bed	60
	Extruder	210
Dimensions (mm)	ϕ extruder	0.4
	Layer height	0.2
	1st Layer Heigth	0.2
	1st Layer Width	120
Velocity (mm/s)	Print	60
	Perimeters	30
	Infill	60
	1st Layer	18
Number of perimeters		1

Figure 4.22 Tensile specimens with gyroid infill 20%, 50% and 80% infill (up to bottom respectively).

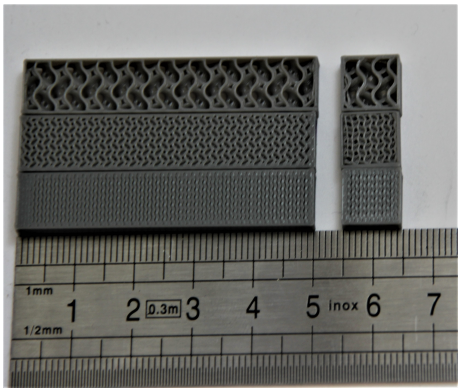

Figure 4.23 Compression specimens with gyroid infill 20%, 50% and 80% infill (up to bottom respectively).

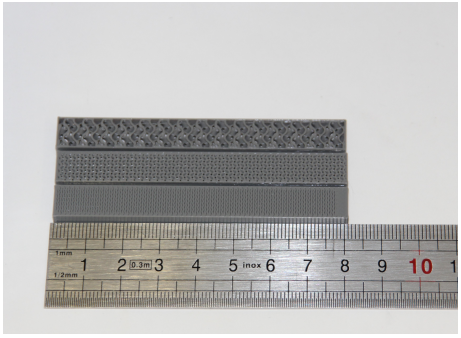

Figure 4.24 Flexural specimens with gyroid infill 20%, 50% and 80% infill (up to bottom respectively).

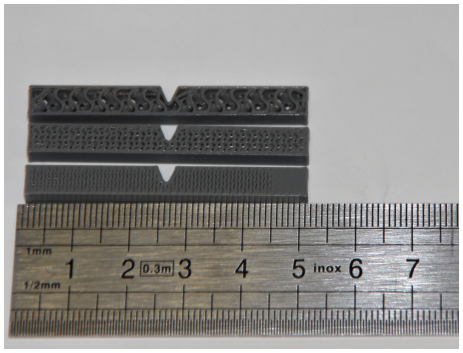

Figure 4.25 Charpy specimens with gyroid infill 20%, 50% and 80% infill (up to bottom respectively).

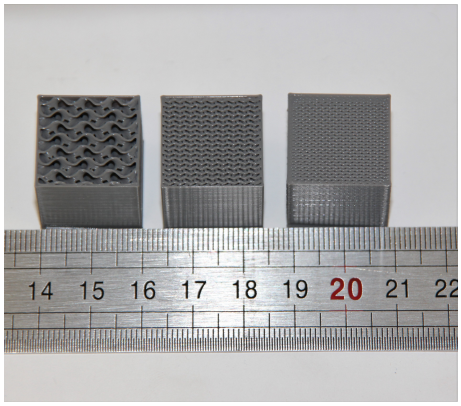

Figure 4.26 Impact specimens with gyroid infill 20%, 50% and 80% infill (left to right respectively).

Since the specimens in this stage aren't dense, the density is below 100%, it is not possible to use the same calculations as in the previous section 4.2.3. Therefore the apparent Modulus was calculated (E_{ap}), expressed in MPa. It is the ratio between the apparent stress ($\sigma_a p$), expressed in MPa, and the apparent strain ($\varepsilon_a p$).

$$E_{ap} = \frac{\sigma_{ap}}{\varepsilon_{ap}} \tag{4.7}$$

The apparent stress ($\sigma_a p$), expressed in MPa, is the ratio between the Load (F) [N] and the apparent cross section area (ignoring the void inside the part) (A) [mm^2]

$$\sigma_{ap} = \frac{F}{A} \tag{4.8}$$

The apparent strain ($\varepsilon_a p$) is the ratio between the displacement (d) [mm] and the initial distance (L_0) [mm].

$$\varepsilon_{ap} = \frac{d}{L_0} \tag{4.9}$$

Finally the coefficient K is the ratio between the load (F) and the displacement (d).

$$k = \frac{F}{d} \tag{4.10}$$

4.5 Specimens to study the gyroid structure

The main goal in stage 4 was to determine what the influence is of the outside perimeter in its behaviour in compression and gyroid's isotropic behaviour in compression. The printing parameters were the same as in the previous stage, however it was decided to lower the extruder temperature to 200 °C, since this temperature allows to achieve a more detailed structure.

In order to understand the importance of the outside perimeter and additionally to test the gyroid behaviour in compression, when the direction of blow is the same as the direction of printing deposition, cubic specimens 20x20x20 mm (the same ones used in the impact test) were tested, with and without an outside perimeter, shown in figure 4.27. Therefore 30 specimens were printed in total (5 for each condition).

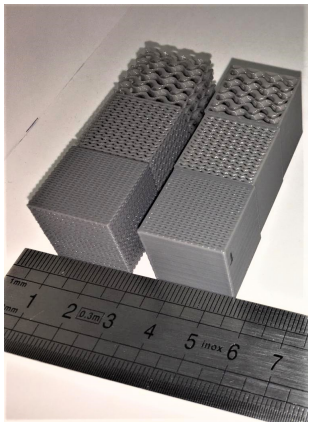

Figure 4.27 Cubic specimens to test in compression with and without an outside perimeter (right and left respectively) with gyroid infill 20%, 50% and 80% (up to bottom respectively).

The structure dimensions are 20x20x20 mm and the machine used to test them was also the *Instron 5996* and the test's velocity was 5 mm/min .

Finally, to achieve the last goal a gyroid unitary cell was printed, both in FDM and in a polyjet, since this is another more expensive technology present in the laboratory and the one used by the MIT team [81]. Therefore, it was tested in the three different directions, the build direction (ZZ) and the perpendicular ones (YY and XX), as shown in figures 4.28 and 4.29. Therefore 18 specimens were printed in total (9 for each technology)

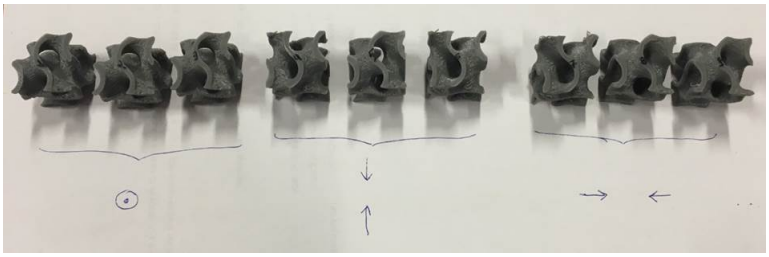

Figure 4.28 FDM Gyroid unitary cell and the directions of compression.

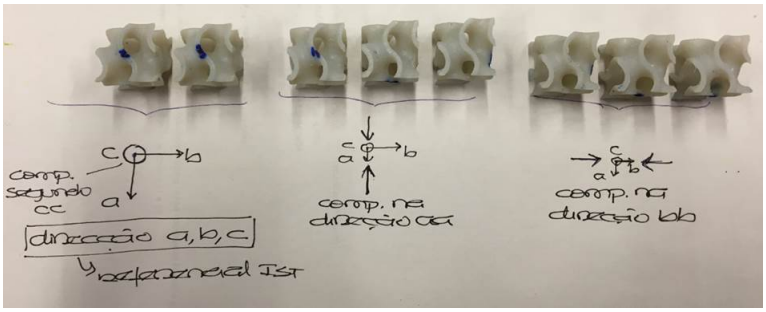

Figure 4.29 Polyjet Gyroid unitary cell and the directions of compression.

The structure dimensions are 20x20x20 mm and the machine used to test them was also the *Instron 5996* and the test's velocity was 5 mm/min in *Instituto Técnico da Universidade de Lisboa*.

Chapter 5

Results and discussion

In this chapter the results of the mechanical test of stages two, three and four of this project, will be presented and discussed. It is important to outline again that all the tensile, compression and flexural tests were conducted at *Laboratório de Caracterização Mecânica, da Secção de Tecnologia Mecânica e Gestão Industrial do Departamento de Eng. Mecânica no Instituto Superior Técnico*, cujos resultados podem ser consultados nos Anexos A, B e C and the treated results and photos are in A, B, C.

5.1 Specimens to study the deposition orientation

In this sections the results regarding the mechanical tests of the second stage of the project will be analysed.

5.1.1 Tensile tests

5.1.1.1 Specimens analysis

Before executing the destructive tests it was possible to analyse the quality of the specimens. Therefore, a visual control was done, in order to check eventual warping that could have happened, and dimensional one according to the ISO 527, shown in table 4.5.

Comparing all the specimens, the ones that showed the most significant defects were the ones with the deposition orientation of 0°, shown in the figure 5.1. This defect can probably be explained by the intersection of the nozzle with the deposited filament.

A dimensional comparison of the specimens in the four different conditions was also done, shown in table 5.1. l_3 is the overall length, l_2 is the distance between the parallel-sided portions, b_1 is the width at narrow portion, b_2 is the width at the end and h is the thickness, these dimensions are explained in detail in chapter 4, table 4.5.

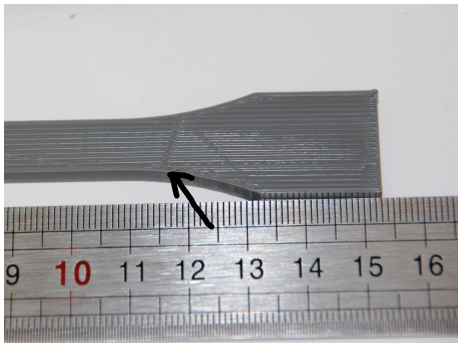

Figure 5.1 Defect of the specimens with the deposition orientation of 0°.

Table 5.1 Dimension of the tensile specimens in Stage 2.

	Dimensions ± SD (mm)						
Orientation	l_3	l_2	b_1	b_2	h	Weight ± SD (g)	Printing time (min)
0°	150.0±0.2	107.6±0.3	10.1±0.1	20.3±0.1	4.0±0.1	10.0±0.0	35
90°	150.1±0.1	107.7±0.3	10.1±0.1	20.1±0.1	4.0±0.1	10.0 ± 0.0	40
45°	150.1±0.0	107.4±0.5	10.1±0.1	20.1±0.1	4.0±0.1	10.0 ± 0.1	39
±45°	150.1 ±0.1	10.7.9 ±0.2	10.1 ±0.0	20.1±0.0	4.1±0.1	10.0±0.0	38
Theoretical	150	106 to 120	10.0±0.2	20.0±0.2	4.0±0.2	10.3875 ∗	

* the specimens' tensile weight was calculated by multiplying the specimens volume by the PLA density: 8.31 cm^3x1.25 g/cm^3

After analysing the table 5.1 it is possible to conclude that all the specimens' dimensions are according to the ISO 527, not showing any particular difference for any of the conditions.

5.1.1.2 Results of the tests

In figure 5.2 the stress-strain curve obtained for five specimens of each condition is shown. Therefore, it is possible to conclude that for all the conditions the specimens present a ductile behaviour with exception of the specimens with 0° that show a brittle fracture, because all of them broke in the region where there was a defect.

As shown in figure 5.3 the specimens with 0° have ruptured all in the same zone, the one with defects referred previously, outside the gauge marks. As it was refered by Lanzotti *et. al* in order to overcome this a modification of the fillet geometry should be done using a parabolic profile tangent to the middle of the specimen [31].

In table 5.2, it is summarised all the data obtained after the tensile test.

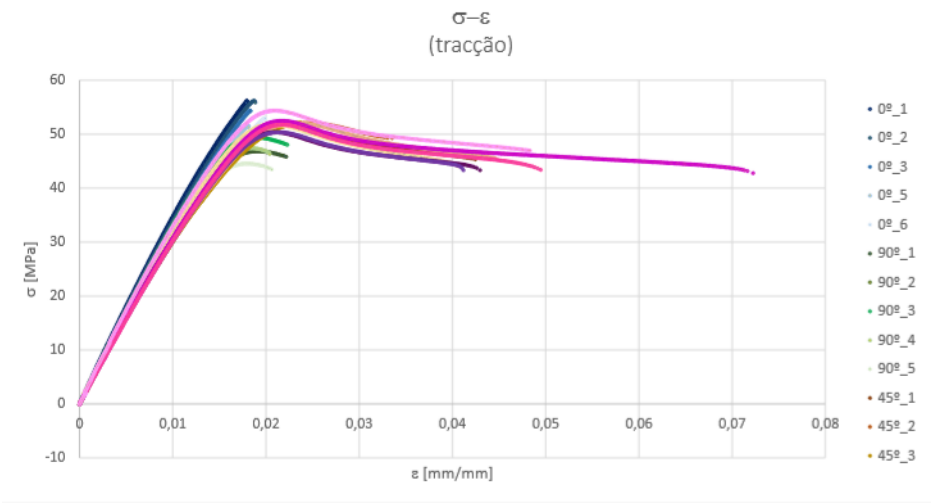

Figure 5.2 Stress-strain curve obtained in the Stage 2.

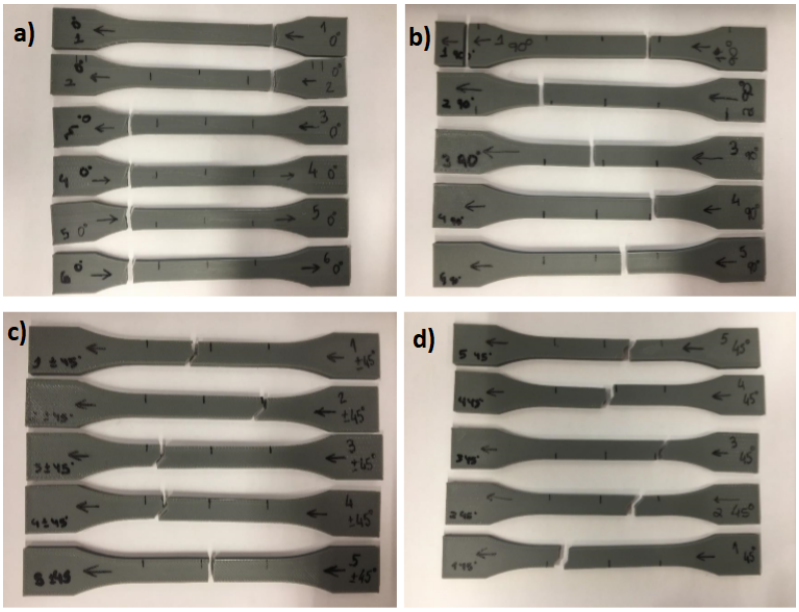

Figure 5.3 Tensile specimens obtained in Stage 2 after rupture with the deposition orientation: a) 0°, b) 90°, c) ±45°, d) 45°.

Table 5.2 Tensile information obtained in the Stage 2.

		Deposition Orientation			
		0°	90°	±45°	45°
Value ± SD	**Tensile stress at yield (σ_y) [MPa]**	-	47.2±1.7	52.1±1.5	52.7±0.8
	Tensile stress at break (σ_B) [MPa]	54.2±20	46.8±0.9	44.1±1.7	46.0±2.4
	Tensile strength (σ_M) [MPa]	54.2±2.0	47.2±1.7	52.1±1.5	52.8±0.8
	Tensile strain at yield (ε_y) [%]	-	1.83±0.08	2.13±0.03	2.11±0.04
	Tensile strain at break (ε_B) [%]	1.87±0.09	2.05±0.21	5.11±1.22	3.81±1.03
	Tensile strain (ε_M) [%]	1.87±0.09	2.05±0.21	5.11±1.22	3.81±1.03
	Young's Modulus (E_t) [MPa]	3454.3±192.4	3482.3±60.9	3304.3±186.9	3358.0±40.6
	Poissons ration (μ_n)	0.38±0.02	0.34±0.02	0.41±0.01	0.41±0.01

The tensile modulus was almost the same for the specimens with 90° and 0°. As proved by Dudescu *et. al* [33] the maximum tensile stress was obtained for the deposition orientation of 0° since the filaments are orientated in the same direction as the load.

5.1.2 Flexural test

5.1.2.1 Specimens analysis

Before conducting the destructive tests it was possible to analyse the quality of the specimens. Therefore, a visual control was done, in order to check eventual warping that could happen, and dimensional one according to the ISO 178, shown in table 5.3. l is the length, b is the width and h is the thickness, these dimensions are explained in detail in chapter 4, table 4.6.

Table 5.3 Dimension of the flexural specimens in Stage 2.

	Dimensions ± SD (mm)				
Orientation	*l*	*b*	*h*	Weight ±SD (g)	Printing time (min)
0°	80.0±0.0	10.2±0.1	4.0±0.1	3.8±0.0	14
90°	80.1±0.1	10.1±0.1	4.0±0.0	3.8±0.0	16
45°	80.2±0.1	10.1±0.1	3.9±0.1	3.8±0.0	16
±45°	80.1±0.1	10.2±0.1	3.9±0.1	3.8±0.0	16
Theoretical	80±2	10.0±0.2	4.0±0.2	4∗	

* the specimens' flexural weight was calculated by multiplying the specimens volume by the PLA density: 3.2 cm^3x1.25 g/cm^3

After analysing table 5.3 it is possible to conclude that all the specimens' dimensions are according to the ISO 178, not showing any particular difference for any of the conditions.

5.1.2.2 Results of the tests

In figure 5.4 the flexural stress-strain for five specimens are shown of each condition. Therefore, it is possible to conclude that for all the conditions the specimens present a ductile behaviour with the exception for the specimens with 90° that break before yielding, since $\sigma_{fB} = \sigma_{fM}$.

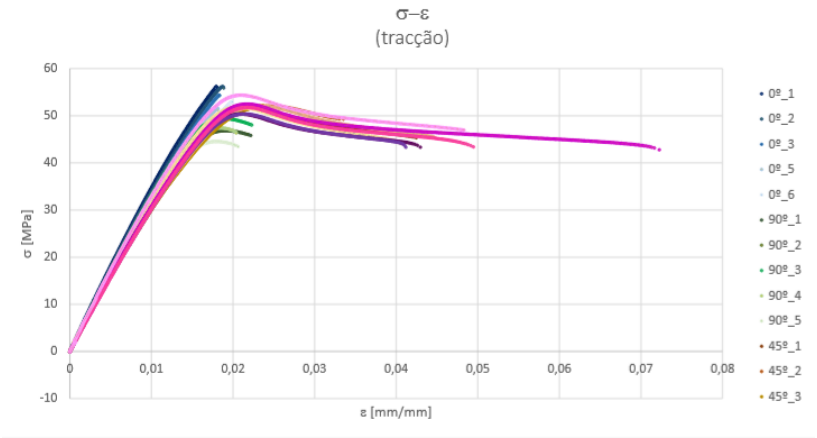

Figure 5.4 Flexural stress-strain obtained in the Stage 2.

This is also possible to observe in figure 5.5, where the different failure modes for the different conditions are shown, and the specimens with 90° are the only ones that show break before bending.

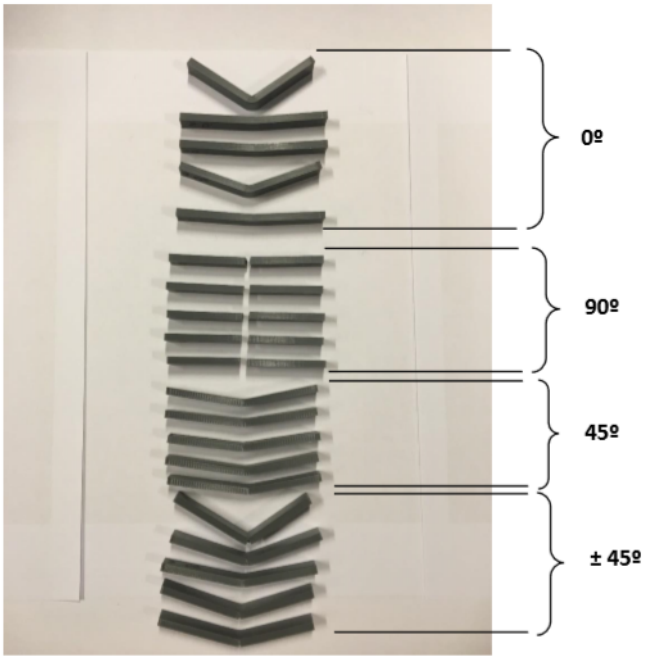

Figure 5.5 Flexural specimens obtained in Stage 2 after the test.

In table 5.4 the data that was obtained after the tensile tests are summarised, according to the ISO 178.

Table 5.4 Flexural information obtained in the Stage 2.

		Deposition Orientation			
		0°	90°	±45°	45°
Value ± SD	**Flexural strength (σ_{fM}) [MPa]**	99.9 ±4.3	76.6±3.1	92.9±6.7	88.9±6.4
	Flexural strain at flexural strength (ε_{fM}) [%]	4.45±0.13	3.05±0.15	4.32±0.12	4.33±0.19
	Flexural modulus (E_f) [MPa]	2838.8±217.5	2433.5±267.1	2521.1±458.6	2318.8±391.6

The flexural results are according to what was obtained by T. Letcher *et. al* [32] since the maximum flexural strength and flexural modulus were obtained for the specimens with 0° orientation.

5.1.3 Compression tests

5.1.3.1 Specimens analysis

Before realising the destructive tests it was possible to analyse the quality of the specimens. Therefore, a visual control was done, in order to check eventual warping that could happen, and dimensional one according to the ISO 604, shown in the tables 5.5, 5.6. l is the length, b is the width and h is the thickness, these dimensions are explained in detail in chapter 4, figure 4.15.

Table 5.5 Dimensions of the compression specimens type A.

	Dimensions ± SD (mm)				
Orientation	*l*	*b*	*h*	Weight ±SD (g)	Printing time (min)
0°	50.0±0.0	10.1±0.0	3.9±0.1	2.4±0.0	9
90°	50.2±0.1	10.1±0.1	3.9±0.1	2.4±0.0	9
45°	50.1±0.0	10.1±0.0	4.0±0.1	2.4±0.0	10
±45°	50.0±0.0	10.1±0.0	4.0±0.1	2.4±0.0	10
Theoretical	50±2	10±0.2	4±0.2	2.5∗	

* the specimens' compression type A weight was calculated by multiplying the specimens volume by the PLA density: 2 cm^3x1.25 g/cm^3

Table 5.6 Dimensions of the compression specimens type B.

	Dimensions ± SD (mm)				
Orientation	*l*	*b*	*h*	Weight ±SD (g)	Printing time (min)
0°	10.4±0.0	10.2±0.1	3.99±0.1	0.5±0.0	5
90°	10.4±0.0	10.1±0.0	4.0±0.0	0.5±0.0	5
45°	10.4±0.1	10.3±0.1	3.9±0.1	0.5±0.0	5
±45°	10.5±0.1	10.4±0.4	3.9±0.1	0.5±0.0	5
Theoretical	10±0.2	10±0.2	4±0.2	0.625 ∗	

* the specimens' compression type B weight was calculated by multiplying the specimens volume by the PLA density: 0.5 cm^3x1.25 g/cm^3

After analysing the tables 5.5, 5.6 it is possible to conclude that all the specimen's dimensions are according to the ISO 604, not showing any particular differences for any conditions.

5.1.3.2 Results of the tests

In the Figures 5.6, 5.7 the compression stress-strain for five specimens of each condition are shown.

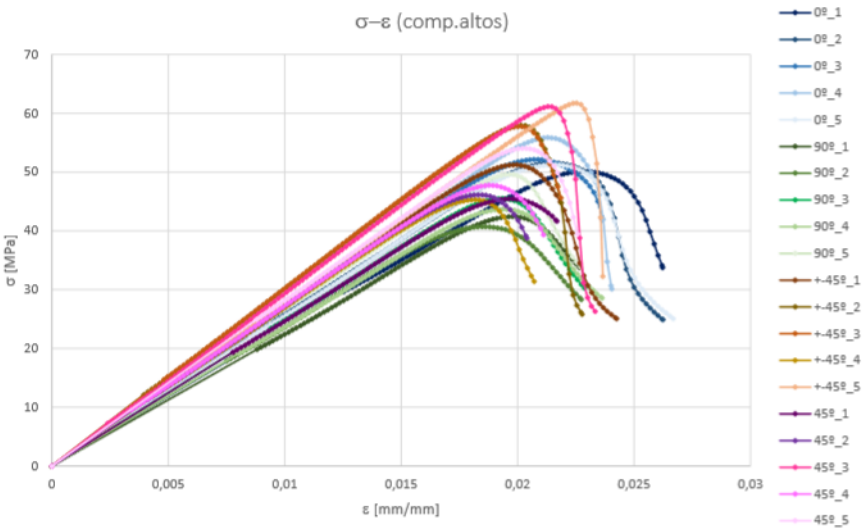

Figure 5.6 Compression stress-strain obtained for the Specimens Type A in the Stage 2.

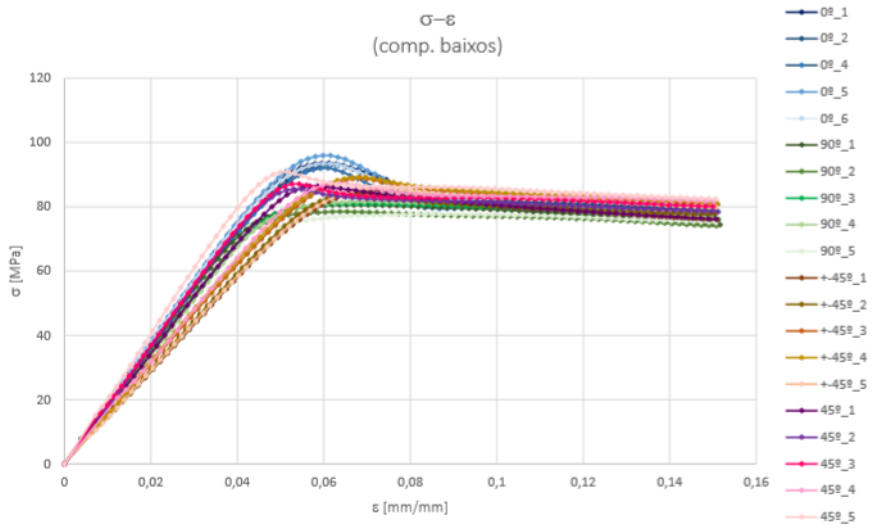

Figure 5.7 Compression stress-strain obtained for the Specimens Type B in the Stage 2.

In table 5.7 it is summarised the data obtained after analysing the compression curves, according to the ISO 604.

Table 5.7 Compression information obtained in the Stage 2.

		Deposition Orientation			
		0°	90°	±45°	45°
Value ± SD	**Modulus (E_t) [MPa]**	2573.3±153.1	2420.0±155.6	2855.2±156.2	2722.5±161.1
	Compressive stress at yield (σ_y) [MPa]	93.6±1.4	79.9±1.7	86.7±2.2	87.5±2.1
	Nominal compressive yield strain (ε_{cY}) [%]	6.07±0.08	6.99±0.71	7.03±0.28	5.62±0.49

The maximum compressive stress at yield was 93.6 MPa with a corresponding strain of 6% for the 0° raster orientation. The maximum compressive modulus was 2855.2 MPa obtained for the ±45° deposition orientation.

5.2 Specimens to study the gyroid infill

In this sections the results regarding to the mechanical tests of the third stage of the project will be analysed.

5.2.1 Tensile tests

5.2.1.1 Specimens analysis

Before realising the destructive tests it was possible to analyse the quality of the specimens. Therefore, a visual control was done, in order to check eventual warping that could happen, and dimensional one according to the ISO 527, shown in table 5.8. l_3 is the overall length, l_2 is the distance between the parallel-sided portions, b_1 is the width at narrowest portion, b_2 is the width at the end and h is the thickness, these dimensions are explained in detail in chapter 4, table 4.5.

Table 5.8 Dimension of the tensile specimens in Stage 3.

	Dimensions ± SD (mm)						
Density	l_3	l_2	b_1	b_2	h	Weight ±SD (g)	Printing time (min)
20%	150.1±0.1	108.0±0.2	9.9±0.0	19.9±0.1	4.0±0.1	2.7±0.0	21
50%	150.0±0.1	108.1±0.3	10.0±0.0	19.84±0.0	4.01±0.1	5.4±0.0	57
80%	150.0±0.1	108.0±0.4	9.9±0.0	19.8±0.0	4.0±0.1	8.2±0.1	95
Theoretical	150	106 to 120	10.0±0.2	20.0±0.2	4.0±	20%:2.08 50%:5.2 80%:8.3 *	

* the specimens' tensile weight was calculated by multiplying the specimens volume by the PLA density by the specimens density: 8.31 cm^3x1.25 g/cm^3xdensity

After analysing the table 5.8 it is possible to conclude that all the specimen's dimensions are according to the ISO 527, not showing any particular difference for any of the conditions. It is also

interesting to outline that even though the specimens are less dense then the ones in the previous stage, the printing time is longer, due to the complex infill structure and the lower speed needed to print it correctly.

5.2.1.2 Results of the tests

In figure 5.8 the load-displacement curve obtained for the five specimens for each density is shown. It is possible to conclude that the greater the density, the greater the load at break and the yield load. It is also interesting to observe that the displacement at break is higher for the specimens with 50% density then for the ones with 80% density, this is coincident to what was found in the literature by Dudescu *et. al* since the elongation at maximum stress for an infill rate of 60% was higher than for an infill rate of 80% [33]. Finally, the specimens with 20% density don't present a yield point.

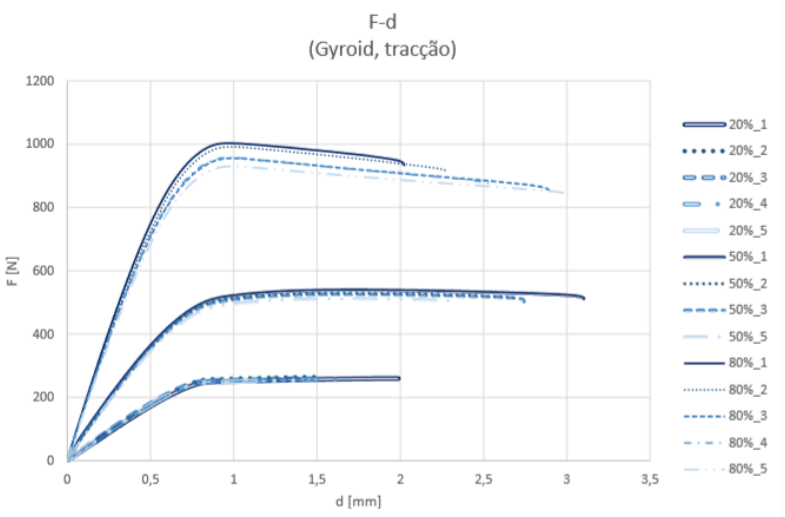

Figure 5.8 Tensile load-displacement curve obtained in the Stage 3.

In figure 5.9 it is shown the specimens after the test, it is possible to observe that the specimens with 20% infill broke outside the gauge marks and where the cross section was not constant anymore. All the 50% infill specimens broke in the same region where there seemed to be a small defect.

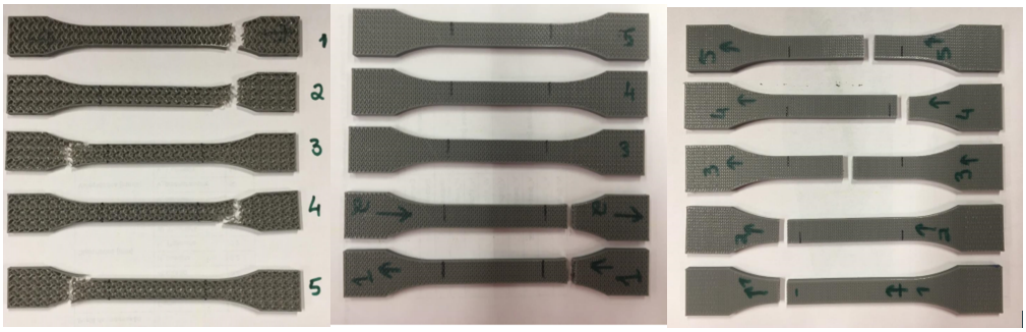

Figure 5.9 Tensile specimens obtained in Stage 3 after rupture: 20% density (left), 50% (middle) and 80% density (right).

In table 5.9 the tensile properties, which are obtained after the tensile test according to the equations shown previously for specimens without 100% infill, are summarised.

Table 5.9 Tensile information obtained in the stage 3.

		Gyroid infill density		
		20%	50%	80%
Value ± SD	**Load at yield (F_y) [N]**	-	526.4±11.2	967.7±
	Load at break (F_B) [N]	257.9±4.5	506.2±8.0	882.5±38.1
	Displacement at yield (d_y) [mm]	-	1.7±0.0	1.0±0.0
	Displacement at break (d_B) [mm]	1.6±0.2	2.7±0.3	2.5±0.4
	Apparent stress (σ_{ap}) [MPa]	5	10	20
	Apparent strain (ε_{ap}) (%)	1	1	1
	Apparent Modulus of elasticity (E_{ap}) [MPa]	500	1000	2000

As it is shown in figure 5.10 the apparent modulus of elasticity of the tensile specimens with the gyroid infill is significantly lower when compared with the greatest one obtained in the previous stage (100% linear infill). This can be explained, since the direction of load is perpendicular to the construction one, therefore, the solicitation is at the gyroid's poorest direction. This is according to what was found in the literature by Alsalla *et. al*[48], since the elasticity modulus, the ultimate tensile stress and the yield strength are all greater when the specimen is built vertically as for horizontally, like the ones in this dissertation. The apparent elasticity modulus increases with the density, as it is observed by Dudescu *et. al* [33].

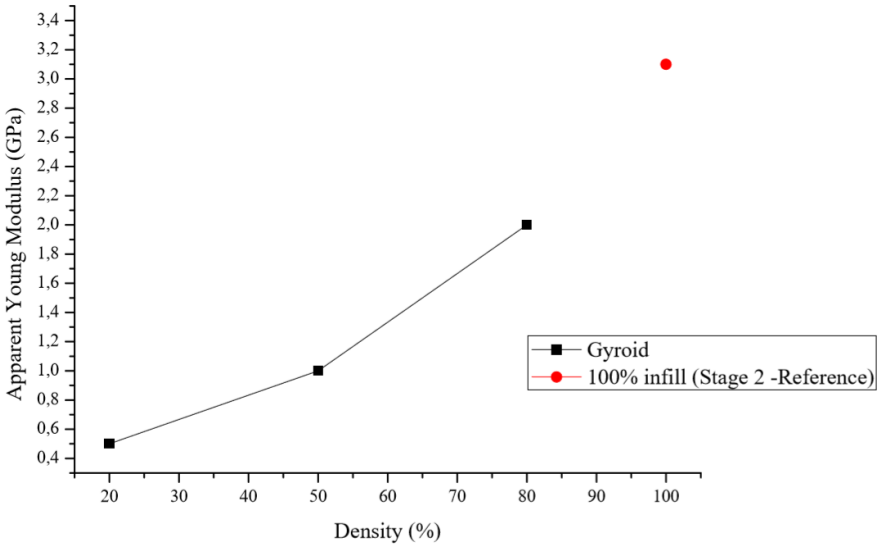

Figure 5.10 Influence of the gyroid infill density on the modulus of elasticity.

In figure 5.10 the maximum elasticity modulus obtained in the previous stage (when the influence of the deposition orientation was studied for specimens with 100% infill) is considered the reference. Its value is the elasticity modulus and not the apparent one because it is solid. This correlation will also be done for the following flexural and compression tests.

5.2.2 Flexural tests

5.2.2.1 Specimens analysis

Before realising the destructive tests it was possible to analyse the quality of the specimens. Therefore, it was done a visual control, in order to check eventual warping that could happened, and dimensional one according to the ISO 178, shown in table 5.10. l is the length, b is the width and h is the thickness, these dimensions are explained in detail in chapter 4, table 4.6.

Table 5.10 Dimension of the flexural specimens in Stage 3.

	Dimensions ± SD (mm)				
Density	*l*	*b*	*h*	Weight ±SD (g)	Printing time (min)
20%	80.0±0.0	9.9±0.0	4.1±0.0	1.2±0.0	9
50%	80.0±0.0	9.9±0.0	4.1±0.0	2.2±0.0	23
80%	80.0±0.0	9.9±0.1	4.0±0.1	3.2±0.0	37
Theoretical	80±2	10.0±0.2	4.0±0.2	20%:0.8 50%:2.0 80%3.2 ∗	

* the specimens' flexural weight was calculated by multiplying the specimens volume by the PLA density by the specimens density: 4 cm^3x1.25 g/cm^3xdensity

After analysing the table 5.10 it is possible to conclude that all the specimens' dimensions are according to the ISO 178, not showing any particular difference for any conditions.

5.2.2.2 Results of the tests

In figure 5.11 the flexural load-displacement curve obtained for the five specimens for each density is shown. It is possible to conclude that the maximum flexural load increases with the specimen's density.

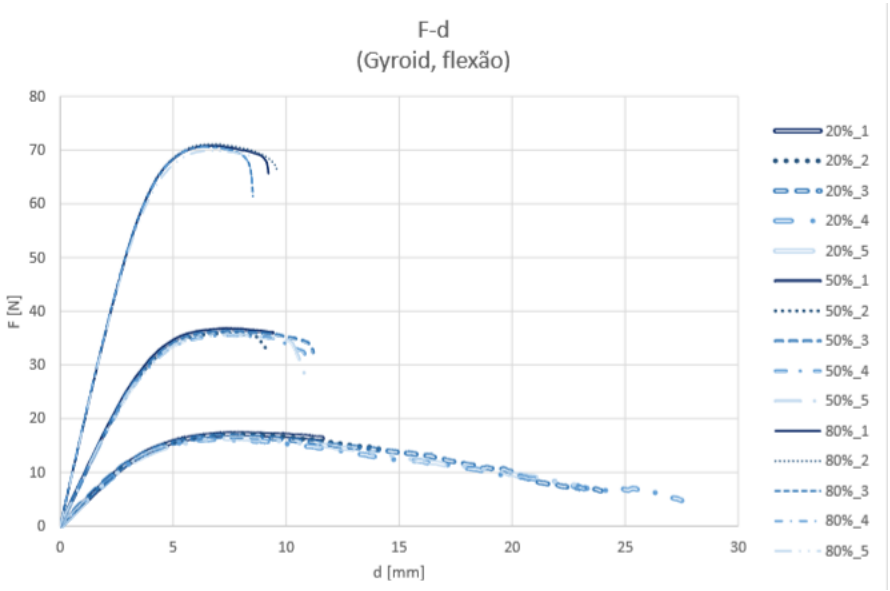

Figure 5.11 Flexural load-displacement curve obtained in the Stage 3.

In figure 5.12 the specimens after the tests are shown. It is possible to observe that some specimens with 80% density broke.

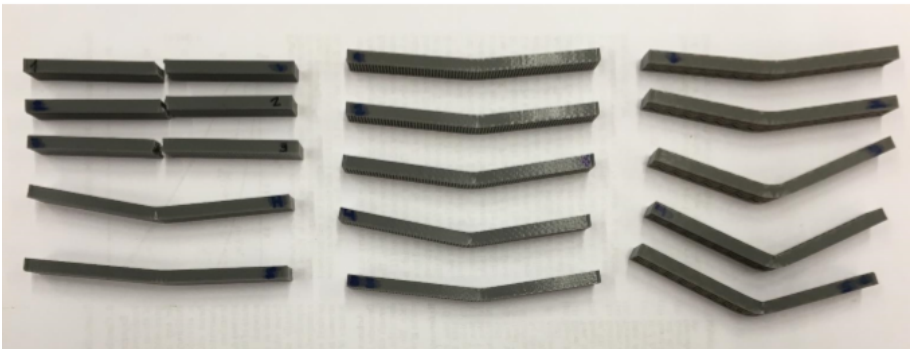

Figure 5.12 Flexural specimens obtained in Stage 3 after the test with 80%, 50% and 20% gyroid infill density (from right to left respectively).

In table 5.11 the flexural properties are summarised. These are obtained after the bending test according to the equation shown previously for specimens without 100% infill.

Table 5.11 Flexural information obtained in stage 4.

		Gyroid infill density		
		20%	50%	80%
Value ± SD	**Maximum flexural load (F_{fM}) [N]**	16.7±0.4	36.0±0.5	70.5±0.6
	Flexural displacement at maximum flexural load (d_{fM}) [mm]	7.6±0.5	7.4±0.1	6.6±0.2
	Apparent stress (σ_{ap}) [MPa]	0.25	0.75	1.5
	Apparent strain (ε_{ap}) [%]	3.13	5	3.75
	Apparent flexural modulus (E_{ap}) [MPa]	8	15	40

As it is shown in figure 5.13 the apparent flexural modulus increases with the increase of density, however it is significantly lower for the specimens with gyroid infill when compared to the 100% traditional infill (obtained in Stage 2). Therefore, it is possible to conclude that this infill doesn't present good properties under flexural situations.

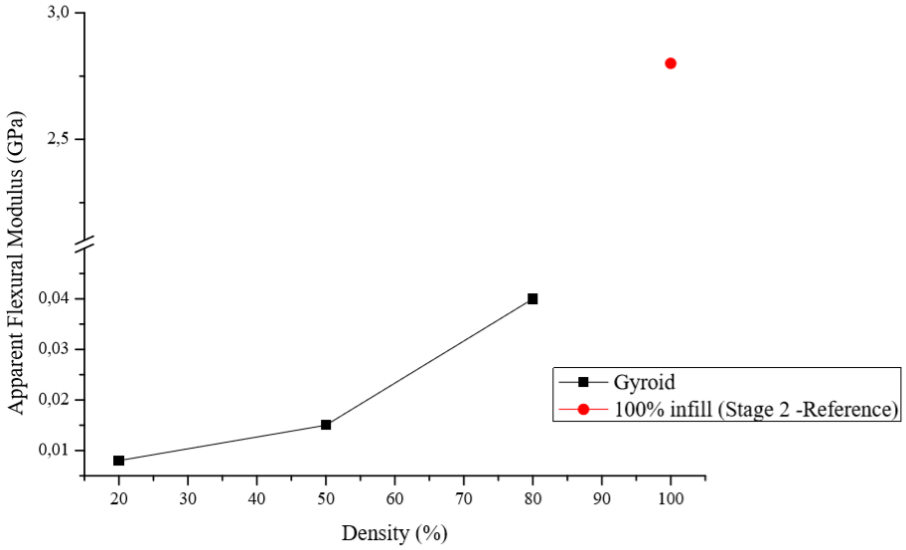

Figure 5.13 Influence of the gyroid infill density on the flexural modulus.

5.2.3 Compression tests

5.2.3.1 Specimens analysis

Before realising the destructive tests it was possible to analyse the quality of the specimens. Therefore, it was done a visual control, in order to check eventual warping that could happen, and dimensional one according to the ISO 604, shown in tables 5.12, 5.13. l is the length, b is the width

and h is the thickness, these dimensions are explained in detail in chapter 4, figure 4.15.

Table 5.12 Dimension of the compression specimens type A in Stage 3.

	Dimensions ± SD (mm)				
Density	*l*	*b*	*h*	Weight ±SD (g)	Printing time (min)
20%	50.0±0.0	9.9±0.0	4.0±0.0	0.75±0.0	6
50%	50.0±0.0	9.9±0.0	4.0±0.0	1.4±0.0	14
80%	50.0±0.0	9.9±0.0	4*pm*0.0	2.1±0.0	25
Theoretical	50±2	10±0.2	4±0.2	20%:0.5 50%:1.3 80%:2.0 ∗	

* the specimens' compression type A weight was calculated by multiplying the specimens volume by the PLA density by the specimens density: 2.5 cm^3x1.25 g/cm^3xdensity

Table 5.13 Dimension of the compression specimens type B in Stage 3.

	Dimensions ± SD (mm)				
Density	*l*	*b*	*h*	Weight ±SD (g)	Printing time (min)
20%	10.0±0.0	10.0±0.0	4.0±0.0	0.2±0.0	3
50%	10.0±0.0	10.0±0.0	4.0±0.0	0.3±0.0	4
80%	10.0±0.0	10.0±0.0	4.0±0.1	0.4±0.0	5
Theoretical	10.0±0.2	10.0±0.2	4.0±0.2	20%:0.1 50%:0.3 80%:0.4 ∗	

* the specimens' compression type B weight was calculated by multiplying the specimens volume by the PLA density by the specimens density: 0.5 cm^3x1.25 g/cm^3xdensity

5.2.3.2 Results of the tests

In figures 5.14, 5.15 the compression load-displacement for the five specimens of each gyroid infill density are shown.

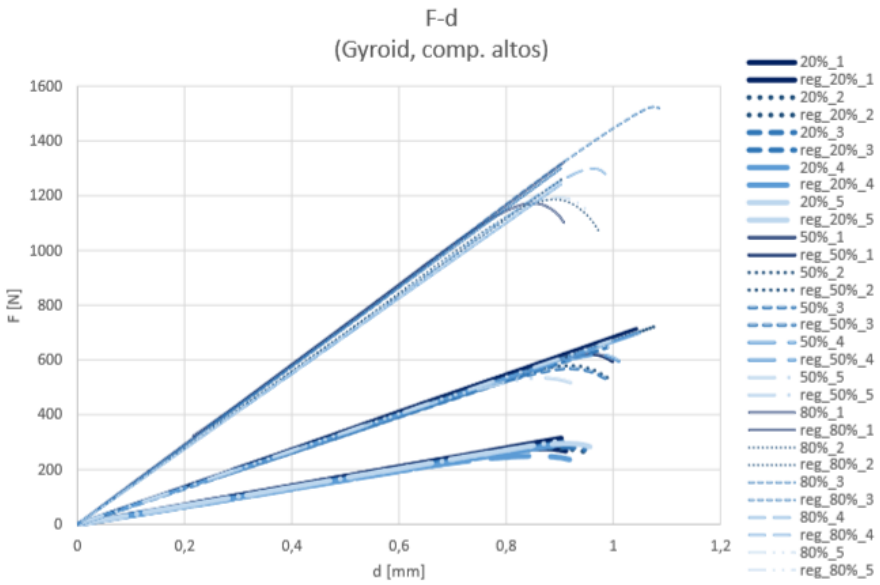

Figure 5.14 Compressive load-displacement for the Specimens Type A in the stage 3.

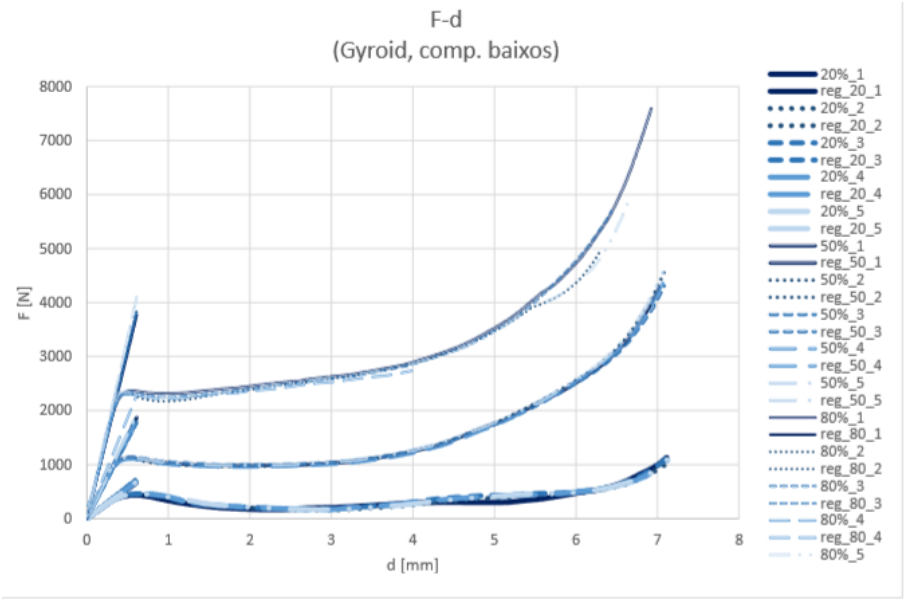

Figure 5.15 Compressive load-displacement for the Specimens Type B in the stage 3.

In figure 5.16 it is shown the compression specimens type B after the conducted tests.

Figure 5.16 Compression specimens type B in Stage 3 after the test: 20% infill density (bottom), 50% infill density and 80% infill density (top).

As shown in table 5.14 the compressive load yield is greater for greater infill densities. In similarity to what happened for the tensile tests, the compressive displacement at yield is the greatest for the 50% density specimens, followed by the 20% one and finally the lowest is for the 80% density specimens. As it was possible to observe in the literature, by Abbas *et. al*, the compressive strength increases with the density increase [34]. Between the 20% density specimens and 50% there was an increase of the load at yield of 40%, and between the 50% and 80% specimens there was an increase of 47%.

Table 5.14 Compressive information obtained in stage 3.

			Gyroid infill density		
			20%	50%	80%
Value ± SD	**Type A**	**Apparent stess (σ_{ap}) [MPa]**	5	10	25
		Apparent strain (ε_{ap}) (%)	1.2	1.2	1.4
		Apparent compressive modulus (E_{ap}) [MPa]	416.7	833.3	1785.7
	Type B	**Load at yield (F_y) [N]**	452.7±9.4	1123.6±16.9	2340.9±23.7
		Displacement at yield (d_y) [mm]	72.9±1.2	80.9±9.2	71.5±9.1

As shown in figure 5.17 the apparent compressive modulus increases with the increase of density. Although it being still significantly lower than the one obtained in the stage 2. This was already observed for the tensile tests and it is expected that this happened for the same reasons, the building direction is perpendicular to the direction load. However this doesn't meet what was observed in the literature, the compressive modulus is similar regardless the soliction's direction [49], the specimens tested in this section were according to the ISO 604 and in the literature it was a gyroid structure, this will be further explored later.

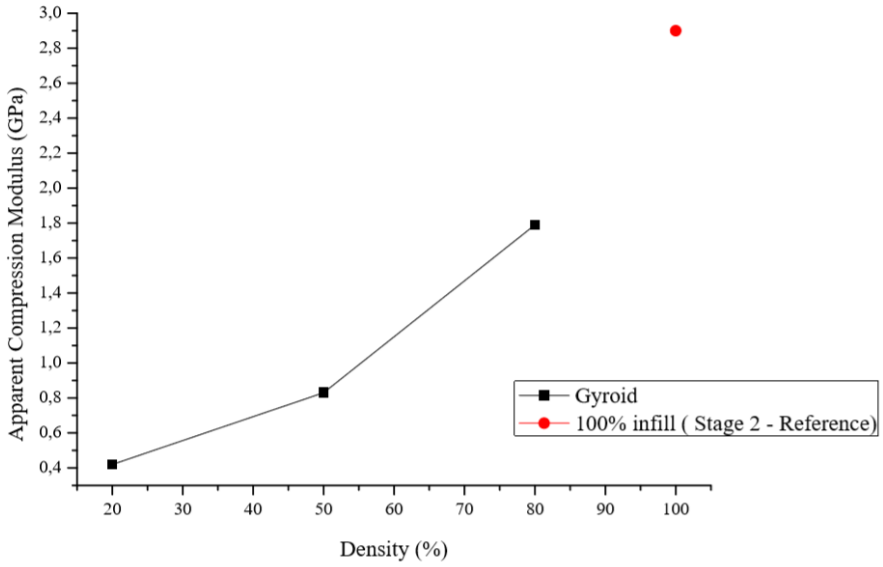

Figure 5.17 Influence of the gyroid infill density on the compressive modulus.

5.2.4 Charpy tests

5.2.4.1 Specimens analysis

Before executing the destructive tests it was possible to analyse the quality of the specimens. Therefore, a visual control was done, in order to check eventual warping that could happen, and dimensional one according to the ISO 179, shown in the table 5.15. b is the width, b_N is the remaining width at the notch tip and h is thickness, these dimensions are explained in detail in chapter 4, table 4.10.

Table 5.15 Dimensions of the Charpy specimens in Stage 3.

	Dimensions ± SD (mm)				
Density	*b*	*h*	b_N	Weight ±SD (g)	Printing time (min)
20%	6.0±0.1	3.8±0.0	3.2±0.1	0.5±0.0	5
50%	6.0±0.1	3.9±0.0	3.2±0.1	0.9±0.0	10
80%	6.0±0.0	3.9±0.0	3.2±0.0	1.2±0.0	15
Theoretical	6.0±0.2	4±0.2	3.2±0.2	20%: 0.2 50% 0.6 80% 0.9 *	

* the specimens' charpy weight was calculated by multiplying the specimens volume by the PLA density by the specimens density: 1.18cm^{3}x1.25g/cm^{3}xdensity

After analysing the table 5.15 it is possible to conclude that all the specimen's dimensions are according to the ISO 179, not showing any particular differences for any of the conditions.

In the figures 5.18, 5.19, 5.20 it is possible to observe the notch in the specimens with 20%, 50% and 80% gyroid infill density. It is noticeable that the printing quality is quite good in all of them.

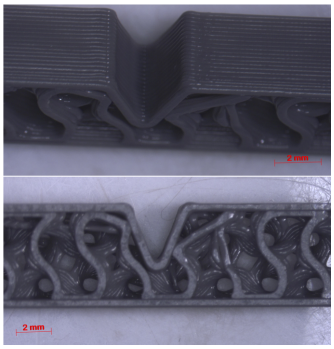

Figure 5.18 Different perspectives of the notch of the charpy specimen with 20% gyroid infill obtained with the stereo binocular microscope.

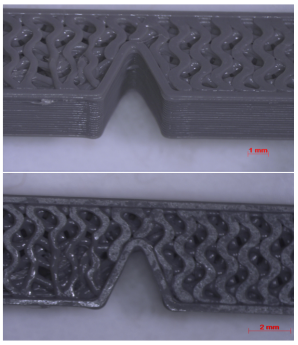

Figure 5.19 Different perspectives of the notch of the charpy specimen with 50% gyroid infill obtained with the stereo binocular microscope.

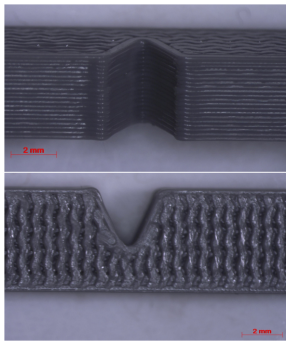

Figure 5.20 Different perspectives of the notch of the charpy specimen with 80% gyroid infill obtained with the stereo binocular microscope.

5.2.4.2 Results of the tests

After conducting the Charpy test it was possible to calculate the Charpy apparent impact strength (α_{cN}), the results are in the following table 5.16.

Table 5.16 Charpy apparent impact strength obtained in the Stage 3.

		Gyroid infill density			**Linear infill (density)**
		20%	50%	80%	100% (reference)
Value ± SD	**Charpy Apparent Impact Strength (α_{cN}) [kJ/mm^2]**	1.51±0.17	1.61±0.14	1.62±0.14	1.79±0.07

As it was to be expected, the impact strength increases with the increase of the specimen density. However, regardless the density it is significantly lower than the 100% linear infill density, 1.79 kJ/mm^2. Since, as it has been referred before, the direction of blow in the Charpy test is perpendicular to the deposition one, justifying the low results obtained with the gyroid when compared with the 100% linear infill. In conclusion the infill is more important than the density used, since the difference between the charpy impact strength of the specimens with 80% gyroid infill and the reference one is 9%, additionally the difference between the 20% gyroid infill one and the 80% gyroid infill is around 7%.

As shown in figure 5.21 using the 50% density is better then using the 80% one, since the gyroid impact strength is very similar and the weight of the specimen with 50% density is approximately 25% lower than the 80% one. It is also predictable that the maximum charpy impact strength obtained with the gyroid infill is for a density between 60% and 80%. Finally it is possible to observe that the charpy impact strength has a significant increase between the densities of 20% and 50% and it is relatively stable afterwards.

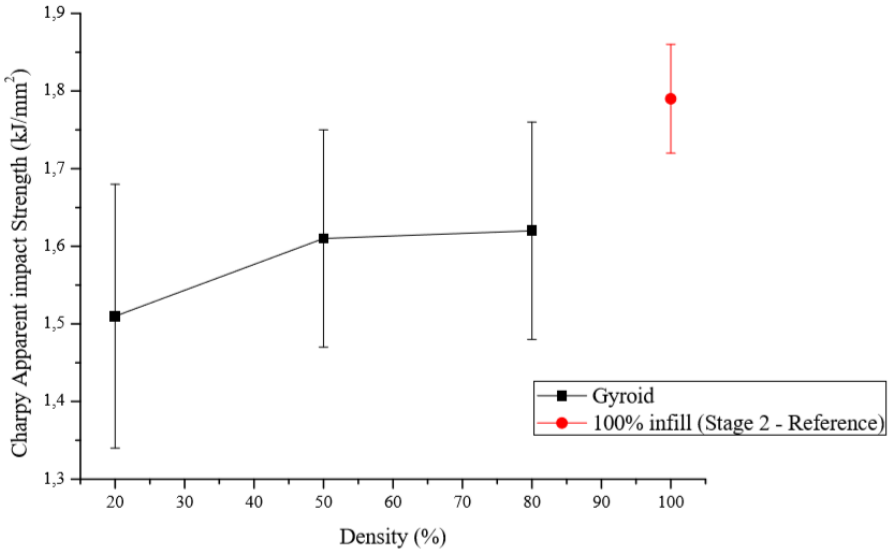

Figure 5.21 Influence of the gyroid infill density on the charpy impact strength.

5.2.5 Impact tests

5.2.5.1 Specimens analysis

Before executing the destructive tests it was possible to analyse the quality of the specimens. Therefore, a visual control was done, in order to check eventual warping that could happen, and dimensional one according to the dimensions established in the previous chapter, shown in the table 5.17.

Table 5.17 Dimensions of the Impact specimens in Stage 3.

	Dimensions ± SD (mm)				
Density	l_1	l_2	l_3	Weight ±SD (g)	Printing time (min)
20%	19.9±0.1	19.9±0.1	19.9±0.1	2.7±0.0	22
50%	20.0±0.1	20.0±0.1	20.0±0.1	5.3±0.1	56
80%	20.0±0.1	19.9±0.1	20.0±0.1	8.0±0.1	93
Theoretical	20.0	20.0	20.0	20%:1.6 50%:4.0 80%:6.4 *	

* the specimens' impact weight was calculated by multiplying the specimens volume by the PLA density by the specimens density: 8 cm^3x1.25 g/cm^3xdensity

After analysing the table 5.17 it is possible to conclude that all the specimens' dimensions are according to the established ones and that, of course, both the time and the weight increase with the increase of the density.

5.2.5.2 Results analysis

In the Figure 5.22 it is represented the force/displacement for each condition and additionally a 100% linear infill.

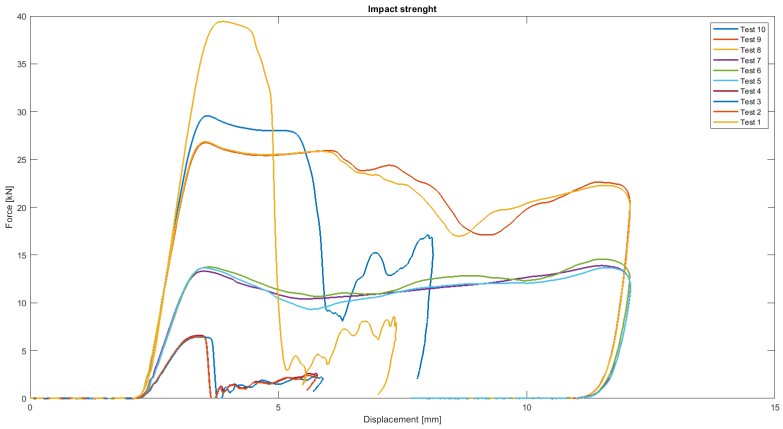

Figure 5.22 Force-displacement curve obtained in the impact test during stage 3.

In the figure 5.22, the tests 10, 9 and 8 had 80% gyroid infill, the tests 7, 6 and 5 had 50% gyroid infill, the tests 4, 3 and 2 had 20% gyroid infill, finally the test 1 is the reference, a cubic specimen with the same dimensions and 100% linear infill. It is noticeable that this last specimen could take a greater force, almost 40 kN, however it absorbed less energy than the specimens with 80% infill, as it is shown in table 5.18, since it fractured earlier. Comparing the test 10 with the tests 9 and 8 it has clearly absorbed less energy, this can be due to a defect on the specimen.

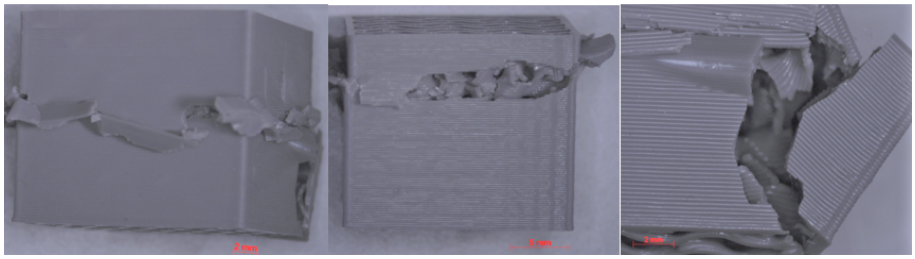

Figure 5.23 Failure mode of the specimens with 20% gyroid infill obtained with the stereo binocular microscope.

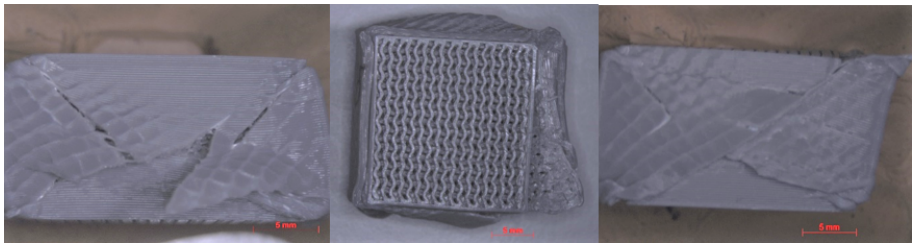

Figure 5.24 Failure mode of the specimens with 50% gyroid infill obtained with the stereo binocular microscope.

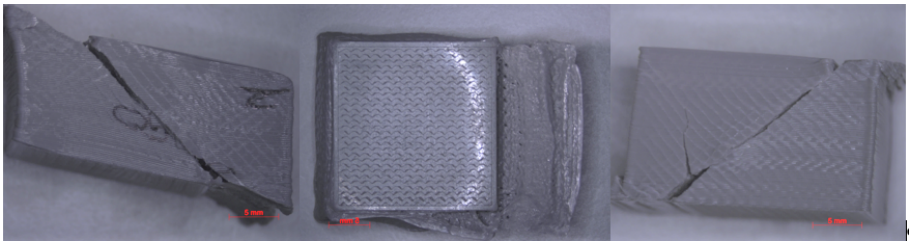

Figure 5.25 Failure mode of the specimens with 80% gyroid infill obtained with the stereo binocular microscope.

Through the observation of the Figures 5.23, 5.24, 5.25, it possible to conclude that depending on the specimens density it has different failure modes. In similarity to what was found in literature by Maskery *et. al* [46], the specimens with 20% density failed due to brittle fracture, in other words it is through the crushing of the specimen, due to the propagation of a crack. On the other hand, both the specimens with 50% and 80% density show failure because of diagonal shear.

In the table 5.18 it is stated the impact strength obtained for each condition.

Table 5.18 Impact strength obtained in the Stage 3.

		Gyroid infill density			**Linear infill (density)**
		20%	50%	80%	100% (reference)
Value ± SD	**Impact Strength [J]**	6.1±0.3	113.6±3.1	188.7±46.6	76.3

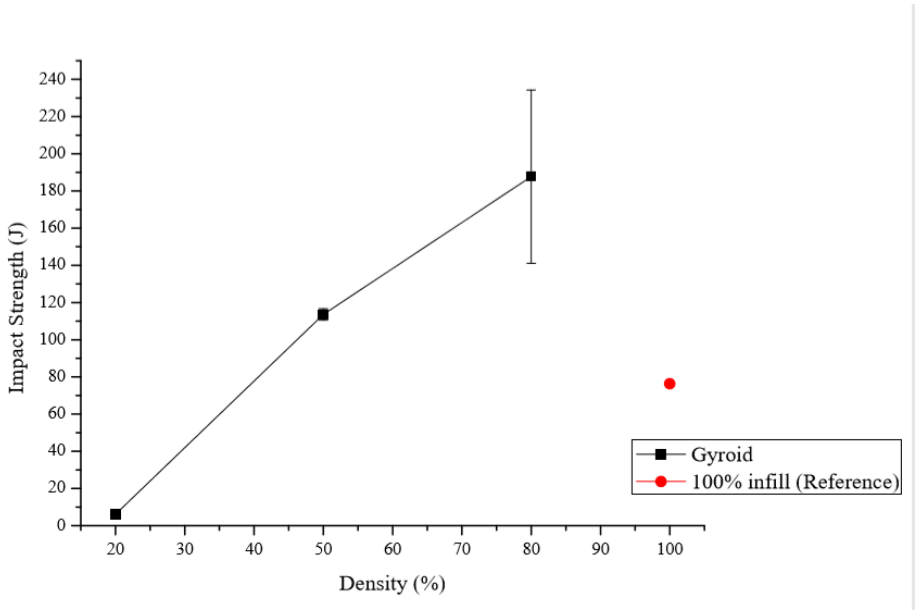

Figure 5.26 Influence of the gyroid infill density on the impact strength.

As expected, the greater the specimens' density the greater the impact strength. When compared with the specimens with 100% the specimens with the gyroid infill show higher impact strength, except the 20% density ones (shown in figure 5.26). The huge difference between the

impact strength calculated by this method and the one calculated by the Charpy test is mainly explained by the direction of the impact blow, since in this test it is in the strongest direction of the gyroid, the deposition one.

5.3 Specimens to test the gryoid structure

In this section the results of the fourth and last stage of the project will be analysed.

5.3.1 Compression of cubic specimen with and without outside perimeter

This test was done in order to study both the influence of an outside perimeter and the behaviour under compression of cubic specimens with gyroid infill, when the direction of the load is the same as building direction.

5.3.1.1 Specimens analysis

Before realising the destructive tests it was possible to analyse the quality of the specimens. Therefore, a visual control was done , in order to check eventual warping that could happen, and dimensional one, shown in table 5.19.

Table 5.19 Dimensions of the gyroid cubes with and without outside perimeter in Stage 4.

		Dimensions ± SD (mm)				
	Density	l_1	l_2	l_3	Weight ± SD	Printing time (min)
With outside perimeter	20%	19.9±0.1	199±0.1	19.9±0.1	2.7±0.0	22
	50%	20.0±0.1	20.0±0.1	20.0±0.1	5.2±0.1	56
	80%	20.0±0.1	19.9±0.1	20.0±40.1	8.0±0.1	93
Without outside perimeter	20%	20.0±0.1	20.0±0.1	20.0±0.0	2.1±0.0	13
	50%	19.9±0.1	20.0±0.1	19.9±0.0	4.8±0.0	54
	80%	20.0±0.1	20.1±0.2	19.9±0.1	7.6±0.1	90
	Theoretical	20.0	20.0	20.0		

After analysing the table 5.19 it is possible to conclude that all the specimens' dimensions are according to the established ones and that, and that, of course, both the time and the weight increase with the increase of the density and the presence of outside perimeter.

5.3.1.2 Results analysis

First of all, it is important to outline that it wasn't possible to compress the specimens with 80% density since the testing machine only has a load cell of 10 kN. Therefore, it only will be studied the specimens with 20% and 50% .

In figure 5.27 it is represented the compressive stress-strain obtained for three specimens for each condition.

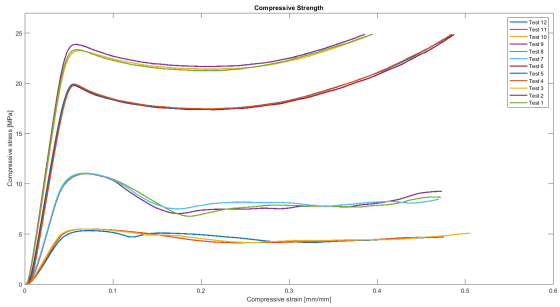

Figure 5.27 Compressive stress-strain curve obtained for the compression of the cubic specimens during stage 4.

In figure 5.27 the tests 1, 2 and 3 presented 50% gyroid infill and the presence of an outside perimeter, the tests 4, 5 and 6 also had 50% gyroid infill but didn't have an outside perimeter. The tests 7,8 and 9 present 20% gyroid infill and an outside perimeter, while, the tests 10, 11 and 12 also had 20% gyroid infill but didn't have an outside perimeter.

It was possible to observe in the stereo binocular microscope the specimens with 20% and 50% density with outside perimeter, shown in figures 5.28, 5.29. After the compression tests the specimens were dipped in liquid nitrogen, in order to freeze and consequently separate them through the existing fracture.

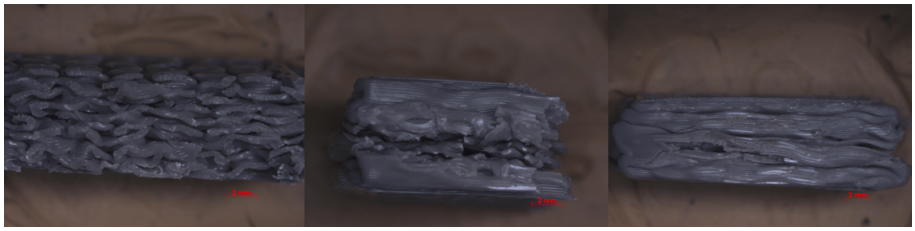

Figure 5.28 Cubic specimens with 20% gyroid infill after the compressive tests obtained with the stereo binocular microscope.

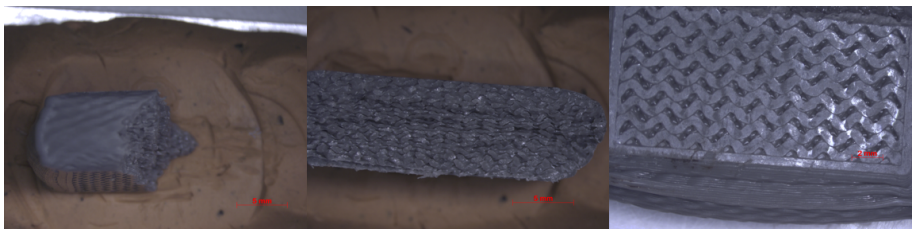

Figure 5.29 Cubic specimens with 50% gyroid infill after the compressive tests obtained with the stereo binocular microscope.

Through the observation of figures 5.28, 5.29, it is possible to conclude that the specimens with 20% density failed due to brittle fracture of the cell walls and was characterised by the propagation of a crack, this is possible to observe by profile of the outside perimeter since it presents a "corrugated profile". On the other hand, the ones with 50% failed due to diagonal shear,

this is possible to observe by the profile of the outside perimeter since it presents a "curved profile" being the maximum in the middle of the specimens, this is coincident to what was found in the literature by Maskery *et. al* [46].

In table 5.20 it is stated the load at yield and compressive modulus obtained for each situation.

Table 5.20 Compressive properties obtained in the Stage 4.

		Gyroid infill density			
		With outside perimeter		**Without outside perimeter**	
		20%	50%	20%	50%
Value ± SD	**Load at yield (F_y) [N]**	4407.3±14.9	9395.3±132.4	2181.9±36.4	7941.4±26.7
	Modulus of elasticity (E) [MPa]	29.5±4.9	56.1±4.9	6.3±1.5	30.2±20.8

As it was already observed in figure 5.27 the compressive modulus increases with the increase of the infill density and with the presence of an outside perimeter.

As shown in figure 5.30 the influence of an outside perimeter is constant, since the difference of the compressive modulus for the two conditions (presence or not of perimeter) wit 20% density gyroid infill is around 23 MPa and between the 50% ones is 26 MPa. Therefore the difference between the two curves (with outside perimeter and without outside perimeter) is relatively constant.

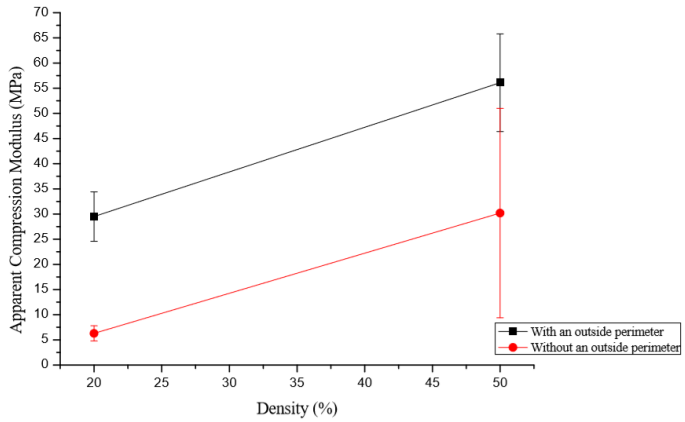

Figure 5.30 Influence of the gyroid infill density and the presence of an outside perimeter on the compressive modulus.

5.3.2 Study of the gyroid structure

In order to study the importance of the load direction in compression and the importance of the material used, the unitary gyroid structure was compressed in three directions aa, bb, cc (it is the printing direction, *zz*), shown in figure 5.31.

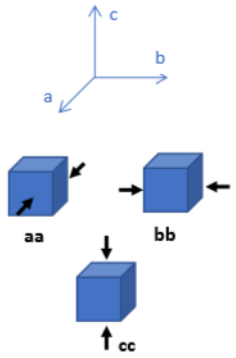

Figure 5.31 Directions of the compression load used for the gyroid structure.

5.3.2.1 Specimens analysis

Before realising the destructive tests it was possible to analyse the quality of the specimens. Therefore, a visual control was done, in order to check eventual warping that could happen, and dimensional one, shown in table 5.21.

Table 5.21 Dimensions of the gyroid structure in Stage 4.

	Dimensions ± SD				
AM technology	aa	bb	cc	Weight ± SD (g)	Printing time (min)
FDM	20.0±0.1	20.1±0.1	20.1±0.1	2.3±0.0	35
Polyjet	20.0±0.1	20.0±0.1	20.0±0.0	2.5±0.0	130 ∗
Theoretical	20.0	20.0	20.0		

* all the polyjet structures were done at the same time, therefore, this printing time is for the set of structures. It is important to note that only one structure wouldn't take 130/9 minutes to print because the set-up time for this machine is almost the same when printing just one structure or more than one.

Since, no support structures were used to print the gyroid in the FDM printer all these gyroid structures showed some defects, as it is possible to observe in the representative gyroid in figure 5.32 (note that this one has twice the size of the ones used, in order to make it easier to observe the defects).

Additionally a tensile tests was also done to specimens made by the polyjet machine in order to make it easier when comparing the tests' results.

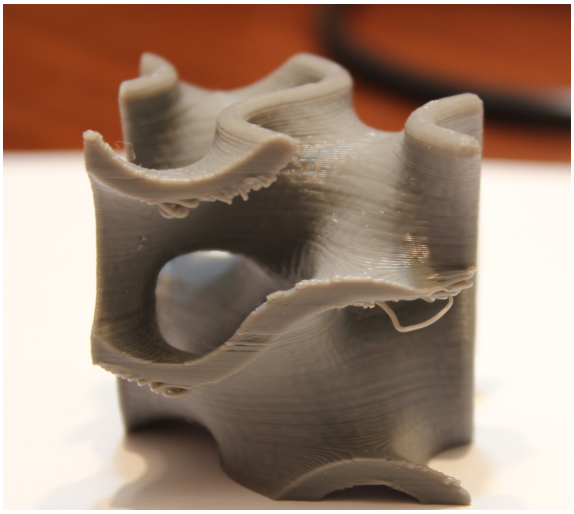

Figure 5.32 Defects of the gyroid structure printed by FDM.

5.3.2.2 Results of the tests

Before presenting the results obtained it is important to outline once more that the FDM printer is a low cost machine and the polyjet is an industrial one. Therefore the difference between the results are not just because of the differences between these technologies but also because of the differences between the machines itself.

In figures 5.33 and 5.34 the compressive load-displacement obtained for the three specimens for each condition are shown. Since the FDM material, PLA, is a plastic and the polyjet material, VeroGray, is a resin they present different type of behaviour under compression, therefore they have different curves.

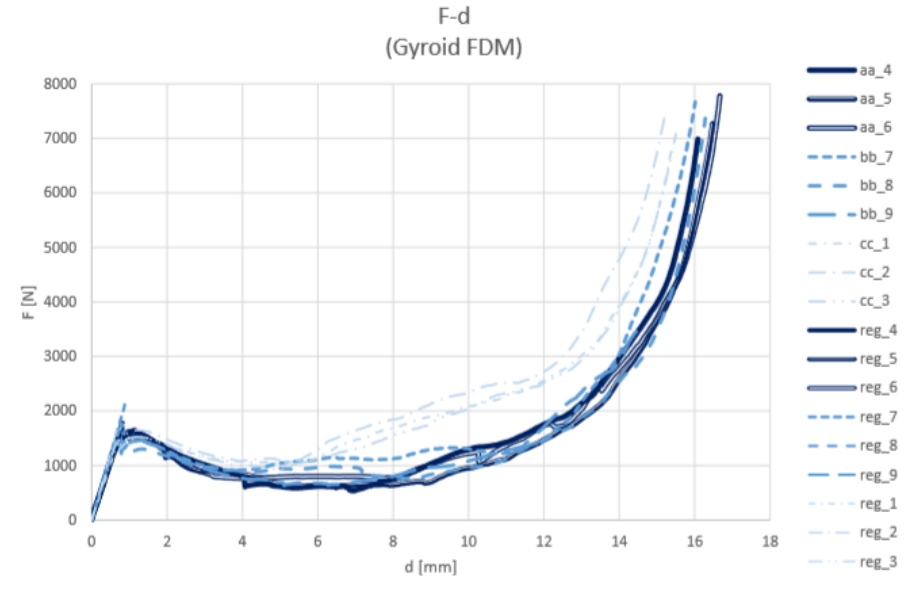

Figure 5.33 Compressive load/displacement curve obtained for the FDM gyroid structure.

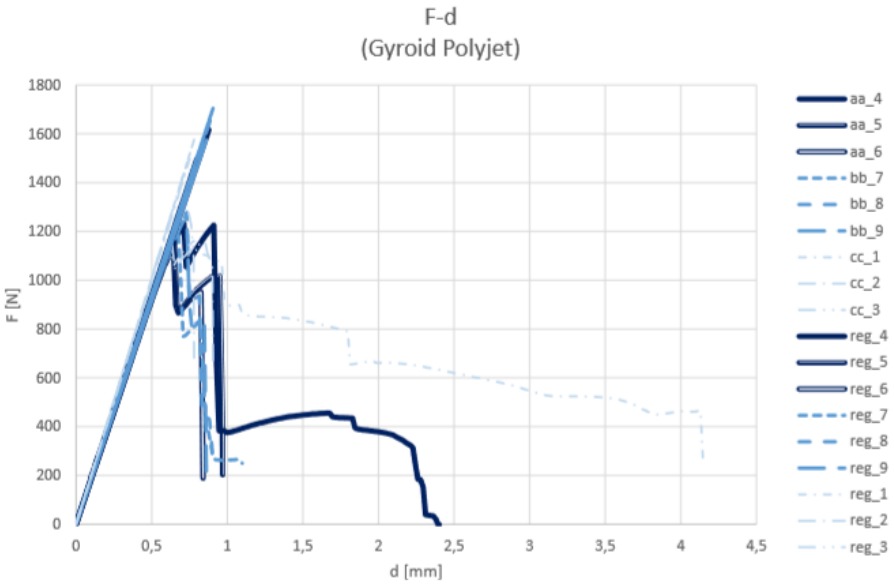

Figure 5.34 Compressive load/displacement curve obtained for the polyjet gyroid structure.

In figures 5.35, 5.36 it is shown the specimens after test for each direction.

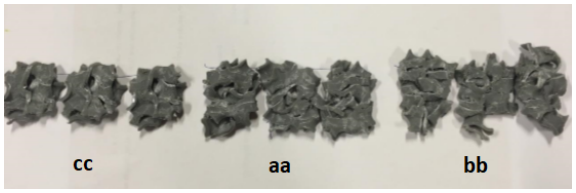

Figure 5.35 FDM gyroid structure obtained after the compressive test: cc direction (left), aa direction (middle) and bb direction (right).

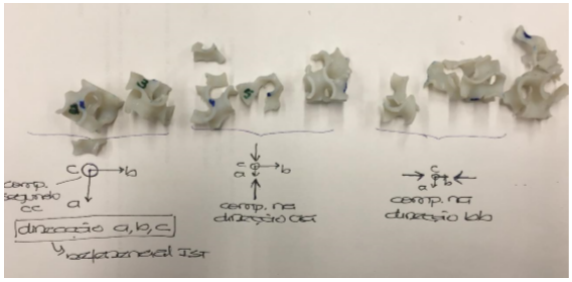

Figure 5.36 FDM gyroid structure obtained after the compressive test: cc direction (left), aa direction (middle) and bb direction (right).

In order to compare the behaviour of each gyroid structure the compression coefficient was calculated (k), to compare the stiffness in compression of the gyroid for each technology. In table **??** the gyroid's properties under compression for each technology are summarised.

Table 5.22 Properties of the gyroid structure for each technology.

		AM techonology					
		FDM			Polyjet		
Value ± SD	**Modulus of elasticity (E) [MPa]**	3485.3±60.3 (PLA)			2570.63±1282.6 (VeroGrey) *		
	Direction of load	*aa*	*bb*	*cc*	*aa*	*bb*	*cc*
	Load at yield (F_y) [N]	1615.3±31.5	1536.1±126.8	1563.9±72.6	1182.2±45.3	1251.4±39.1	1193.4±73.7
	Displacement at yield (d_y) [mm]	1.0±0.1	0.8±0.0	1.2±0.1	0.7±0.0	0.7±0.0	0.7±0.1
	Compression coefficient (k) [N/mm]	1570.8±128.2	**1879.5±187.4**	1262.6±104.6	1770.8±33.8	1757.2±28.3	**1802.7±78.6**

* this value was obtained by the tensile test done to the VeroGrey tensile specimens done in the Polyjet (Appendix C)

In figure 5.37 it is possible to observe the influence of the direction of solicitation on the compression coefficient. In conclusion, the gyroid structure done in the polyjet technology presents isotropic behaviour in compression, since *k* doesn't present significant differences for the different directions of solicitation, this was also observed by Abueida *et. al* when the gyroid structure was done by SLS technology [49]. On the other hand, the gyroid structure done by FDM presents higher anisotropy, this can be explained by the anisotropic properties of the technology itself not the structure anisotropy.

Additionally, it is possible to conclude that the elasticity modulus of the PLA is around 23.4% higher than the VeroGrey one. However when comparing the greatest compression coefficient of the two the difference is around 4%. Therefore, it is possible to conclude that the structure (how the material is arranged) is more important, when discussing the compression properties, then the material itself (the material used to build the structure) this is coincident to what was found by the MIT team that did a research on the gyroid structure [50].

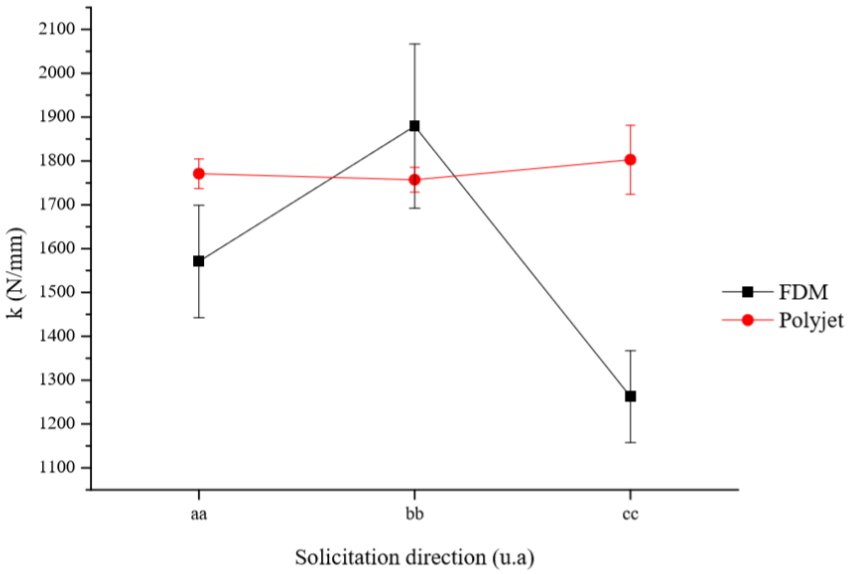

Figure 5.37 Influence of the direction of solicitation on the compression coefficient.

5.4 Summary of results

Summarising the results collected from the tests for each stage of the dissertation, it is possible to conclude:

- **Stage 2 - Study about the influence of the deposition orientation:**
  - The maximum tensile strength is 54.2 MPa and it is obtained for the 0° deposition orientation for 1.87% strain. The maximum Young's Modulus is 3482.3 MPa for the 90° deposition orientation;
  - The maximum flexural strength is 99.9 MPa for a 4.45% strain and the maximum flexural modulus is 2838.8 MPa both for the 0° deposition orientation;
  - The maximum compressive stress at yield is 93.6 MPa with a corresponding strain of 6% for the 0° raster orientation. The maximum compressive modulus is 2855.2 MPa obtained for the ±45° deposition orientation.
- **Stage 3 - Study about the influence of the gyroid infill density on the mechanical properties:**
  - The maximum load at yield is 967.7 N with a corresponding displacement of 1 mm and the maximum apparent modulus of elasticity is 200 MPa both obtained for 80% infill;
  - The maximum flexural load is 70.5 N with a corresponding displacement of 6.6 mm and the maximum apparent flexural modulus is 40 MPa both obtained for 80% infill;
  - The maximum compressive load at yield is 2340.9 N with a corresponding displacement of 71.5 mm and the maximum compressive modulus is 1785.7 MPa both obtained for 80% infill;
  - The maximum charpy strength is 1.62 kJ/mm^2 and it is obtained for the maximum density (80%). However, for the 50% infill it is 1.61 kJ/mm^2 and this one is 25% lighter;
  - The maximum impact strength is 188.7 J and is obtained for the specimens with 80% infill density.
- **Stage 4 - Study about the gyroid structure:**
  - The maximum load at yield is 9395.3 N and the maximum modulus of elasticity is 44.9 MPa both are obtained for the specimens with 50% infill and outside perimeter;
  - The highest compression coefficient obtained by polyjet gyroid is 1802.7 N/mm and the lowest is 1757.2 N/mm, around 2,5% difference;
  - The difference between the greatest compression coefficients of the FDM and polyjet unitary gyroid is around 4%.

Esta página foi intencionalmente deixada em branco.

Chapter 6

Conclusions

Throughout this thesis, a description of the fundamental research topics were made, leading to a more specific review about fused filament fabrication, low cost 3D printers and the importance of the infill used. After doing the review it was possible to plan the tests that needed to be done in order to achieve the proposed goals of this dissertation.

Therefore the connection between the research done and the experimental work developed made it possible to conclude the main advantages and disadvantages of building a 3D printer from scratch, the deposition orientation when using a 100% linear infill, the influence of the gyroid infill density and the gyroid structure itself. Afterwards the main characteristics and conclusions of each stage are mentioned.

Initially after the assembly of a 3D printer from scratch it was possible to conclude that there aren't many advantages of building a 3D printer from scratch, for that reason the one built was based on an existing one. Nevertheless this part would not be possible without the knowledge of the researches from the *Laboratório de desenvolvimento de produto e serviços* from FEUP because there are a lot of different details that must be taken into consideration. In conclusion, instead of building a 3D printer it is more appealing to assemble an existing one and do the necessary upgrades.

Regarding to the following stage (Stage 2 - Study about the influence of the deposition orientations) it is possible to conclude that:

- The best **tensile properties** are obtained for the 0° raster orientation because all the filament is orientated in the load direction.The maximum tensile stress at break is obtained for this raster orientation. However, the maximum tensile modulus is obtained for the 90° raster orientation, the difference between the one obtained for this orientation and for the 0° is just 0.8%;

- The best **flexural properties** are also obtained for the 0° raster orientation because all the filament is orientated in the load direction;

- The maximum **compressive strength** is obtained for the 0° raster orientation and the maximum **compressive modulus** is obtained for the $\pm 45^\circ$ raster orientation

On the third stage where the influence of the gyroid infill density on the mechanical properties was studied, it was possible to conclude that:

- With the **increase of the gyroid infill density** there is **an increase on the mechanical properties**, with exception of the Charpy test since the difference between the charpy impact strength of the specimens with 50% and 80% is not significant;
- In **none of the cases studied**, with exception of the impact strength at high velocity, **the gyroid infill showed better results** than the traditional linear infill used. Because the gyroid infill is perpendicular to the load direction the standards used for testing it does not fully comply with the structure of the gyroid;
- The cubic specimens with the two higher gyroid infill densities (50% and 80%) subjected to impact present greater impact strength than the 100% linear infill one used as reference, increase of 32.8% for the 50% infill and of 40.4% for the 80% infill. Therefore it is possible to conclude that the gyroid infill is a good choice for situations where the impact load direction is the same as the deposition direction (zz).

Finally, about the gyroid structure itself (last stage of the project) it was possible to achieve that:

- The **presence of an outside perimeter** in cubic specimens under compression showed a **constant influence**;
- When the gyroid structure is built by a process with less anisotropy (polyjet) it presents **similar properties under compression regardless the load direction**;
- When comparing gyroid structures built with different technologies it is possible to conclude that the **structure itself has a higher influence on the compression properties than the material**. It means that materials with different modulus of elasticity present similar compression coefficients when used to build a gyroid structure.

6.1 Future work

Due to the versatility and low price of fused filament fabrication low cost 3D printer and the superior structure that can be used as an infill there are still many studies that should be carried out in order to make it possible for these printer to be widely used. Consequently, there are many future scopes possible to study in order to understand better the behaviour of gyroid structures:

- Develop standard specimens that are more appropriate to study the gyroid structure, in other words that the gyroid infill is not built in the perpendicular direction of the test load;
- Study both the traditional and the gyroid infill specimens on their fatigue behaviour;

- Test cubic metal gyroid specimens under compression, in order to study the influence of the material. Compare the PLA and the metal ones and analyse the differences between the respective compressive strengths;
- Compare the FDM and polyjet gyroid structure with a metal gyroid structure built by a metal additive manufacturing system. Compare the PLA, the polyjet and the metal ones and analyse the differences between the respective compression coefficients ;
- Use the gyroid infill to build a functional prototype and subject it to impact load to test the the gyroid infill in a practical situation.

Esta página foi intencionalmente deixada em branco.

References

[1] G. T. Wohlers Terry, "History of additive Manufacturing," Wohlers associates, Tech. Rep., 2018. [Online]. Available: http://www.wohlersassociates.com/history2018.pdf

[2] U. M. Dilberoglu, B. Gharehpapagh, U. Yaman, and M. Dolen, "The Role of Additive Manufacturing in the Era of Industry 4.0," *Procedia Manufacturing*, vol. 11, pp. 545–554, jan 2017. [Online]. Available: https://www.sciencedirect.com/science/article/pii/S2351978917303529

[3] Wohlers Terry, I. Campbell, O. Diegel, and J. Kowen, *Wohlers Report 2018 - 3D Printing and Additive Manufacturing State of the Industry - Annual Worldwide Progress Report*. Wohlers associates, INC, 2018.

[4] C. K. Chua, K. F. Leong, and C. S. Lim, *Rapid Prototyping*. World Scientific, jan 2010. [Online]. Available: https://www.worldscientific.com/worldscibooks/10.1142/6665

[5] H. Kamerlingh, "3D printing techniques and rapid prototyping," leapfrog 3D printers, Tech. Rep. [Online]. Available: www.lpfrg.com

[6] N. Volpato, C. Henrique Ahrens, A. Luiz Jardini Munhoz, C. Costa, J. De Carvalho, J. dos Santos, J. Silva, J. Foggiatto, and M. S. de Lima, *Manufatura Aditiva - Tecnologias e aplicações da impressão 3D*. Editora Blucher, 2017.

[7] S. Gómez González, *Impresión 3D*. Marcombo, 2016.

[8] "Fused filament fabrication - RepRap," Date accessed: 2019-05-21. [Online]. Available: https://reprap.org/wiki/Fused_filament_fabrication

[9] "15 Best Professional 3D Printers of 2018 | All3DP," Date accessed: 2019-05-27. [Online]. Available: https://all3dp.com/1/best-professional-3d-printer-small-business/

[10] "3D PRINTER : geeetech 3d printers onlinestore, one-stop shop for 3d printers,3d printer accessories,3d printer parts," Date accessed: 2019-05-27. [Online]. Available: https://www.geeetech.com/3d-printer-c-24.html

[11] "The 4 Types of FFF / FDM 3D Printer Explained (Cartesian, Delta, Polar) - 3Dnatives," Date accessed: 2019-05-27. [Online]. Available: https://www.3dnatives.com/en/four-types-fdm-3d-printers140620174/

[12] "Parts of a 3D Printer: List of Major 3D Printing Components - 3D Insider," Date accessed: 2019-05-27. [Online]. Available: https://3dinsider.com/3d-printer-parts/

[13] "The parts of a 3D Printer - All About 3D Printing," Date accessed: 2019-05-27. [Online]. Available: http://allabout3dprinting.com/the-parts-of-a-3d-printer/

[14] "Direct vs Bowden Extruder – 3D Printing Technology Shootout | All3DP," Date accessed: 2019-05-27. [Online]. Available: https://all3dp.com/2/direct-vs-bowden-extruder-technology-shootout/

[15] *CES EduPack 2018*, 2018, cambridge: Granta.

[16] M. Kaseem, "Properties and medical applications of polylactic acid: A review Poly(lactic acid) Composites View project." [Online]. Available: https://www.researchgate.net/publication/275655694

[17] P. Gritten, "Aspectos técnicos e nocivos dos principais filamentos usados em impressão 3D," *Gest. Tecnol. Inov*, vol. 01, no. 3, 2017. [Online]. Available: http://www.opet.com.br/faculdade/revista-engenharias/pdf/n3/Artigo2-n3-Bilyk.pdf

[18] E. Canessa, C. Fonda, and M. Zennaro, "Low-cost 3D printig for science, education & sustainable development," International Centre for Theoretical Physics, Tech. Rep., 2013. [Online]. Available: https://azdoc.tips/documents/low-cost-3d-printing-5c16aa35428cd

[19] "RepRap Firmware - RepRap," Date accessed: 2019-05-27. [Online]. Available: https://reprap.org/wiki/RepRap_Firmware

[20] Stratasys, "FDM and Polyjet 3D Printing," Tech. Rep., 2017. [Online]. Available: https://www.stratasys.com/resources/search/white-papers/fdm-vs-polyjet

[21] A. Prototypes, "Object Eden260V," 2014. [Online]. Available: https://www.axisproto.com/app/uploads/2018/03/E260V_Letter.pdf

[22] S. Horie, *3D printing: Consumer vs. Professional*. xometry, 2018. [Online]. Available: https://docplayer.net/22557981-3d-printing-consumer-vs-professional.html

[23] "Impressora 3D barata 2019: as melhores máquinas a baixo preço | All3DP," Date accessed: 2019-05-21. [Online]. Available: https://all3dp.com/pt/1/mehlor-impressora-3d-barata-impressora-3d-preco/

[24] "2019 Creality Ender 3 Review – Best 3D Printer Under $200 | All3DP," Date accessed: 2019-05-21. [Online]. Available: https://all3dp.com/1/creality-ender-3-3d-printer-review/

[25] "2019 Anycubic i3 Mega Review – Best 3D Printer Under $300 | All3DP," Date accessed:: 2019-05-21. [Online]. Available: https://all3dp.com/1/anycubic-i3-mega-3d-printer-review/

[26] "2019 Creality CR-10S – Review the Specs | All3DP," Date accessed: 2019-05-21. [Online]. Available: https://all3dp.com/1/creality-cr-10s-review-s4-s5-3d-printer/

[27] "Original Prusa i3 MK3S Review – The Best 3D Printer in 2019 | All3DP," Date accessed: 2019-05-21. [Online]. Available: https://all3dp.com/1/original-prusa-i3-mk3-review/

[28] K. T. Ulrich and S. D. Eppinger, *Product Design and Development: Fifth Edition: About the Authors*. McGraw-Hill Education, 2011.

[29] "3D Systems White Paper 3D printer buyer guide," Tech. Rep. [Online]. Available: https://pt.slideshare.net/QuocTuanDuonging/2014-white-paper3dprinterbuyersguideweb

[30] A. Kohad, R. Dalu, and P. G. Student, "Optimization of Process Parameters in Fused Deposition Modeling: A Review," Research Development Cell, Government College of Engineering, Jalagon (M. S), India, Tech. Rep. 1, 2007. [Online]. Available: www.ijirset.com

[31] A. Lanzotti, M. Grasso, G. Staiano, and M. Martorelli, "The impact of process parameters on mechanical properties of parts fabricated in PLA with an open-source 3-D printer," *Rapid Prototyping Journal*, vol. 21, no. 5, pp. 228–235, 2008. [Online]. Available: https://www.emeraldinsight.com/doi/pdfplus/10.1108/RPJ-09-2014-0135

[32] T. Letcher and M. Waytashek, "Material Property Testing of 3D-Printed Specimen in PLA on an Entry-Level 3D Printer," in *ASME International Mechanical Engineering Congress and Exposition, Proceedings (IMECE)*, vol. 2, 2014.

[33] C. DUDESCU and L. Racz, "Effects of Raster Orientation, Infill Rate and Infill Pattern on the Mechanical Properties of 3D Printed Materials," *ACTA Universitatis Cibiniensis*, vol. 69, 2017. [Online]. Available: https://www.researchgate.net/publication/322459350_Effects_of_Raster_Orientation_Infill_Rate_and_Infill_Pattern_on_the_Mechanical_Properties_of_3D_Printed_Materials

[34] D. Abbas, D. Mohammad Othman, H. Basil Ali, and C. Author, "Effect of infill Parameter on compression property in FDM Process," *Int. Journal of Engineering Research andApplication www.ijera.com*, vol. 7, pp. 16–19, 2017. [Online]. Available: www.ijera.com

[35] C. Lubombo and M. A. Huneault, "Effect of infill patterns on the mechanical performance of lightweight 3D-printed cellular PLA parts," *Materials Today Communications*, vol. 17, pp. 214–228, dec 2018. [Online]. Available: https://www.sciencedirect.com/science/article/pii/S2352492818301600

[36] I. Maskery, L. Sturm, A. Aremu, A. Panesar, C. Williams, C. Tuck, R. Wildman, I. Ashcroft, and R. Hague, "Insights into the mechanical properties of several triply periodic minimal surface lattice structures made by polymer additive manufacturing," *Polymer*, vol. 152, pp. 62–71, sep 2018. [Online]. Available: https://linkinghub.elsevier.com/retrieve/pii/S0032386117311175

[37] F.-J. Ulm, "Construction: Cellular Materials," *Encyclopedia of Materials: Science and Technology*, pp. 1570–1574, jan 2001. [Online]. Available: https://www.sciencedirect.com/science/article/pii/B0080431526002801

[38] B. E. Obi and B. E. Obi, "Fundamentals of Polymeric Foams and Classification of Foam Types," *Polymeric Foams Structure-Property-Performance*, pp. 93–129, jan 2018. [Online]. Available: https://www.sciencedirect.com/science/article/pii/B9781455777556000057

[39] M. Kucewicz, P. Baranowski, J. Małachowski, A. Popławski, and P. Płatek, "Modelling, and characterization of 3D printed cellular structures," *Materials & Design*, vol. 142, pp. 177–189, mar 2018. [Online]. Available: https://www.sciencedirect.com/science/article/pii/S0264127518300364

[40] "Polymeric Foams Market Trends, Market Analysis, and Forecasts by Global Industry Analysts, Inc.,," Date accessed: 2019-02-18. [Online]. Available: https://www.strategyr.com/MarketResearch/ViewInfoGraphNew.asp?code=MCP-1174

[41] A. Bonfanti, A. Bhaskar, and M. Ashby, "Plastic Deformation of Cellular Materials," in *Reference Module in Materials Science and Materials Engineering*. Elsevier, 2016. [Online]. Available: https://linkinghub.elsevier.com/retrieve/pii/B9780128035818030095

[42] S. Khaderi, V. Deshpande, and N. Fleck, "The stiffness and strength of the gyroid lattice," *International Journal of Solids and Structures*, vol. 51, no. 23-24, pp. 3866–3877, nov 2014. [Online]. Available: https://linkinghub.elsevier.com/retrieve/pii/S002076831400256X

[43] K. Monkova, P. Monka, I. Zetkova, P. Hanzl, and D. Mandulak, "Three Approaches to the Gyroid Structure Modelling as a Base of Lightweight Component Produced by Additive Technology," *DEStech Transactions on Computer Science and Engineering*, no. cmsam, dec 2017. [Online]. Available: http://dpi-proceedings.com/index.php/dtcse/article/view/16361

[44] L. Yang, C. Yan, H. Fan, Z. Li, C. Cai, P. Chen, Y. Shi, and S. Yang, "Investigation on the orientation dependence of elastic response in Gyroid cellular structures," *Journal of the Mechanical Behavior of Biomedical Materials*, vol. 90, pp. 73–85, feb 2019. [Online]. Available: https://www.sciencedirect.com/science/article/pii/S1751616118308506

[45] L. Yang, C. Yan, C. Han, P. Chen, S. Yang, and Y. Shi, "Mechanical response of a triply periodic minimal surface cellular structures manufactured by selective laser melting," *International Journal of Mechanical Sciences*, vol. 148, pp. 149–157, nov 2018. [Online]. Available: https://www.sciencedirect.com/science/article/pii/S0020740317333970

[46] I. Maskery, N. Aboulkhair, A. Aremu, C. Tuck, and I. Ashcroft, "Compressive failure modes and energy absorption in additively manufactured double gyroid lattices," *Additive Manufacturing*, vol. 16, pp. 24–29, aug 2017. [Online]. Available: https://www.sciencedirect.com/science/article/pii/S2214860417301203

[47] R. Vrana, D. Koutny, and D. Paloušek, "Impact resistance of different types of lattice structures manufactured by SLM," *MM Science Journal*, vol. 2016, pp. 1579–1585, 2016. [Online]. Available: https://www.researchgate.net/profile/Radek_Vrana2/publication/311655460_Impact_resistance_of_different_types_of_lattice_structures_manufactured_by_SLM/links/5b27a994458515cad5605608/Impact-resistance-of-different-types-of-lattice-structures-manufactured-by-SLM.pdf

[48] H. Alsalla, L. Hao, and C. Smith, "Fracture toughness and tensile strength of 316L stainless steel cellular lattice structures manufactured using the selective laser melting technique," *Materials Science and Engineering: A*, vol. 669, pp. 1–6, jul 2016. [Online]. Available: https://www.sciencedirect.com/science/article/abs/pii/S0921509316305925

[49] D. W. Abueidda, M. Elhebeary, C.-S. A. Shiang, S. Pang, R. K. Abu Al-Rub, and I. M. Jasiuk, "Mechanical properties of 3D printed polymeric Gyroid cellular structures: Experimental and finite element study," *Materials & Design*, vol. 165, p. 107597, mar 2019. [Online]. Available: https://www.sciencedirect.com/science/article/pii/S0264127519300176

[50] "Researchers design one of the strongest, lightest materials known | MIT News," Date accessed: 2019-03-22. [Online]. Available: http://news.mit.edu/2017/3-d-graphene-strongest-lightest-materials-0106

[51] "Premium PLA - Robotic Grey | Formfutura." [Online]. Available: https://www.formfutura.com/shop/product/premium-pla-robotic-grey-288?category=175

[52] Stratasys, "Vero Family," 2018. [Online]. Available: https://www.stratasys.com/material-spec-sheets/vero-material

[53] "Stratasys, VeroGray Polyjet technology - material specification," 2015.

[54] "How to Build a 3D Printer: Parts list and Basic Steps - 3D Insider," Date accessed: 2019-04-23. [Online]. Available: https://3dinsider.com/how-to-build-a-3d-printer/

[55] "Arduino Mega Pololu Shield - RepRap," Date accessed: 2019-04-23. [Online]. Available: https://reprap.org/wiki/Arduino_Mega_Pololu_Shield

[56] "Rambo - RepRap," Date accessed: 2019-04-23. [Online]. Available: https://reprap.org/wiki/Rambo

[57] "Smoothieboard - RepRap," Date accessed: 2019-04-23. [Online]. Available: https://reprap.org/wiki/Smoothieboard

[58] "Choosing a Power Supply for your RepRap - RepRap," Date accessed: 2019-04-23. [Online]. Available: https://reprap.org/wiki/Choosing_a_Power_Supply_for_your_RepRap#LED_strip_PSUs_or_ATX_PSUs_.3F

[59] "MEAN WELL Switching Power Supply Manufacturer," Date accessed: 2019-04-23. [Online]. Available: https://www.meanwell.com/productSeries.aspx?i=16{&}c=6{#}tag-6-16

[60] "MK3 21*21*3mm 12V/24V 120W Aluminum Heated Bed Plate for 3D Printer," Date accessed: 2019-04-23. [Online]. Available: https://www.reprap.me/mk3-21-21-3mm-12v-24v-120w-aluminum-heated-bed-plate-for-3d-printer.html

[61] "MK8 hotend | 3D printing experts | reprapworld.com," Date accessed: 2019-04-24. [Online]. Available: https://reprapworld.com/listing/mk8_hotend/

[62] "MK8 hotend | 3D printing experts | reprapworld.com," Date accessed: 2019-04-24. [Online]. Available: https://reprapworld.com/listing/mk8_hotend/

[63] "MK8 hotend | 3D printing experts | reprapworld.com," Date accessed: 2019-04-24. [Online]. Available: https://reprapworld.com/listing/mk8_hotend/

[64] W. Gorman, C. Hastings, and D. Pfaff, "Building a 3D Printer: Motors and Controls," Tech. Rep. [Online]. Available: https://web.wpi.edu/Pubs/E-project/Available/E-project-042517-160045/unrestricted/Motors_and_Controls_Final.pdf

[65] "3D Printer: 21 Steps," Date accessed: 2019-04-27. [Online]. Available: https://www.instructables.com/id/3D-Printer-2/

[66] "Wallace - RepRap," Date accessed: 2019-04-27. [Online]. Available: https://reprap.org/wiki/Wallace

[67] "Wallace Build Manual - RepRap," Date accessed: 2019-04-27. [Online]. Available: https://reprap.org/wiki/Wallace_Build_Manual

[68] Creality, *Ender-3 Pro Series 3D Printer - Guide Book*, 2018. [Online]. Available: https://www.creality3d.cn/creality3d-ender-3-pro-3d-printer-p00251p1.html

[69] "HowTo Calibrate, Tune and Fine Tune your printer and filament - Talk Manufacturing | 3D Hubs," Date accessed: 2019-03-27. [Online]. Available: https://www.3dhubs.com/talk/t/howto-calibrate-tune-and-fine-tune-your-printer-and-filament/5695

[70] "Calibration - RepRap," Date accessed: 2019-03-27. [Online]. Available: https://reprap.org/wiki/Calibration

[71] Mitutoyo Corporation, "Digital Caliper CD-AX/APX Series," Tech. Rep., 2015. [Online]. Available: https://www.mitutoyo.co.jp/eng/support/service/catalog/08/E12021.pdf

[72] Scale House, "Industrial Weighing Sytems," Tech. Rep. [Online]. Available: http://www.iwsystems.ca/1-Scales/Gram/Manuals/DINI-HLD.pdf

[73] "Plastics-Determination of tensile properties-Part 1: General principles," Tech. Rep., 1996. [Online]. Available: http://file.yizimg.com/305304/2009031608292782.pdf

[74] "Plastics-Determination of tensile properties-Part 2: Test conditions for moulding and extrusion plastics," Tech. Rep., 1996.

[75] "Plastics-Determination of flexural properties," Tech. Rep., 2003.

[76] "Plastics - Determination of compressive properties," Tech. Rep., 2002.

[77] "5960 Series Universal Testing Systems - Instron," Date accessed: 2019-06-14. [Online]. Available: https://www.instron.us/en-us/products/testing-systems/universal-testing-systems/electromechanical/5900-series/5960-dual-column

[78] "Impact Strength - an overview | ScienceDirect Topics," Date accessed: 2019-05-29. [Online]. Available: https://www.sciencedirect.com/topics/chemistry/impact-strength

[79] "Plastics-Determination of Charpy impact properties - Part 1: Non-instrumental impact test," Tech. Rep., 1982.

[80] R. Vrana, D. Koutny, D. Palousek, and T. Zikmund, "Impact resistance of lattice structure made by selective laser melting from AlSi12 alloy," *MM Science Journal*, vol. 2015, no. 04, pp. 852–855, dec 2015. [Online]. Available: http://www.mmscience.eu/december-2015.html{#}201547

[81] Z. Qin, G. S. Jung, M. J. Kang, and M. J. Buehler, "The mechanics and design of a lightweight three-dimensional graphene assembly," *Science Advances*, vol. 3, no. 1, p. e1601536, jan 2017. [Online]. Available: http://advances.sciencemag.org/lookup/doi/10.1126/sciadv.1601536

Appendix A

Results obtained on the study about the influence of the deposition orientation

Ensaios de tracção – ISO 527

Dimensões do provete : L – 150 mm
L_0 – 60 mm
w – 10 mm
t – 4 mm

Velocidade do ensaio : 1 mm/min

Numeração dos provetes ensaiados :

	0º	90º	+-45º	45º
1	1	1	1	1
2	2	2	2	2
3	3	3	3	3
4	5	4	4	4
5	6	5	5	5

σ_m	0º	90º	+-45º	45º
1	56,1847	46,87368	50,38674	52,09715
2	55,83688	47,54128	51,37121	53,18433
3	54,36974	49,4133	52,48209	53,802
4	51,54163	47,40615	51,77408	52,93125
5	52,95836	44,55895	54,38165	51,87243
med	54,17826	47,15867	52,07916	52,77743

ε_m	0º	90º	+-45º	45º
1	0,01781	0,022172	0,042967	0,042457
2	0,019273	0,017186	0,042665	0,033551
3	0,018295	0,022295	0,072251	0,023246
4	0,018092	0,020395	0,049475	0,050767
5	0,019855	0,02061	0,0483	0,04054
med	0,018665	0,020532	0,051132	0,038112

σ_y	0º	90º	+-45º	45º
1	-	46,87368	50,38674	52,09715
2	-	47,54128	51,37121	53,18433
3	-	49,4133	52,48209	53,802
4	-	47,40615	51,77408	52,93125
5	-	44,55895	54,38165	51,87243
med	-	47,15867	52,07916	52,77743

ε_y	0º	90º	+-45º	45º
1		0,019161	0,020967	0,021355
2		0,017074	0,021253	0,02112
3		0,018998	0,021661	0,021222
4		0,018407	0,021641	0,021498
5		0,018082	0,020957	0,020518
med		0,018344	0,021296	0,021142

σ_b	0º	90º	+-45º	45º
1	56,1847	45,83188	43,33854	45,36206
2	55,83688	47,33498	43,82866	45,70581
3	54,36974	48,04344	42,7823	50,04988
4	51,54163	46,34543	43,40765	44,66323
5	52,95836	43,46833	46,98518	44,1152
med	54,17826	46,20481	44,06847	45,97923

ε_b	0º	90º	+-45º	45º
1	0,01781	0,022172	0,042967	0,042457
2	0,019273	0,017186	0,042665	0,033551
3	0,018295	0,022295	0,072251	0,023246
4	0,018092	0,020395	0,049475	0,050767
5	0,019855	0,02061	0,0483	0,04054
med	0,018665	0,020532	0,051132	0,038112

E	0º	90º	+-45º	45º
1	3712,7	3398,3	3297,5	3348,2
2	3483,6	3546,2	3224,5	3306,8
3	3512,4	3525	3198,2	3410
4	3374	3442,6	3173,1	3386,4
5	3188,7	3499,2	3628,2	3338,7
med	3454,28	3482,26	3304,3	3358,02

ν	0º	90º	+-45º	45º
1	0,399	0,3271	0,4151	0,3971
2	0,3869	0,3548	0,4112	0,4329
3	0,3753	0,3173	0,4014	0,4021
4	0,4056	0,3514	0,409	0,4
5	0,3533	0,3341	0,4021	0,4096
med	0,38402	0,33694	0,40776	0,40834

Provetes após ensaio:

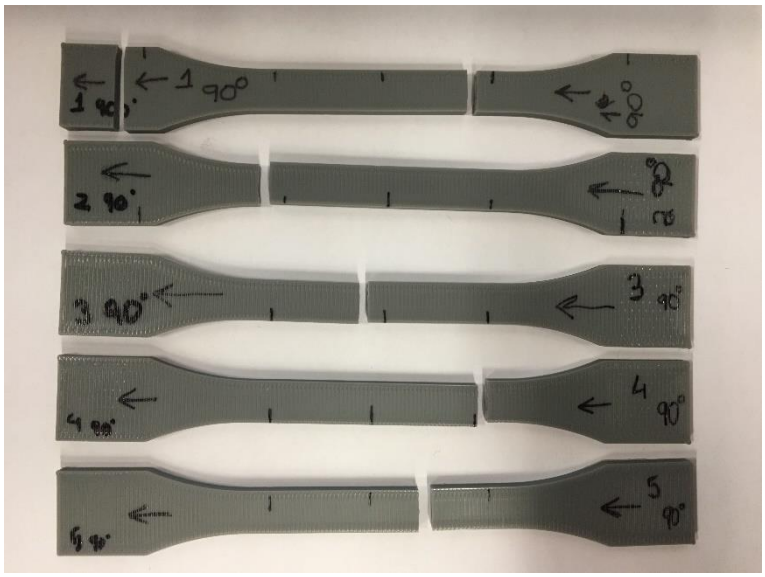

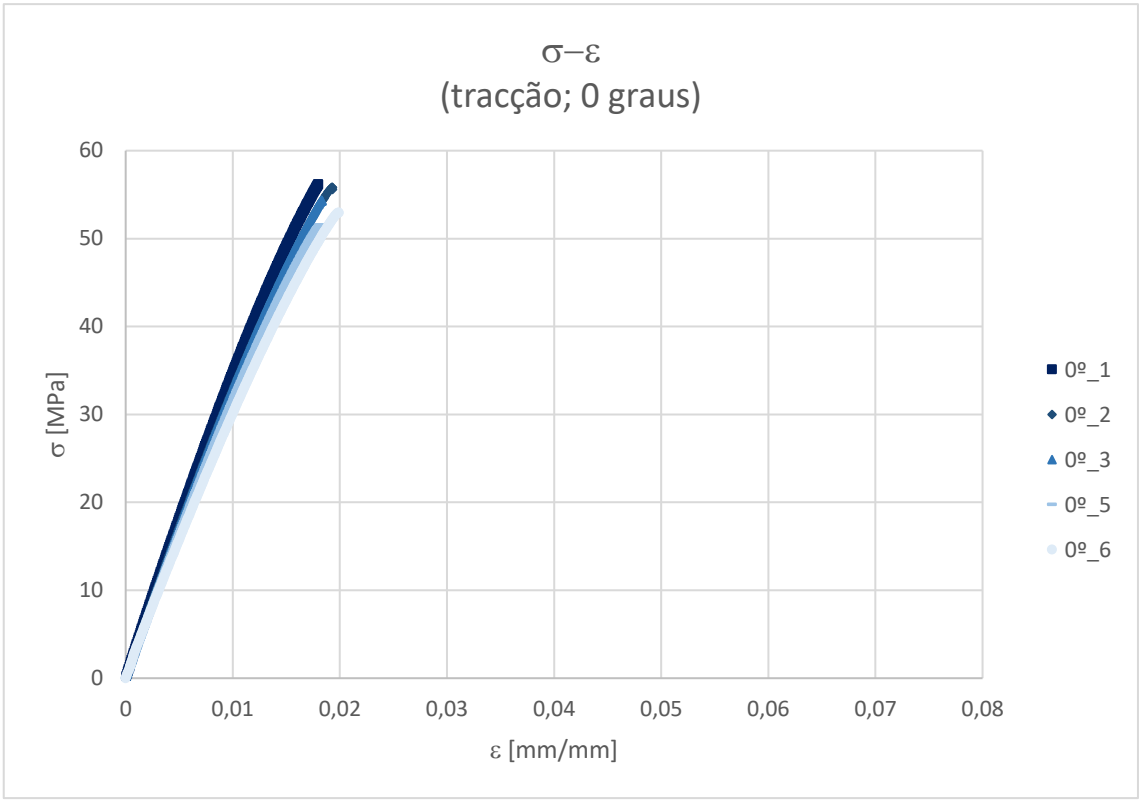
σ–ε
(tracção; 0 graus)
60
50
40
30
20
10
0
σ [MPa]
0
0,01
0,02
0,03
0,04
0,05
0,06
0,07
0,08
ε [mm/mm]
0º_1
0º_2
0º_3
0º_5
0º_6

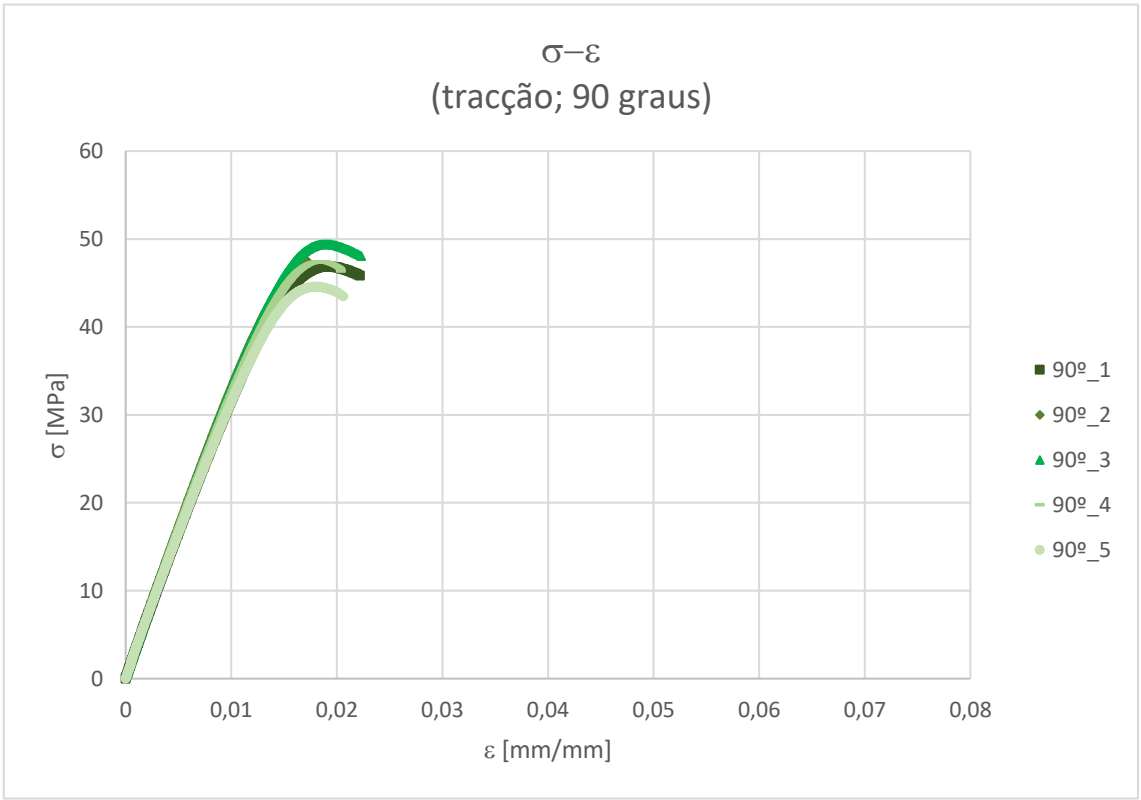
σ–ε
(tracção; 90 graus)
60
50
40
30
20
10
0
σ [MPa]
0
0,01
0,02
0,03
0,04
0,05
0,06
0,07
0,08
ε [mm/mm]
90º_1
90º_2
90º_3
90º_4
90º_5

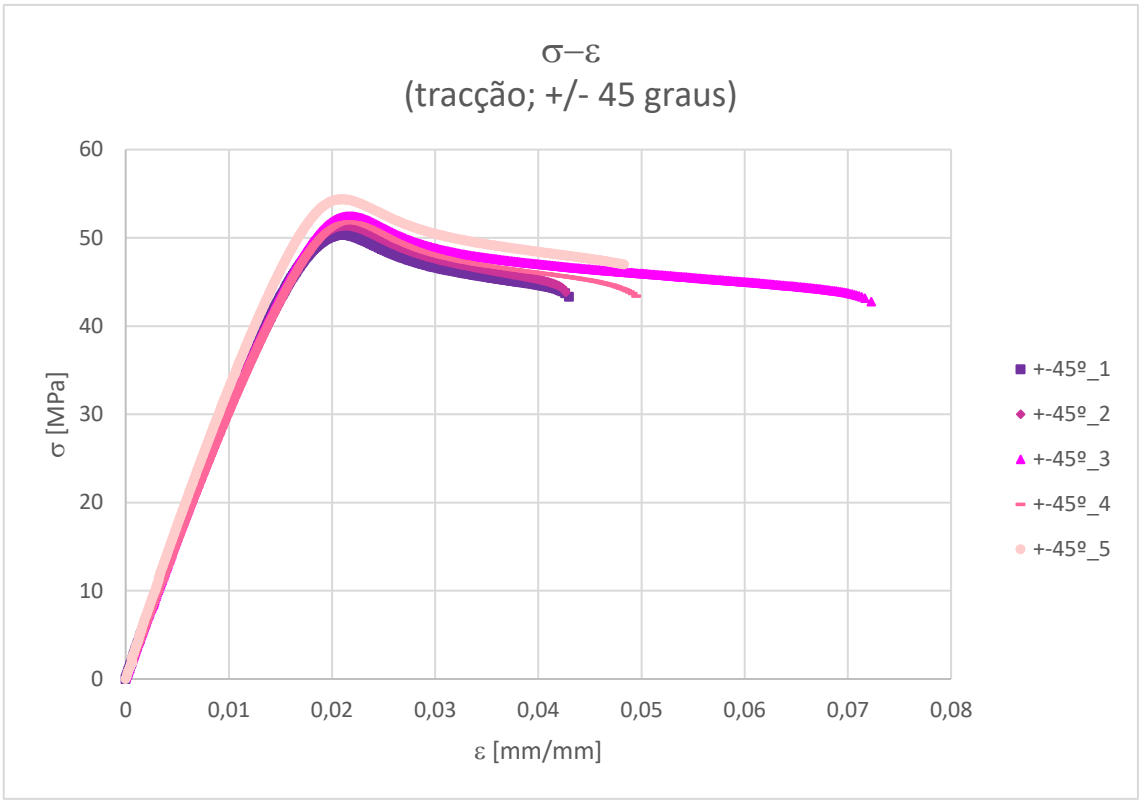
σ–ε
(tracção; +/- 45 graus)
60
50
40
30
20
10
0
σ [MPa]
0
0,01
0,02
0,03
0,04
0,05
0,06
0,07
0,08
ε [mm/mm]
+-45º_1
+-45º_2
+-45º_3
+-45º_4
+-45º_5

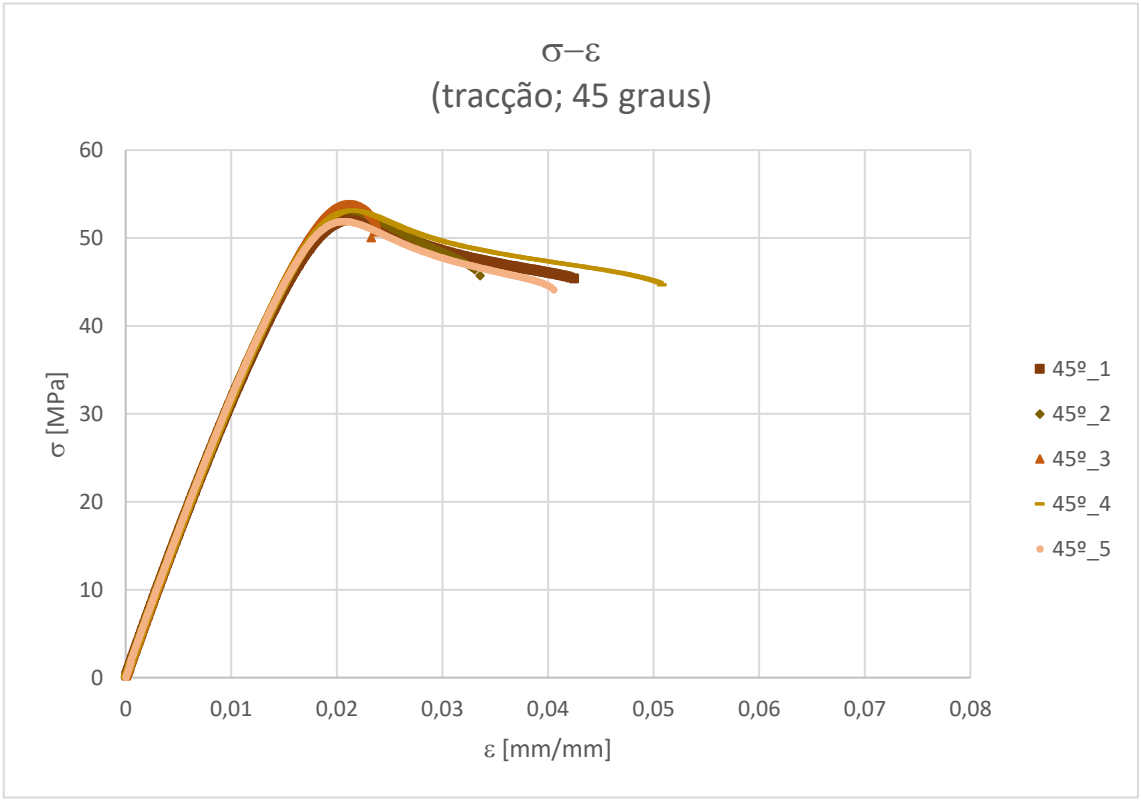
σ–ε
(tracção; 45 graus)
60
50
40
30
20
10
0
σ [MPa]
0
0,01
0,02
0,03
0,04
0,05
0,06
0,07
0,08
ε [mm/mm]
45º_1
45º_2
45º_3
45º_4
45º_5

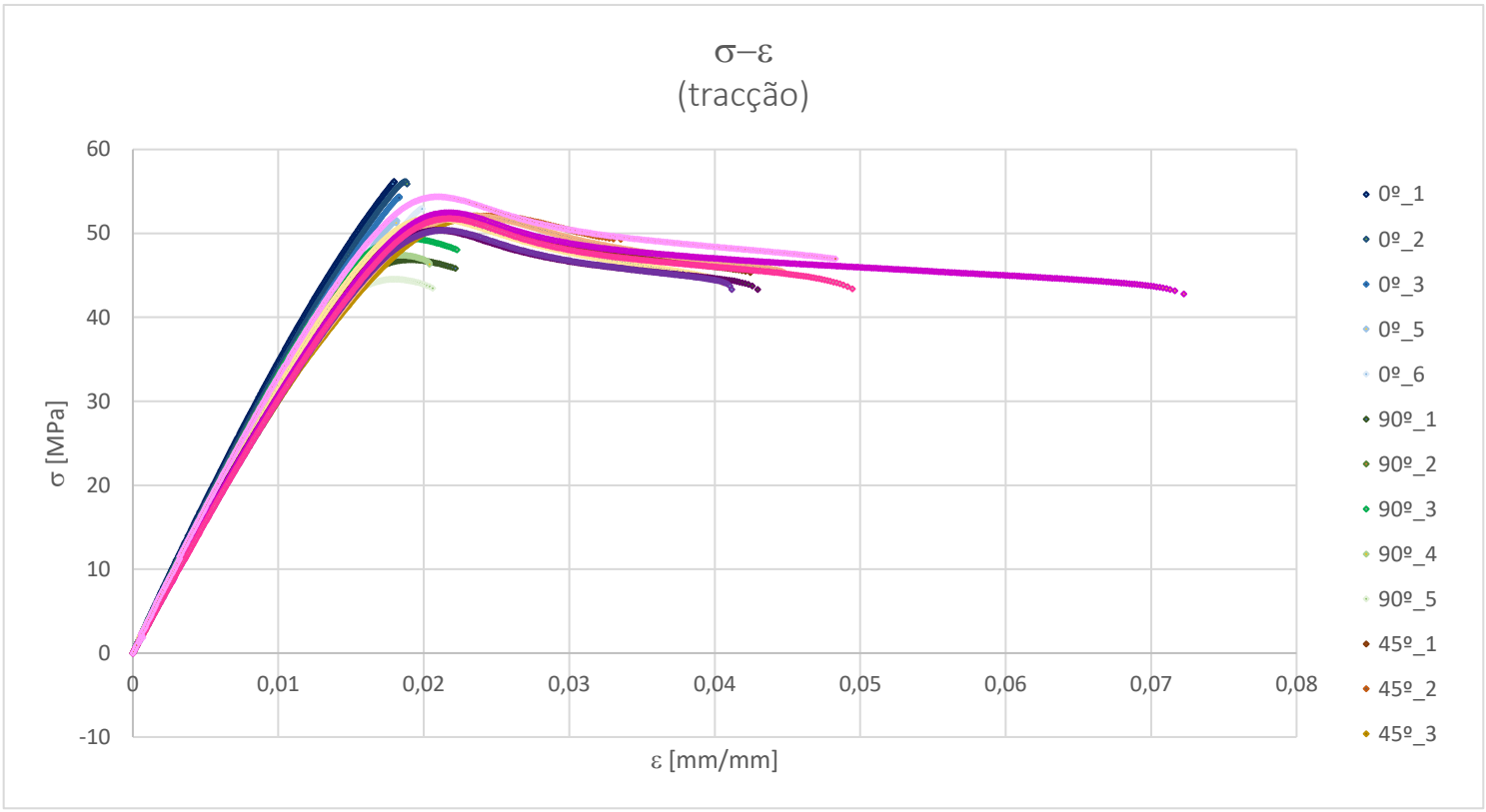
σ–ε
(tracção)
60
50
40
30
20
10
0
-10
σ [MPa]
0
0,01
0,02
0,03
0,04
0,05
0,06
0,07
0,08
ε [mm/mm]
0º_1
0º_2
0º_3
0º_5
0º_6
90º_1
90º_2
90º_3
90º_4
90º_5
45º_1
45º_2
45º_3

Ensaios de flexão – ISO 178

Dimensões do provete : L – 80 mm
w – 10 mm
t – 4 mm

Velocidade do ensaio : 2 mm/min

Numeração dos provetes ensaiados :

	0º	90º	+-45º	45º
1	1	1	1	1
2	2	2	2	2
3	3	3	3	3
4	6	4	4	4
5	7	5	5	5

σ_m	0º	90º	+-45º	45º
1	98,8485	71,34965	88,2453	94,10094
2	102,548	77,64005	92,78883	81,63396
3	92,93561	78,31989	102,8774	86,5533
4	101,192	79,25784	95,22752	96,98544
5	103,7778	76,41569	85,60223	85,59254
med	99,86037	76,59662	92,94825	88,97324

ε_m	0º	90º	+-45º	45º
1	0,0439	0,02849	0,04338	0,04084
2	0,04272	0,03063	0,0429	0,04492
3	0,04622	0,03013	0,04217	0,045
4	0,04414	0,0306	0,04238	0,04173
5	0,0453	0,03269	0,04526	0,04398
med	0,044456	0,030508	0,043218	0,043294

E	0º	90º	+-45º	45º
1	2827,615	2640,752	2266,889	2785,621
2	3051,01	2254,207	2905,888	1898,285
3	2893,855	2398,048	3069,171	2187,063
4	2943,246	2760,527	2402,964	2675,846
5	2478,15	2114,117	1960,586	2047,298
med	2838,775	2433,53	2521,1	2318,823

Provetes após ensaio:

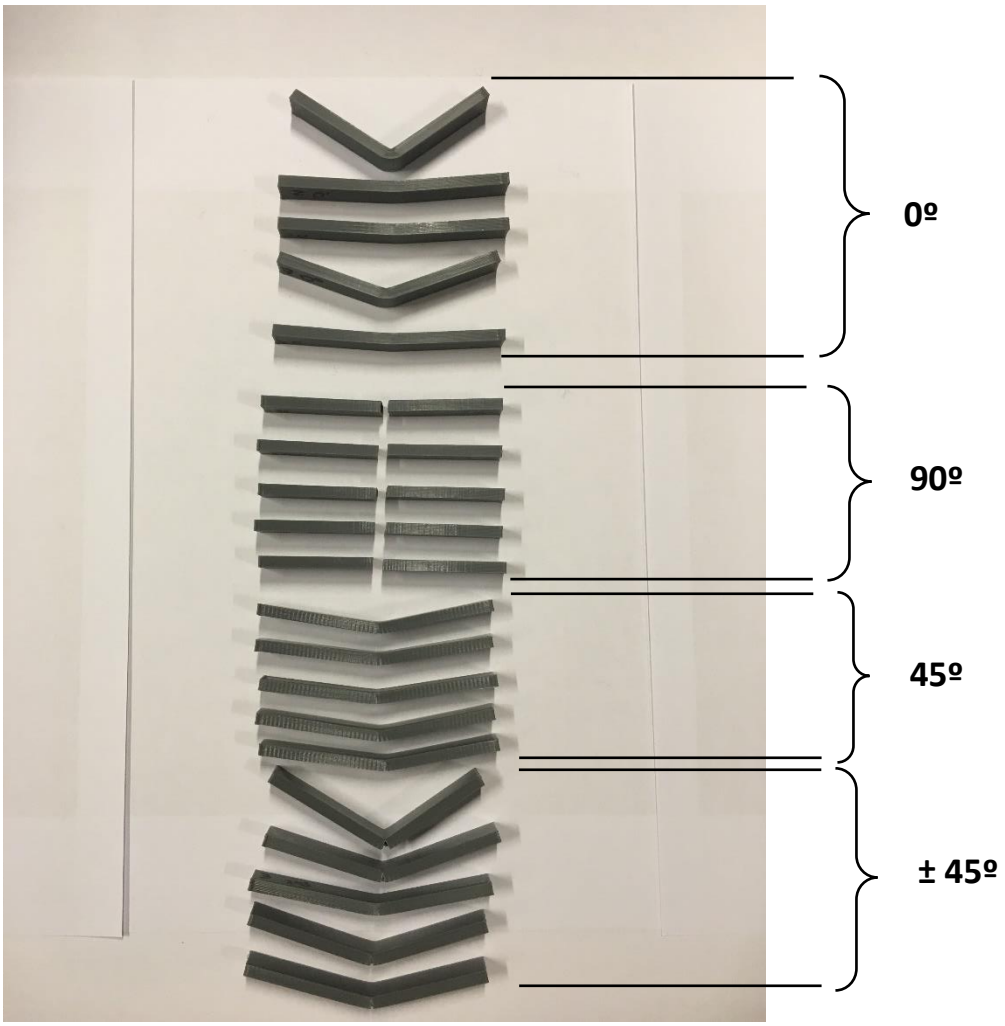

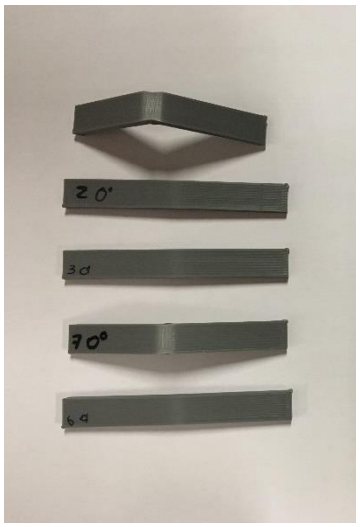

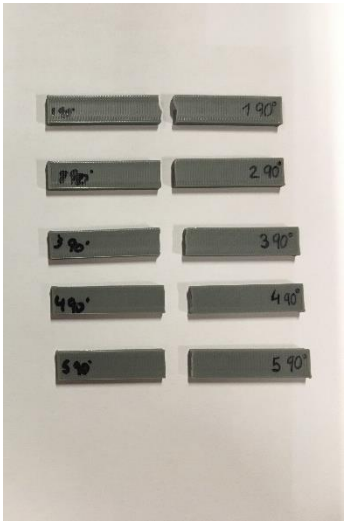

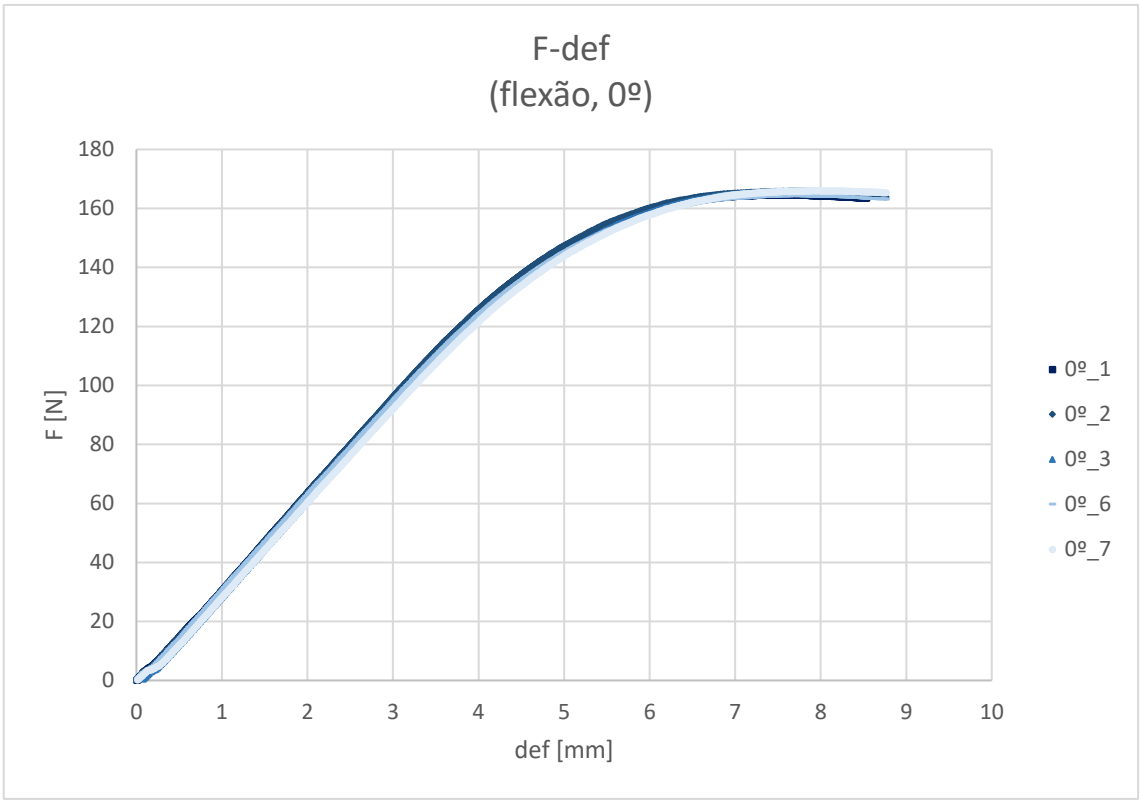
F-def
(flexão, 0º)
F [N]
def [mm]
0
20
40
60
80
100
120
140
160
180
0
1
2
3
4
5
6
7
8
9
10
0º_1
0º_2
0º_3
0º_6
0º_7

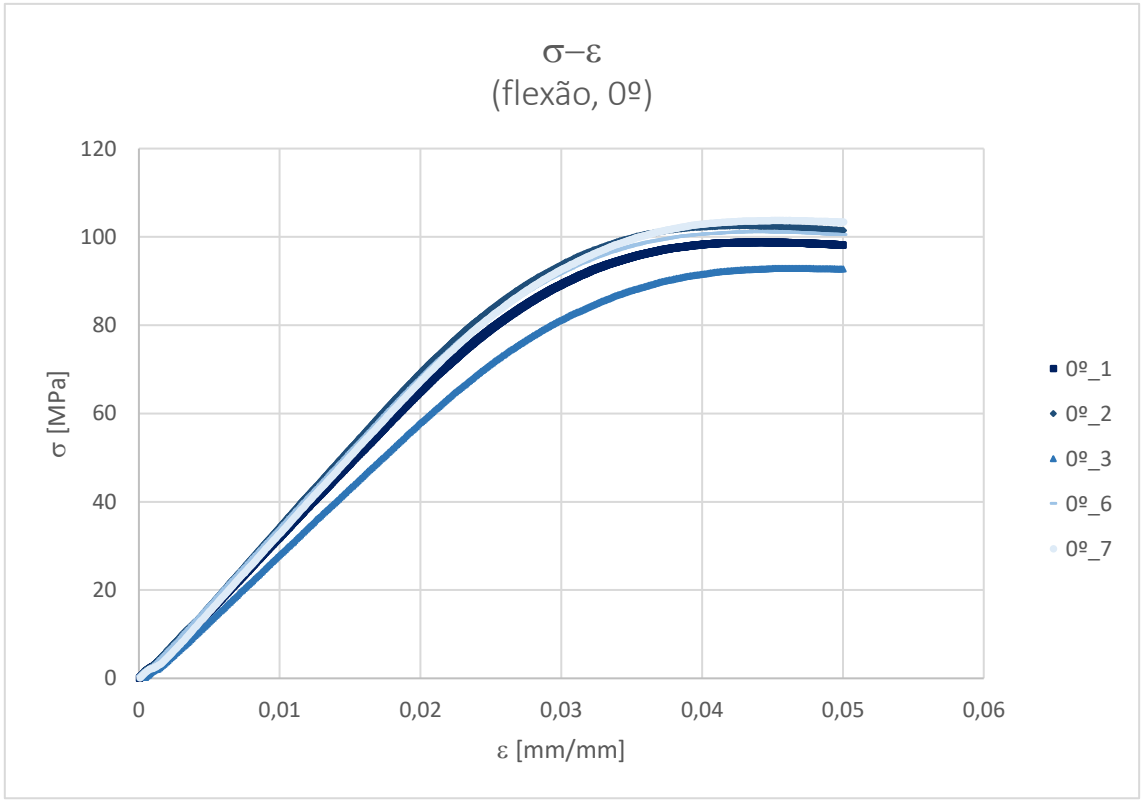
σ–ε
(flexão, 0º)
σ [MPa]
ε [mm/mm]
0
20
40
60
80
100
120
0
0,01
0,02
0,03
0,04
0,05
0,06
0º_1
0º_2
0º_3
0º_6
0º_7

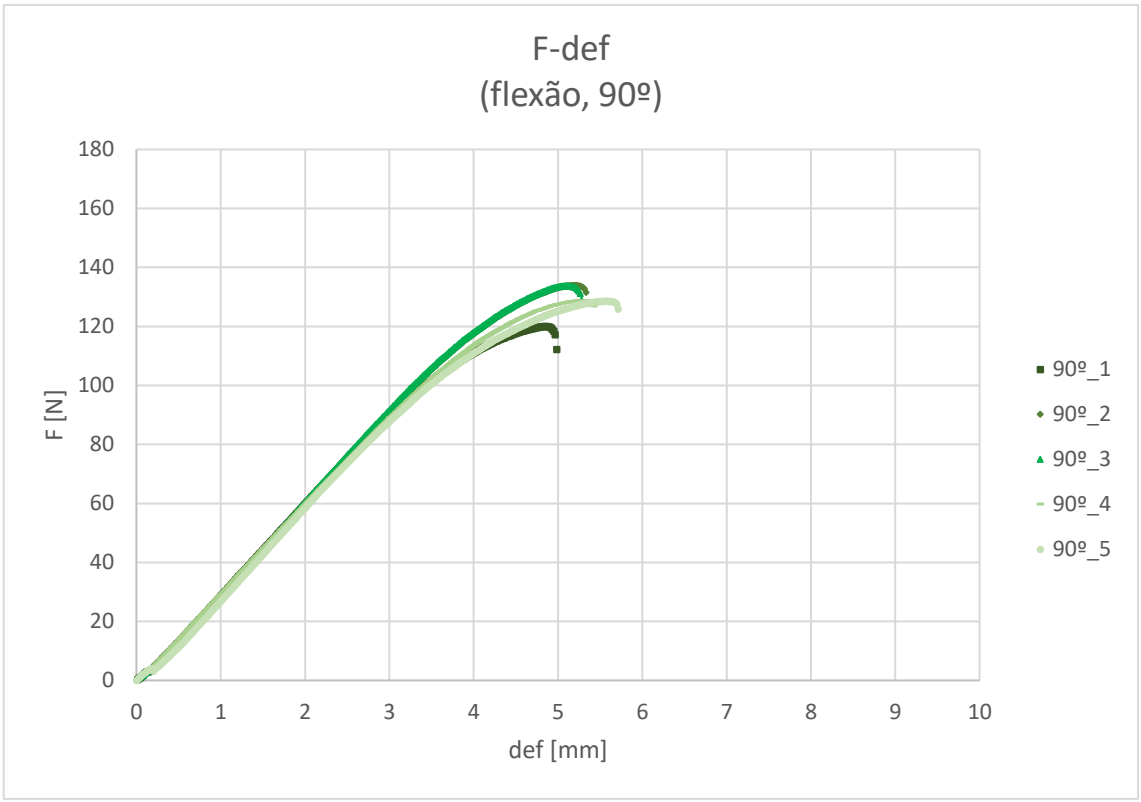
F-def
(flexão, 90º)
F [N]
def [mm]
0
20
40
60
80
100
120
140
160
180
0
1
2
3
4
5
6
7
8
9
10
90º_1
90º_2
90º_3
90º_4
90º_5

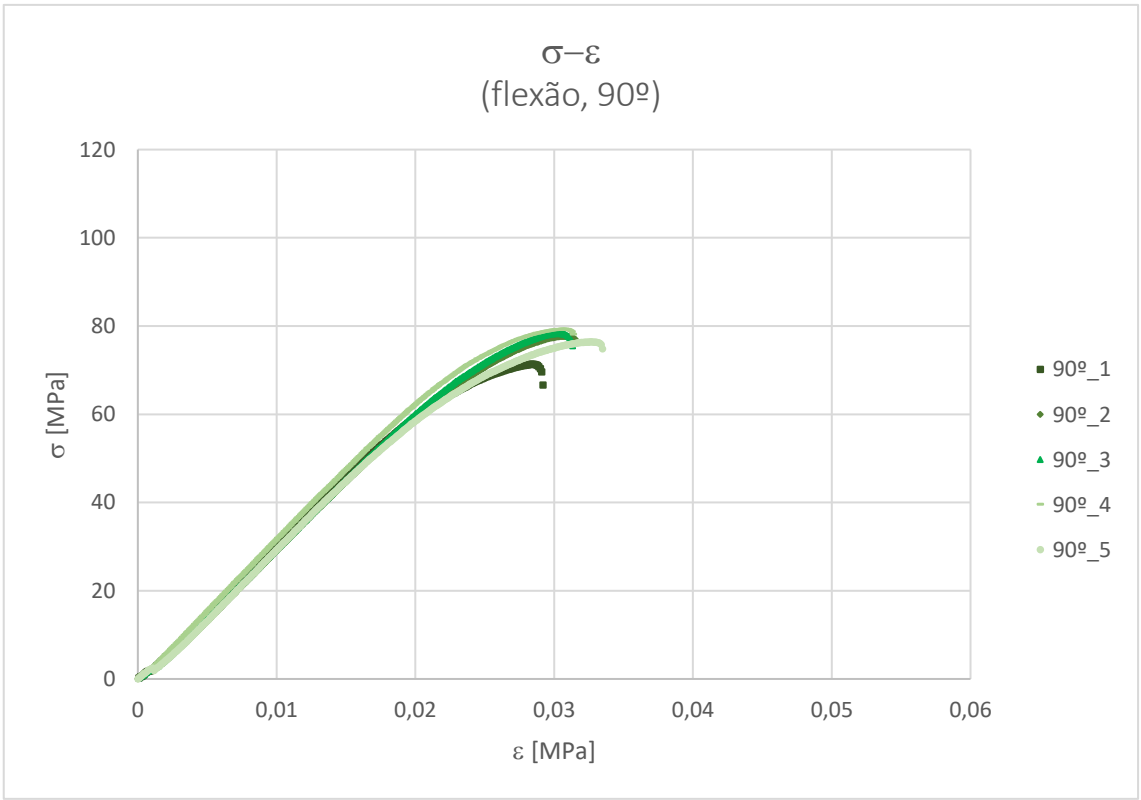
σ–ε
(flexão, 90º)
σ [MPa]
ε [MPa]
0
20
40
60
80
100
120
0
0,01
0,02
0,03
0,04
0,05
0,06
90º_1
90º_2
90º_3
90º_4
90º_5

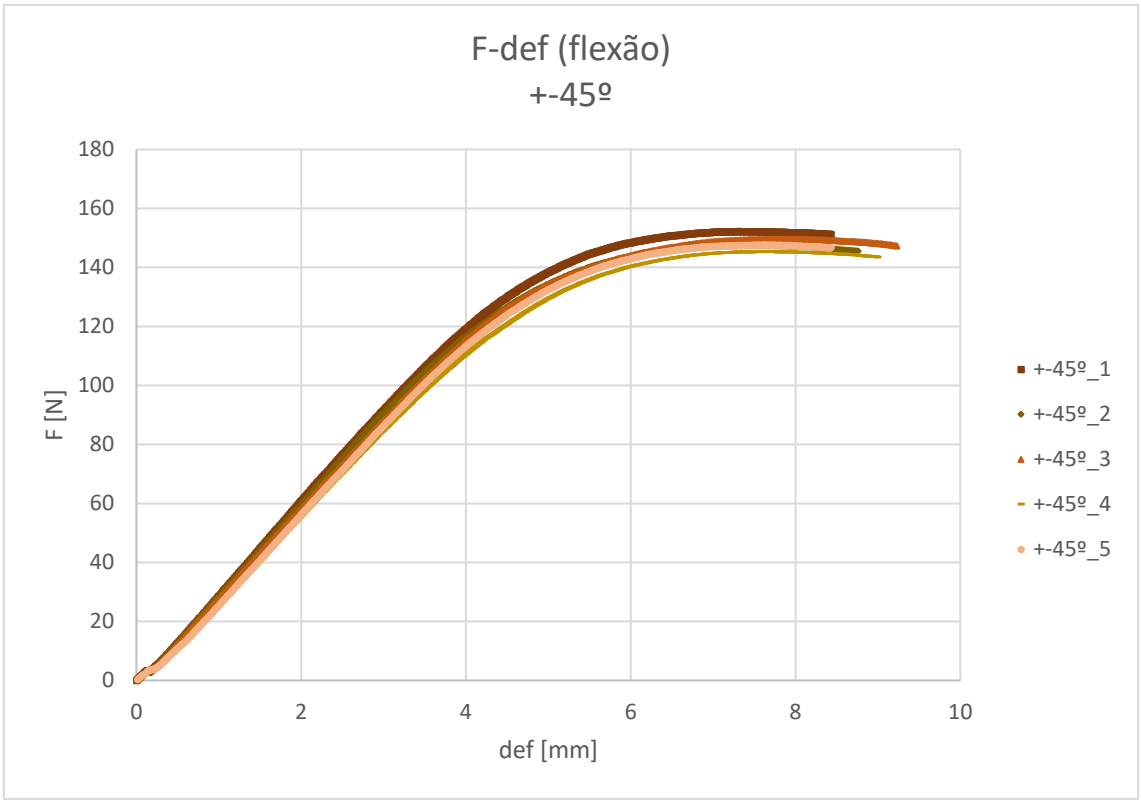
F-def (flexão)
+-45º
180
160
140
120
100
80
60
40
20
0
F [N]
0
2
4
6
8
10
def [mm]
+-45º_1
+-45º_2
+-45º_3
+-45º_4
+-45º_5

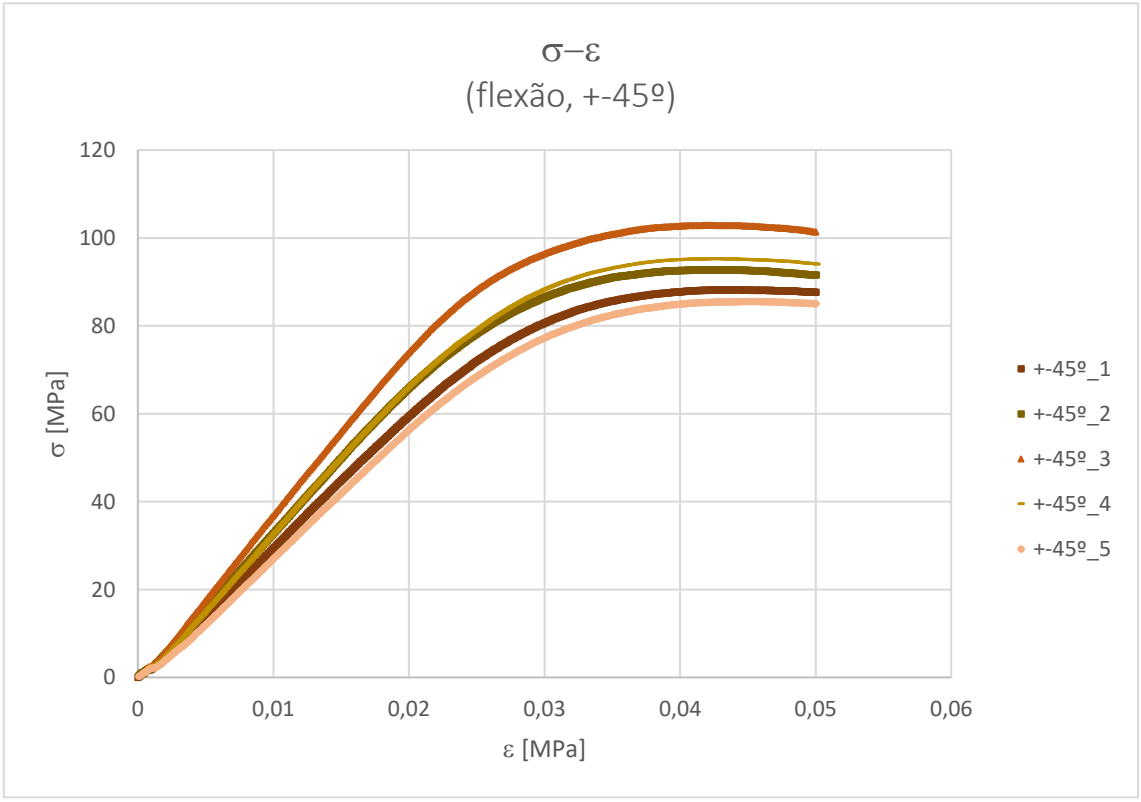
σ–ε
(flexão, +-45º)
120
100
80
60
40
20
0
σ [MPa]
0
0,01
0,02
0,03
0,04
0,05
0,06
ε [MPa]
+-45º_1
+-45º_2
+-45º_3
+-45º_4
+-45º_5

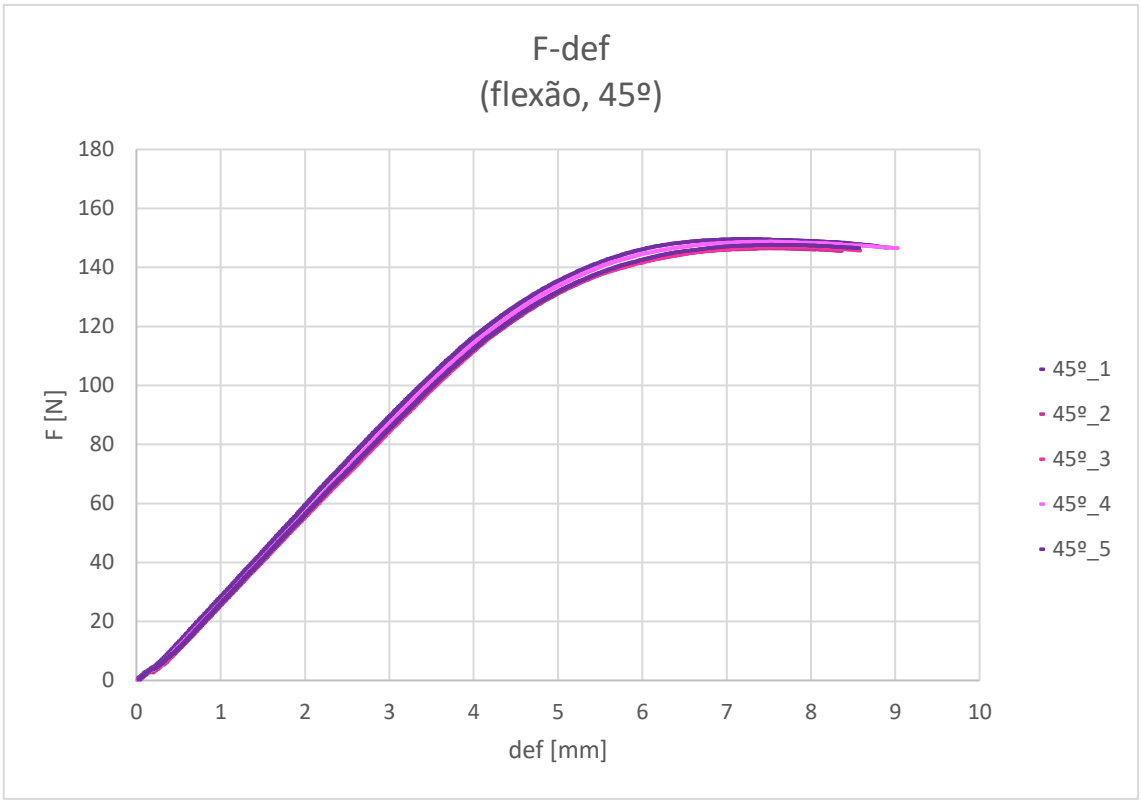
F-def
(flexão, 45º)
F [N]
def [mm]
0
20
40
60
80
100
120
140
160
180
0
1
2
3
4
5
6
7
8
9
10
45º_1
45º_2
45º_3
45º_4
45º_5

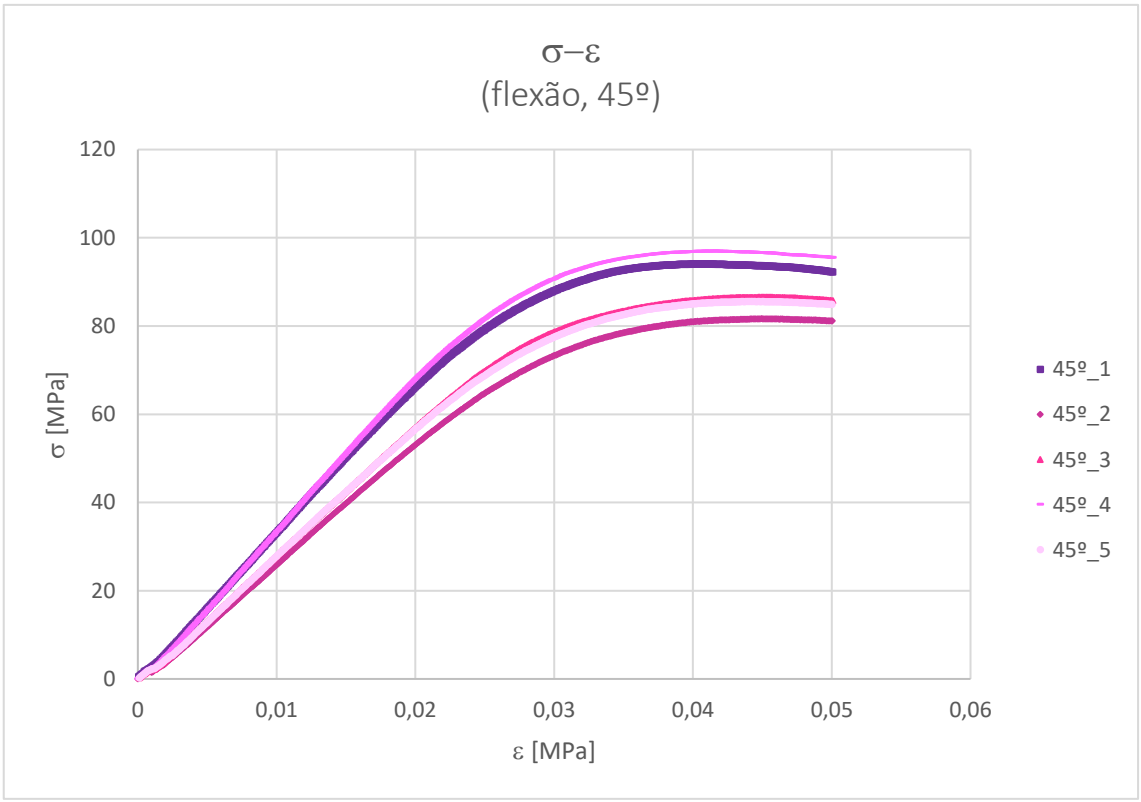
σ–ε
(flexão, 45º)
σ [MPa]
ε [MPa]
0
20
40
60
80
100
120
0
0,01
0,02
0,03
0,04
0,05
0,06
45º_1
45º_2
45º_3
45º_4
45º_5

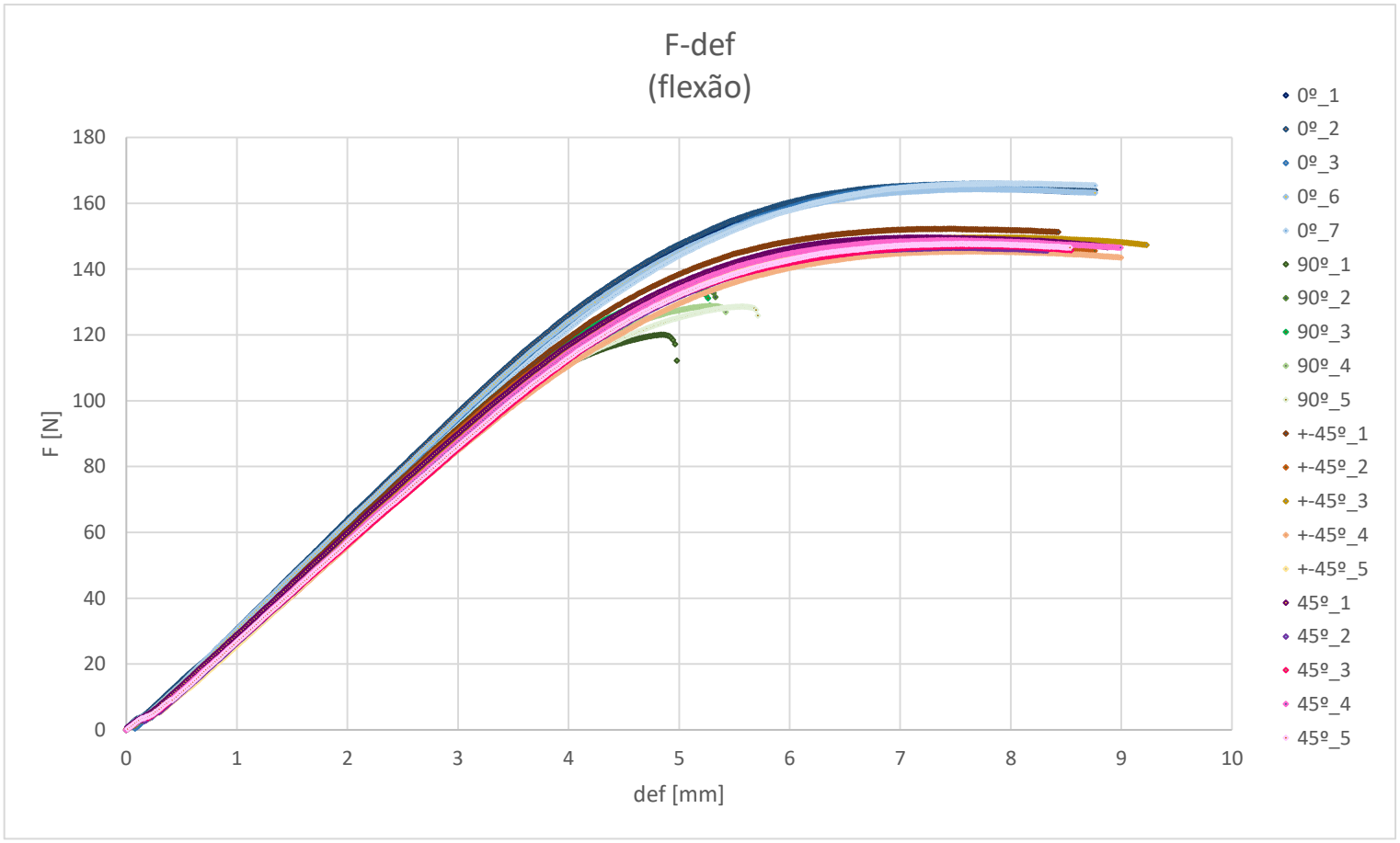
F-def
(flexão)
F [N]
def [mm]
0
20
40
60
80
100
120
140
160
180
0
1
2
3
4
5
6
7
8
9
10
0º_1
0º_2
0º_3
0º_6
0º_7
90º_1
90º_2
90º_3
90º_4
90º_5
+-45º_1
+-45º_2
+-45º_3
+-45º_4
+-45º_5
45º_1
45º_2
45º_3
45º_4
45º_5

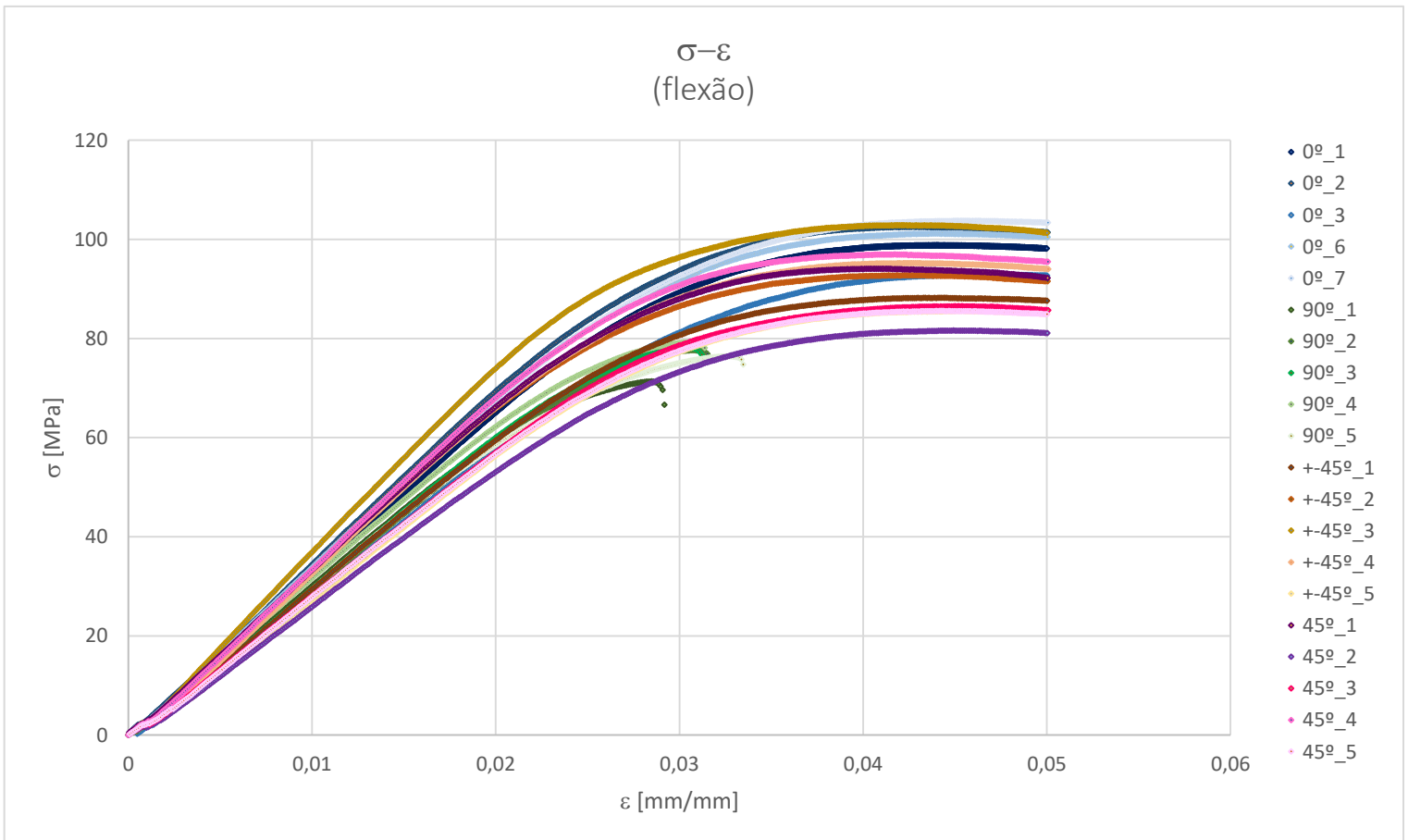
σ–ε
(flexão)
σ [MPa]
ε [mm/mm]
0
20
40
60
80
100
120
0
0,01
0,02
0,03
0,04
0,05
0,06
0º_1
0º_2
0º_3
0º_6
0º_7
90º_1
90º_2
90º_3
90º_4
90º_5
+-45º_1
+-45º_2
+-45º_3
+-45º_4
+-45º_5
45º_1
45º_2
45º_3
45º_4
45º_5

Ensaios de compressão – ISO 604

- **Provetes altos para a determinação do módulo de elasticidade**

Dimensões do provete : L – 50 mm
w – 10 mm
t – 4 mm

Velocidade do ensaio : 1 mm/min

Numeração dos provetes ensaiados :

	0º	90º	45º	+-45º
1	1	1	1	1
2	2	2	2	2
3	3	3	3	3
4	4	4	4	4
5	5	5	5	5

E	0º	90º	+-45º	45º
1	2333,88	2242,13	2732,4	2467,61
2	2568,65	2361,24	3016,48	2710,97
3	2684,57	2471,06	3025,05	2898,86
4	2726,92	2368,17	2696,65	2725,29
5	2552,36	2657,63	2805,59	2809,98
med	2573,276	2420,046	2855,234	2722,542

NOTA: As curvas dos ensaios de compressão apresentavam inícios não lineares que se devem à adaptação entre as imperfeições dos provetes e a máquina. Assim, todas as curvas foram corrigidas através de uma regressão linear, de acordo com o estabelecido na norma.

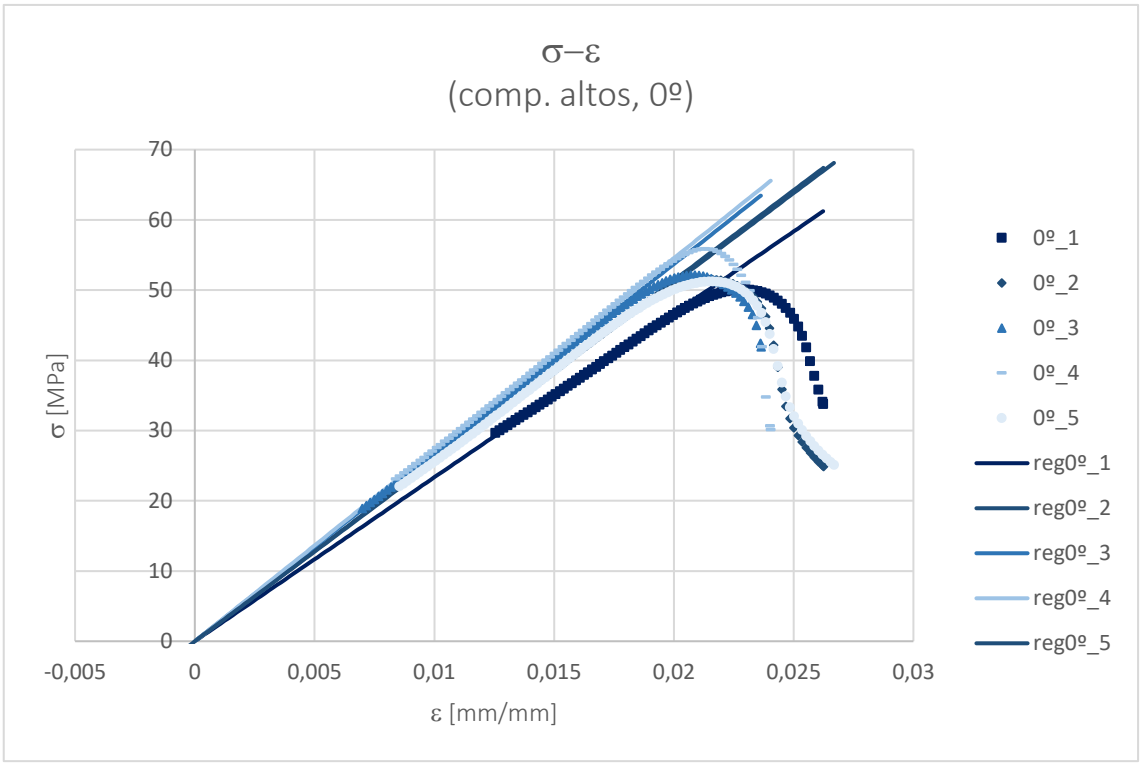
σ–ε
(comp. altos, 0º)
70
60
50
40
30
20
10
0
σ [MPa]
-0,005
0
0,005
0,01
0,015
0,02
0,025
0,03
ε [mm/mm]
0º_1
0º_2
0º_3
0º_4
0º_5
reg0º_1
reg0º_2
reg0º_3
reg0º_4
reg0º_5

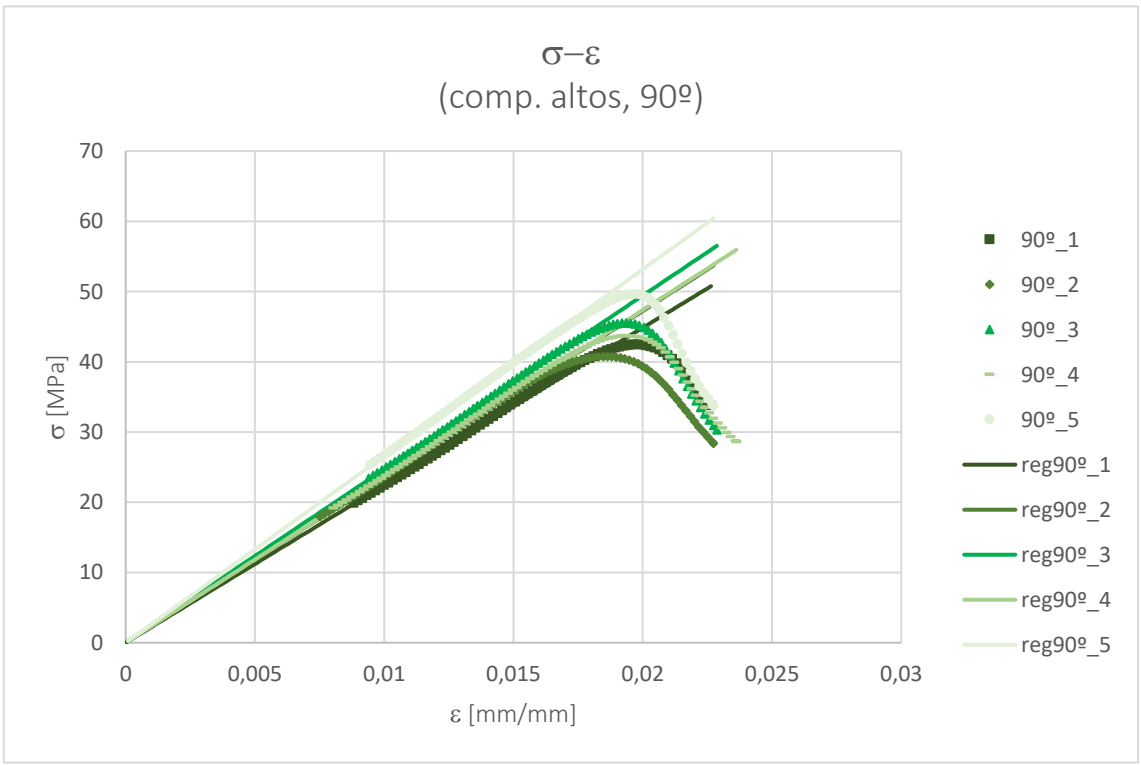
σ–ε
(comp. altos, 90º)
70
60
50
40
30
20
10
0
σ [MPa]
0
0,005
0,01
0,015
0,02
0,025
0,03
ε [mm/mm]
90º_1
90º_2
90º_3
90º_4
90º_5
reg90º_1
reg90º_2
reg90º_3
reg90º_4
reg90º_5

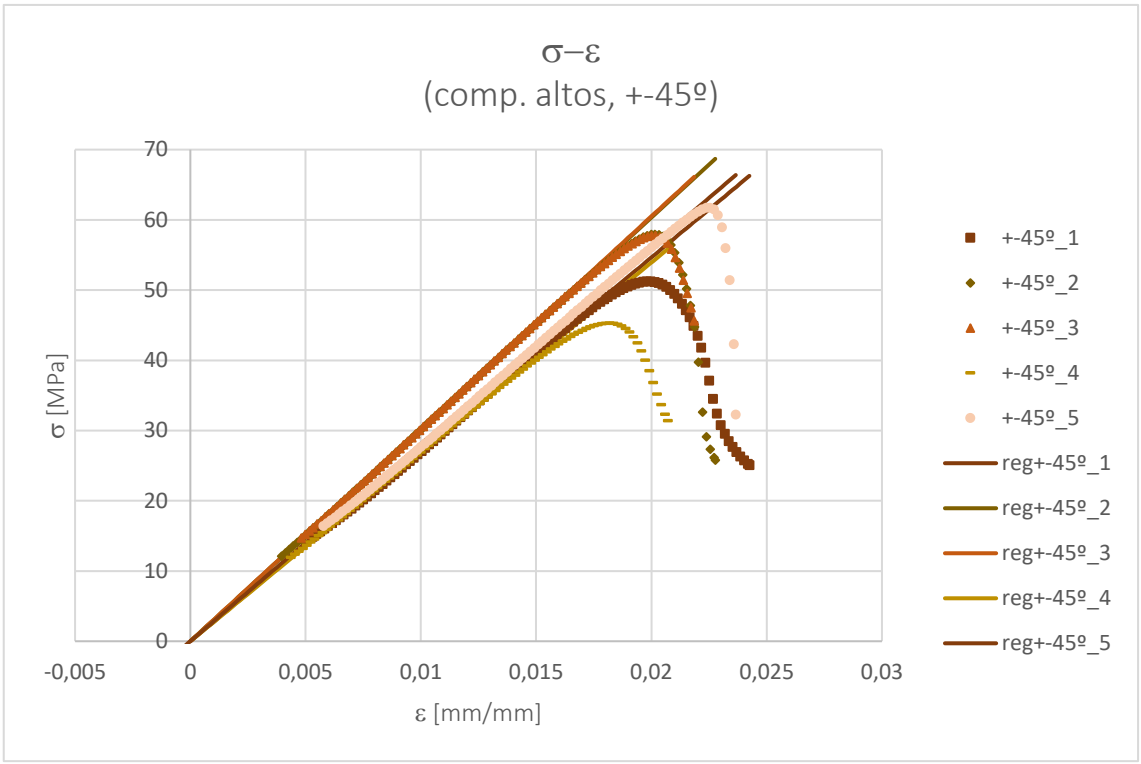
σ–ε
(comp. altos, +-45º)
70
60
50
40
30
20
10
0
σ [MPa]
-0,005
0
0,005
0,01
0,015
0,02
0,025
0,03
ε [mm/mm]
+-45º_1
+-45º_2
+-45º_3
+-45º_4
+-45º_5
reg+-45º_1
reg+-45º_2
reg+-45º_3
reg+-45º_4
reg+-45º_5

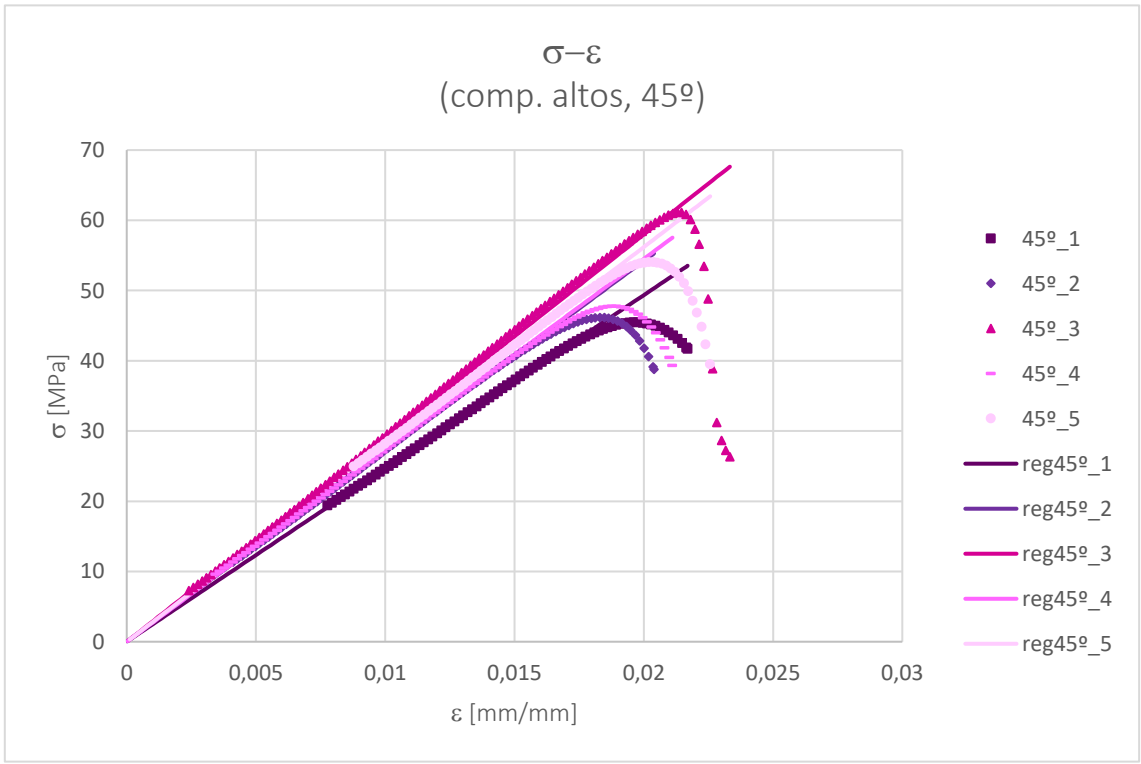
σ–ε
(comp. altos, 45º)
70
60
50
40
30
20
10
0
σ [MPa]
0
0,005
0,01
0,015
0,02
0,025
0,03
ε [mm/mm]
45º_1
45º_2
45º_3
45º_4
45º_5
reg45º_1
reg45º_2
reg45º_3
reg45º_4
reg45º_5

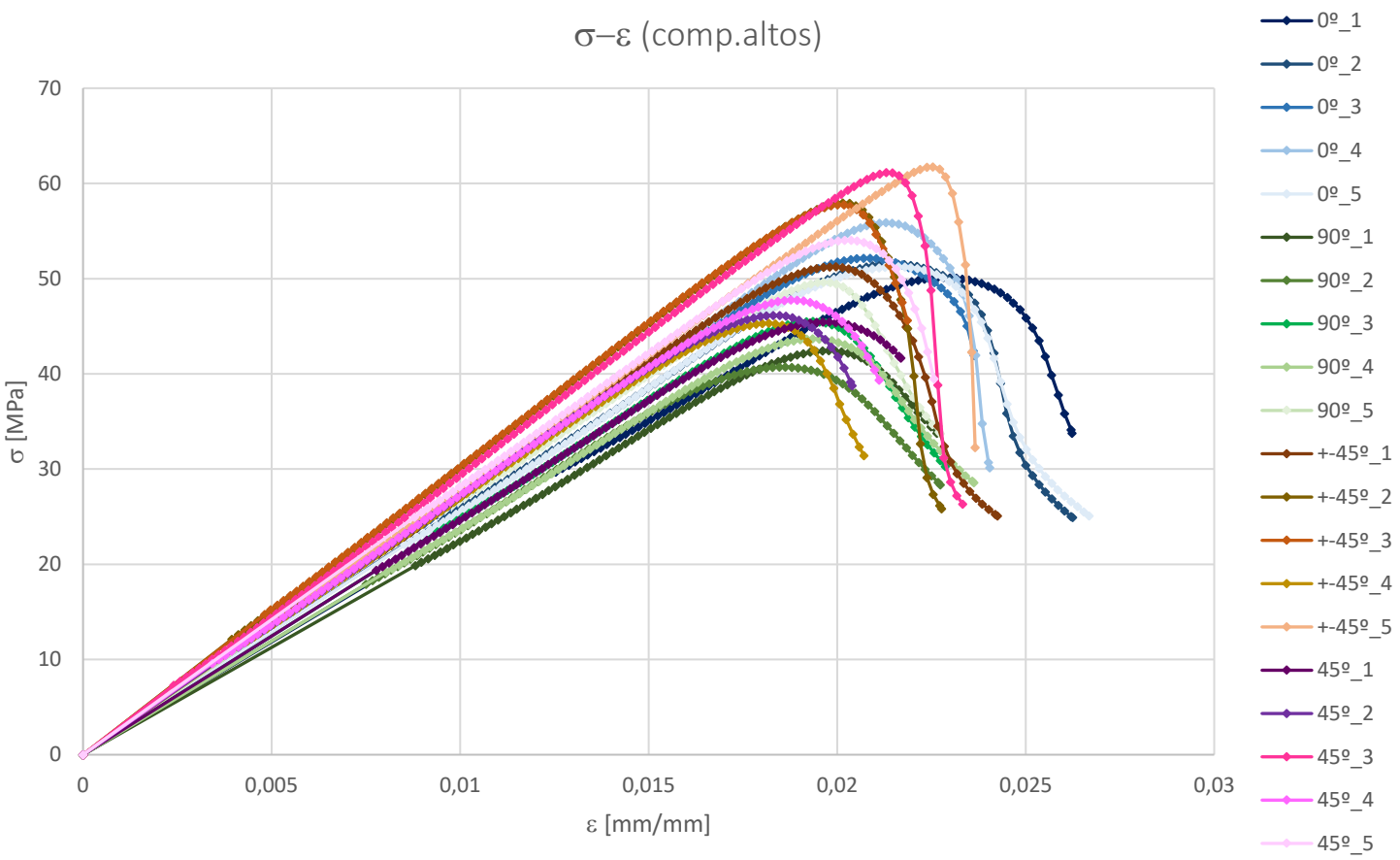
σ–ε (comp.altos)
σ [MPa]
ε [mm/mm]
0
10
20
30
40
50
60
70
0
0,005
0,01
0,015
0,02
0,025
0,03
0º_1
0º_2
0º_3
0º_4
0º_5
90º_1
90º_2
90º_3
90º_4
90º_5
+-45º_1
+-45º_2
+-45º_3
+-45º_4
+-45º_5
45º_1
45º_2
45º_3
45º_4
45º_5

- **Provetes baixos para determinação da curva σ–ε**

Dimensões do provete : L – 10 mm
w – 10 mm
t – 4 mm

Velocidade do ensaio : 5 mm/min

Numeração dos provetes ensaiados :

	0º	90º	45º	+-45º
1	1	1	1	1
2	2	2	2	2
3	4	3	3	3
4	5	4	4	4
5	6	5	5	5

σ_y	0º	90º	+-45º	45º
1	93,63476	80,60928	85,04744	86,41801
2	93,11346	78,4795	84,35704	85,48269
3	92,04047	80,95044	88,86728	87,08171
4	95,9532	81,64307	89,18031	87,39183
5	93,46178	77,7199	86,07408	90,9099
med	93,64073	79,88044	86,70523	87,45683

ε_y	0º	90º	+-45º	45º
1	0,061268	0,065289	0,073061	0,058581
2	0,059992	0,065405	0,067223	0,05303
3	0,060972	0,065793	0,068317	0,054309
4	0,061529	0,071117	0,069627	0,063572
5	0,059832	0,081784	0,073268	0,051623
med	0,060718	0,069878	0,070299	0,056223

NOTA: As curvas dos ensaios de compressão apresentavam inícios não lineares que se devem à adaptação entre as imperfeições dos provetes e a máquina. Assim, todas as curvas foram corrigidas através de uma regressão linear, de acordo com o estabelecido na norma.

Provetes após ensaio:

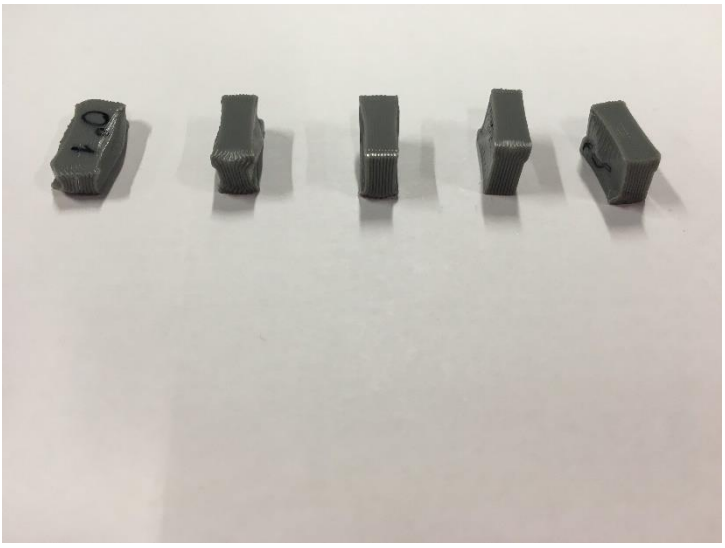

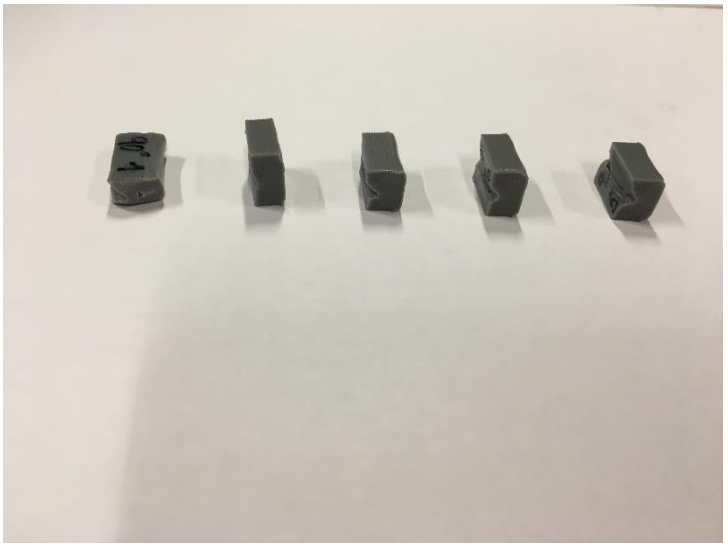

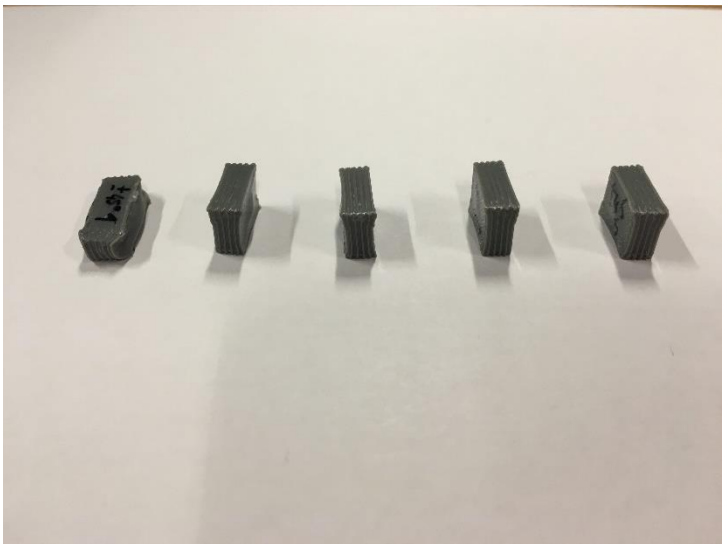

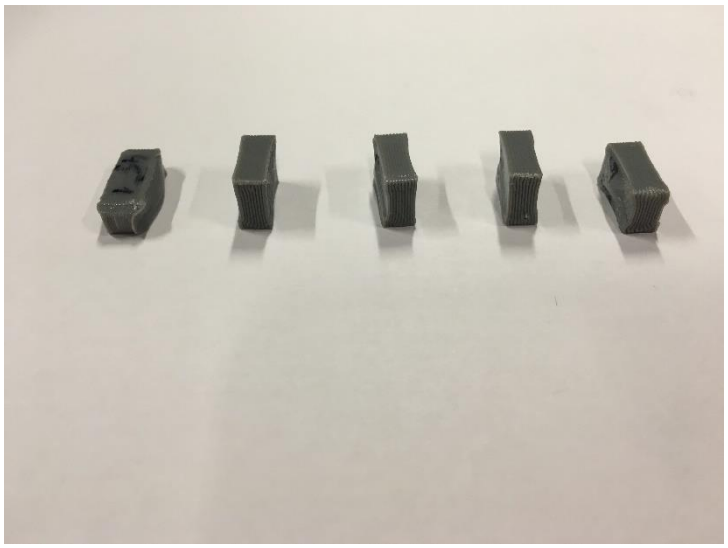

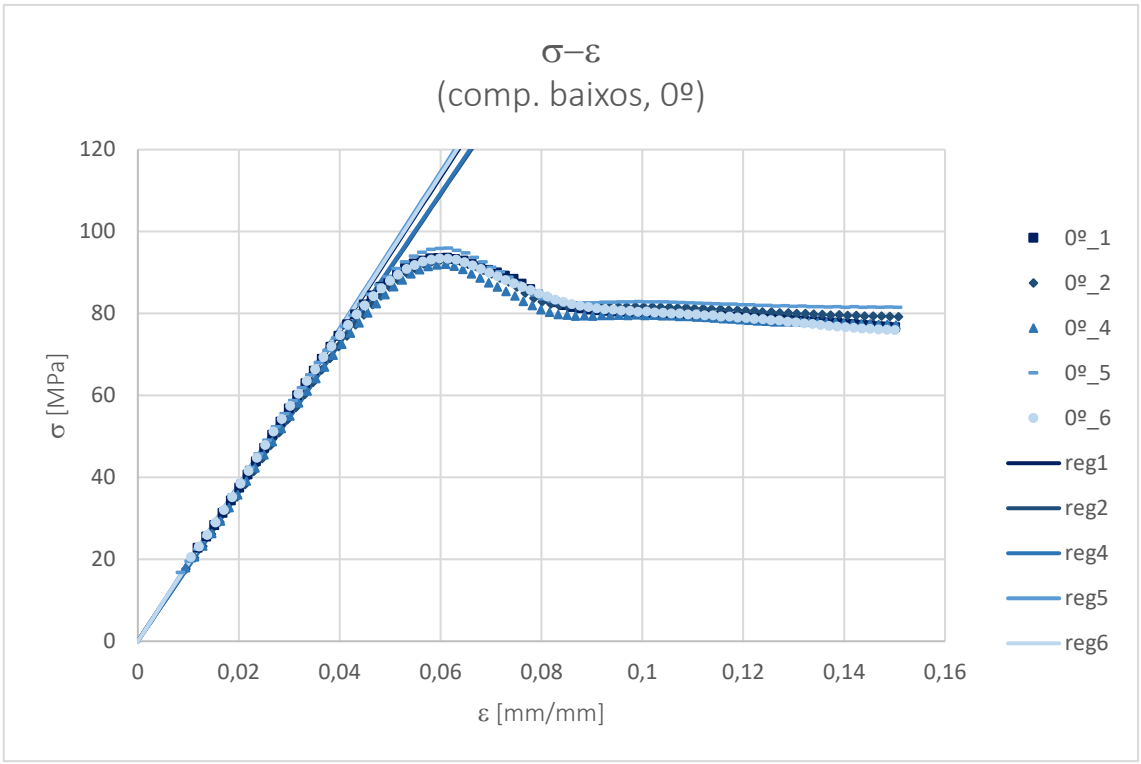
σ–ε
(comp. baixos, 0º)
120
100
80
60
40
20
0
σ [MPa]
0
0,02
0,04
0,06
0,08
0,1
0,12
0,14
0,16
ε [mm/mm]
0º_1
0º_2
0º_4
0º_5
0º_6
reg1
reg2
reg4
reg5
reg6

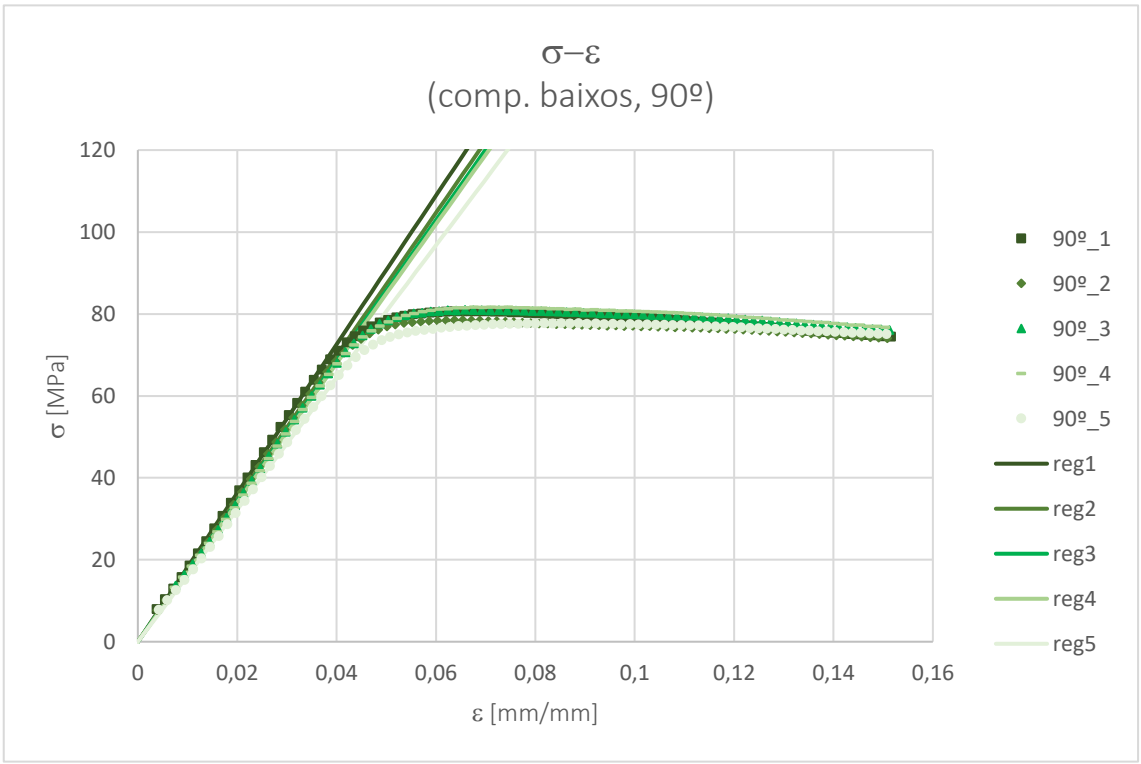
σ–ε
(comp. baixos, 90º)
120
100
80
60
40
20
0
σ [MPa]
0
0,02
0,04
0,06
0,08
0,1
0,12
0,14
0,16
ε [mm/mm]
90º_1
90º_2
90º_3
90º_4
90º_5
reg1
reg2
reg3
reg4
reg5

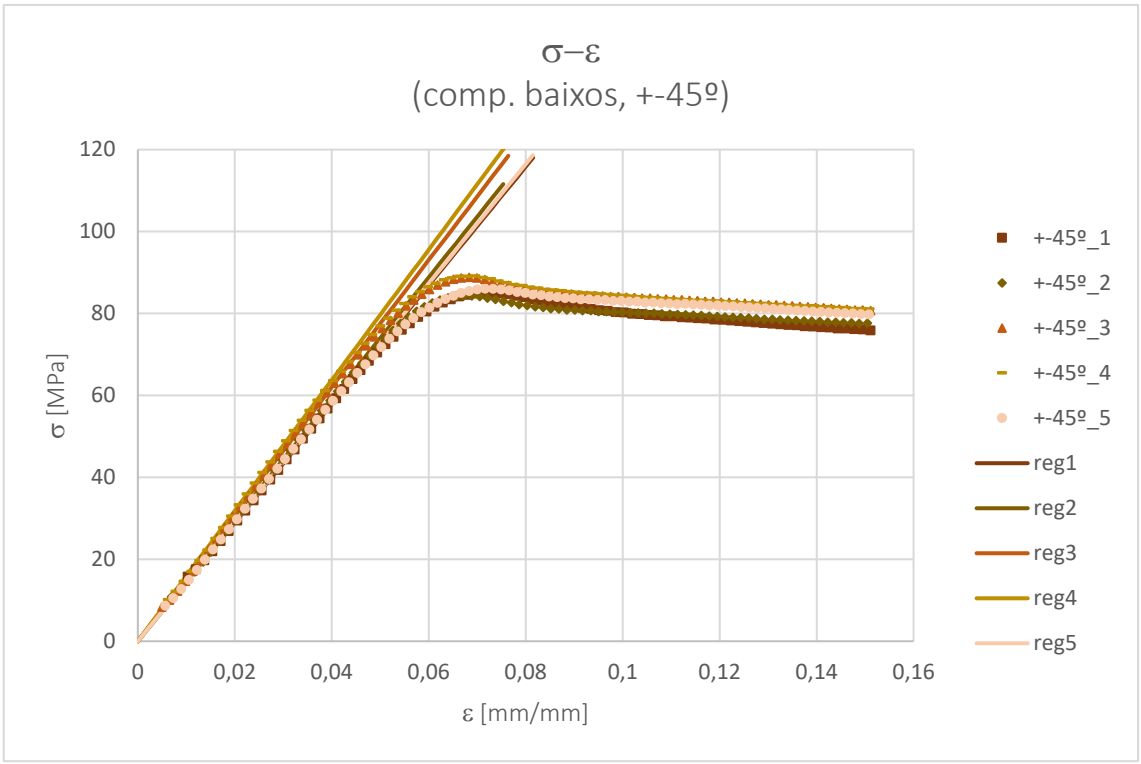
σ–ε
(comp. baixos, +-45º)
120
100
80
60
40
20
0
σ [MPa]
0
0,02
0,04
0,06
0,08
0,1
0,12
0,14
0,16
ε [mm/mm]
+-45º_1
+-45º_2
+-45º_3
+-45º_4
+-45º_5
reg1
reg2
reg3
reg4
reg5

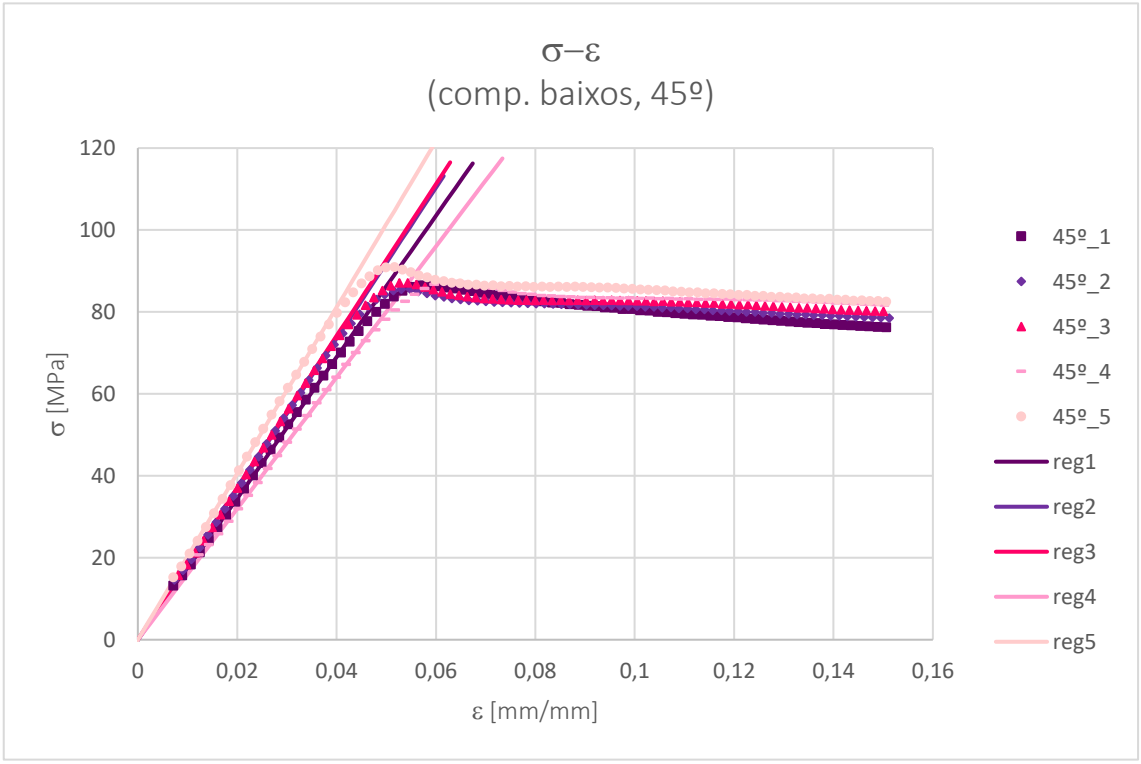
σ–ε
(comp. baixos, 45º)
120
100
80
60
40
20
0
σ [MPa]
0
0,02
0,04
0,06
0,08
0,1
0,12
0,14
0,16
ε [mm/mm]
45º_1
45º_2
45º_3
45º_4
45º_5
reg1
reg2
reg3
reg4
reg5

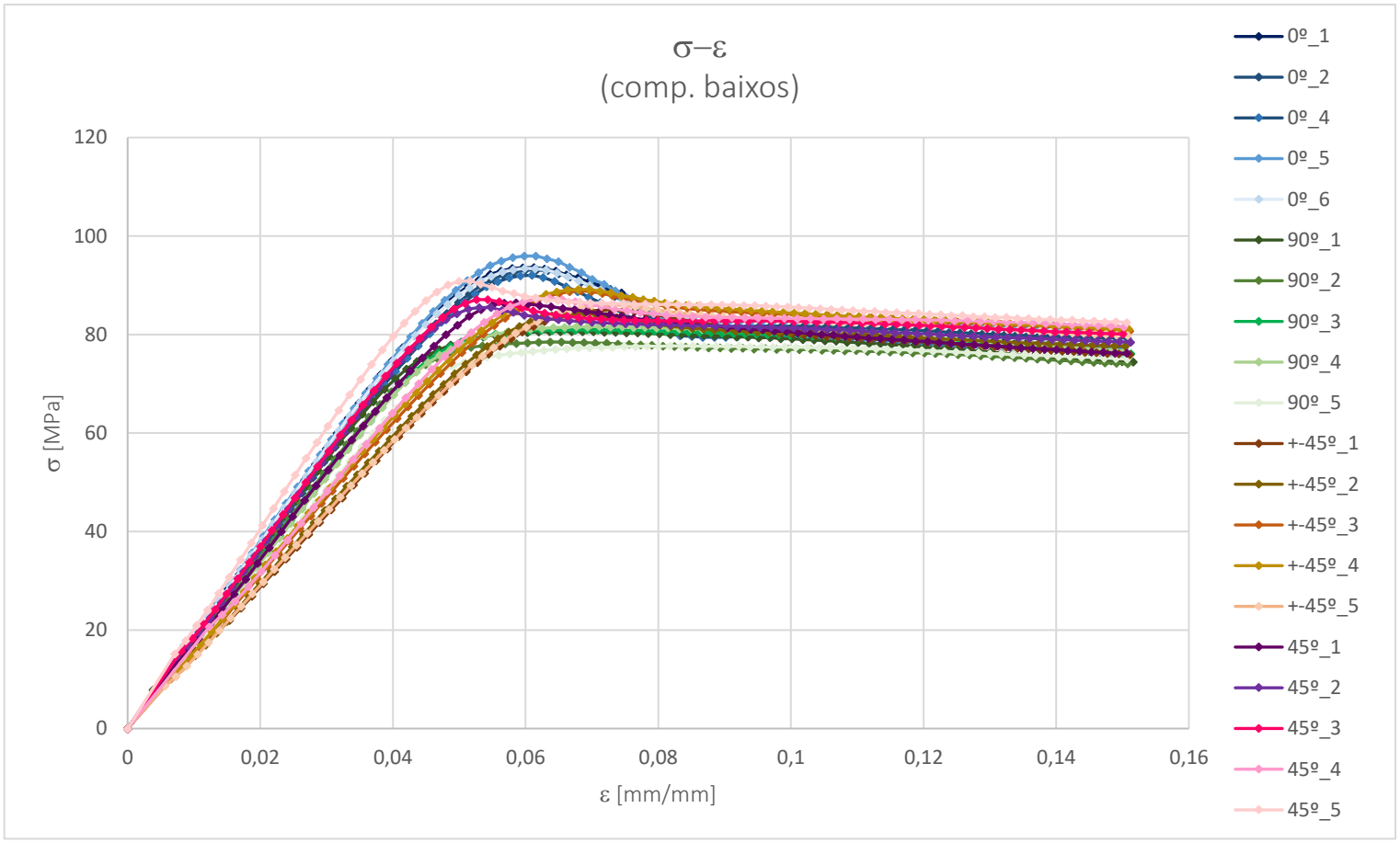
σ–ε
(comp. baixos)
120
100
80
60
40
20
0
σ [MPa]
0
0,02
0,04
0,06
0,08
0,1
0,12
0,14
0,16
ε [mm/mm]
0º_1
0º_2
0º_4
0º_5
0º_6
90º_1
90º_2
90º_3
90º_4
90º_5
+-45º_1
+-45º_2
+-45º_3
+-45º_4
+-45º_5
45º_1
45º_2
45º_3
45º_4
45º_5

Appendix B

Results obtained on the study about the influence of the gyroid infill

Ensaios de tracção – ISO 527

- Provetes com preenchimento gyroid e diferentes percentagens de enchimento

Dimensões do provete : L – 150 mm
L_0 – 60 mm
w – 10 mm
t – 4 mm

Velocidade do ensaio : $v = 1\ mm/min$

Fy [N]	20%	50%	80%
1	-	539,066	1002,985
2	-	529,316	991,899
3	-	525,282	955,664
4	-	-	957,607
5	-	512,079	930,183
med	-	526,4358	967,6676

dy [mm]	20%	50%	80%
1	-	1,72335	0,97373
2	-	1,6581	0,98444
3	-	1,67869	0,99161
4	-	-	0,97566
5	-	1,70626	0,99478
med	-	1,6916	0,984044

Fb [N]	20%	50%	80%
1	259,632	511,582	933,287
2	262,712	514,002	909,901
3	258,768	501,955	852,786
4	257,605	-	872,752
5	250,626	497,136	843,809
med	257,8686	506,1688	882,507

db [mm]	20%	50%	80%
1	1,98869	3,10187	2,02316
2	1,51055	2,69436	2,27168
3	1,46286	2,74208	2,8977
4	1,61184	-	2,54038
5	1,40275	2,34505	2,98914
med	1,595338	2,72084	2,544412

Nota: No caso de provetes com preenchimento gyroid com percentagens de enchimento inferiores a 100%, as dimensões exteriores não podem ser usadas como referência para o cálculo das tensões e extensões nominais. Consequentemente, não é também possível calcular módulos de elasticidade nem *coeficientes de Poisson*, sendo então apresentados apenas valores e gráficos força-deslocamento.

Provetes após ensaio:

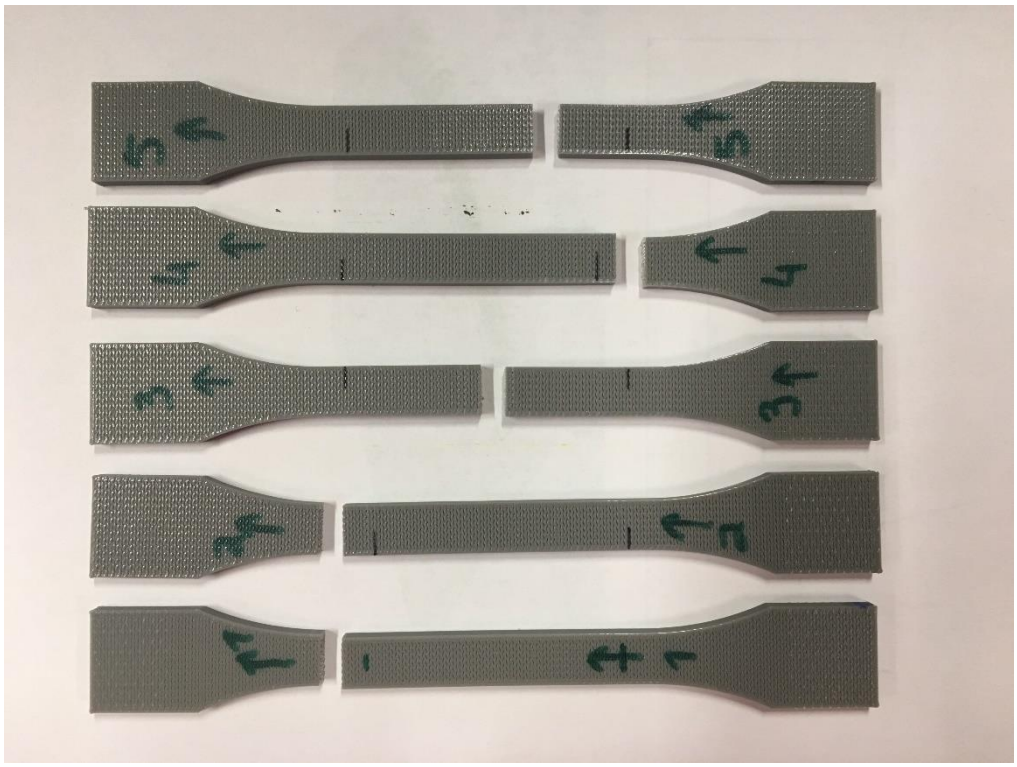

80%

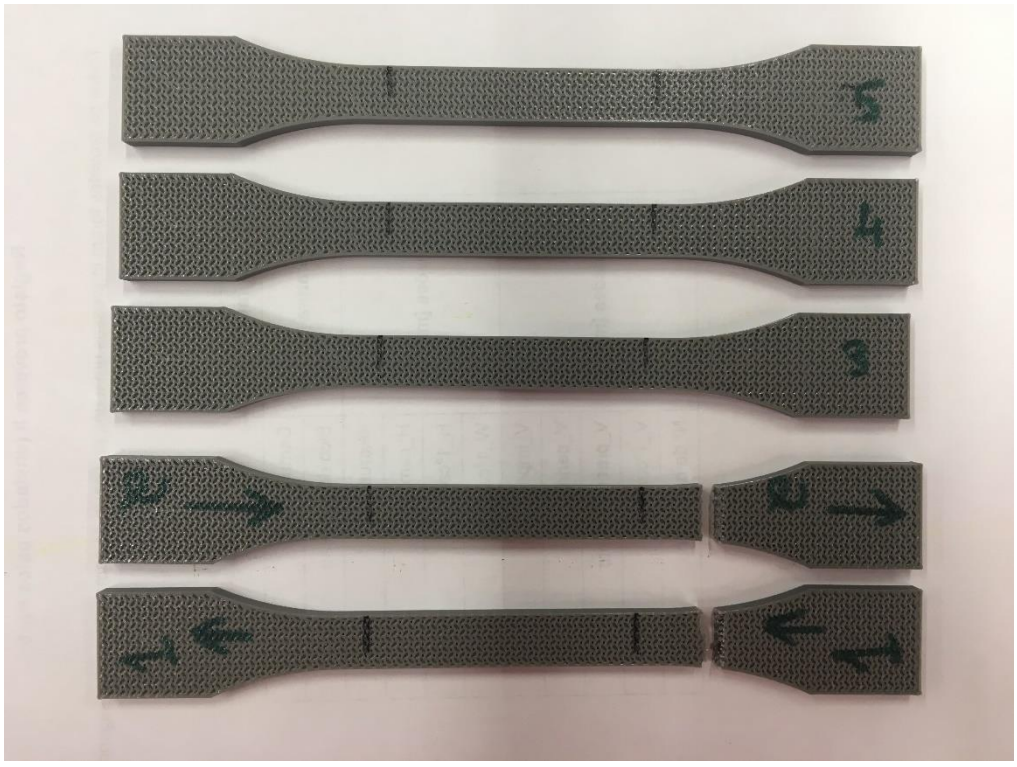

50%

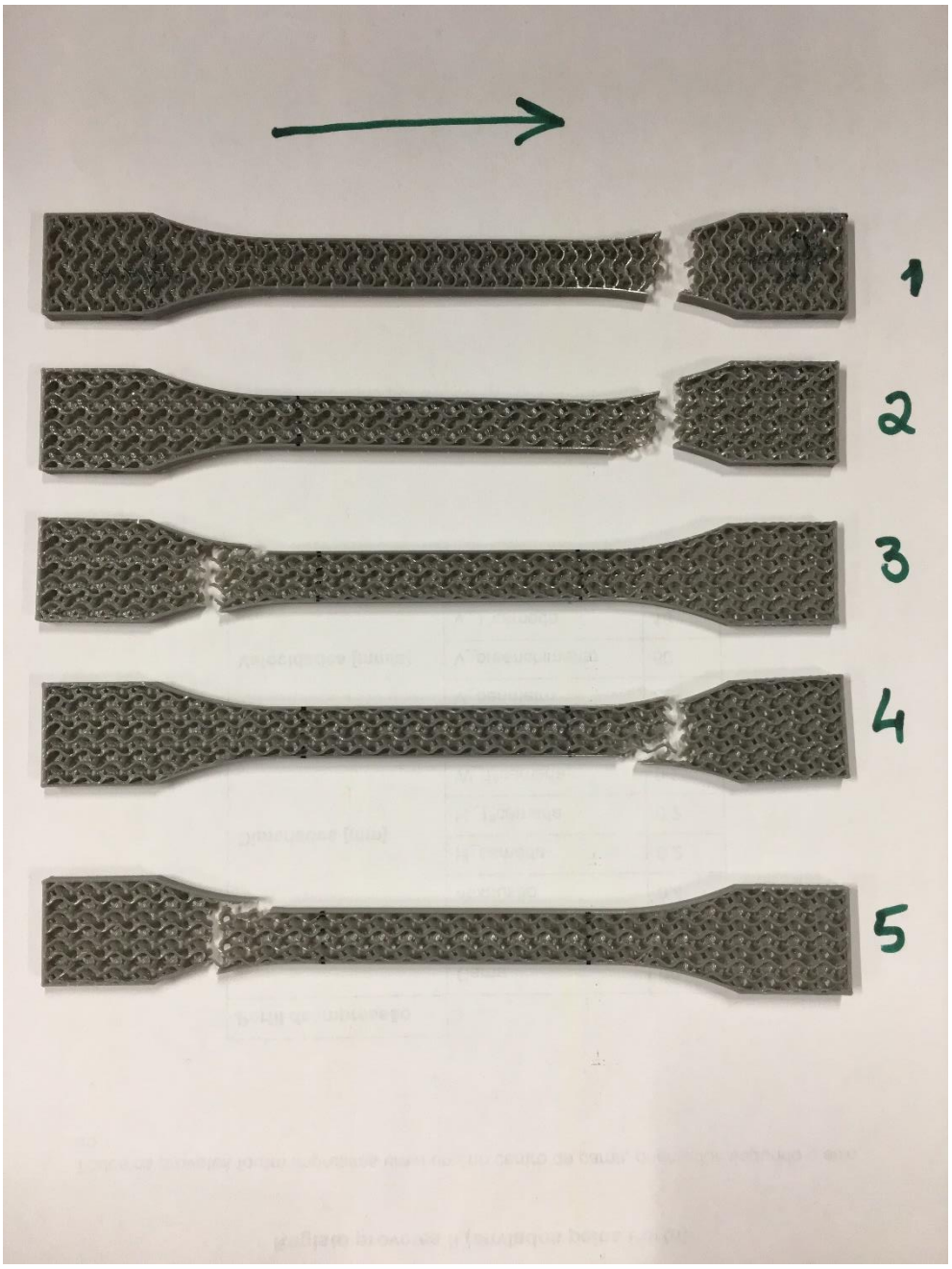

20%

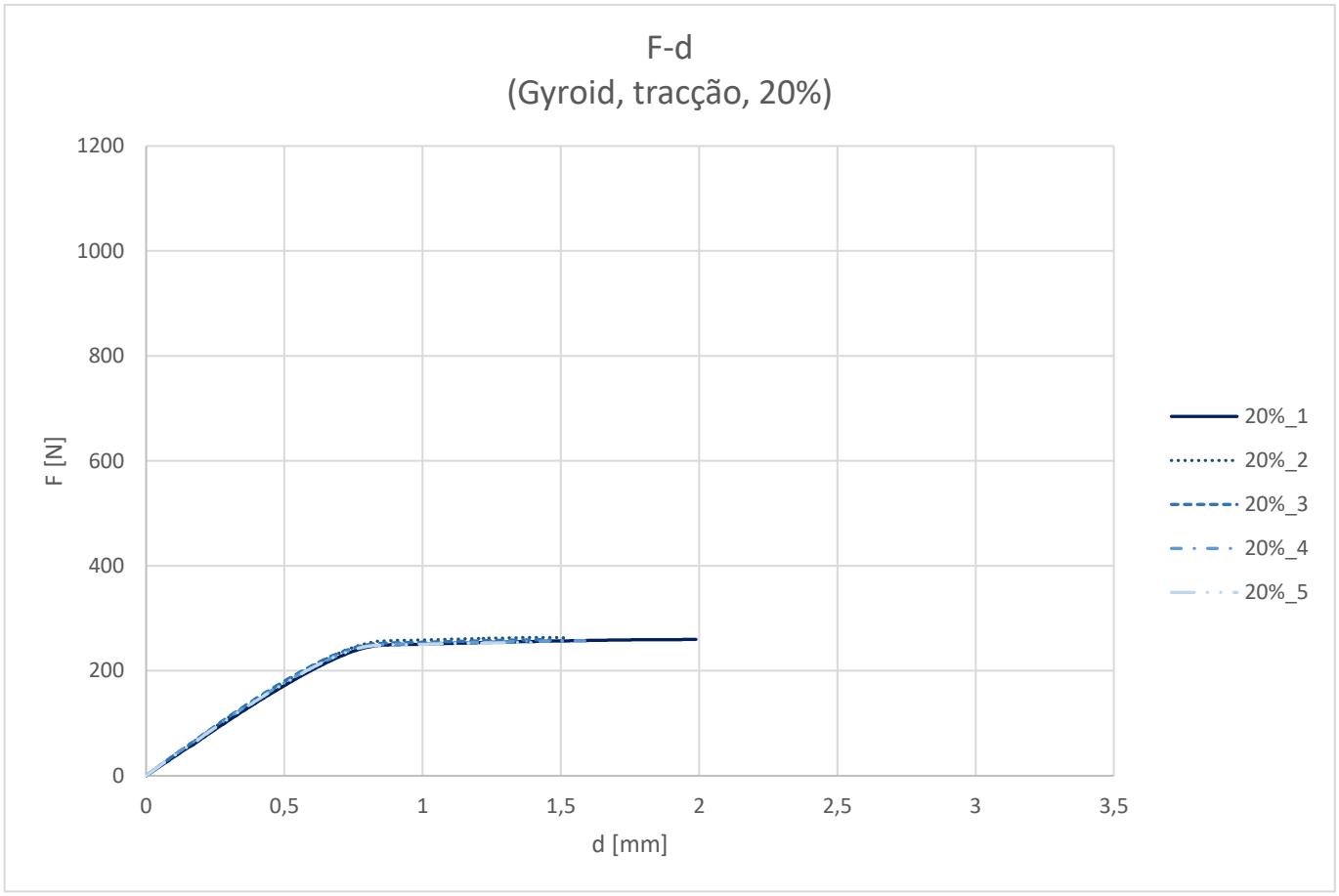
F-d
(Gyroid, tracção, 20%)
1200
1000
800
600
400
200
0
F [N]
0
0,5
1
1,5
2
2,5
3
3,5
d [mm]
20%_1
20%_2
20%_3
20%_4
20%_5

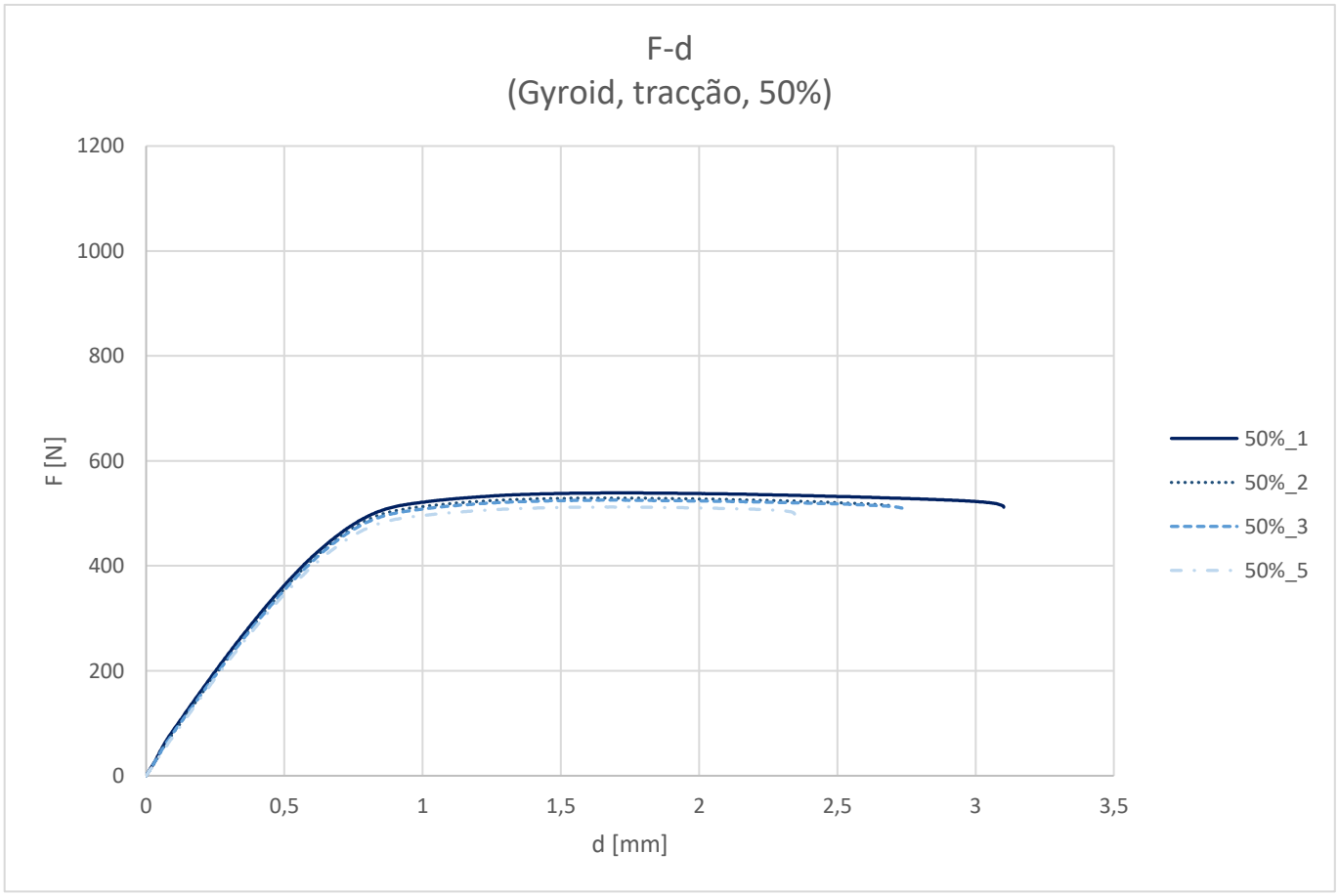
F-d
(Gyroid, tracção, 50%)
1200
1000
800
600
400
200
0
F [N]
0
0,5
1
1,5
2
2,5
3
3,5
d [mm]
50%_1
50%_2
50%_3
50%_5

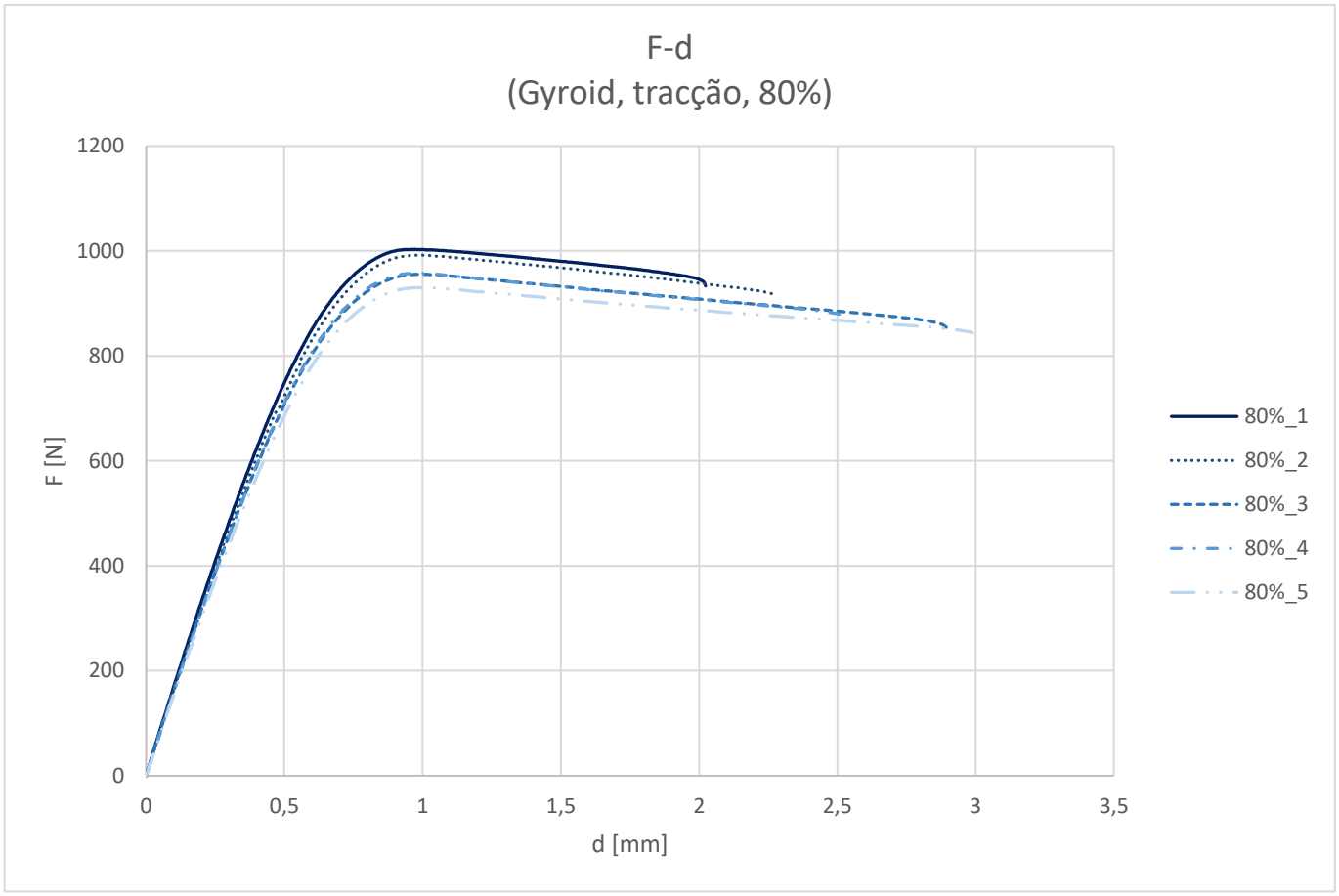
F-d
(Gyroid, tracção, 80%)
F [N]
d [mm]
0
200
400
600
800
1000
1200
0
0,5
1
1,5
2
2,5
3
3,5
80%_1
80%_2
80%_3
80%_4
80%_5

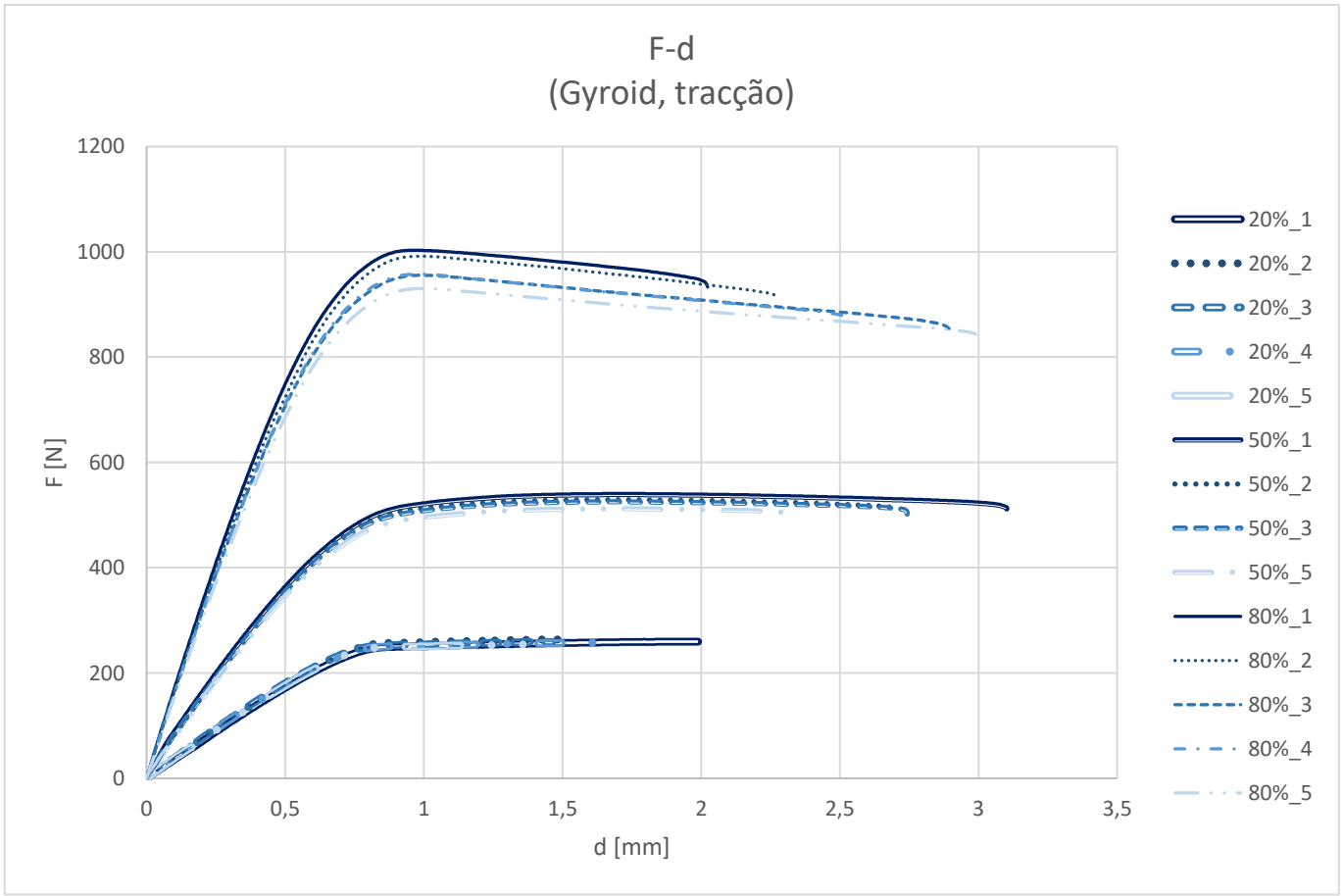
F-d
(Gyroid, tracção)
F [N]
d [mm]
0
200
400
600
800
1000
1200
0
0,5
1
1,5
2
2,5
3
3,5
20%_1
20%_2
20%_3
20%_4
20%_5
50%_1
50%_2
50%_3
50%_5
80%_1
80%_2
80%_3
80%_4
80%_5

Ensaios de flexão – ISO 178

- Provetes com preenchimento gyroid e diferentes percentagens de enchimento

Dimensões do provete : L – 80 mm
w – 10 mm
t – 4 mm

Velocidade do ensaio : v = 1 mm/min

FfM [N]	20%	50%	80%
1	17,21818	36,72878	70,89259
2	17,06649	35,89162	71,14951
3	16,78247	36,2434	70,64494
4	16,21806	35,52877	69,70033
5	16,39189	35,64714	69,91111
med	16,73542	36,00794	70,4597

dfM [mm]	20%	50%	80%
1	7,92521	7,37967	6,47987
2	7,99763	7,27916	6,92956
3	7,21791	7,54619	6,3799
4	6,99526	7,39653	6,47611
5	7,94497	7,29621	6,81291
med	7,616196	7,379552	6,61567

Nota: No caso de provetes com preenchimento gyroid com percentagens de enchimento inferiores a 100%, as dimensões exteriores não podem ser usadas como referência para o cálculo das tensões e extensões nominais. Consequentemente, não é também possível calcular deflecções nem módulos de flexão, sendo então apresentados apenas valores e gráficos força-deslocamento.

Provetes após ensaio:

20% :

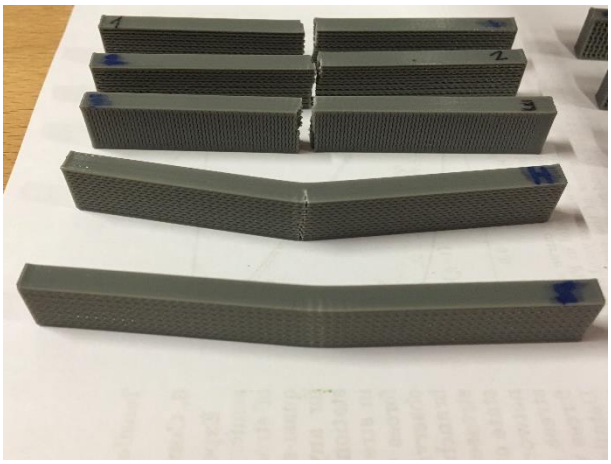

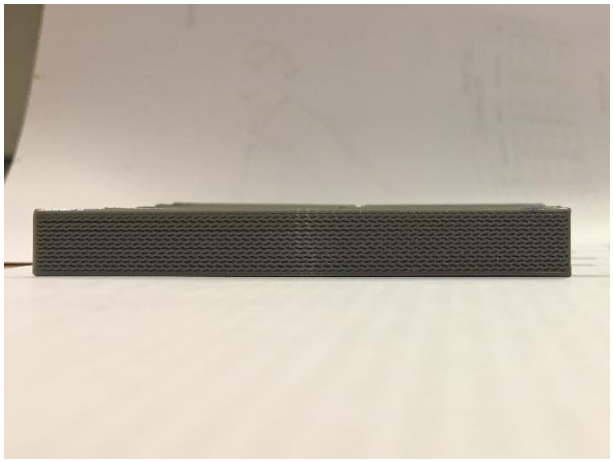

50% :

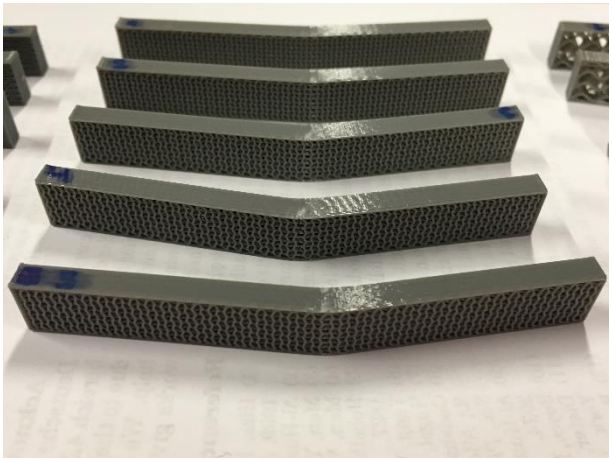

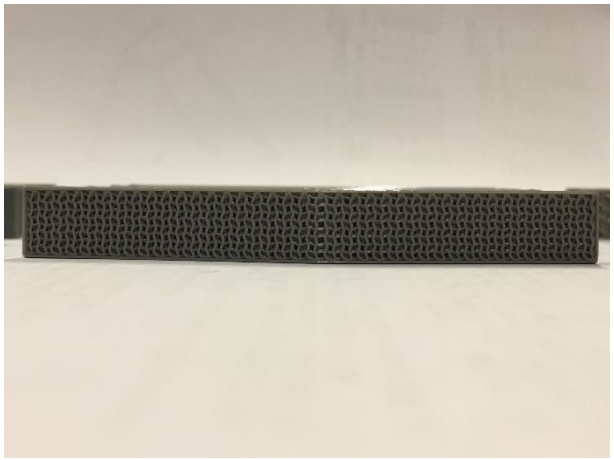

80% :

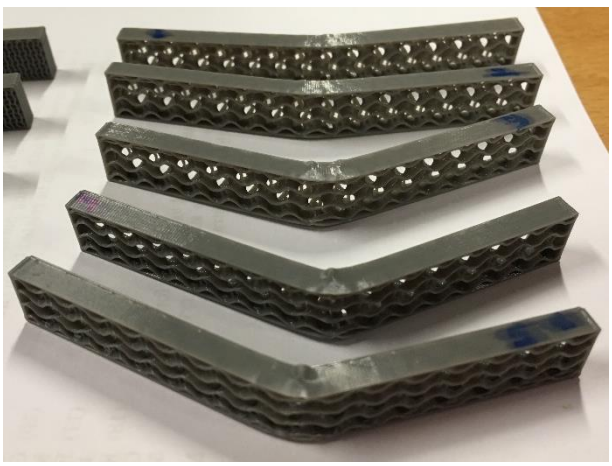

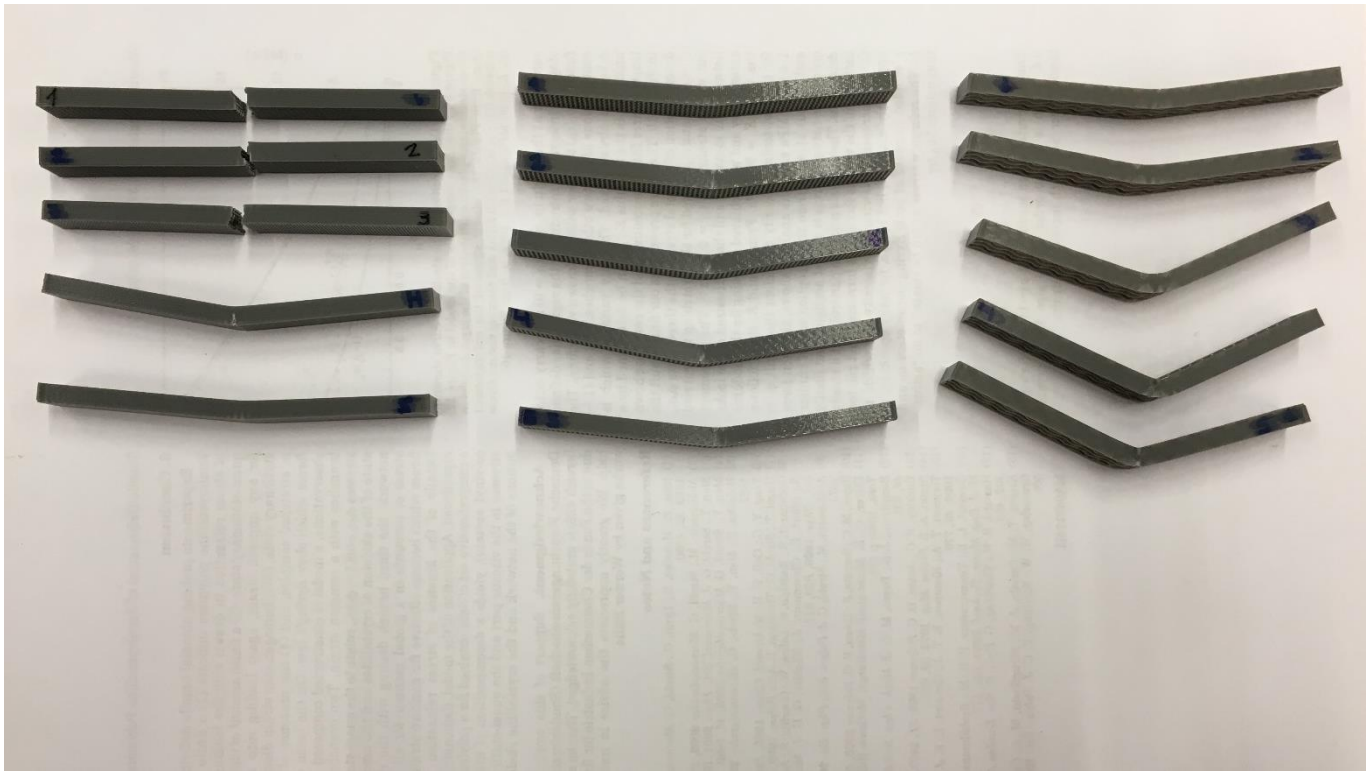

20%

50%

80%

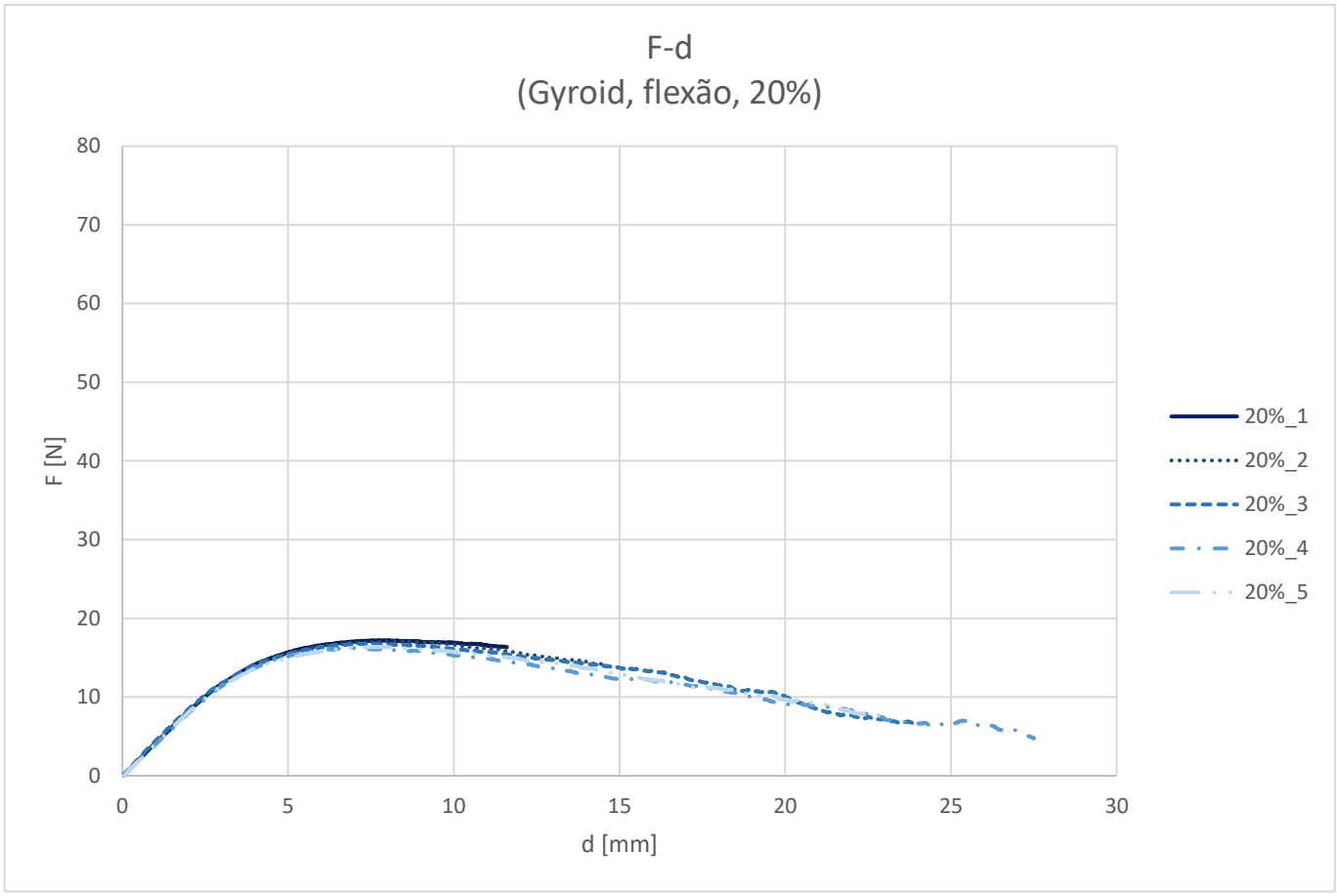
F-d
(Gyroid, flexão, 20%)
F [N]
d [mm]
0
10
20
30
40
50
60
70
80
0
5
10
15
20
25
30
20%_1
20%_2
20%_3
20%_4
20%_5

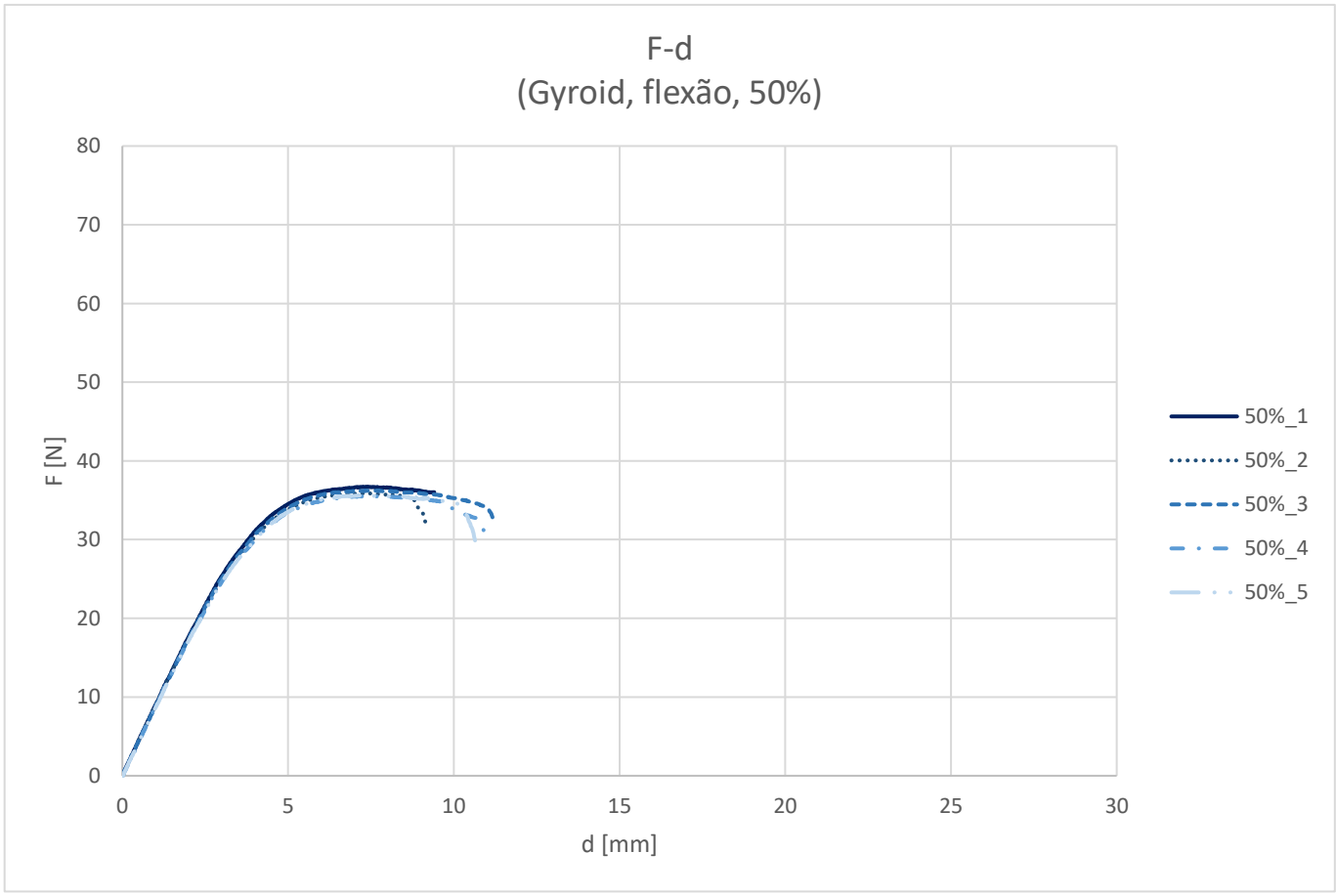
F-d
(Gyroid, flexão, 50%)
F [N]
d [mm]
0
10
20
30
40
50
60
70
80
0
5
10
15
20
25
30
50%_1
50%_2
50%_3
50%_4
50%_5

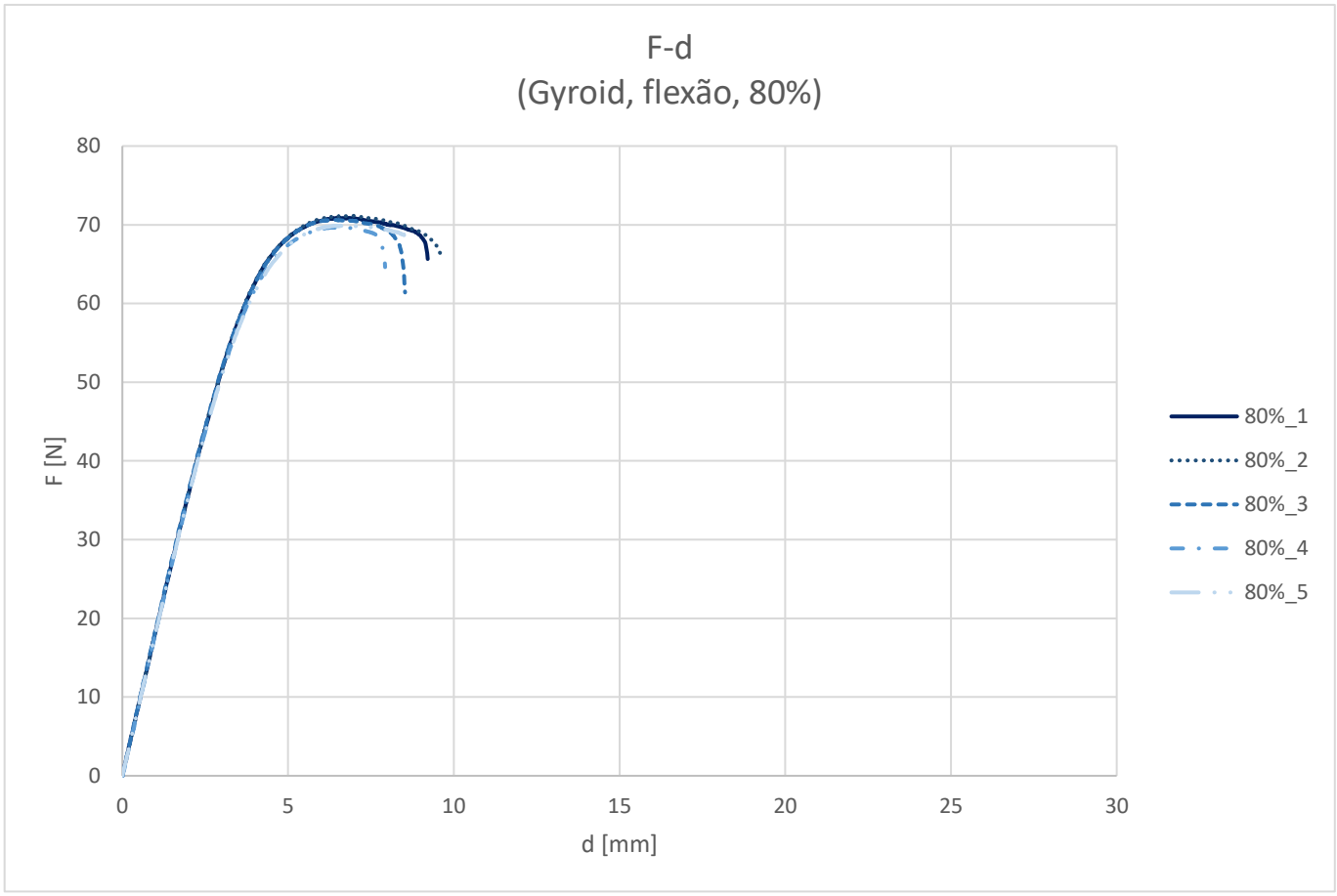
F-d
(Gyroid, flexão, 80%)
F [N]
d [mm]
0
10
20
30
40
50
60
70
80
0
5
10
15
20
25
30
80%_1
80%_2
80%_3
80%_4
80%_5

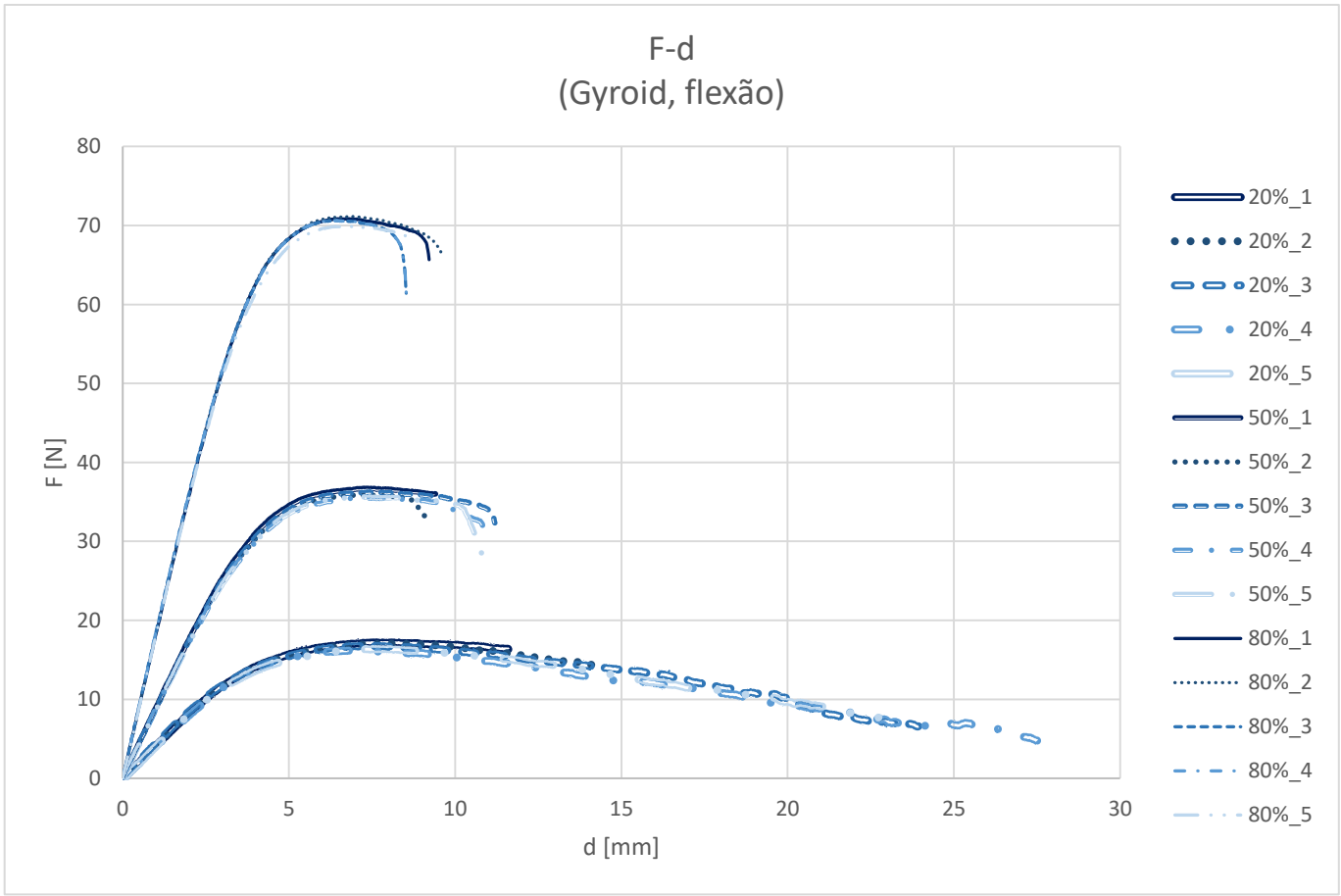
F-d
(Gyroid, flexão)
F [N]
d [mm]
0
10
20
30
40
50
60
70
80
0
5
10
15
20
25
30
20%_1
20%_2
20%_3
20%_4
20%_5
50%_1
50%_2
50%_3
50%_4
50%_5
80%_1
80%_2
80%_3
80%_4
80%_5

Ensaios de compressão

- Provetes baixos com preenchimento gyroid e diferentes percentagens de enchimento

Dimensões do provete : L – 10 mm
w – 10 mm
t – 4 mm

Velocidade do ensaio : 5 mm/min

F_Y [N]	20%	50%	80%
1	437,2669	1129,718	2370,169
2	450,5371	1107,183	2327,393
3	459,1516	1138,603	2344,127
4	460,058	1104,05	2308,863
5	456,4414	1138,667	2354,084
med	452,691	1123,644	2340,927

d_Y [mm]	20%	50%	80%
1	0,70899	0,75892	0,74219
2	0,72553	0,77579	0,62538
3	0,72528	0,99218	0,74191
4	0,74194	0,77582	0,85867
5	0,74244	0,74236	0,60852
med	0,728836	0,809014	0,715334

Nota: No caso de provetes com preenchimento gyroid com percentagens de enchimento inferiores a 100%, as dimensões exteriores não podem ser usadas como referência para o cálculo das tensões e extensões nominais. Assim, são apresentados apenas valores e gráficos força-deslocamento.

Provetes após ensaio:

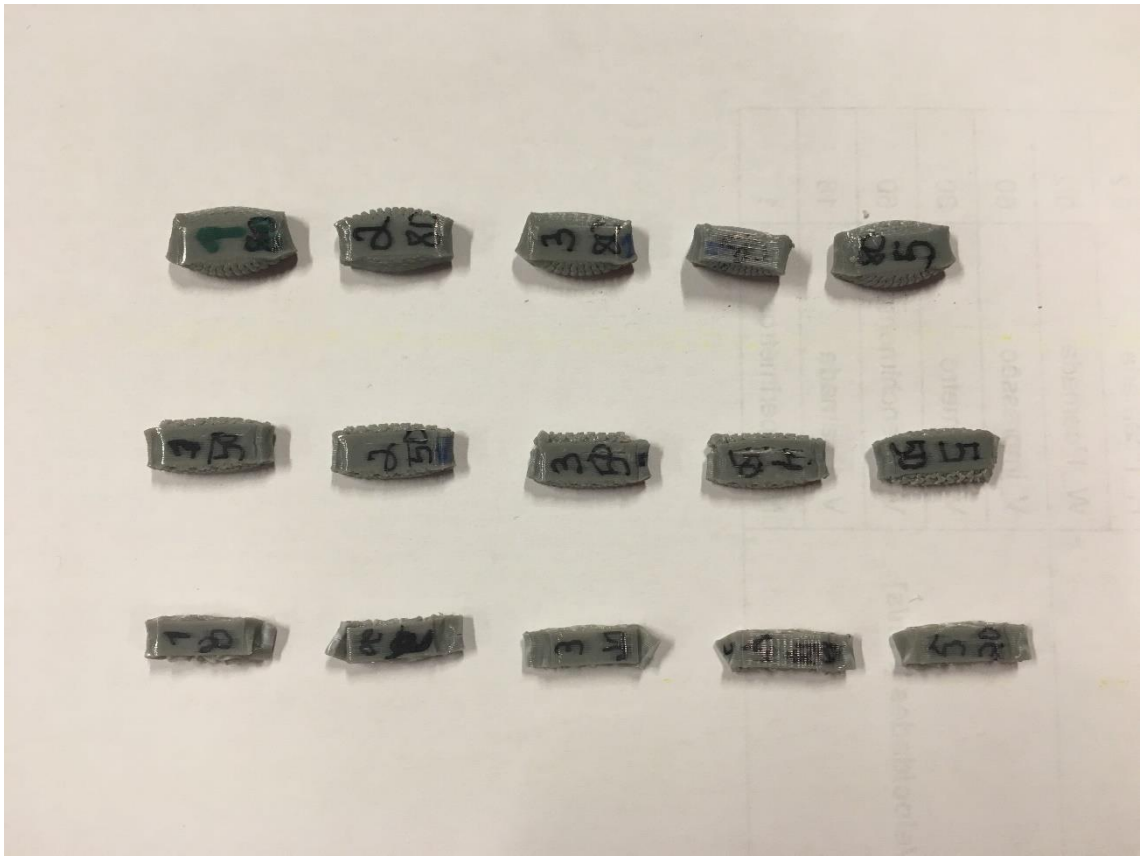

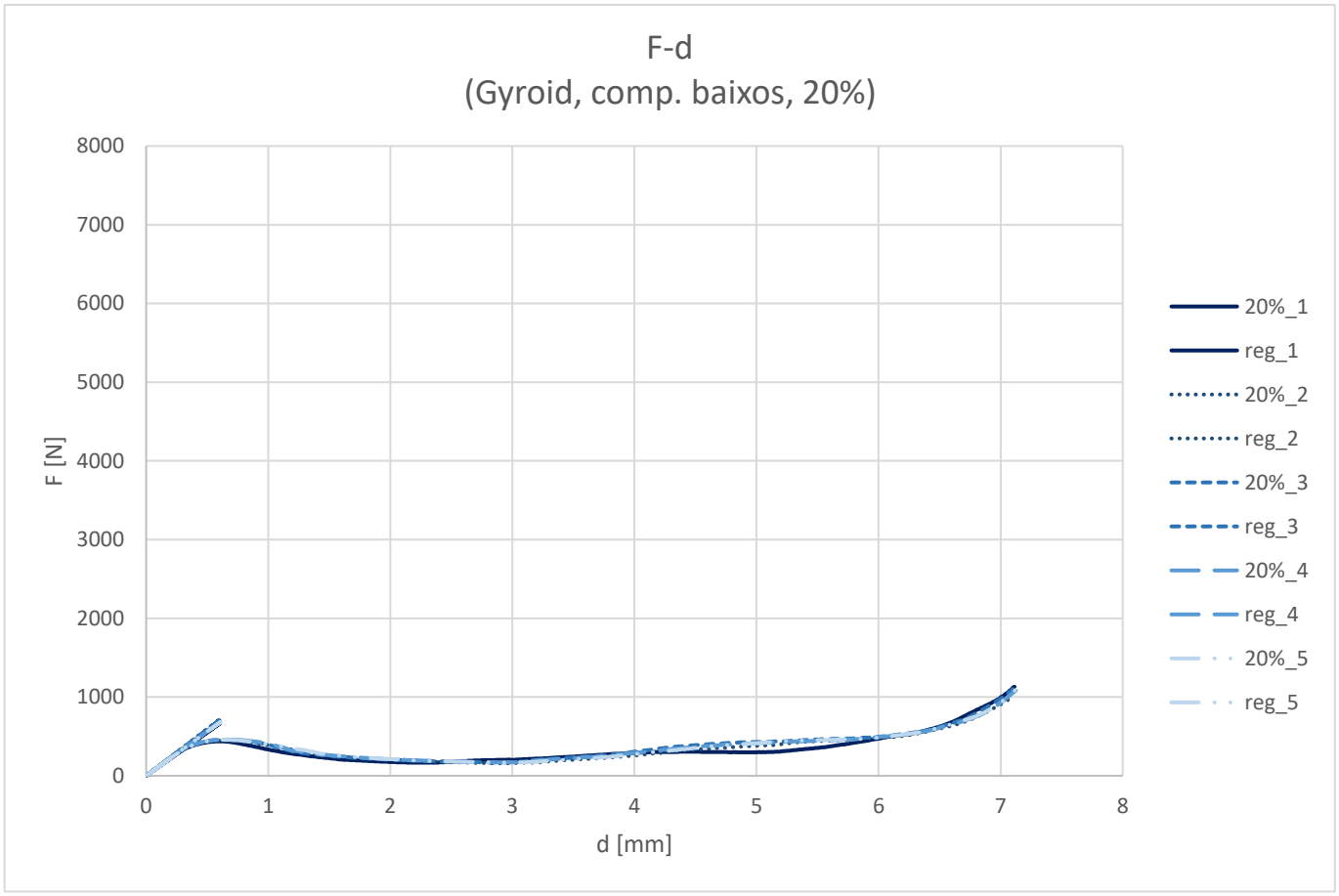
F-d
(Gyroid, comp. baixos, 20%)
F [N]
d [mm]
0
1000
2000
3000
4000
5000
6000
7000
8000
0
1
2
3
4
5
6
7
8
20%_1
reg_1
20%_2
reg_2
20%_3
reg_3
20%_4
reg_4
20%_5
reg_5

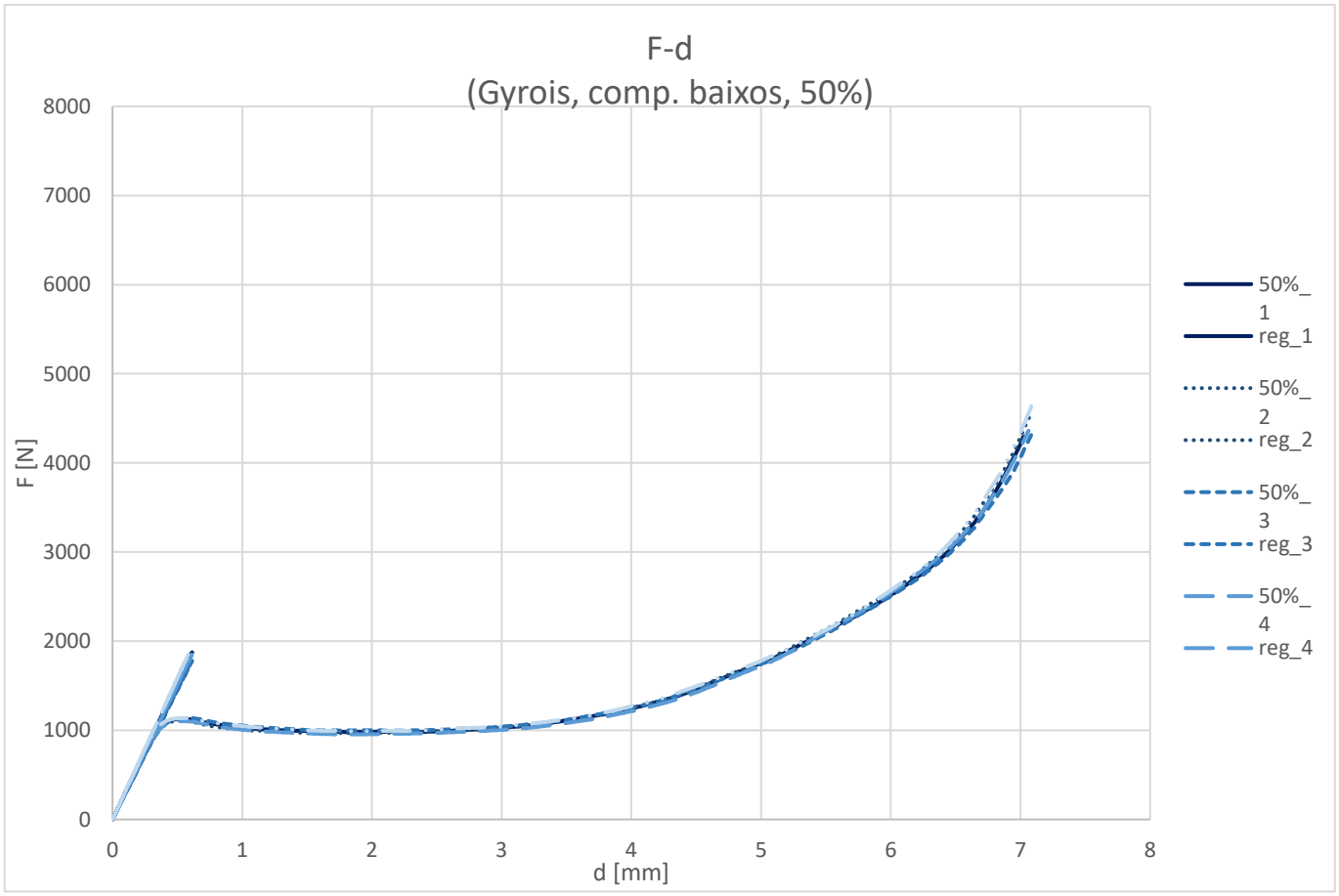
F-d
(Gyrois, comp. baixos, 50%)
F [N]
d [mm]
0
1000
2000
3000
4000
5000
6000
7000
8000
0
1
2
3
4
5
6
7
8
50%_1
reg_1
50%_2
reg_2
50%_3
reg_3
50%_4
reg_4

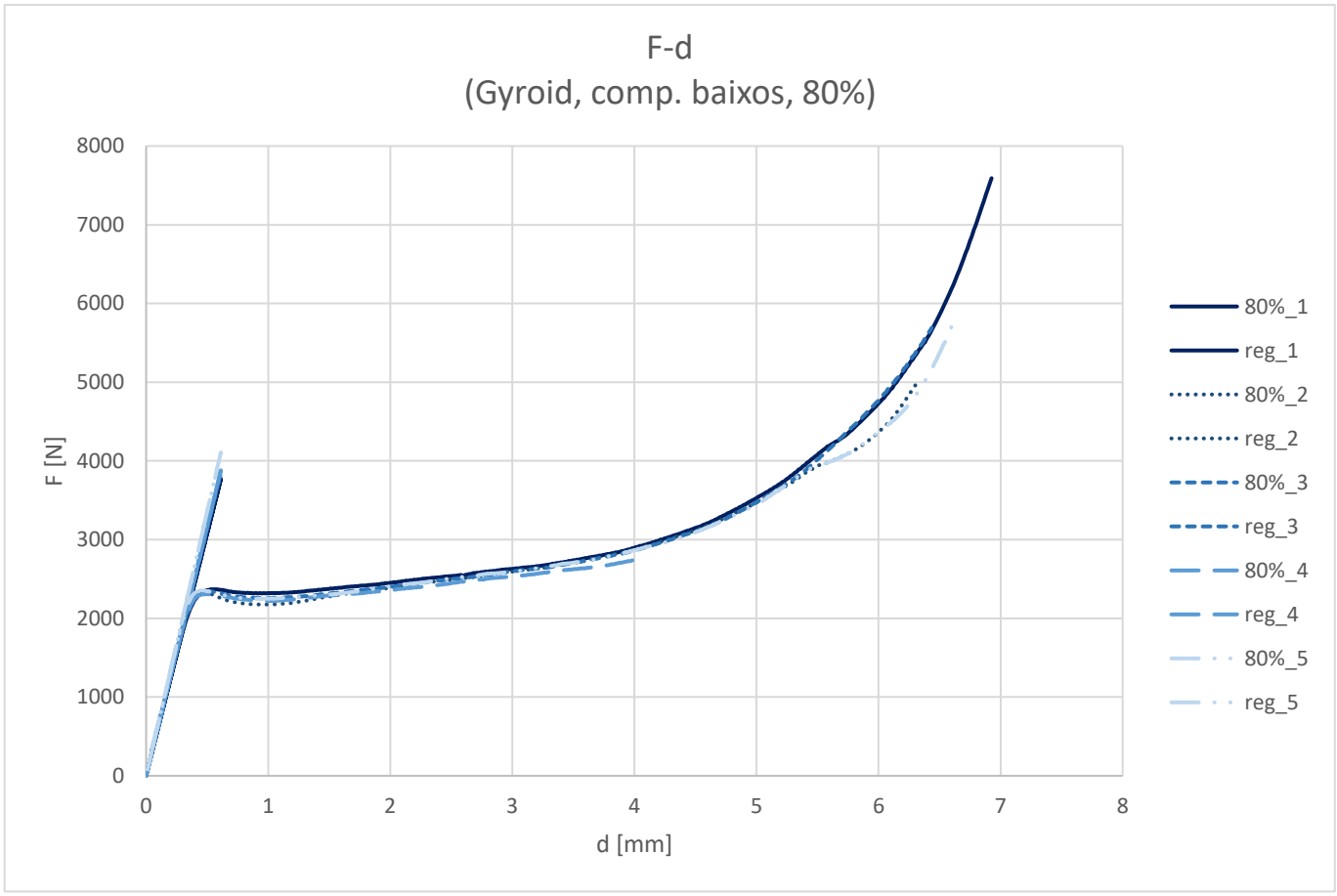
F-d
(Gyroid, comp. baixos, 80%)
F [N]
d [mm]
0
1000
2000
3000
4000
5000
6000
7000
8000
0
1
2
3
4
5
6
7
8
80%_1
reg_1
80%_2
reg_2
80%_3
reg_3
80%_4
reg_4
80%_5
reg_5

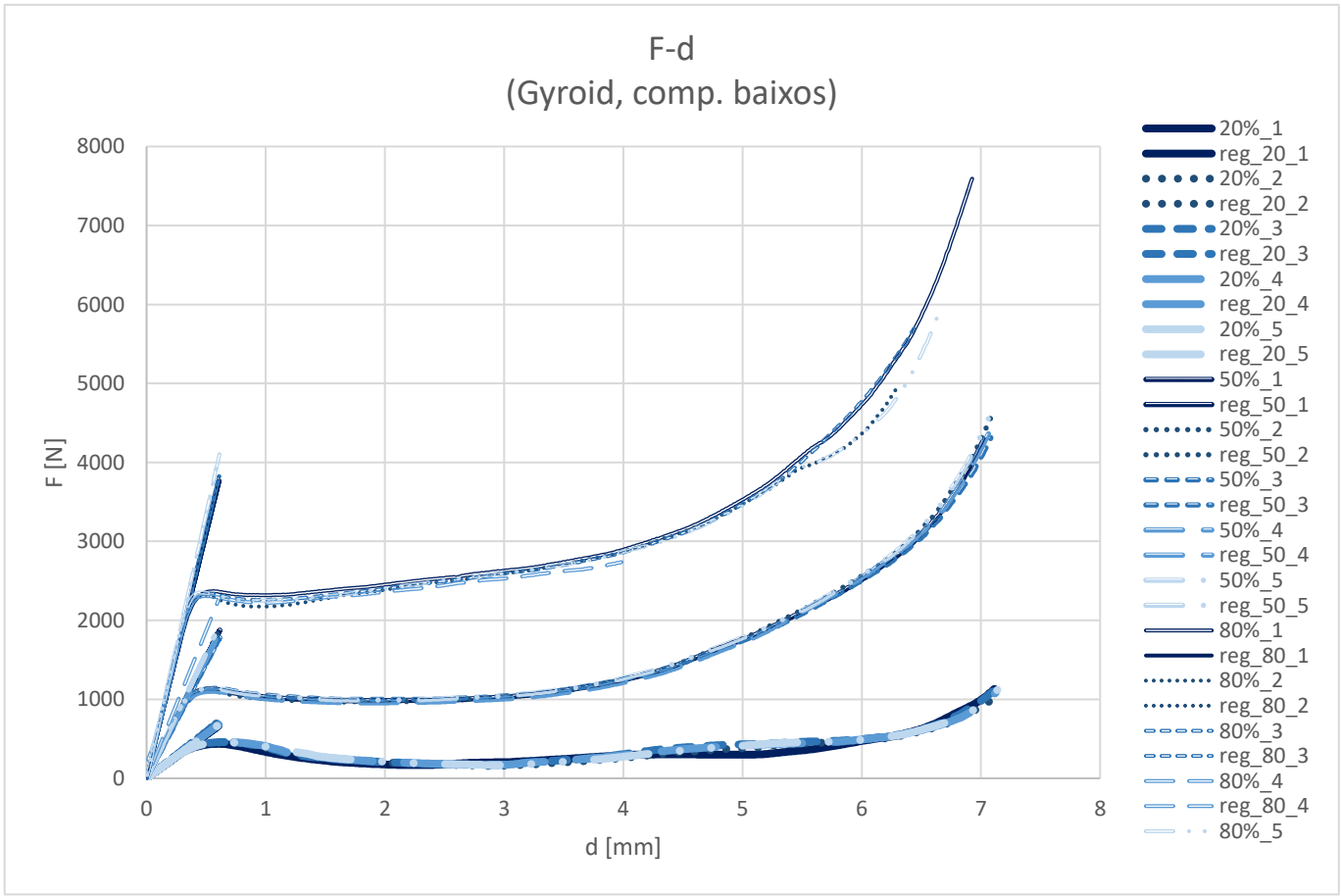
F-d
(Gyroid, comp. baixos)
F [N]
d [mm]
0
1000
2000
3000
4000
5000
6000
7000
8000
0
1
2
3
4
5
6
7
8
20%_1
reg_20_1
20%_2
reg_20_2
20%_3
reg_20_3
20%_4
reg_20_4
20%_5
reg_20_5
50%_1
reg_50_1
50%_2
reg_50_2
50%_3
reg_50_3
50%_4
reg_50_4
50%_5
reg_50_5
80%_1
reg_80_1
80%_2
reg_80_2
80%_3
reg_80_3
80%_4
reg_80_4
80%_5

Ensaios de compressão – ISO 604

- Provetes altos com preenchimento gyroid e diferentes percentagens de enchimento

Dimensões do provete : $\mathrm{L} - 50\ \mathrm{mm}$
$\mathrm{w} - 10\ \mathrm{mm}$
$\mathrm{t} - 4\ \mathrm{mm}$

Velocidade do ensaio : $1\ \mathrm{mm/min}$

Nota: Os provetes de compressão altos destinam-se exclusivamente ao cálculo do módulo de elasticidade, sendo as restantes propriedades determinadas com recurso aos provetes de compressão baixos. No caso de provetes com preenchimento gyroid com percentagens de enchimento inferiores a 100%, as dimensões exteriores não podem ser usadas como referência para o cálculo das tensões e extensões nominais. Consequentemente, também não é possível determinar o módulo de elasticidade e, assim, são apresentados apenas os gráficos força-deslocamento.

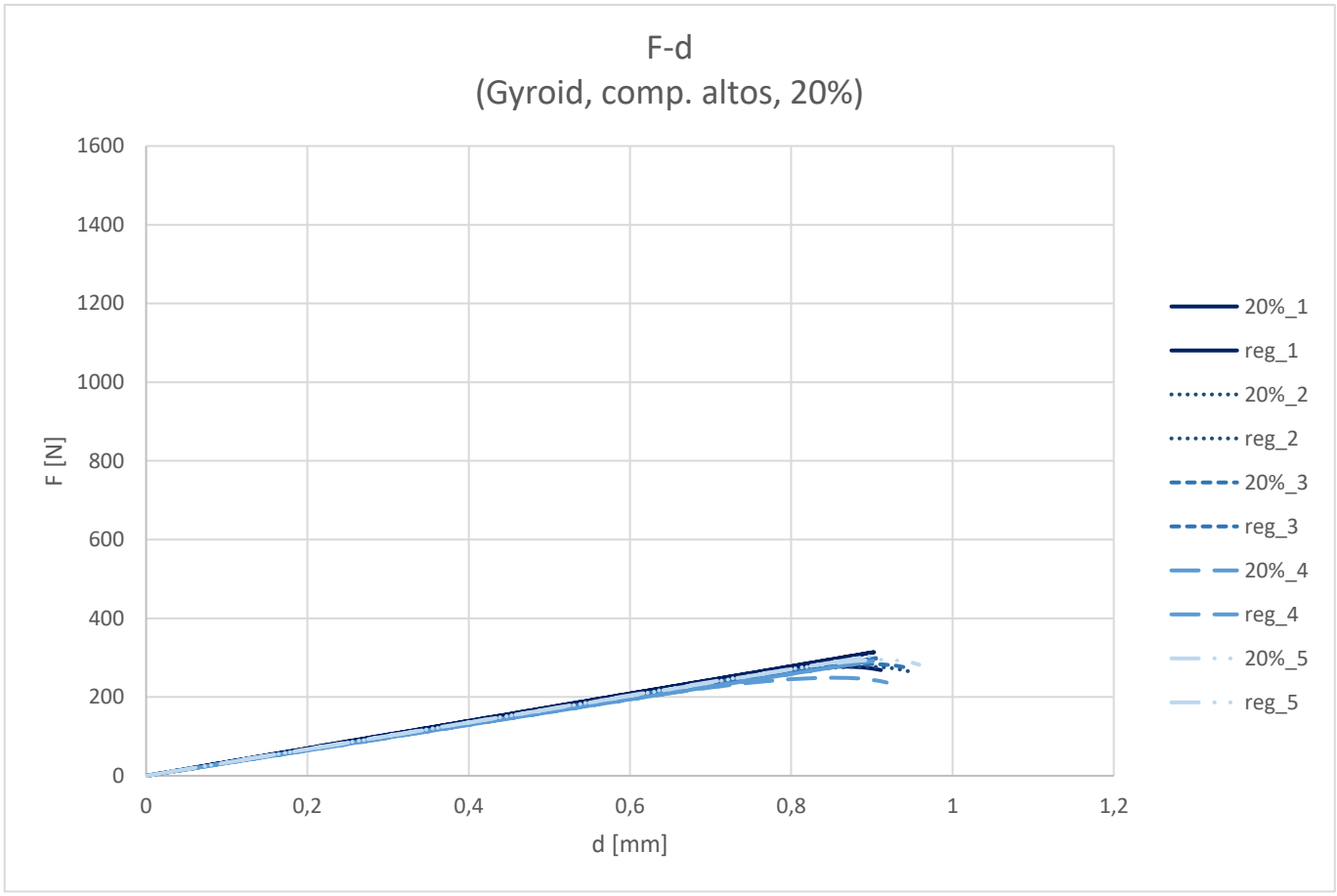
F-d
(Gyroid, comp. altos, 20%)
F [N]
1600
1400
1200
1000
800
600
400
200
0
0
0,2
0,4
0,6
0,8
1
1,2
d [mm]
20%_1
reg_1
20%_2
reg_2
20%_3
reg_3
20%_4
reg_4
20%_5
reg_5

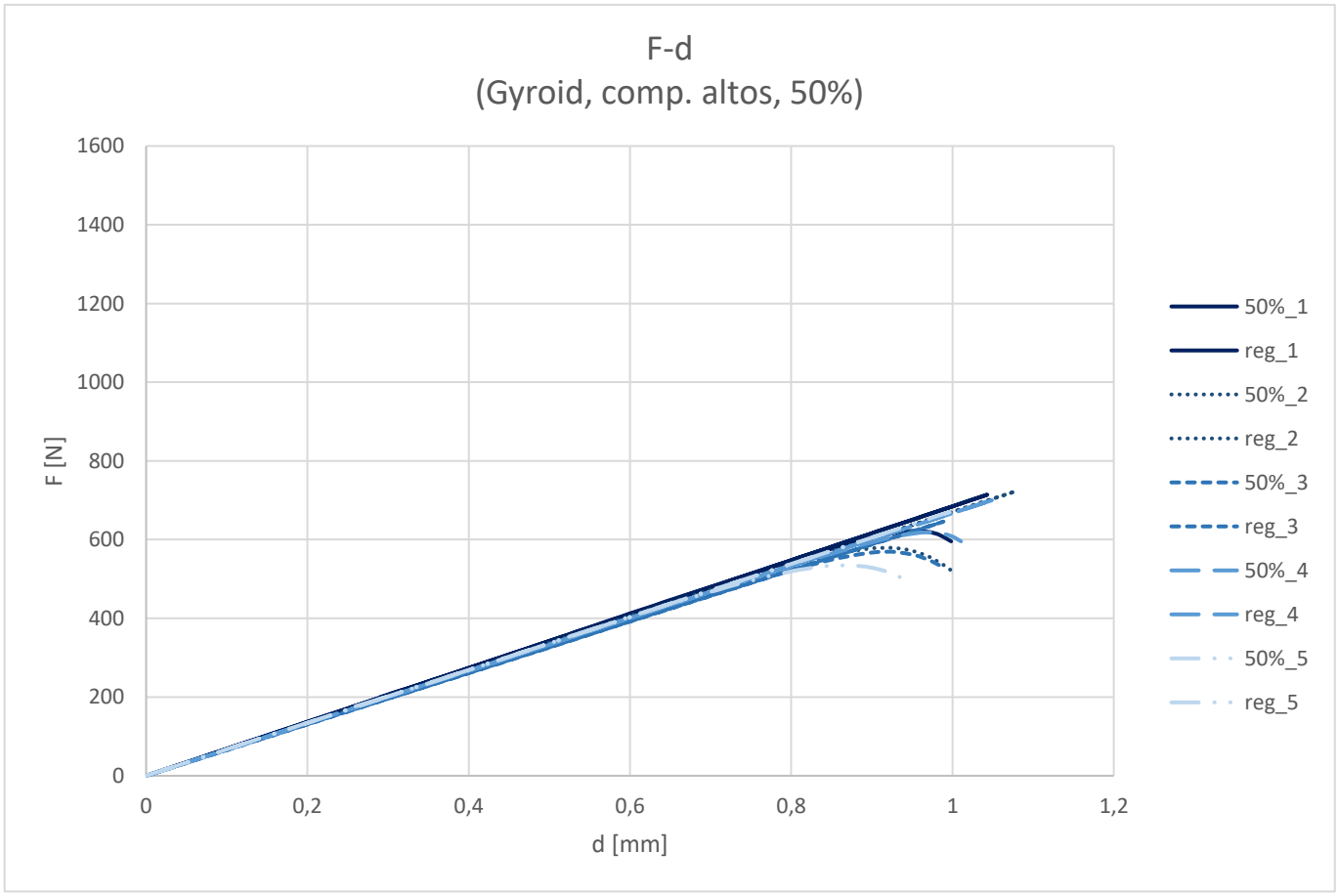
F-d
(Gyroid, comp. altos, 50%)
F [N]
1600
1400
1200
1000
800
600
400
200
0
0
0,2
0,4
0,6
0,8
1
1,2
d [mm]
50%_1
reg_1
50%_2
reg_2
50%_3
reg_3
50%_4
reg_4
50%_5
reg_5

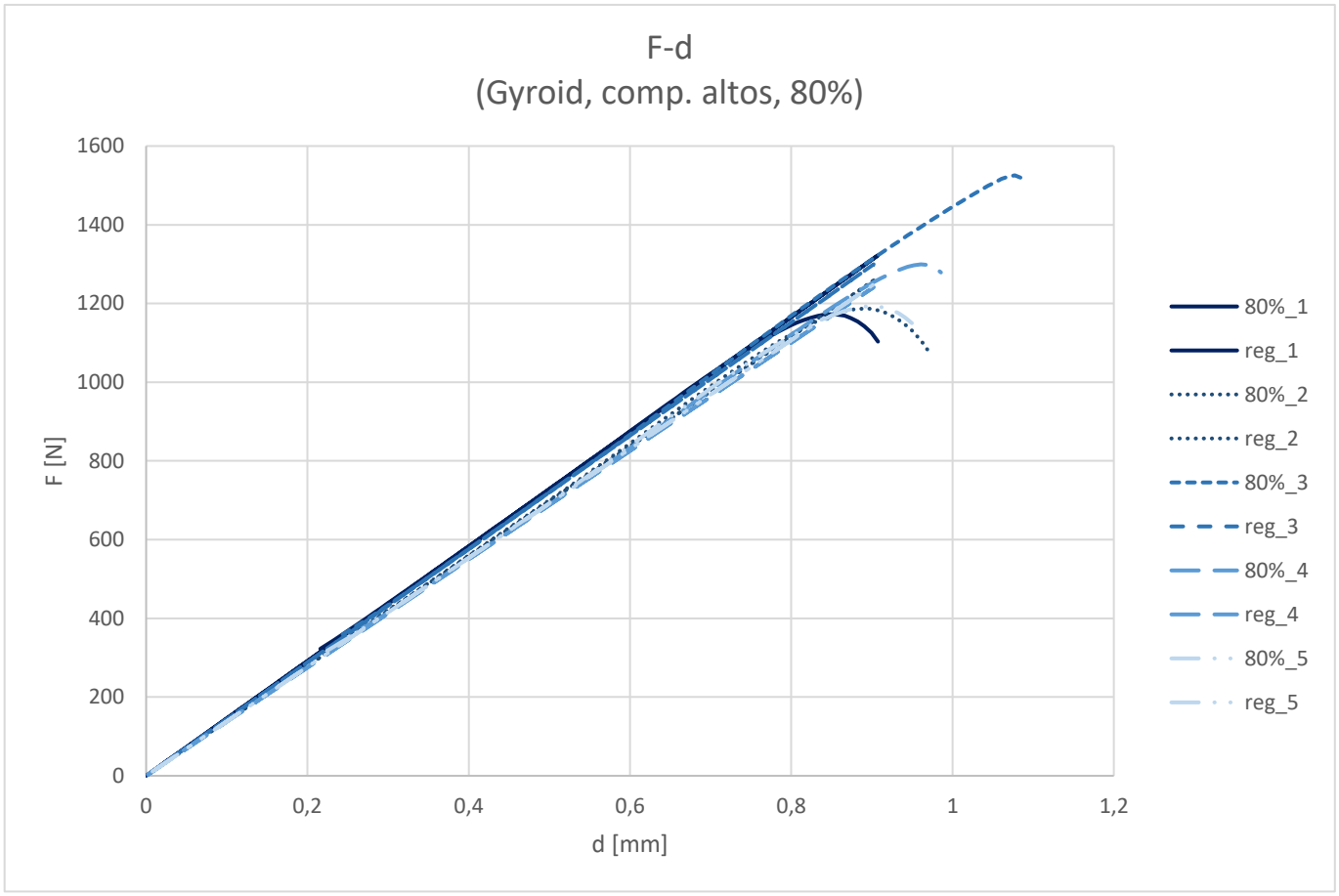
F-d
(Gyroid, comp. altos, 80%)
F [N]
d [mm]
0
200
400
600
800
1000
1200
1400
1600
0
0,2
0,4
0,6
0,8
1
1,2
80%_1
reg_1
80%_2
reg_2
80%_3
reg_3
80%_4
reg_4
80%_5
reg_5

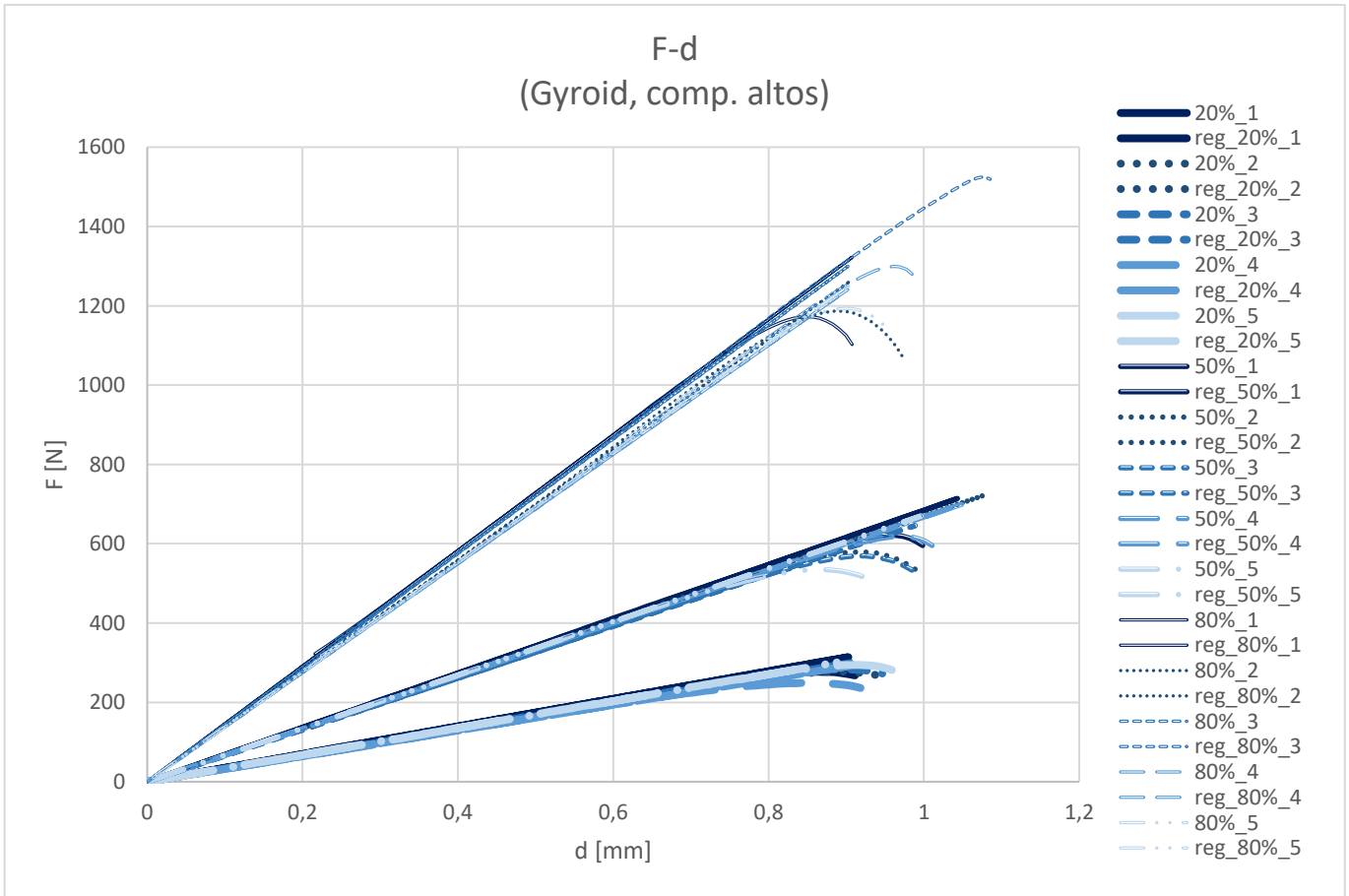
F-d
(Gyroid, comp. altos)
F [N]
d [mm]
0
200
400
600
800
1000
1200
1400
1600
0
0,2
0,4
0,6
0,8
1
1,2
20%_1
reg_20%_1
20%_2
reg_20%_2
20%_3
reg_20%_3
20%_4
reg_20%_4
20%_5
reg_20%_5
50%_1
reg_50%_1
50%_2
reg_50%_2
50%_3
reg_50%_3
50%_4
reg_50%_4
50%_5
reg_50%_5
80%_1
reg_80%_1
80%_2
reg_80%_2
80%_3
reg_80%_3
80%_4
reg_80%_4
80%_5
reg_80%_5

Appendix C

Results obtained on the study about the gyroid structure

Ensaios de tracção – ISO 527

- Provetes impressos com através de *Polyjet*

Dimensões do provete : L – 150 mm
L0 – 60 mm
w – 10 mm
t – 4 mm

Velocidade do ensaio : $1\ \mathrm{mm/min}$

	σ_m
1	50,83818
2	51,24484
3	48,76912
med	50,28405

	ε_m
1	0,131088
2	0,120001
3	0,161404
med	0,137498

	σ_y
1	50,83818
2	51,24484
3	48,76912
med	50,28405

	ε_y
1	0,036936
2	0,037766
3	0,037548
med	0,037416

	σ_b
1	36,12817
2	37,22071
3	34,69881
med	36,0159

	ε_b
1	0,131088
2	0,120001
3	0,161404
med	0,137498

	E
1	2617,9
2	2590,3
3	2503,7
med	2570,633

	ν
1	0,4458
2	0,4711
3	0,4628
med	0,4599

Provetes após ensaio:

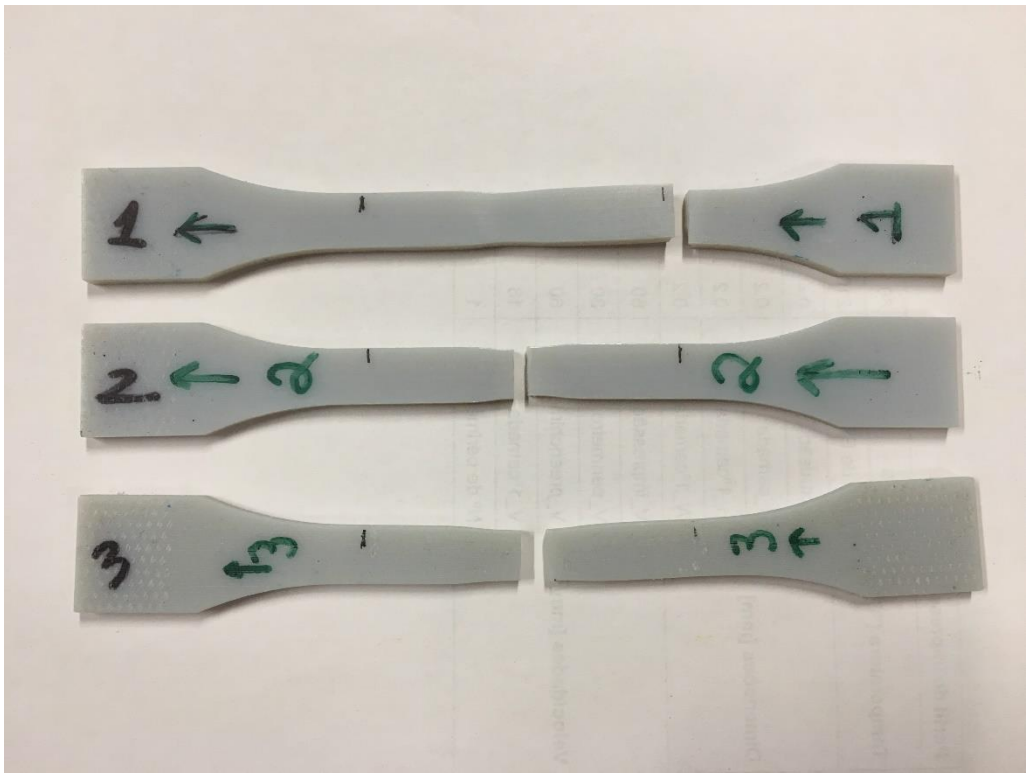

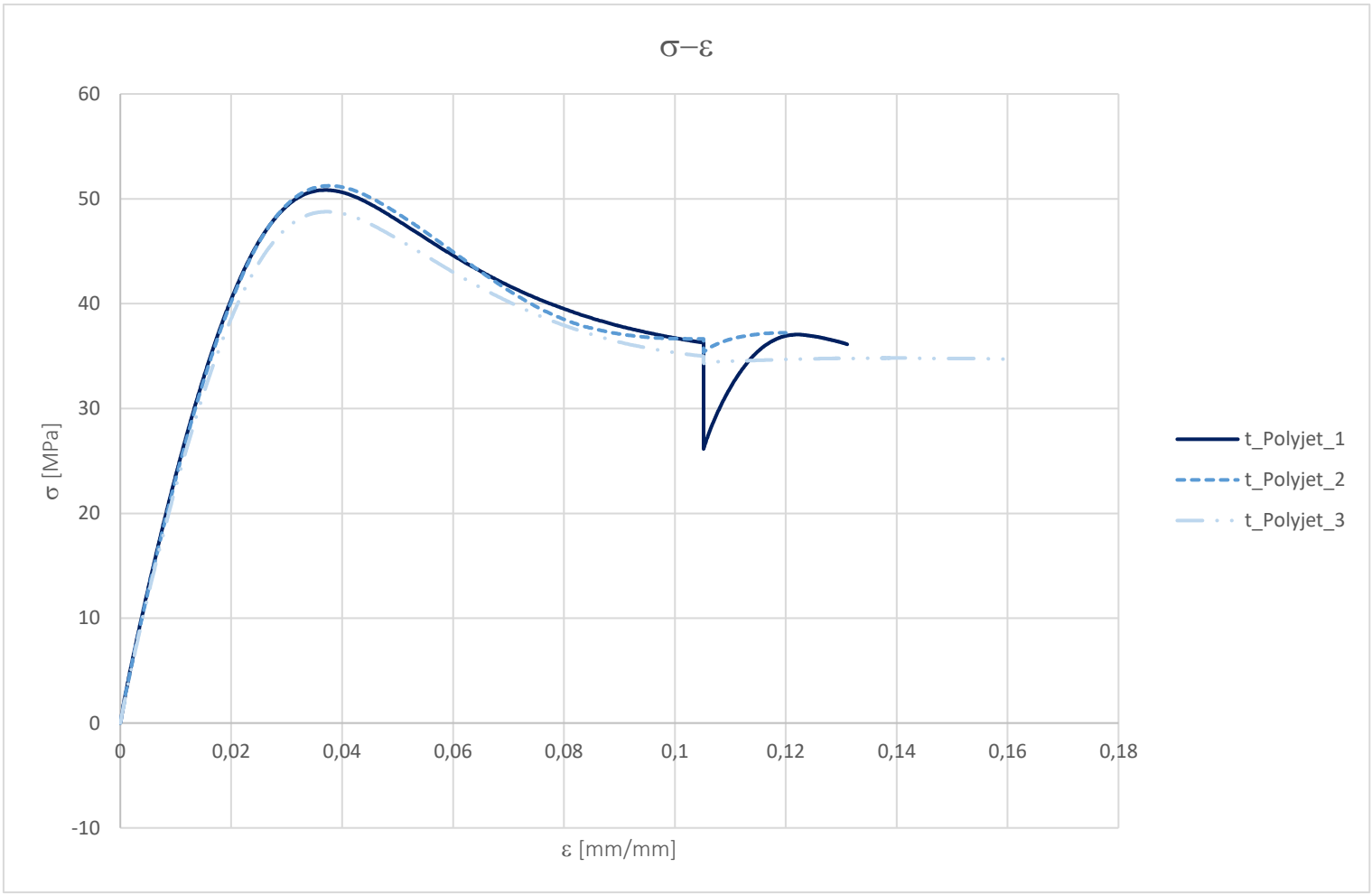
σ–ε
60
50
40
30
20
10
0
-10
σ [MPa]
0
0,02
0,04
0,06
0,08
0,1
0,12
0,14
0,16
0,18
ε [mm/mm]
t_Polyjet_1
t_Polyjet_2
t_Polyjet_3

Ensaios de compressão

- Provetes com geometria Gyroid

- **Provetes obtidos através de FDM**

Dimensões do provete : $20\text{mm} \times 20\text{mm} \times 20\text{mm}$

Velocidade do ensaio : $5\ \text{mm/min}$

Numeração dos provetes ensaiados :

	aa	bb	cc
1	4	7	1
2	5	8	2
3	6	9	3

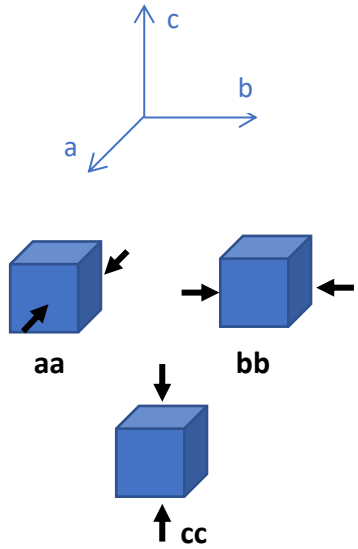

F_y [N]	aa	bb	cc
1	1642,255	1660,56	1517,54
2	1623,111	1407,027	1647,511
3	1580,627	1540,806	1526,521
med	1615,331	1536,131	1563,857

d_y [mm]	aa	bb	cc
1	1,150328	0,849781	1,318773
2	1,008336	0,844426	1,213159
3	0,943582	0,763435	1,193528
med	1,034082	0,819214	1,24182

Provetes após ensaio:

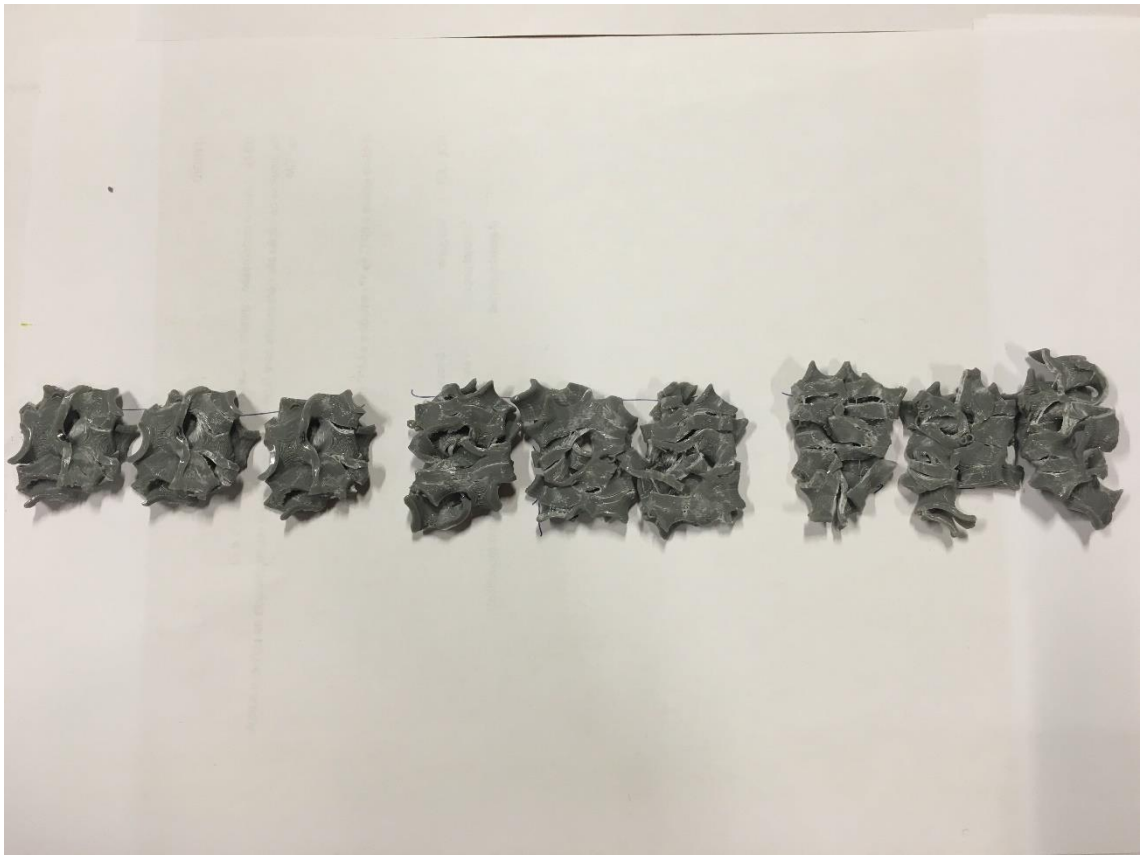

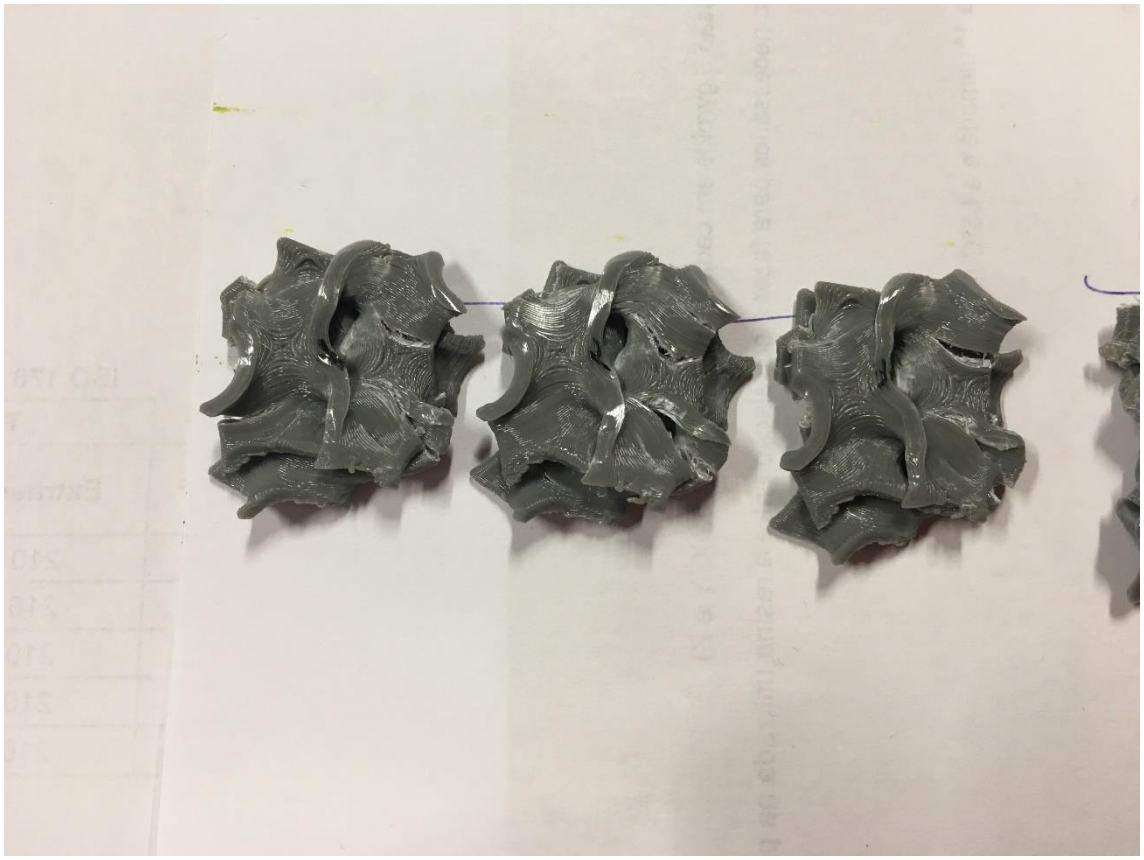

direcção cc

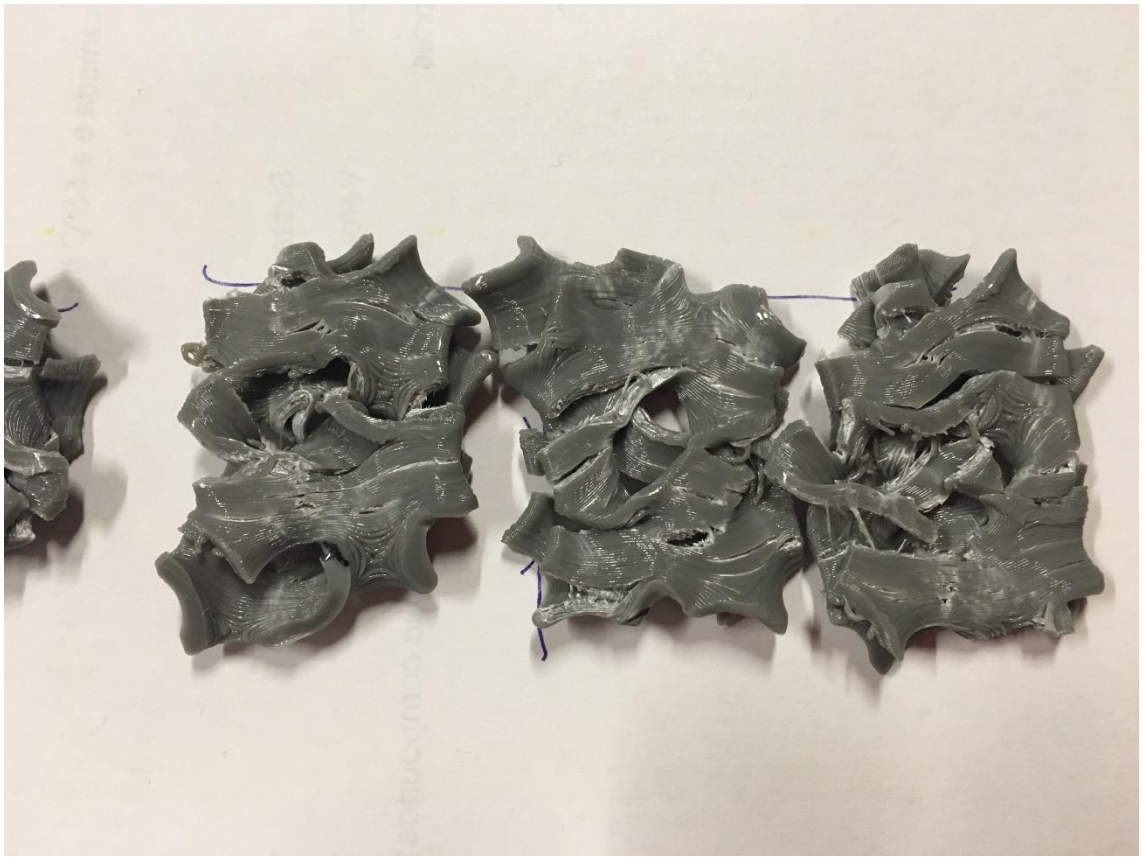

direcção aa

direcção bb

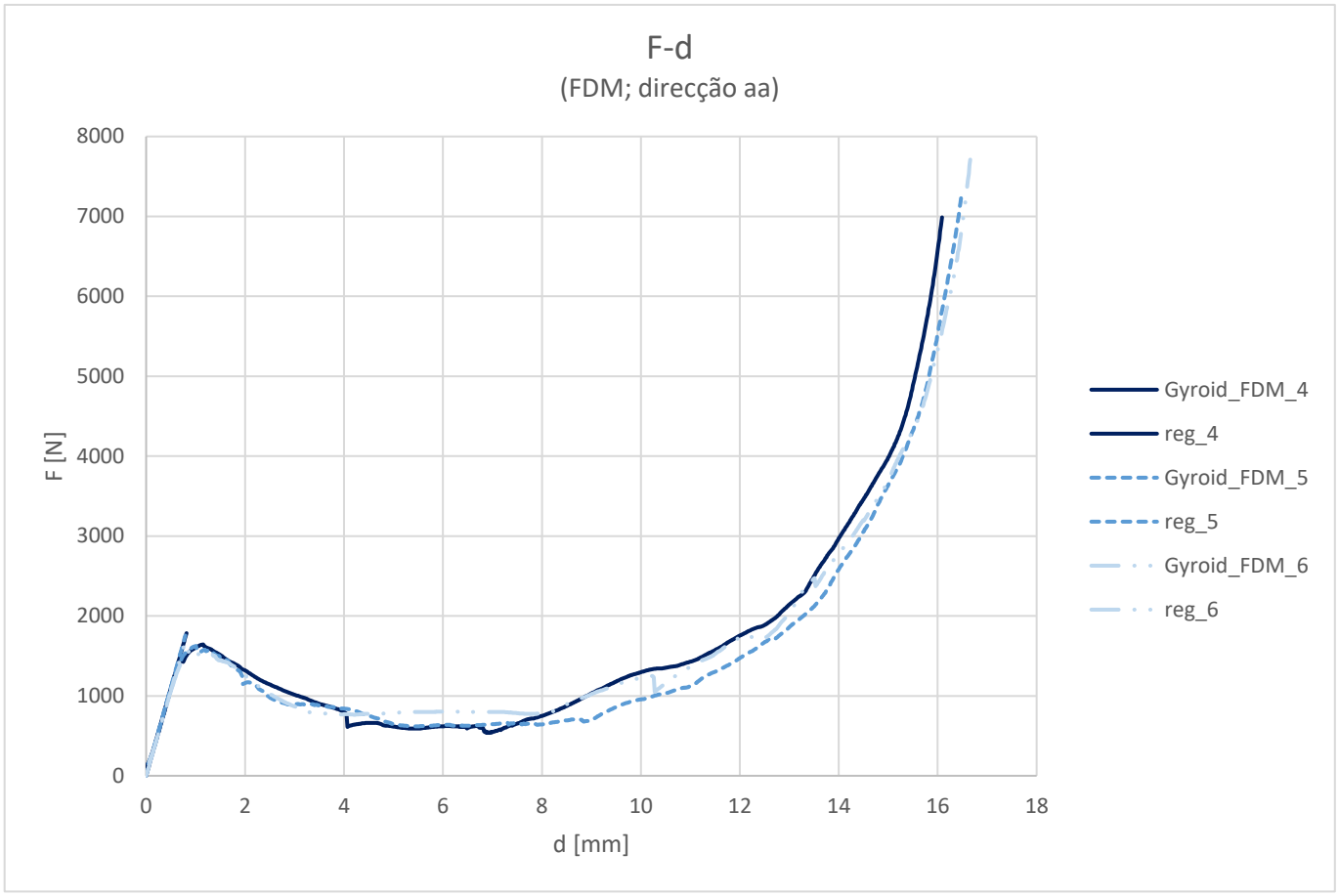
F-d
(FDM; direcção aa)
F [N]
d [mm]
0
1000
2000
3000
4000
5000
6000
7000
8000
0
2
4
6
8
10
12
14
16
18
Gyroid_FDM_4
reg_4
Gyroid_FDM_5
reg_5
Gyroid_FDM_6
reg_6

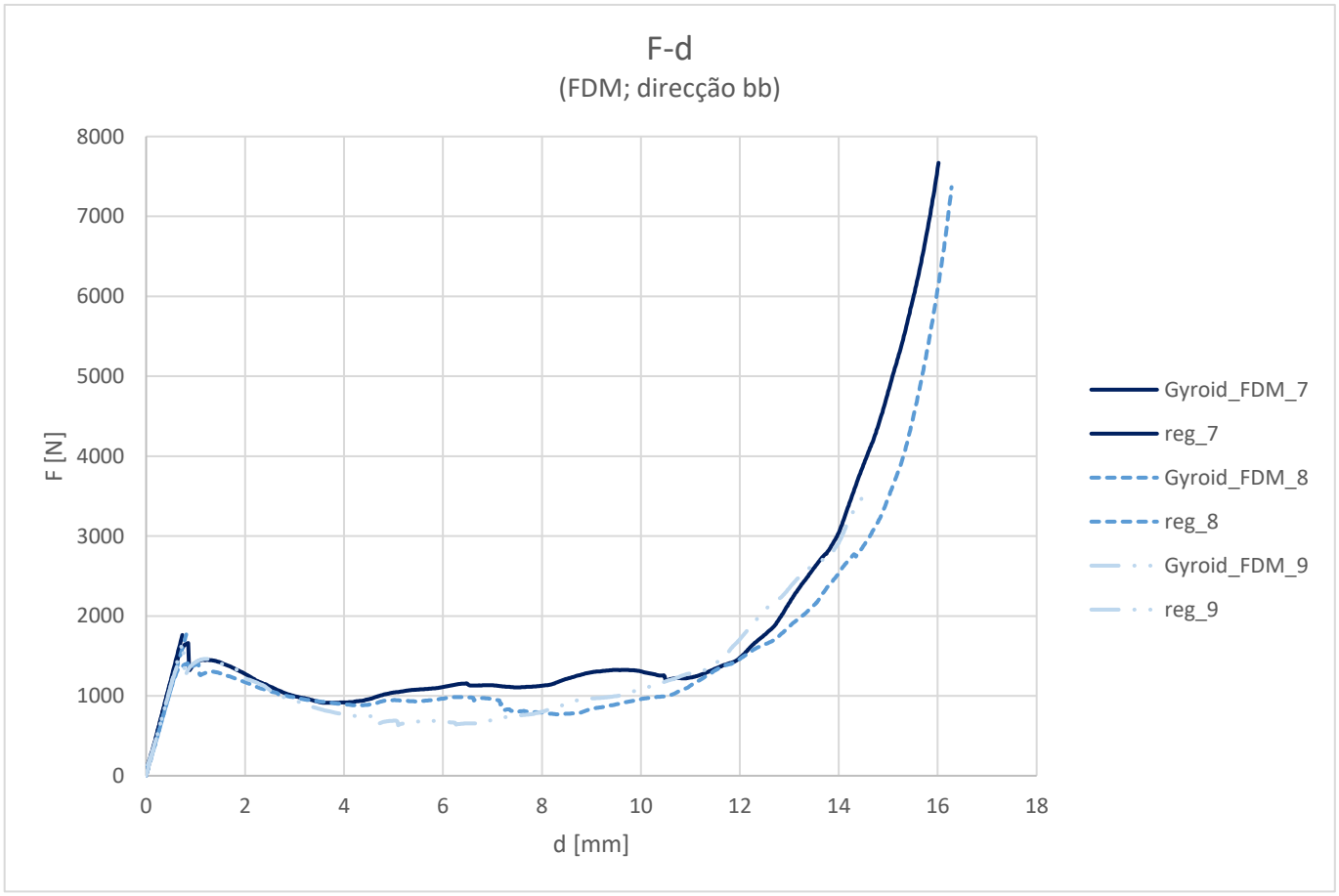
F-d
(FDM; direcção bb)
F [N]
d [mm]
0
1000
2000
3000
4000
5000
6000
7000
8000
0
2
4
6
8
10
12
14
16
18
Gyroid_FDM_7
reg_7
Gyroid_FDM_8
reg_8
Gyroid_FDM_9
reg_9

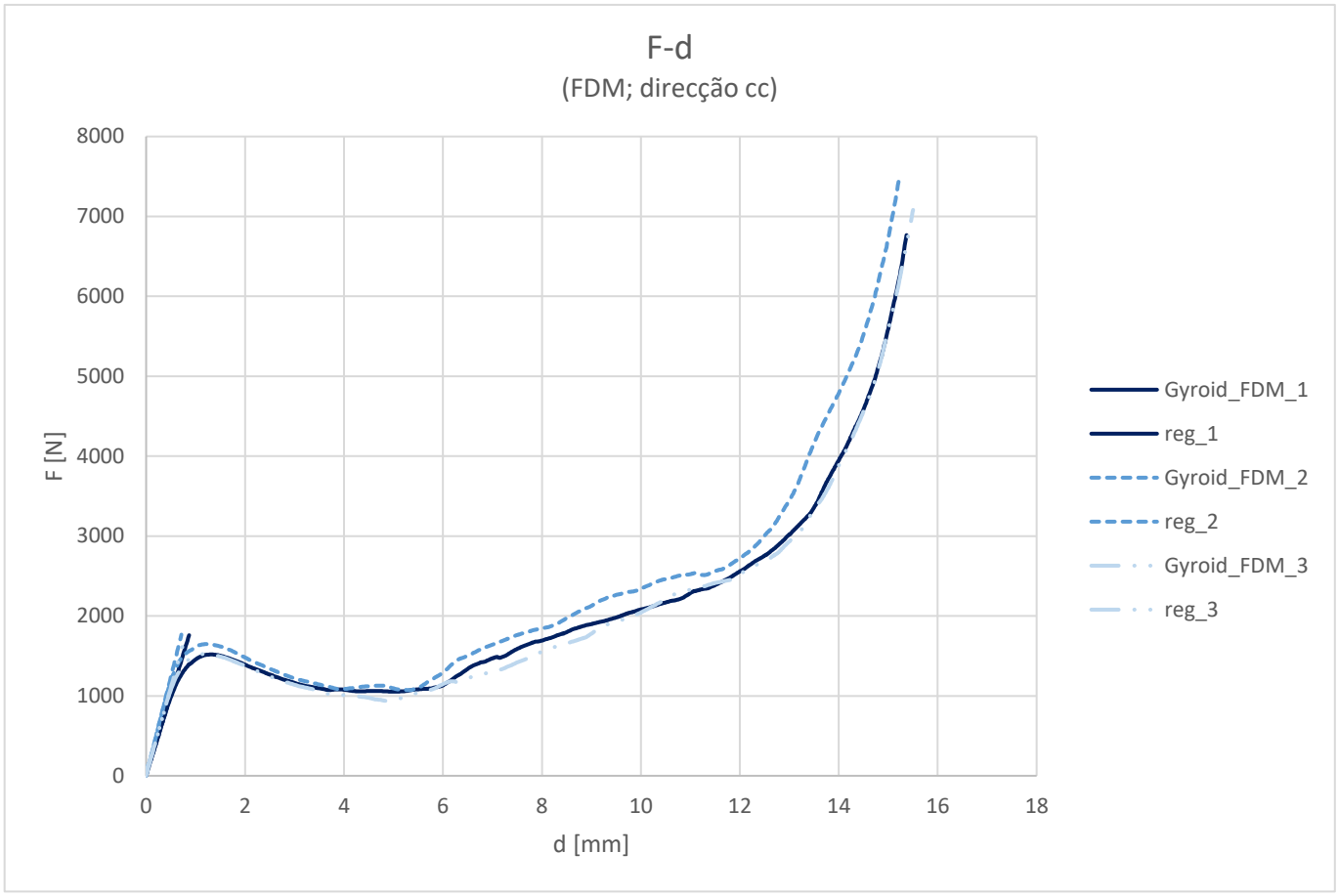
F-d
(FDM; direcção cc)
F [N]
d [mm]
0
1000
2000
3000
4000
5000
6000
7000
8000
0
2
4
6
8
10
12
14
16
18
Gyroid_FDM_1
reg_1
Gyroid_FDM_2
reg_2
Gyroid_FDM_3
reg_3

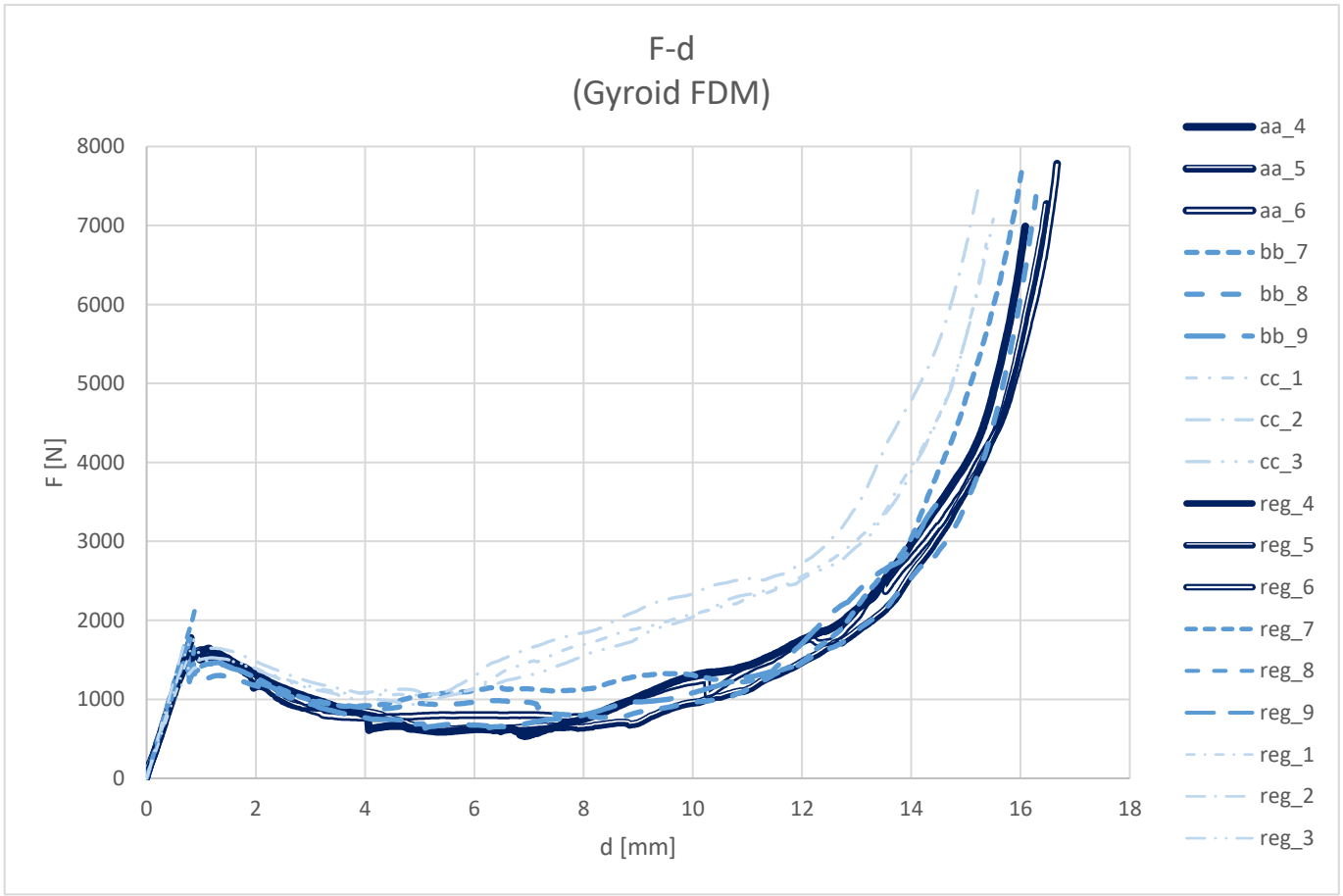
F-d
(Gyroid FDM)
F [N]
d [mm]
0
1000
2000
3000
4000
5000
6000
7000
8000
0
2
4
6
8
10
12
14
16
18
aa_4
aa_5
aa_6
bb_7
bb_8
bb_9
cc_1
cc_2
cc_3
reg_4
reg_5
reg_6
reg_7
reg_8
reg_9
reg_1
reg_2
reg_3

- **Provetes obtidos através de Polyjet**

Dimensões do provete : $20\text{mm} \times 20\text{mm} \times 20\text{mm}$

Velocidade do ensaio : $5\ \text{mm/min}$

Numeração dos provetes ensaiados :

	aa	bb	cc
1	4	7	1
2	5	8	2
3	6	9	3

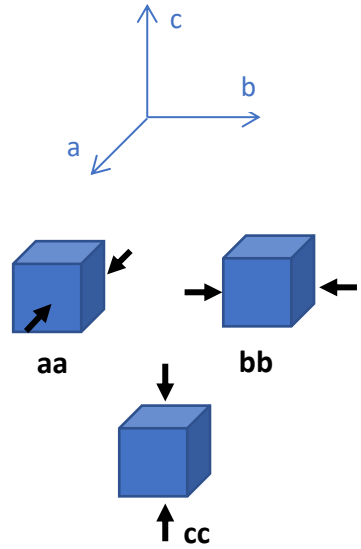

F_Y [N]	aa	bb	cc
1	1233,481	1206,607	1147,457
2	1165,014	1278,387	1154,306
3	1147,988	1269,169	1278,406
med	1182,161	1251,388	1193,389

d_Y [mm]	aa	bb	cc
1	0,712103	0,674309	0,612859
2	0,649186	0,732216	0,634846
3	0,64286	0,730998	0,744336
med	0,66805	0,712508	0,664014

Provetes ensaiados:

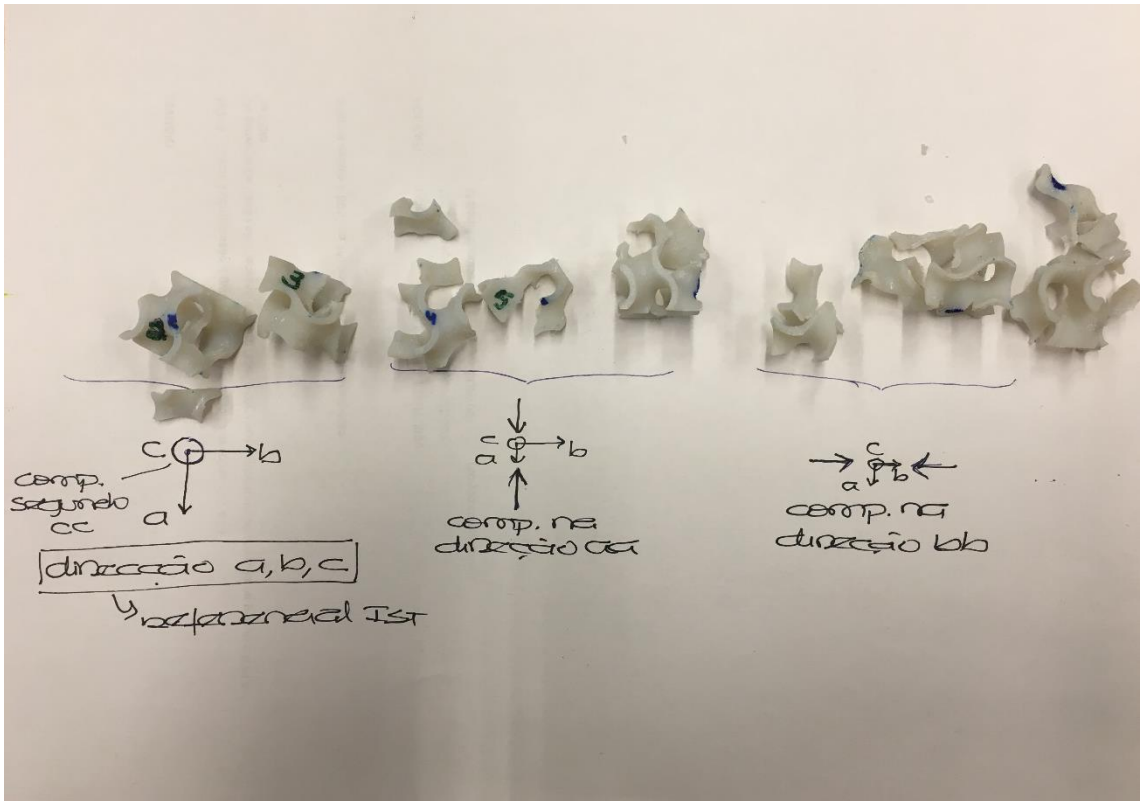

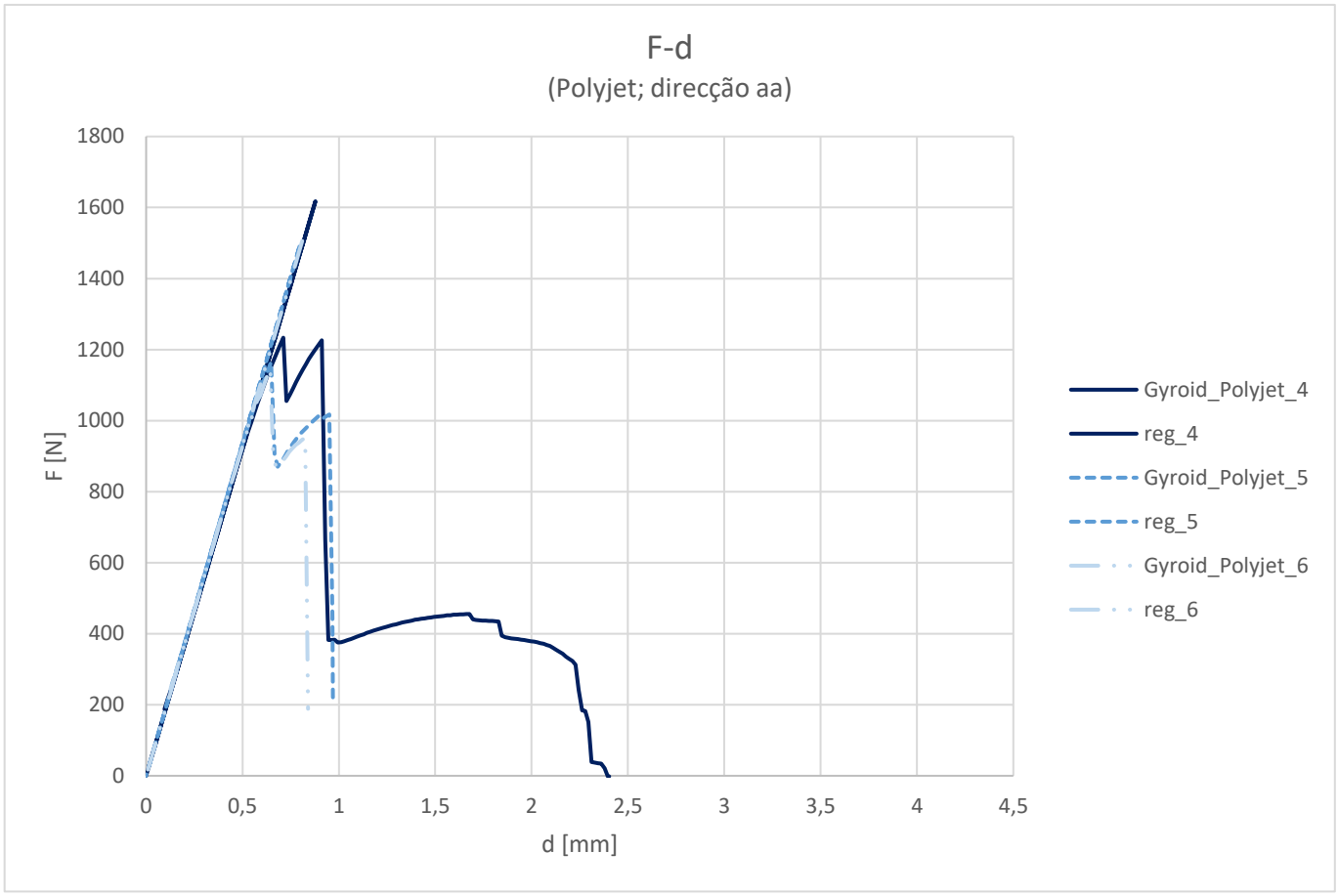
F-d
(Polyjet; direcção aa)
F [N]
d [mm]
0
200
400
600
800
1000
1200
1400
1600
1800
0
0,5
1
1,5
2
2,5
3
3,5
4
4,5
Gyroid_Polyjet_4
reg_4
Gyroid_Polyjet_5
reg_5
Gyroid_Polyjet_6
reg_6

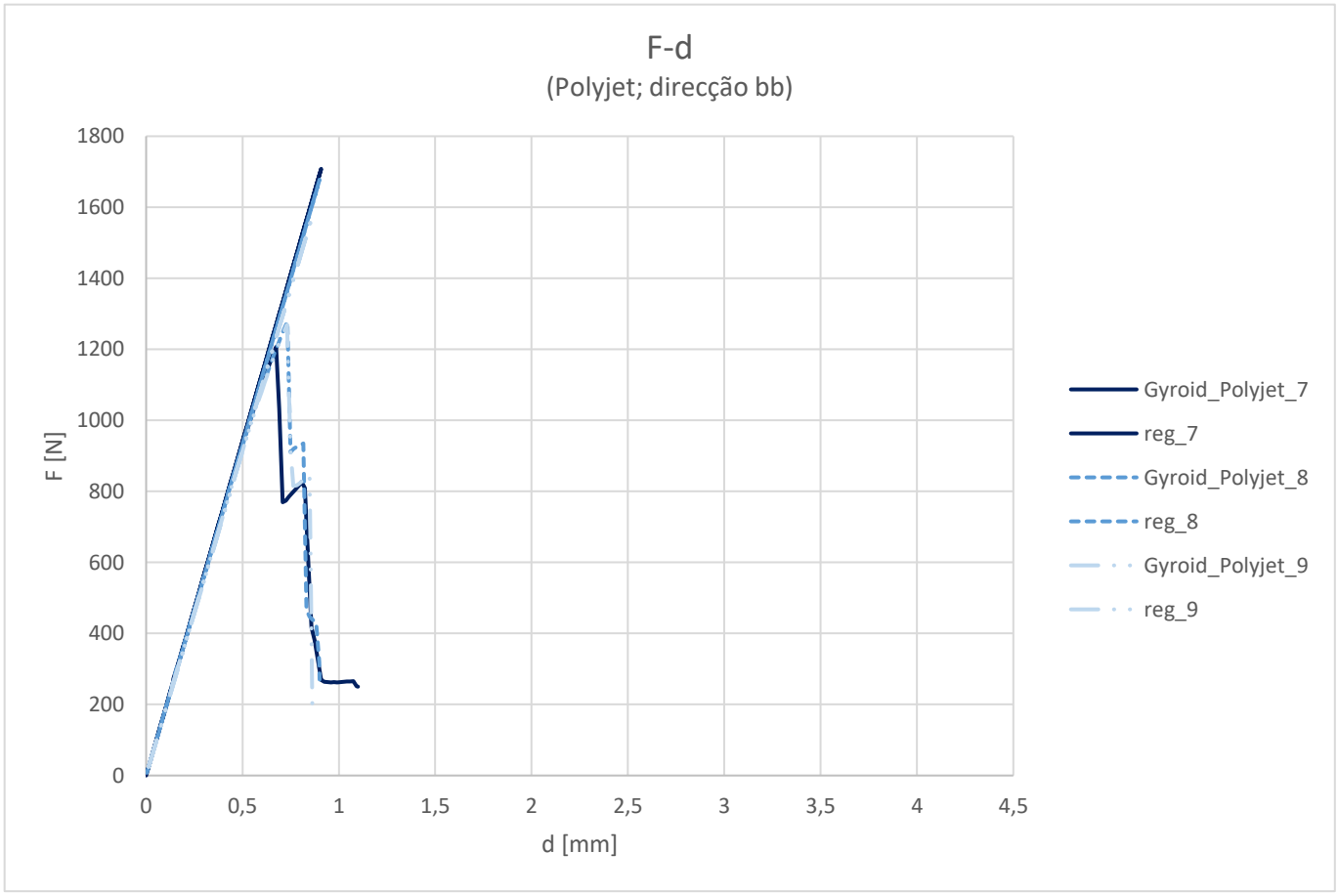
F-d
(Polyjet; direcção bb)
F [N]
d [mm]
0
200
400
600
800
1000
1200
1400
1600
1800
0
0,5
1
1,5
2
2,5
3
3,5
4
4,5
Gyroid_Polyjet_7
reg_7
Gyroid_Polyjet_8
reg_8
Gyroid_Polyjet_9
reg_9

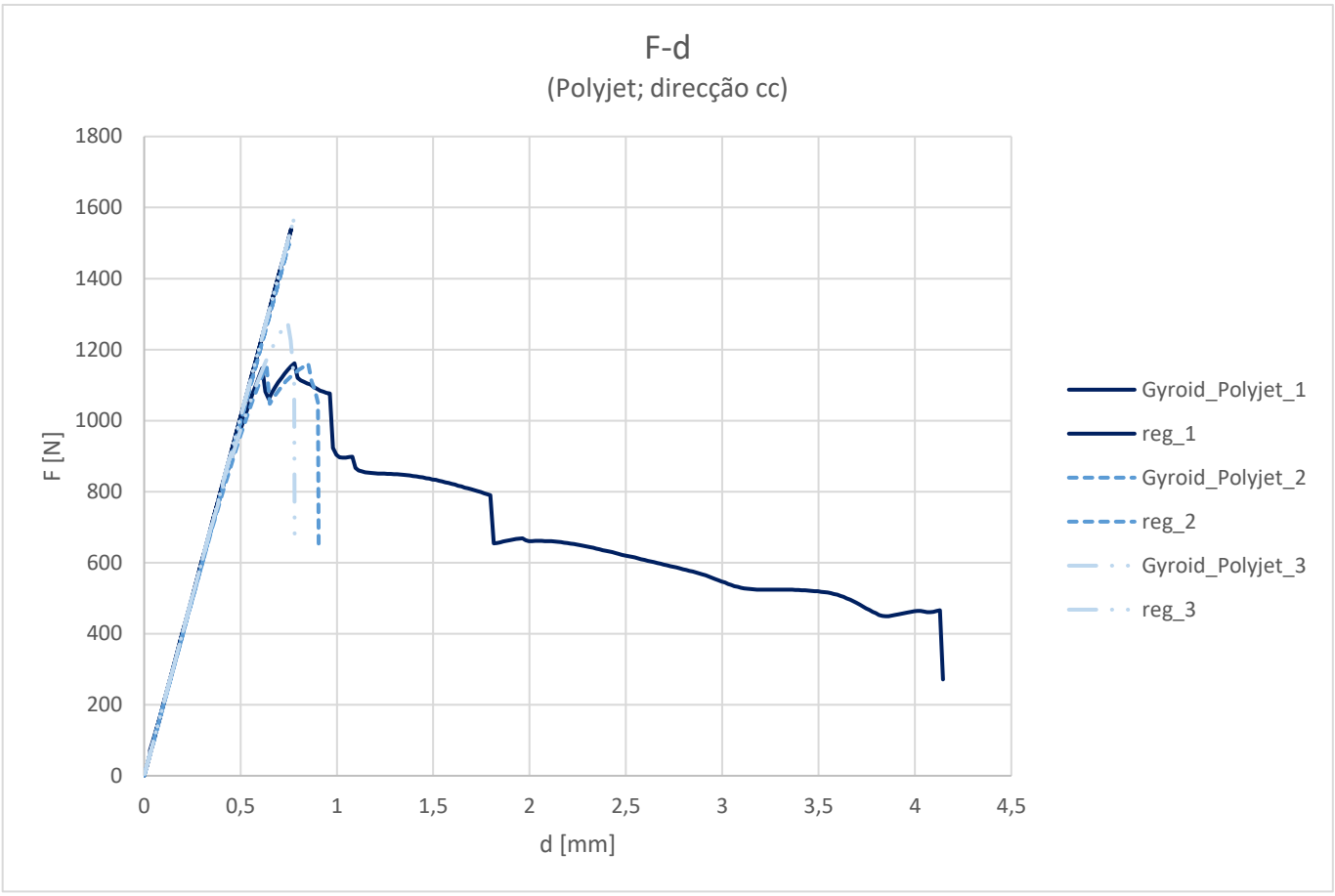
F-d
(Polyjet; direcção cc)
F [N]
d [mm]
0
200
400
600
800
1000
1200
1400
1600
1800
0
0,5
1
1,5
2
2,5
3
3,5
4
4,5
Gyroid_Polyjet_1
reg_1
Gyroid_Polyjet_2
reg_2
Gyroid_Polyjet_3
reg_3

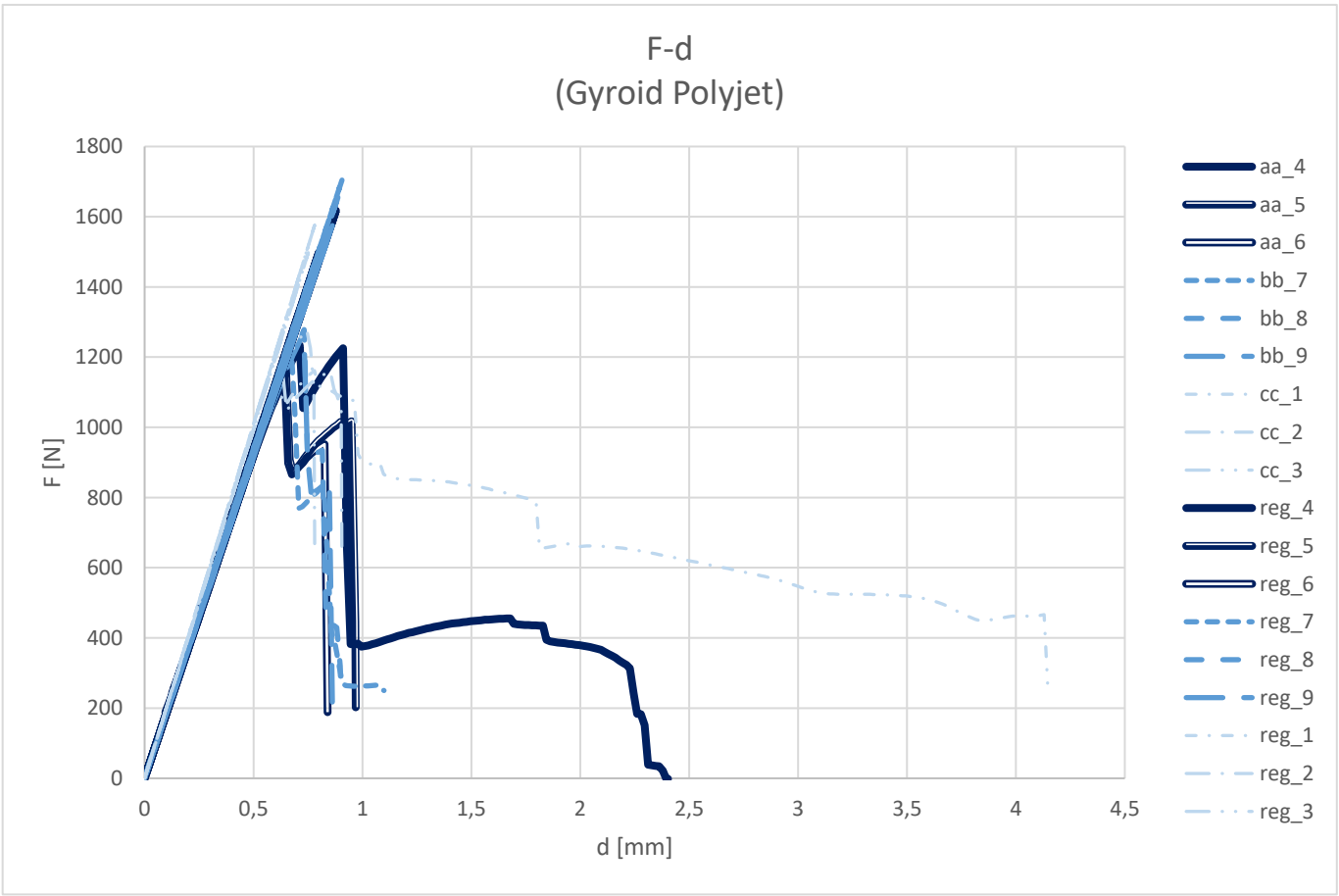
F-d
(Gyroid Polyjet)
F [N]
d [mm]
0
200
400
600
800
1000
1200
1400
1600
1800
0
0,5
1
1,5
2
2,5
3
3,5
4
4,5
aa_4
aa_5
aa_6
bb_7
bb_8
bb_9
cc_1
cc_2
cc_3
reg_4
reg_5
reg_6
reg_7
reg_8
reg_9
reg_1
reg_2
reg_3